ABSTRACT

Application Of Adaptive Optics To The Spectroscopic Investigation Of Small-Scale Solar Structures

by
Klaus Hartkorn

We study bright points, umbral dots and the G-band using a two-dimensional spectrometer and an Adaptive Optics system, which allows us to record high-resolution dopplergrams and residual intensity images. We find evidence that bright points are smaller than 120 km in diameter. Bright points are situated exclusively in regions of enhanced G-band brightness and do not show a change in their shape or a displacement in their position of more than 120 km horizontally over a height range from 0 km to 320 km above photospheric level $\tau = 1$. We do not find velocity differences of more than 100 m/s and a size of 120 km at the locations of bright points compared to the surroundings. Bright points have a higher contrast in the G-band as well as in the atomic spectral lines. We suspect the existence of two contrast enhancement mechanisms for bright points one exclusively for the G-band, one independent of specific spectral lines. We perform calculations using the results of a three-dimensional magneto-hydrodynamical model as input for a radiative transfer calculation, but find little agreement with our observations. The core intensity of the G-band CH lines is significantly influenced by the atmospheric conditions in heights of 160 km and 320 km, but not heights of 40 km. The velocity investigation of a sunspot shows that umbral dots seem to consist of two different types. The first type is the bright part of an intensity pattern of 1000-2000 km size with a corresponding negatively correlated velocity pattern which is probably related to umbral oscillations. The second type consists of localized brightening of a size of not more than 300 km that are associated with down-flowing plasma. Furthermore, we find penumbral grains that have penetrated the umbra and appear as brightenings. We study the velocity signature of penumbral grains and find strong up-flows of solar plasma associated with the inner, bright parts of penumbral grains, where as the general correlation between intensity and velocity within the penumbra is weak.

APPLICATION OF ADAPTIVE OPTICS TO THE SPECTROSCOPIC INVESTIGATION OF SMALL-SCALE SOLAR STRUCTURES

by
Klaus Hartkorn

A Dissertation
Submitted to the Faculty of
New Jersey Institute of Technology
and Rutgers, The State University of New Jersey-Newark
In Partial Fulfillment of the Requirements of the Degree of
Doctor of Philosophy in Applied Physics

Federated Physics Department

May 2003

Approval Page

Application of Adaptive Optics to the Spectroscopic Investigation of Small-Scale Solar Structures

by
Klaus Hartkorn

Dr. Ken Chin, Committee Member
Professor of Physics, NJIT — Date

Dr. Carsten Denker, Committee Member
Assistant Professor of Physics, NJIT — Date

Dr. Dale Gary, Committee Member
Professor of Physics, NJIT — Date

Dr. Philip Goode, Committee Member
Distinguished Professor and Director of Center for Solar Physics and
Director of Big Bear Solar Observatory, NJIT — Date

Dr. Thomas Rimmele, Thesis Advisor
Scientist, NSO — Date

Dr. Haimin Wang, Committee Member
Professor and Associate Director of Center for Solar Research and
Associate Director or Big Bear Solar Observatory, NJIT — Date

Dr. Zhen Wu, Committee Member
Associate Professor of Physics, Rutgers University — Date

BIOGRAPHICAL SKETCH

Author: Klaus Hartkorn

Degree: Doctor of Philosophy

Date: May, 2003

Education:

- Diploma in Mathematics, Technical University Munich, 1998
- Diploma in Physics, Ludwigs-Maximilians-University, Munich, 1998

Presentations and Publications:
Publications

Hartkorn K., Buchner K., 1997, "On Causality In the Exterior Schwarzschild Space-Time," Romanian Journal of Pure and Applied Mathematics, TOME XLII, Nr. 9-10 (1997), 767-773.

Hartkorn K., Moser H.-G., 1999, A New Method of Measuring $\frac{\Delta\Gamma}{\Gamma}$ In The B_s^0 - B_s^0 – System, European Physical Journal C 8, 381.

Harkorn K., 2001, High Resolution Solar Imaging using Blind Deconvolution, 2001 dysu.conf..211He.

Hartkorn K., Rimmele T., 2003, Residual Intensity and Velocity Measurements of Bright Points, in "Current Theoretical Models and High Resolution Solar Observations: Preparing for ATST," ASP Conf. Series, Volume 286, Alexei A. Pevtsov and Han Uitenbroek (eds.), pp. 193-200, (ASP: San Francisco).

Hartkorn K., Rimmele T., 2003, Velocity Measurements of Umbral Dots, in "Current Theoretical Models And High Resolution Solar Observations: Preparing for ATST," ASP Conf.Series, Volume 286, Alexei A. Pevtsov and Han Uitenbroek (eds.), pp. 281-290, (ASP: San Francisco).

Presentations

Hartkorn K., 2001, High Resolution Solar Imaging Using Blind Deconvolution, 2001 dysu.conf..211H.

Hartkorn K., Rimmele T., 2002, Properties Of Bright Points, Abstract booklet of 21st International NSO/SP Workshop on Current Theoretical Models and Future High Resolution Solar Observations: Preparing for ATST held March 11-15, 2002 at the National Solar Observatory at Sacramento Peak, p. 21, (NSO: Sunspot).

Hartkorn K., Rimmele T., 2002, Velocity Measurements of Umbral Dots And Penumbral Grains, Abstract booklet of 21st International NSO/SP Workshop on Current Theoretical Models and Future High Resolution Solar Observations: Preparing for ATST held March 11-15, 2002 at the National Solar Observatory at Sacramento Peak, p. 22, (NSO: Sunspot).

Acknowledgement

Before you write a PhD thesis, you may read other people's PhD thesis and you wonder why they thank so many people in their acknowledgment section. Once you have written a PhD thesis, you don't wonder anymore. Without the help of a lot of people, it is almost impossible complete a thesis successfully. Indeed, you *do* feel very thankful for all the help you have received. Here are some people I want to thank for their help.

- Thomas Rimmele

  Thomas Rimmele was my advisor for this PhD, and it is almost impossible to list all the things he has done for me. He has given me the chance to continue my PhD thesis at the National Solar Observatory and provided me with the opportunity to observe numerous times at the only solar telescope with an Adaptive Optic system. This was essential for the success of this thesis. He made many good suggestions for my observing runs and for the data-evaluation. I never left his office without a new idea or a helpful hint. He always had time for my questions, even though his schedule was extremely busy due to his many responsibilities.

  What can I say more? Thomas Rimmele was the advisor everyone wishes for!

  Thank you Thomas !!!

- Phil Goode

  Phil Goodie has provided me with the opportunity to work in the Unites States at the Sacramento Peak Solar Observatory. He has been very helpful with all problems I encountered and I want to thank him for his suggestions and remarks that helped me to improve my thesis.

- Haimin Wang

  I want to thank Haimin Wang for being my official advisor and for all the help he gave me during the various administrational problems during this PhD thesis. I am looking forward to work with him in the future.

- Han Uitenbroek

  I want to thank Han Uitenbroek very much for his contributions in this thesis. He has provided his radiative transfer program RH-code for the calculations presented in this thesis. Such a program is the result of many years of hard work, and I appreciate his willingness to share it with me very much. He also processed the data from MHD simulations to provide an input for the radiative transfer calculations. Every time I encountered a problem during the calculations, he was very helpful and patient in resolving them. I also had

many discussions with Han about the data that I took and the results that came from it.

- Steve Keil

  Steve Keil, the director of the NSO, taught me how to play volleyball and how to mix a perfect Sunspot Margarita. I want to thank him for his hospitality and warm welcome to the Sunspot community.

- DST Observing Staff

  I want to thank the DST observing staff, Steve Hegwer, Brian Armstrong, Mike Bradford, Jo Elrod, Steve Fletcher and Doug Gilliam for their excellent support during all of my observation runs. The DST and especially the camera and control system is several years old and it is not easy to operate or maintain this system. Nevertheless, the whole observing team did and excellent job in making all my observation runs successful (except for the seeing part, sometimes). Good results come from good observations, and good observations come from good observers! Thank you !!

- Doug Gilliam

  I want to mention Doug separately here, since his effort and dedication to his job is outstanding and never stopped to amaze me. He works as much as two people, yet he is always friendly and helpful. He also did the drawings for my observing setups and he has very much contributed to my PhD.

- Brady Jones

  Brady helped me with all the computer problems that I encountered during my work. He was always extremely helpful, friendly and knowledgeable. I am very much indebted to him for helping my out and contributing to the success of my work.

- My fellow Students

  ... had a big part in making my stay in Sunspot more enjoyable. I want to in the order of appearance: Arnaud Premat, Larry Murray and Jose Marino. Surviving on a mountain is much easier if you have company!

TABLE OF CONTENTS

Chapter **Page**

TABLE OF CONTENTS
(continued)

Chapter **Page**

TABLE OF CONTENTS
(continued)

Chapter **Page**

LIST OF TABLES

LIST OF FIGURES

Figure **Page**

LIST OF FIGURES
(continued)

Figure **Page**

LIST OF FIGURES
(continued)

Figure **Page**

LIST OF FIGURES
(continued)

Figure **Page**

LIST OF FIGURES
(continued)

Figure **Page**

LIST OF FIGURES
(continued)

Figure **Page**

LIST OF FIGURES
(continued)

Figure **Page**

LIST OF FIGURES
(continued)

Figure **Page**

Figure **Page**

Figure **Page**

LIST OF FIGURES
(continued)

Figure **Page**

Figure **Page**

LIST OF FIGURES
(continued)

Figure **Page**

LIST OF FIGURES
(continued)

Figure **Page**

Figure **Page**

- Arcsec

  One arc-second is defined as the 3600 part of one angular degree. At the average distance of 149597870 km from the earth to the sun, it is equivalent to about 720 km.

- Blaze Angle

  Angle of the reflection off a grating with the highest ratio of incoming intensity to reflected intensity. Blazing is achieved by shaping a grating like a saw-tooth. blazing has the purpose to concentrate the light reflected off a grating into one particular order to achieve higher intensity and therefore shorter exposure-times.

- Dark Image

  Thermal noise and read-out noise causes each pixel of a CCD camera to record an intensity even when no light reached the CCD chip. This offset is corrected by recording an image with the same exposure-time as the observation but without any light (dark image) and subtracting it from each observed image.

- Dopplergram

  In Solar physics, velocity maps are also called Dopplergrams since the Doppler effect is used to measure the velocity. The classic dopplergram measures the shift of a spectral line using only two images (red wing and blue wing). The process is explained in detail in Chapter 2.4.3 and in Chapter 2.3.2.

- Dual Mode

  The dual mode is a special operting mode of the Universal Birefringent filter that allows us to option two images with slightly different wavelength at the same time. This mode is described in Chapter 2.3.2.

- Flat-Field

  All pixels of a CCD camera have a slightly different sensitivity. Therefore, an image of an equal intensity object (every pixel is supposed to have the same intensity) is recorded with each observing run. This image is called flat-field. By dividing any recorded image by this flat-field, the different sensitivity if the CCD pixels is corrected.

- Full Width at Half Maximum (FWHM)

  The FWHM describes the bandpass of a spectral filter. It is the distance in mÅ of the the points in the spectral bandpass of a filter where the transmission has dropped to 50 percent (Chapter 2.3).

- Grating

  A grating is a mirror with equidistant missing parts. Therefore, reflection does not only occur at the angle of incidence, but also at angles where positive inter

- Magneto-Hydrodynamical Simulations

  MHD simulations are used to calculate the dynamic behavior of conductive plasma, e.g. in the solar atmosphere. MHD uses a set of equations that are a combination of the Navier-Stokes hydrodynamical equations and the Maxwell electrodynamic equations [45].

- Modulation Transfer Function (MTF)

  The two-dimensional Fourier transform of the PSF is called MTF. When integrated over the angular component, the resulting one-dimensional MTF is a measure for the average suppression of spatial frequencies.

- Landee Factor

  The Landee- factor represents the intrinsic strength of the Zeeman effect of an atomic transition and is explained in Chapter 2.4.1.

- Photosphere

  The photosphere is a layer of about 600 km height in the solar atmosphere. The light that we can see in the visible, from about 400 nm to 750 nm originates almost exclusively in the photosphere.

- Point-Spread Function (PSF)

  The PSF is defined as the image of a points source rendered by an optical system. In the ideal case, the PSF is the airy disc with rings due to the diffraction of light at the entrance aperture. In reality however, the PSF is changed from an Airy disc by imperfections of the optical system and the disturbances of the earth atmosphere. These disturbances are discussed in Chapter 2.2.

- Radiative Transfer Calculations

  Radiative transfer is used to calculate the final emergent intensity from the solar surface, one the physical parameters like temperature, pressure and composition of the solar atmosphere is know, e.g. as the result of a MHD simulation. This method is described in 'The sun' [66].

- Residual Intensity

  The residual intensity is the core intensity of a spectral line divided by the continuum intensity. This comparison of the core and the continuum intensity is also a comparison of the atmospheric conditions in different heights in the

solar atmosphere, since the core of a photospheric spectral line always forms higher than the nearby continuum. This is explained in Chapter 2.4 and Chapter 3.1.

- RMS Image Contrast

  The root-mean-square (RMS) image contrast is a measure for the inherent intensity variation within an image. When a sequence of images of the same area on the sun is recorded, the image with the highest RMS value was recorded during the best seeing conditions. The RMS image contrast is defined as

$$RMS = \sqrt{\sum_{i=allpixels} (x_i - x_{mean})^2}$$

- Solar Dynamo

  The solar dynamo generates the solar magnetic field from the shearing motion of the conducting solar plasma. This is explained in detail in 'The sun' of Stix /citestix. The magnetic field of the earth is generated in a similar way.

- Strehl Ratio

  The Strehl ratio is a measure for the performance of an optical system. It is defined as the ration of the peak intensity of the measures PSF and the theoretical possible peak intensity of the PSF. This is also described in Chapter 2.2.

- Universal Birefringent Filter (UBF)

  The UBF is a spectral filter with as FWHM of about 200 mÅ. It is used to record two-dimensional images of the solar surface at a specific wavelength. It is described in Chapter 2.3.2.

- Wilson Depression

  The temperature profile within a sunspot is similar to the photospheric temperature profile shifted several hundred kilometers lower. Therefore, sunspots appear as slight dips in the solar surface that can be seen when a sunspot is close to the limb. This dip is called Wilson effect or Wilson depression.

CHAPTER 1

Introduction

1.1 The Structure of the Sun

The radius of the sun, defined as the radius in the visible wavelength, is $r = (6.9626 \pm 0.0007) \cdot 10^8\ m$. The average density of the sun is $1.498\ g/cm^3$. The temperature of the solar surface is about 5578 K and the total luminosity is $L = (3.845 \pm 0.006) \cdot 10^{26}\ W$. The structure of the sun is shown in Figure 1.1. The core of the sun extends to about 0.25 solar radii. In the core of the sun, energy is produced by nuclear fusion at a temperature of about $T = 1.5 \cdot 10^7\ K$. The energy is transported by radiation through the radiative envelope, which extends to about 0.86 solar radii. In the next layer of the solar atmosphere, the convective layer, the convection of solar plasma becomes the main mechanism of energy transport. The convective envelope extends outwards to the solar surface, defined as the height of the solar atmosphere where $1 - 1/e$ of the photons reach the interstellar space without further scattering. The atmospheric layer that includes the solar surface is called photosphere. Almost all solar light visible to the naked eye originates in the photosphere, which is only about 400 km high. The next layer of the sun, about 2500 km in height, is the chromosphere. Even more outward is the solar corona, that extends far into space, and the solar wind, related to coronal mass ejections, that generate the Northern Lights on earth.
In our study, we concentrate on the solar photosphere. The solar photosphere is the deepest layer of the sun we can investigate directly, and it is therefore the closest atmospheric layer to the generation and emergence of the solar magnetic fields, one of the main underlying topics of this investigation.

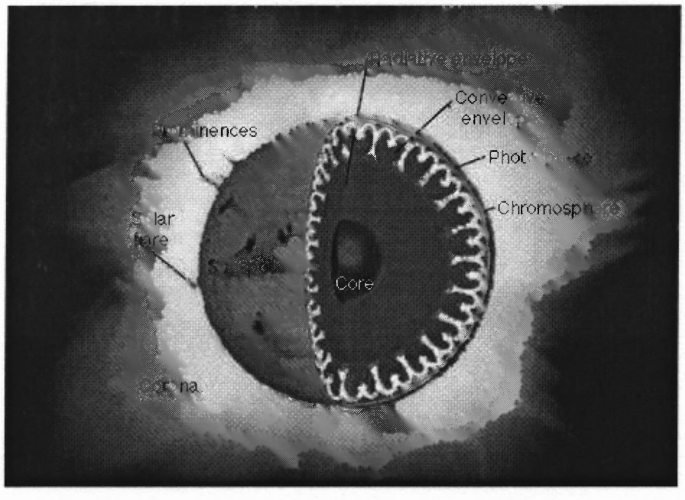

Figure 1.1 The structure of the solar atmosphere. Image from [37].

1.2 Introduction to Solar Physics

The motion of the sun has been studied for thousands of years, yet the study of the sun itself started with the invention of the telescope. The first telescopic observations revealed that the surface of the sun is covered by dark areas, the sunspots. With the improvement of telescopes, more solar structures such as umbra and penumbra, facula, and granulation were discovered. The progress can be studied in the classic book of this era, 'Le Soleil' by Secchi [55], whose detailed drawings are still astounding today.

In many cases however, the physical nature of these features was not well understood. It was the application of spectroscopy to solar research that finally made it possible to explore the physical properties of solar features. The solar spectral lines were discovered by Fraunhofer [19] who used spectral lines for measuring the refractive index of glass. The physical importance of spectral lines was realized later by Kirchhoff [27], who used spectroscopy for chemical analysis and applied it to the study of the sun. Studying the solar spectrum, Lockyer [31] discovered the element helium. Later, Hale [23] and Evershed [17] were the first to obtain dopplergrams and magnetograms of sunspots. This was the beginning of solar physics. Spectroscopy in various forms is still the main tool of solar research.

To discover new small-scale structures and investigate their properties, solar researchers tried to achieve better spatial resolution. Over the years many new structures were discovered. This raised the question if there is a spatial limit for small structures on the solar surface or if the spectrum of spatial scales continues on indefinitely. One can address this question by looking at the photon mean free path. The photon mean free path in the continuum is in the order of 100 km, although it can be much smaller for wavelength in the core of a spectral line. If two points in the solar atmosphere are closer than the photon mean free path there is a substantial energy transfer due to radiation. The smaller a structure is, the harder to sustain its individuality. This line of reasoning was used by Bruls [11] to demonstrate that little fine structure on scales smaller than 10-30 km exists. Telescopes of an aperture larger than 4 m are required to resolve this scale at a wavelength of 500 nm. Several new projects to build a solar telescope with a large aperture include GREGOR of the Kiepenheuer Institute of Solar Physics with an aperture of 1.5 m, an upgrade of the Dutch Open Telescope to 1.4 m, a 1.6 m New Solar Telescope at Big Bear Solar Observatory and the Advanced Technology Solar Telescope project with an aperture of 4.0 m of the National Solar Observatory.

1.3 Problems of High Resolution Solar Observations

A large telescope alone is not enough to perform studies of small solar structures. Early observers (e.g Secchi [55]) already saw granules, penumbral grains and filaments, and umbral dots and made impressive drawings of these features. The

desire to further resolve and understand these features stimulated the development of better instruments and telescopes. However, progress has been slow until it was realized that special measures are needed to reduce the effect of daytime seeing. To eliminate local seeing effects from ground-turbulence [9], telescopes were put on towers and/or placed at specific locations. Some telescopes were evacuated to reduce the seeing inside the telescope caused by optical elements heated to a higher temperature than their surroundings. The most drastic and very successful approach was to place telescopes above the earth's atmosphere. Balloon experiments [2] or spacecraft [18] were used for this purpose. The drawback of the latter method is the high cost, the limited aperture, and the limited number of post-focus instruments. It is difficult to maintain and upgrade these telescopes. Further disadvantages are the low data-transfer rate and the short lifetime of such an instrument.

All measures for ground-based telescopes cannot eliminate the seeing effects of the earth atmosphere completely. Usually, an average to good site has a daytime seeing of about 1.0 arcsec. On a very good site one can expect a few hours of 0.5 arcsec seeing within a period of two weeks. Nevertheless it is sometimes possible to obtain diffraction limited images. An example is the (almost) diffraction-limited eleven-hour time-series at the Swedish Vacuum Telescope (SVST). This time series was obtained using only a correlation-tracker and frame-selection [56]. Data like this time-series is very valuable for solar research, but unfortunately it does not contain any information about velocity, magnetic field and temperature of the solar plasma. The use of this kind of data is limited to morphological studies.

For high-resolution observations using broad band-imaging a short exposure-time in the order of the correlation-time of the earth's atmosphere around 10 ms are sufficient. These short-exposures make it possible to freeze moments of good seeing and therefore reach the diffraction limit of the telescope occasionally. Observations with sufficient spectral resolution for physical analysis require a much longer-exposure-time, typically longer than 1000 ms. The long exposure-times compensate for the fact that the instrument cuts off most of the light. This fundamental problem has made it impossible up to now to obtain diffraction-limited dopplergrams, magnetograms, and spectra. These types of observations were limited to a spatial resolution of 0.5 arcsec. Only the recent development of an Adaptive Optics (AO) system made the combination of high spatial and high spectral observations possible. We use the AO system of the Dunn Solar Telescope to obtain dopplergrams and residual intensity measurements with a spatial resolution never reached before. This allows us to investigate the physical properties of solar fine structure.

1.4 The Importance of Fine Structure

It is important to study the fine structure of the sun, because the small structures are often the essential detail needed to understand a solar phenomenon. One example is

the umbra of a sunspot. Low-resolution observations were in perfect agreement with a monolithic flux-tube model of a sunspot. Theoretical calculations show that a monolithic flux-tube that suppressed convection would have a much lower temperature than observed in a sunspot [8]. The energy transferred by radiation alone only produces one percent of the energy that is actually measured [8]. This contradiction is called umbral heating problem. However, if observed at higher spatial resolution, the sunspot umbra shows fine structure in the form of bright dots, the umbral dots [56]. The umbral dots are hotter than the surrounding umbra [21]. Even though the mechanism is not understood yet, it is evident that understanding these features is essential to solving the umbral heating problem.
Another example that demonstrates the importance of solar fine structure concerns photospheric bright points, which are small brightenings occurring mostly in the intergranular lanes. They are related to the magnetic flux elements [6] and perhaps individual flux-tubes. High-resolution observations of active regions show that there are about 0.5 bright points per $arcsec^2$ [7]. Bright points and their magnetic field may carry substantial energy and hence make a significant contribution to the heating of the corona. Coronal heating is one of the big outstanding problems in solar research since it is unclear how the photosphere with a temperature of about 5800 K can heat the coronal plasma to temperatures of over several million Kelvin.
Furthermore, bright points occur mainly in active regions and are believed to be the first manifestation of emerging flux [6]. It is possible that a combination of many of these flux elements may result in a flux concentration large enough to form a pore, and eventually a sunspot [42]. Bright points are often referred to as the elementary building blocks of all solar magnetic structures. Understanding them is essential in understanding the fundamental processes that form structures on the solar surface [15]. In summary solar fine structure is needed to explain and understand many large-scale phenomena on the solar surface.

In this thesis we focus on three main topics: bright points, the G-band, and umbral dots. Bright points and umbral dots are the fine structures found in the quiet sun and the umbra of a sunspot, respectively. The G-band is the band-head of the CH molecule.
In the three following sections, we describe the importance of each of these main topics including their specific importance to solar research, the current state of knowledge and open questions.

1.5 Bright Points

1.5.1 The Importance of Bright Points

Most of the structures on the solar surface such as sunspots, facula, plages, prominences, flares, etc. are associated with the solar magnetic field. It is not entirely understood how this magnetic field forms, though some kind of dynamo process must

be involved [66]. The dynamo can work on a large (global) scale at the bottom of the convection zone or it can be a small-scale (surface) dynamo [66] or both. The magnetic field affects the activity of the sun, the solar cycle, and space weather.
It is believed that most of the magnetic flux outside of sunspots is localized in small-scale, kilo Gauss magnetic concentrations called flux-tubes [64]. These elements have a size of 100 km or less and are associated with bright points [6]. The bright points occur in regions of high magnetic flux, sometimes before the formation of sunspots or after their decay. Therefore, they may be a signature of the large-scale field, generated by a large-scale, sub-photospheric dynamo. Understanding these flux-tubes may provide insight about the dynamo processes generating the solar magnetic field.

1.5.2 Current Knowledge

1.5.2.1 Observations Bright Points were discovered around 1973 in filtergrams of the wings of broad spectral lines like H_α (Dunn [16], Mehltretter [33]). First they were called plages or intergranular network because even the highest-resolution images at that time did not have sufficient resolution to reveal that plages consist of unresolved bright points. As telescope resolution improved it became clear that this new structure has the form of small, more or less round points located in the intergranular lanes [35]. Subsequently, bright points were found in the continuum [35]. Morphological studies of bright points including the lifetime, proper motion and the shape and size of bright points were done by Mueller [35], [36] and Berger [6], [7]. Newer studies by Berger et al. [6], [7] use more sophisticated methods of data processing including the automated selection of bright points. These studies show that bright points have a life-time of a few minutes and an average size of about 220 km (0.30 arcsec). Bright points can be as small as the resolution-limit of the telescope (120 km or 0.17 arcsec). The shape of bright points is mainly round although about 30 percent are elliptic [7].
The bright point brightness in the continuum is comparable to granule brightness if no PSF deconvolution is performed, but bright points are significantly brighter in a region of spectral lines called the G-band. This increase in contrast is about 30 percent relative to the quiet sun and is almost independent of the size of the bright point. The higher contrast in the G-band provides a possibility for easy identification of bright points. The term G-band bright points was adapted, although the connection between the solar features bright point and the spectral lines remained unclear. We will not use this term.
It was speculated [59] that there is a connection between small-scale emerging magnetic flux and bright points, since the plages and the regions of emerging magnetic flux often coincide. The difficulties of obtaining high-resolution magnetograms made a proof very difficult and only recently this connection was observationally verified by Berger [6].

With the exception of Berger [6] all studies of bright points have been limited to imaging. Images alone (Fig. 1.2) cannot provide any information about the physical conditions in bright points. Spectral information is necessary to extract this information, but this requires long exposure-times as explained in Chapter 1.2 and therefore an AO system to reach the required resolution.

1.5.2.2 Model-Calculations Models of flux-tubes have very different levels of sophistication. The one-dimensional, semi-empirical model of Solanki [59] describes the atmospheric conditions within a flux-tube. Steiner [63] and Sanchez-Almeida [50] used this model to calculate the contrast enhancement of bright points in the G-Band. These calculations predict bright point contrast and the formation height of the G-band. Steiner [63] also makes predictions about the contrast enhancement of atomic lines like Fe and Ti. He predicts a contrast enhancement for bright points for atomic lines with a low ionization potential like Fe I but finds no contrast enhancement for spectral lines with a higher ionization potential like Ti II.

Two-dimensional magneto-hydrodynamic calculations were performed by Steiner [64], [65] which confirm that bright points are formed by convection. He used a grid of 240×120 data-points with a spacing of 10 km covering 2400 km horizontally and a vertical range from -800 km to $+600$ km. In a first simulation, a plane parallel atmosphere from Spruit [60] is perturbed with a small velocity field and no magnetic field. After the convective pattern of granulation has evolved, he superimposes a uniform magnetic field of 400 G. Within 150 seconds of evolution flux-tubes develop according to the following process which can be seen in Figures 1.3 and 1.4.
The thermal convection of solar plasma sweeps the magnetic field initially evenly distributed in an active region to the intergranular lanes because the plasma and magnetic field cannot move independently due to the high conductivity of the solar plasma. The concentrated magnetic field is further intensified by the 'convective collapse' [41], [60]. The down-flowing plasma inside the forming flux-tubes is thermally insulated by the magnetic field and therefore its temperature increases nearly adiabatic with depth. The atmosphere on the outside is significantly super-adiabatic, i.e. the temperature rises more rapidly than the temperature inside of the flux-tube. This way the flux-tube is compressed until the magnetic pressure balances the outside pressure. The growing field suppresses further down-flow of plasma, because it prevents plasma entering through the sides of the flux-tube and the replenishing can only occur from the top of the flux-tube where the density of the plasma is very small. This process leads to a flux-tube that is almost evacuated. In the beginning, a strong down-flow of plasma occurs at the location of the forming flux-tube which reaches several km/s. When the down-flowing plasma reaches the much denser layers of the solar atmosphere, it produces an upward shock-front that can reach a velocity of several km/s. After the formation of the flux-tube, the model predicts narrow down-drafts at the boundary of flux-tube and photosphere.

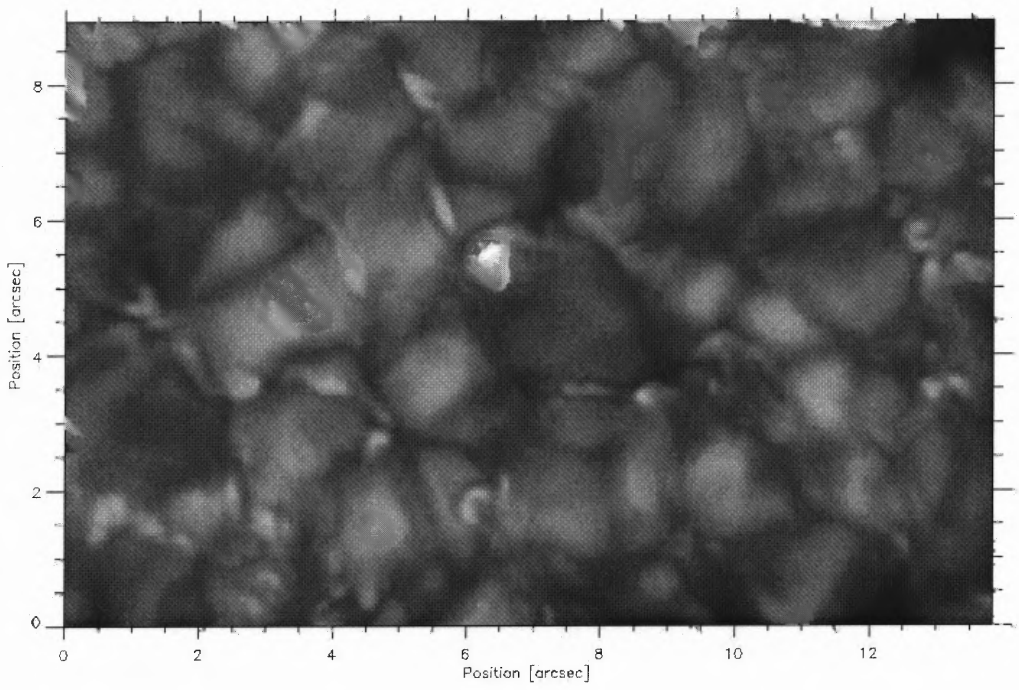

Figure 1.2 High Resolution image of G-band bright points recorded at the Dunn Solar Telescope by Klaus Hartkorn and Kai Langhans in a previous observation run.

The reason for these down-flows is radiative cooling of hot plasma at the boundary because the flux-tube is evacuated. These predicted down-flows have a velocity of up to several km/s at very small spatial size of about 0.1-0.3 arcsec.
In the last time-step the disappearance of a flux-tube can be seen. Bright points should dissolve by fragmentation due to the inherit instability of flux-tubes [40]. The reason for this instability is that the total energy of a flux-tube does not change if its border is perturbed in a way that the enclosed area does not change, i.e., there is no confining force for a bright point. Thus, flux-tubes change their shape more and more until they finally split or dissolve. Twisting the magnetic field in a flux-tube or surrounding the flux-tube by a whirl-flow can stabilize bright points. No observational evidence for these mechanisms has been found yet.
In the second part of the simulation different initial conditions are applied. The calculation starts with a flux-sheet already embedded into the same plane parallel atmosphere from Spruit [60]. In this simulation, the behavior of a single flux sheet is studied in more detail. The model also predicts the strong down-drafts around the flux-sheet with a size of about 100 km (0.15 arcsec) and velocities of 3 km/s. This model also suggests a larger appearance of a bright point in higher atmospheric layers. This is is due to the enlarged surface area of the magnetic field in Figure 1.5 which is a result of the decreasing atmospheric pressure relative to the magnetic pressure. Whether this enlarged magnetic surface area translates into a larger size of bright points in intensity images can only be answered by a radiative transfer calculation. No such calculation has been performed to our knowledge. Nevertheless, we are checking for any size differences or shifts of bright points for different atmospherics heights using residual intensity images and for the down-drafts at the edges of flux-tubes and flux-sheets.
Nordlund, Stein, and Bercik [62] developed the most sophisticated model. They conducted a full three-dimensional numerical simulation of magneto-convection of the solar plasma. The stunning intensity-maps resulting from these simulations (Fig. 1.6) show features resembling bright points although they were not put in there intrinsically. The initial conditions of the calculations are a field-free atmosphere with an evenly distributed magnetic field superimposed. The time evolution using the MHD equations is calculated. We will use these calculations together with a radiative transfer code developed by Uitenbroek [68] to calculate intensities, residual intensities, and velocities. We compare the results of these calculations to our observations in Chapter 4.

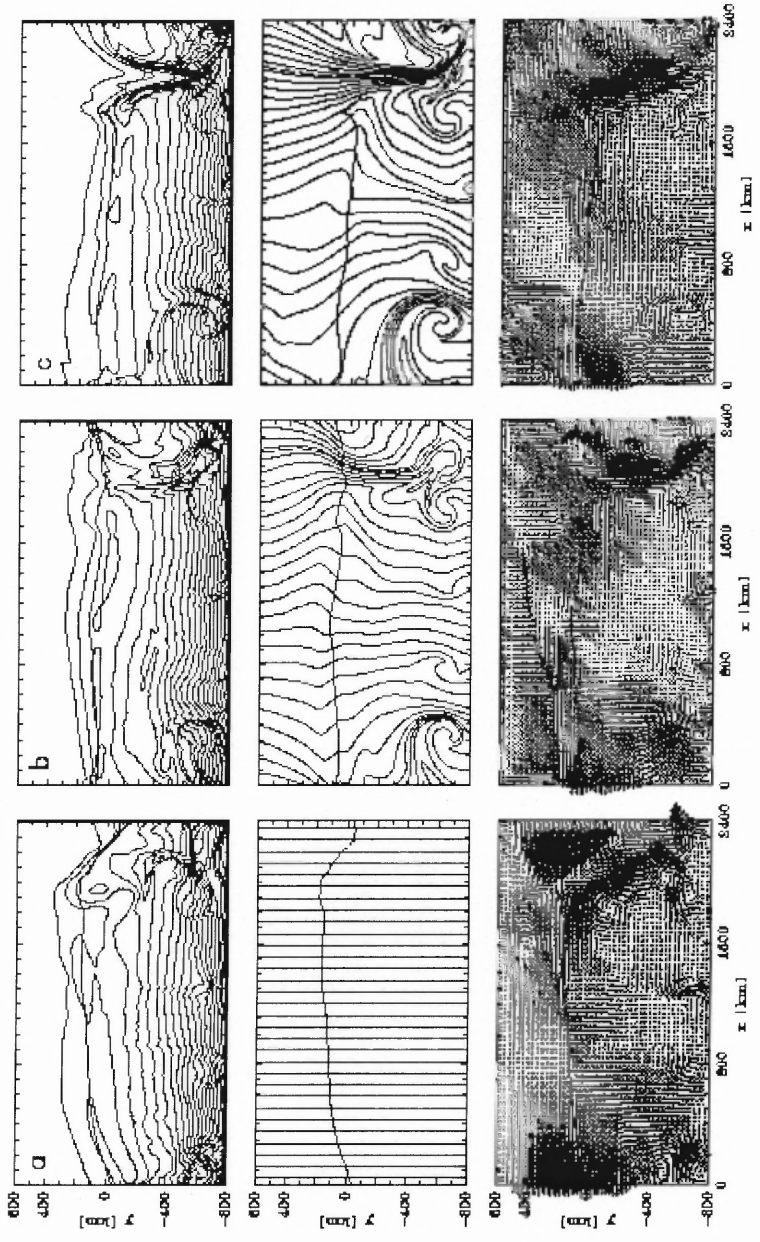

Figure 1.3 The formation process of a flux-tube calculated with the two-dimensional model of Steiner [65] (part 1). The top images are the density of the solar plasma, the middle images are the magnetic field lines and the bottom images are the velocity. Image 'a' is at time-step 0 s after the uniform magnetic field of 400 Gauss is superimposed, image 'b' is at the time-step 50 s and image 'c' is at the time-step 100 s. One can see the formation of a flux-tube at the position 2000 km.

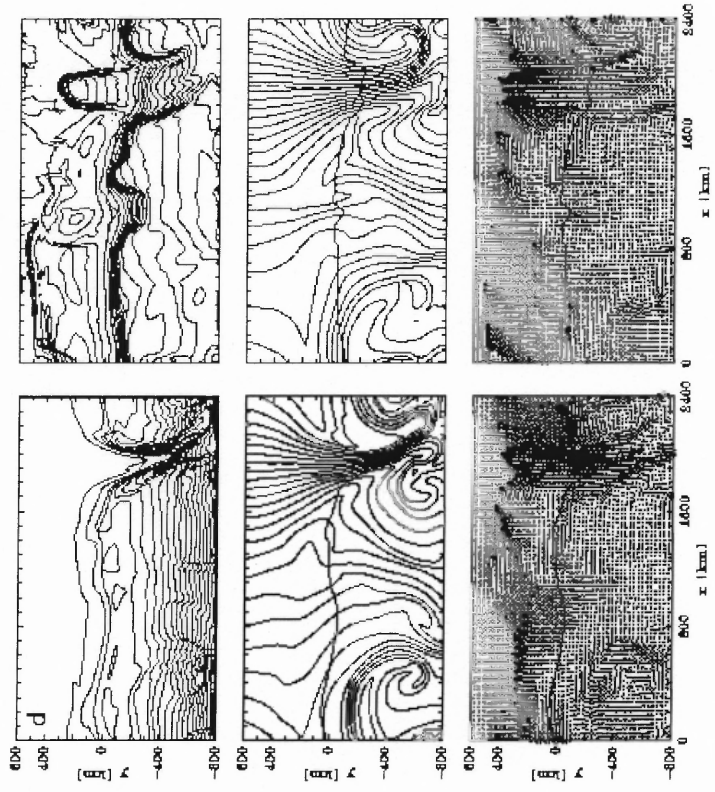

Figure 1.4 The formation process of a flux-tube calculated with the two-dimensional model of Steiner [65]. This is the second part of figure 1.3 and shows the time-steps 150 s ('d') and 250 s ('e').

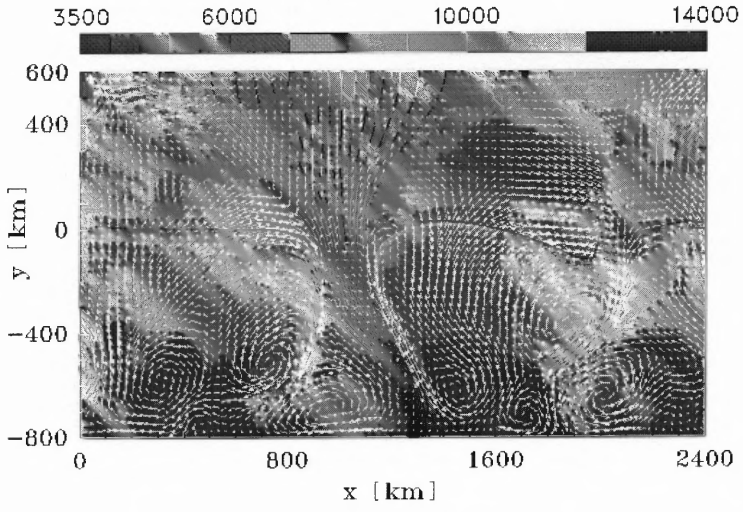

Figure 1.5 Example of a flux-tube as calculated with the two-dimensional model of Steiner [64]. For this simulation, the initial state already contained a flux-tube. One can see the down-drafts at the borders of the flux-tube and the increasing surface area of the magnetic field with increasing height.

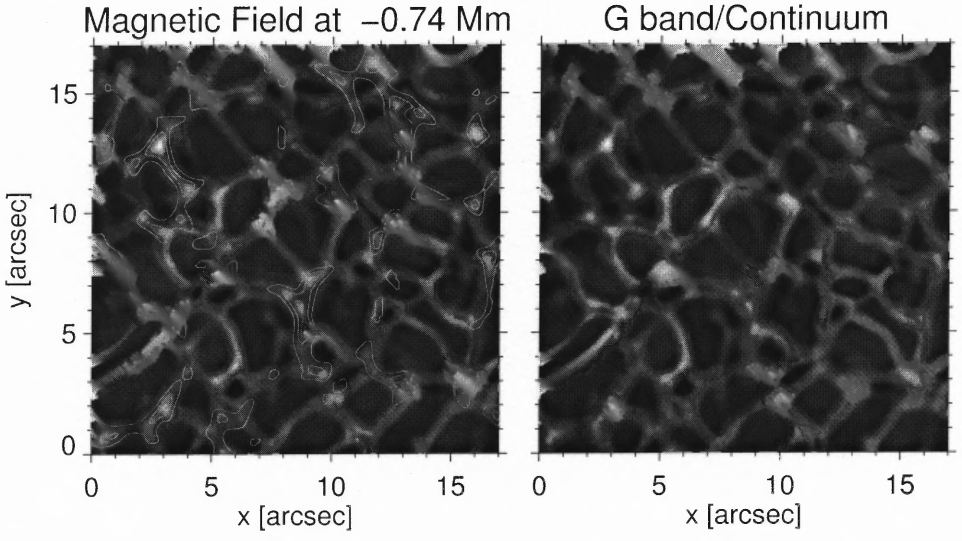

Figure 1.6 The residual intensity of the G-band CH-lines (right) and the same image with the magnetic field superimposed (contours). Calculations by Uitenbroek.

1.5.3 Summary

The investigation of bright points is still at the beginning. We know their apparent size, lifetime and proper motion as well as their connection with the magnetic field. It is unclear how the bright points form. Theoretical models suggest a concentration of magnetic flux by convective collapse as described above, but this has not been verified by observations yet. It is not known how these structures sustain themselves or how they dissolve. It is unclear why they are bright and why they have an especially high contrast in the G-band. Their connection to other solar features (e.g. sunspots or pores) is also poorly understood. Can they form pores and/or sunspots when they merge? Do they merge at all? What is their connection to the global or local solar dynamo?

There might also be a connection between the bright points and the coronal heating problem, since bright points are numerous and carry substantial magnetic energy. Moreover, bright points also exist in the chromosphere. This provides further evidence that energy may be transported to the outer layers of the solar atmosphere. Explaining the brightening mechanism of bright points, i.e the reason why the brightness id higher than in pores and intergranular lanes, may provide important clues on the problem of coronal heating.

1.5.4 Plan of Investigation

We use dopplergrams to attempt to answer the question of the motion of plasma in bright points. The measurement of plasma motion in bright points allows us to determine if up-flowing hot plasma is causing the bright points to appear bright. Velocity measurements also allow us to test the theoretical model of Steiner [64], who predicts down-flows in bright points during their formation and down-flows at their boundaries during their lifetime.

We record residual intensity images in different spectral lines for a comparison of the atmospheric properties at the formation height of the specific spectral line with the atmospheric properties at the continuum level. This data allows us to test the predictions of Steiner [63] about the different behavior of the Fe I and Ti II atomic lines in terms of bright points contrast. We also check for a different size or horizontal displacement of bright points in different atmospheric heights as this may be predicted by the two-dimensional MHD calculations of Steiner [64], [65].

We selected several spectral lines to obtain information about the bright points in different layers of the photosphere. We used the high forming Fe I 5576 Å line, the two lines Fe I 5691 Å and Ti II 5381 Å which form in medium height and the C I 5380 Å line which forms close to the photospheric level $\tau_{5000\mathring{A}} = 1$. All these lines and their use for the different measurements are described in detail in Chapter 2.4.2.

The determination of physical properties of the solar atmosphere is generally difficult and in our case almost impossible, since we record only very limited spectral information and no information about polarization at all. Instead we perform forward

modeling (Ch. 4). We use the calculations of Stein and Bercik [62] to evaluate intensity, residual intensity, and velocity using a radiative transfer program by Uitenbroek [68]. This approach allows us to compare theoretical predictions with our observations. We test how accurate the bright points and the G-band CH lines can be modeled by current state-of-the-art simulations.

We use the AO system of the Dunn Solar Telescope to perform our observations. This system provides the possibility to record diffraction-limited, long-exposure images and allows us to perform studies of the physical properties of very small scale structures.
Several instruments were considered for this investigation such as the spectrograph, the Fabry-Perot system, and the Universal Birefringent Filter (UBF). We choose a two-dimensional spectrometer instead of the one-dimensional spectrograph, because it is easier to locate bright points in a two-dimensional image. The UBF was chosen over the Fabry-Perot system because it allows imaging two (close-by) wavelength at the same time. This dual mode greatly reduces residual seeing effects and decreases the measurement error as described in detail in Chapter 2.3.2.

1.6 G-band

1.6.1 Importance of the G-band

Fraunhofer discovered the G-band and other strong solar lines in 1817 [19]. Due to the poor resolution of Fraunhofer's spectrograph, he classified the G-band as a single line around 430 nm while it is actually a region of many close-by solar lines. The spectral lines in the G-band include a band-head of the CH molecule and provide the opportunity to study the behavior of a molecule in the solar atmosphere. From an observational point of view the G-band is attractive because the bright points have higher contrast in this wavelength region hence are easier to identify. Bright points are known to be associated with the emerging magnetic flux [6]. This provides the possibility of the identification and proxy measurements of regions of high magnetic flux density by using a simple broadband-filter image. To exploit these proxy measurements to the fullest extent the reasons for the high contrast of bright points in the G-band have to be fully understood. Therefore the behavior of the CH molecule has to be understood.
Furthermore, since the CH molecules can dissociate, the G-band is likely to be sensitive to temperature changes in the solar atmosphere and may therefore be used to determine the temperature of solar structures. Again, it is necessary to understand the behavior of the CH molecule to be able to convert the intensity measurements to temperature measurements.

1.6.2 Current Knowledge

1.6.2.1 Observations The CH lines were first investigated in 1947 by Hunaerts [26] and observed until late 1960's [34], [20]. These studies compared the observed average line profiles to calculated line profiles and found a quite good agreement. Measurements of the formation height of the G-band have been derived from the center-to-limb variation, which state values from 0 km to 160 km above the photosphere. All these spectroscopic studies were done with low spatial resolution.
The interest in the G-band was revived after Mueller [36] discovered that bright points have a high contrast when imaged through a 10 Å G-band interference filter. This discovery linked the G-band to the smallest solar fine structure and indicated that observations with high spectral and spatial resolution have to be performed to understand the G-band and the bright points. Understanding the G-band will help to understand bright points, because bright points have the highest contrast in the G-band which means that their brightening mechanism works especially well for the molecular CH lines. There have only been a few observations of the G-band spectral profiles in recent years. Langhans [30] measured the center-to-limb variation. He also took spectra of plage regions, which proof that it is actually the reduced core intensity of the CH lines that causes the bright point contrast enhancement (Fig. 1.7).

1.6.2.2 Model-Calculations The formation of the G-band spectrum in the solar atmosphere is only partly understood. Steiner [63] and Uitenbroek [69] (Fig. 1.8) have performed calculations that replicate the spectral line profile of the G-band using one-dimensional atmospheric models and radiative transfer. The calculations were performed for different atmospheric models like quiet sun and plage regions of bright point atmospheres. Nevertheless, each model predicts a different formation height of the G-band.
Two mechanisms for the contrast enhancements in bright points have been proposed. The first mechanism, supported by Sanchez-Almeida [50] and Steiner [63], suggests that the higher temperature in a flux-tube dissociates the CH molecule and therefore weakens the CH line, which results in a higher intensity. Steiner predicts a contrast enhancement of bright points for Fe I, CO and CN lines as well, but not for Fe II or the Ti II lines. A goal of this study is to check this prediction.
Rutten [49] proposes a different mechanism for the contrast enhancement of bright points. He believes that the contrast-enhancement of bright points is a result of the dissociation of the CH molecules by radiation entering the flux-tube from the surrounding, hot photosphere. This mechanism is called hot wall effect. If the hot wall effect is responsible for the brightening of the bright points the total intensity of bright point will decrease with increasing size. The reason is that the ratio of the circumference to the surface area decreases with increasing size meaning that a relatively smaller wall has to heat and brighten a relatively larger bright point area.

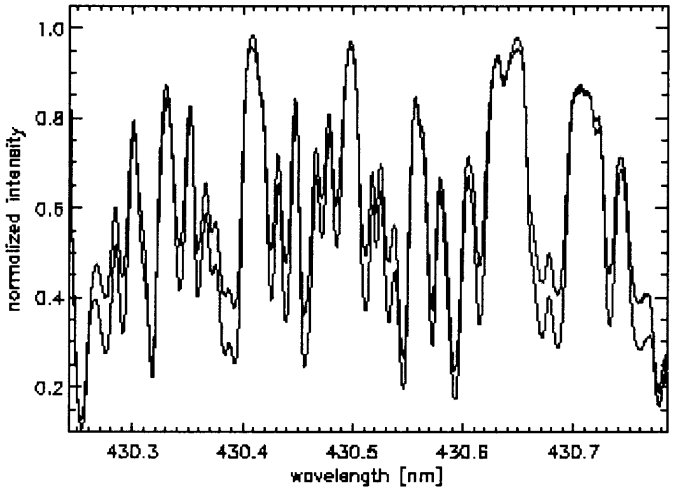

Figure 1.7 Measured spectra of the quiet sun (upper line) and a plage region (lower line). The measurements were conducted by Langhans [30].

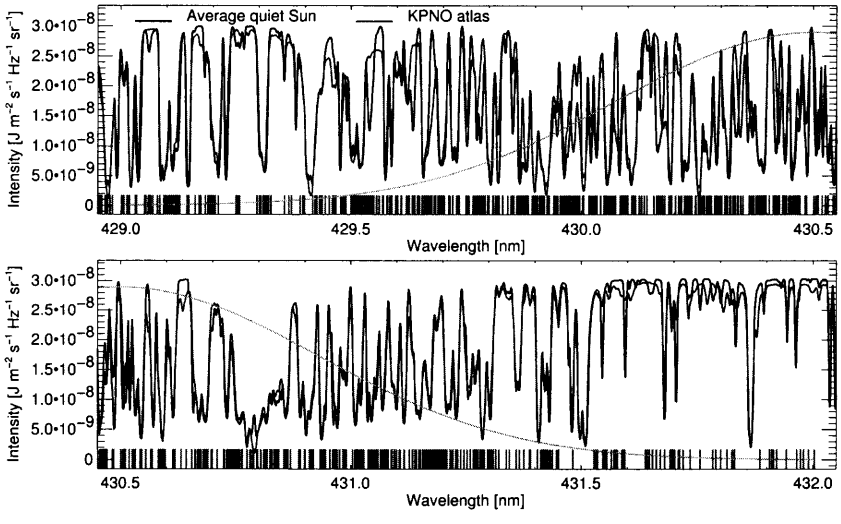

Figure 1.8 Comparison of the calculated and the measured CH lines in the G-band. The calculations were performed by Uitenbroek [68].

If a single bright point is smaller than the resolution limit and one can only observe clusters of bright points, one would expect to find the intensity of a bright point to be independent of the size, since an individual bright point – as a building block – has a constant ratio of circumference to area on average. This behavior can be checked by our observations.

1.6.3 Summary

The G-band can be modeled well using semi-empirical models of the quiet sun and the flux-tube atmosphere. The G-band spectral profile is reproduced by these calculations, but a lot of open questions remain. It is unclear in which height the G-band forms in the solar atmosphere. The theoretical estimates range from 40 km below the photosphere [50] to 160 km above the photosphere [63] or even a broad range for the formation height [69]. This disagreement is a result of the fact that the atmospheric models used for the calculations are semi-empirical which means they contain many free parameters. This indicates a poor understanding of the physics of the solar atmosphere. More observational input is required to refine and test these models. The second open question is the connection between the G-band and bright points. It is not clear what physical mechanism causes the enhanced contrast of bright points in the G-band. Understanding the G-band may provide an important input for theories of bright points contrast enhancement.

The G-band is often used in solar observations for the identification of bright points. It is fairly easy to obtain a G-band filtergram since a simple 10 Å interference filter can be used. This wide filter still transmits much light and therefore the exposure-time is short and one can obtain diffraction-limited pictures without an AO system. It is known that bright points are a signature of emergent magnetic flux [6]. Measuring the total G-band intensity or counting the number of bright points in an active region may be used to calculate the total magnetic flux. This process may provide the possibility of in proxy measurements of the magnetic field with very simple instruments.

The G-band alone cannot answer questions about the formation and the properties of the CH molecule. It is necessary to use other solar lines with known properties for the investigation of the physical properties of the G-band. Since these spectral lines are much narrower than the combined width of all the CH lines in the G-band their observation requires a much more complicated filter system. The goal of these spectral line investigations is to compare the behavior of the CH lines to spectral lines with known properties. Once the properties of the G-band are known, it can be used much more efficiently in solar studies, with the big advantage over the other spectral lines that the measurement of the CH lines only requires a very simple filter and short exposure-time and therefore no AO system.

1.6.4 Plan of Investigation

We obtain G-band images for identification of bright points in all observing runs. We perform a comparison between the G-band and the other spectral lines by measuring the correlation between the intensities of the G-band and the other solar lines as well as the corresponding residual intensities. This correlation analysis will reveal information about the formation height of the G-band because of the different heights of formation of the spectral lines. We measure two Fe I lines and one Ti II line to test the prediction of Steiner [63] that bright points have an enhanced contrast in the Fe I lines but not in the Ti II lines. This also allows us to check if the principle mechanism of contrast enhancement proposed by theoretical calculations for bright points is correct.

1.7 Umbral Dots

1.7.1 The Importance of Umbral Dots

Sunspots are one of the most prominent features on the solar surface. They are formed by strong magnetic fields of about 2000 Gauss (0.2 Tesla) that emerge from the convective zone. A sunspot consists of a darker, central part – the umbra, which is surrounded by a brighter part – the penumbra. This two part structure of a sunspot is not completely understood.

Each part of a sunspot exhibits a small-scale structure. The penumbra consists of bright and dark filaments. Most bright filaments have a distinct, bright dot at the inner end pointing towards the umbra. This bright dot is called penumbral grain. The umbra consists of brighter and darker areas. High-resolution images show that the bright areas contain small, bright dots called umbral dots [56], [57]. Sunspot umbrae are dark because the strong magnetic field suppresses the convection and therefore reduces the energy transport. Radiative heating remains as an energy transferring process. However, if this was the only effect, the umbra of a sunspot should actually be much cooler than measured [8]. This implies the existence of an additional heating mechanism within the umbra. Umbral dots are bright which implies a higher temperature than the surrounding plasma. This higher temperature suggests a connection between umbral dots and the umbral heating problem. Due to their small size little is known about the nature of umbral dots and the details of this heating mechanism are unknown.

Umbral dots may also reveal information about the topology of the magnetic field of sunspots. Are sunspots a loosely connected bundle of smaller flux-tubes or do they have a monolithic structure? If the umbral dots are field free regions then the sunspot magnetic field cannot be monolithic, but filamentary. This is important for understanding sunspot formation and the solar dynamo as well as to distinguish between the two existing sunspot models by Weiss [29] and Parker [42].

1.7.2 Current Knowledge

1.7.2.1 Observations Secchi [55] saw umbral dots and made drawings of them, which correctly described their morphology. With the development of film and later CCD imaging, more comprehensive morphological studies have been performed. The standard work of the film era was Bray and Loughead [10], one of the best recent works of the CCD era was done by Sobotka et al. [56], [57] who succeeded in obtaining an eleven hour diffraction-limited times series. This time series allowed to determine the typical size, shape, proper motion, intensity, and lifetime of umbral dots. The diameter histogram shows no peak but a steady increase towards small diameters down to the diffraction limit of 0.18 arcsec of the SVST indicating that umbral dots are smaller than the resolution limit of the telescope used. The average lifetime of umbral dots is 13.8 minutes, but a substantial fraction of umbral dots lives longer then ten minutes or more and some umbral dots exist longer than 100 minutes. The average lifetime is 13.8 minutes. Long-lived umbral dots are generally found in the inner part of the umbra. Umbral dots in the outside of the umbra are generally shorter lived. The horizontal motions parallel to the solar surface (proper motion) is up to 200 m/s for short-lived umbral dots and 35 m/s or less for longer lived ones. Some penumbral grains penetrate the umbra and become umbral dots. The intensity of umbral dots is up to 50 percent the intensity of the average photosphere. The brighter umbral dots are found mostly on the outer side of the umbral. This led to a division of umbral dots depending on their brightness by [56], [57].
Many studies have been performed to determine the physical properties of umbral dots, e.g., the temperature, the magnetic field, and the vertical velocity. Unfortunately, there is little agreement between the various studies. Almost all studies find umbral dots to be hotter than the surrounding umbra, which is expected since they are brighter than the average umbra ([21], [67]). However, the derived temperatures vary. Some authors point out the need to distinguish between central and periphal umbral dots because of different temperatures [21]. There is almost no agreement on the magnetic field measurements. Some studies find a reduction of magnetic field strength at the location of umbral dots [67], other studies find no reduction at all [73]. The situation is quite similar for the velocity measurements. Wiehr [73], Schmidt [53], Rimmele [46] find velocities compatible with 0 m/s. Kneer [28], on the other hand, finds up-flows of 3 km/s.

1.7.2.2 Calculations There are two main types of sunspot models. Weiss [29], [71], [72] proposed a monolithic sunspot with no field-free regions (Fig. 1.9). Umbral dots are explained as convection within the umbra, even though this convection is altered and suppressed by the magnetic field (Fig. 1.10). In this picture, umbral dots are the brightenings that result from upflowing, hot plasma that cools off by radiation when it reaches the 'surface'-level of the umbra.

In the model proposed by Parker [42], [43], [44] the umbra is an inhomogeneous structure consisting of many small flux-tubes held together by the buoyancy of the Wilson depression (Fig. 1.11). The field-free regions between the flux-tubes extend almost up to the solar surface and sometimes even above the solar surface. When a plume of hotter, field-free plasma penetrates the cluster of flux-tubes and reaches the solar surface, it shows up as a brightening (Fig 1.10). This model was later evaluated numerically by Choudhuri [12]. He predicts that these field-free regions would result in up-flows of about 300 m/s. He also applied this principle to explain the nature of penumbral grains, which he assumes to be of the same nature.

1.7.3 Summary

The nature of umbral dots is not understood well, primarily due to the lack of observational data. What are umbral dots? Why are they hotter than the umbra? Is there a plasma up-flow in the umbral dots? Is the magnetic field reduced in umbral dots? Are there different types of umbral dots? Is there a connection between umbral dots and penumbral grains? The answer to these questions will help to distinguish between the various sunspot models and provide insight in the mechanisms of umbral heating.

1.7.4 Plan of Investigation

We will study umbral dots using the UBF and the spectrograph to obtain velocity measurements. We address the question of material flow in umbral dots. These velocity measurements allow us to test the predictions about the velocity in umbral dots predicted by the theoretical models by Weiss [29] and Parker [42].

The same dataset also includes velocity information about penumbral grains. This enables us to investigate the connection between umbral dots and penumbral grains. Especially, we can test the prediction of Choudhuri [12], who proposes that umbral dots and penumbral grains are formed by the same mechanism.

We use the spectra of umbral dots to validate the velocity-measurements made with the UBF. The spectra provide much more detailed information about the physical conditions of umbral dots since the full spectral profiles contain much more information. On the other hand, no morphological parameters of umbral dots can be derived from this kind of study. The spectrograph data is complementary to the two-dimensional filtergrams of the UBF.

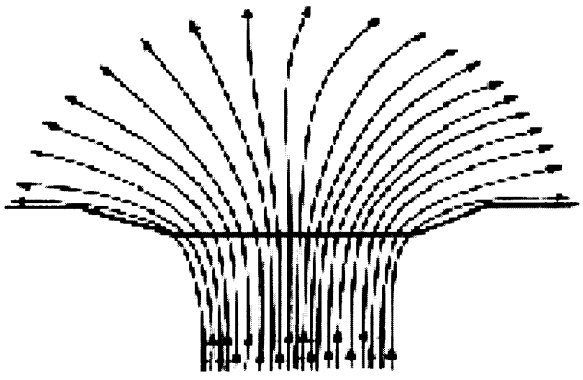

Figure 1.9 The sunspot model proposed by Weiss [29], a monolithic flux tube. Umbral dots are explained as magneto-convection, a granulation-like convection pattern altered by the magnetic field.

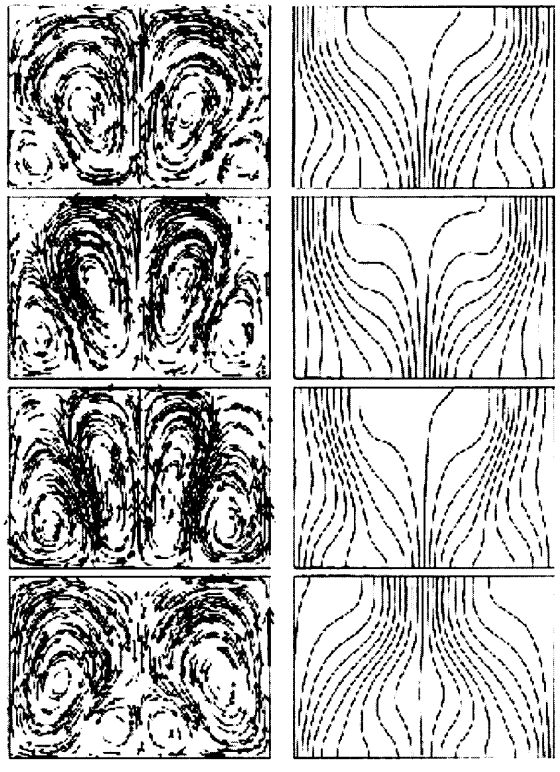

Figure 1.10 The altered convection of the solar plasma in the presence of a magnetic field. In the center of each time-slice, one can see an up-flow of hot plasma, which forms an umbral dot at the solar surface [29].

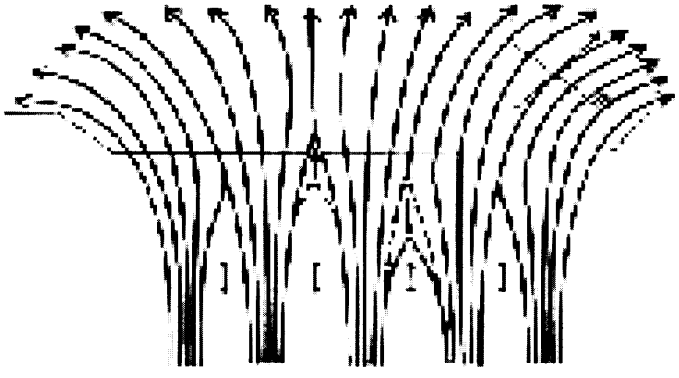

Figure 1.11 The sunspot model proposed by Parker [42] consists of individual flux-tubes held together by the Wilson depression.

1.8 Summary of Questions

Bright points

- What are the general properties of bright points?
- Is there a change in shape or a displacement of bright points with height?
- Why are bright points bright?
- Why do bright points have such a high contrast in the G-band?
- Do bright points have an enhanced contrast in other solar lines as well?
- Do bright points have different contrast in spectral lines with higher ionization potential as Ti II?
- Is there a material flow in or near bright points?
- Are the current bright point models accurate?

G-Band

- Is the G-band more temperature sensitive because it originates from a molecule?
- At which height does the G-band form?
- Why do bright points have an enhanced contrast in the G-band?
- Which theoretical model does make the right predictions about the G-band?

Umbra

- What are umbral dots?
- Are there different types of umbral dots?
- What is the relation between umbral dots and penumbral grains?
- Do umbral dots have a velocity different from 0 m/s?
- What is the heating mechanism of umbral dots?
- Are umbral dots responsible for the heating of the umbra?
- Which sunspot model is correct?

To answer these questions, we take dopplergrams, residual intensity images and spectra. We are able to reach beyond formed studies, because we use the AO system of the Dunn Solar Telescope of the Sacramento Peak Observatory. The AO system and the use of the UBF in the dual mode enables us to take diffraction-limited filtergrams, dopplergrams, and residual intensity images.

1.9 Outline

Chapter 2 describes the technical details of the instruments and methods used for our observations. It gives a description of the telescope, the AO system, the UBF and the spectrograph. The general process of spectral line formation is described in this Chapter as well as the specific spectral lines. We describe the methods to measure physical parameters of the solar plasma using spectral lines.
Chapter 3 describes our observations. Three different observing runs were performed. During the first run, we recorded residual intensity pictures, mainly of bright points but of some solar pores as well. In the second run, we obtained dopplergrams of a medium-size sunspot with umbral dots and penumbral grains, but also of some bright points. In the third run, we recorded spectra of umbral dots to determine their velocity and residual intensity.
In Chapter 4, we perform theoretical calculations of bright points using models of the solar surface from Nordlund, Stein and Bercik [62] and a radiative transfer code by Uitenbruck [68]. This enables us to compare theoretical predictions with observations.
Chapter 5 summarizes the methods used for our observations as well as the results obtained in this thesis. We discuss, which questions posed in Chapter 1 we were able to answer. We give a short discussion on new methods of observations, instruments, and telescopes that could be used to further investigate the structures examined here.

CHAPTER 2

Technical Aspects

2.1 The Dunn Solar Telescope

The Dunn Solar Telescope was dedicated in 1973. It rises 41.5 m above ground level and extends 67 m below ground level (Fig. 2.1, Fig. 2.2). It uses a turret-system where two 45° flat mirrors with a diameter of 1.1 m direct the light down an evacuated tube to the main mirror at the very bottom of the telescope (Fig. 2.3). The telescope is evacuated to suppress local seeing distortions created by the air inside the telescope. In order to make evacuation possible, there is a 76 cm entrance window before the first turret mirror. This window also forms the telescope pupil, therefore the aperture is 76 cm although the main mirror has a diameter of 1.6 m to avoid vignetting. The focal-length of the Dunn Solar Telescope (DST) is 55 m yielding an f-number of 72. The turret system results in a rotation of the solar image which is compensated by the rotation of the entire telescope. Although expensive, de-rotation is elegant and has the advantage that the telescope pupil is circular during the day. This is especially important for the AO system, since a change in pupil shape requires a frequent update of the flat-field image. These problems are common to coelostat systems such as the German VTT.

After the incoming light has been focused by the primary mirror it is directed horizontally onto the observation floor by a flat mirror. It passes through to AO System, and is then focused in the secondary focus, from where it is directed to the various science instruments.

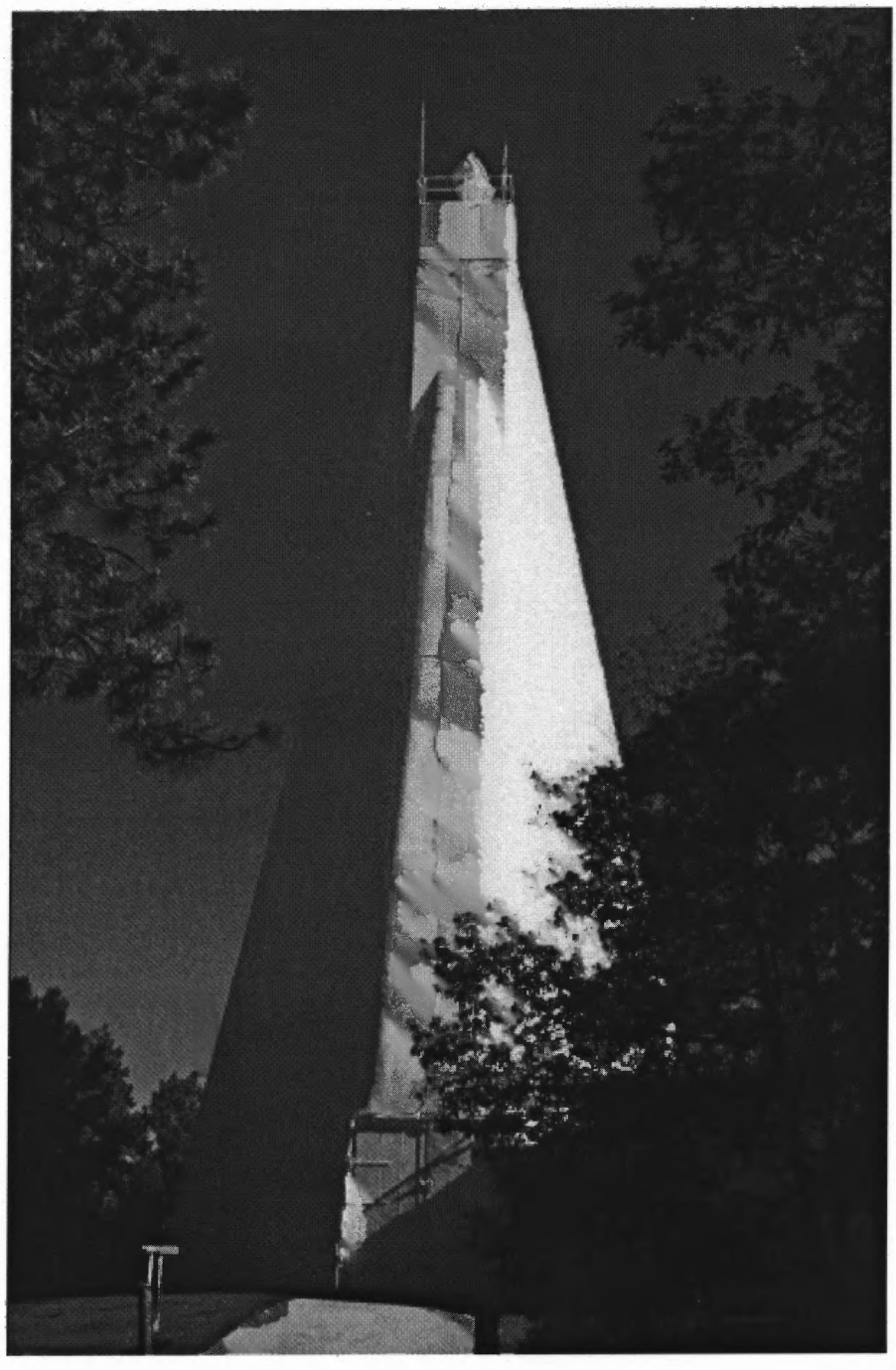

Figure 2.1 An outside view of the Dunn Solar Telescope at the Sacramento Peak Observatory. The height above ground level is 41.5 m.

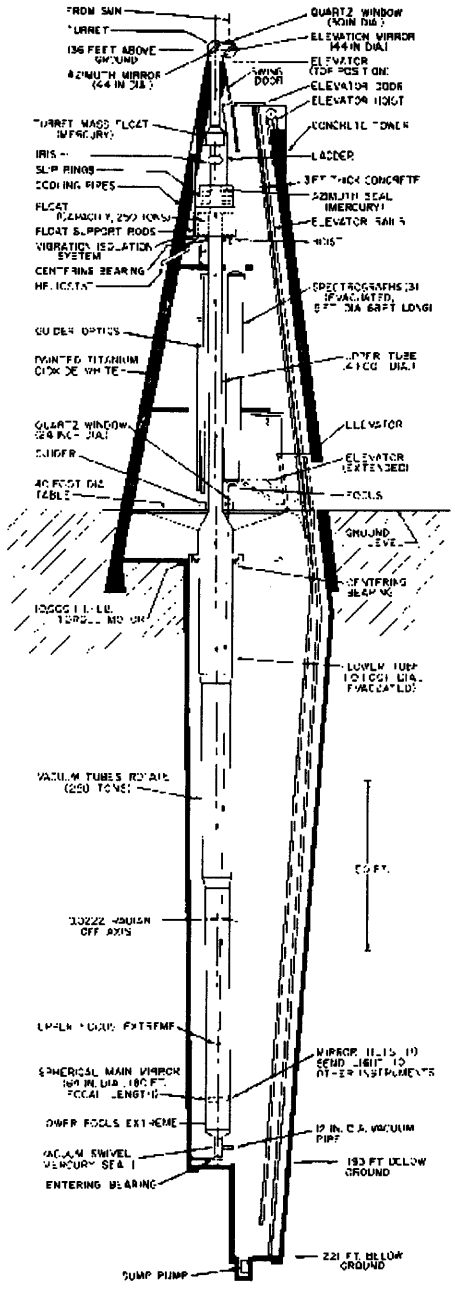

Figure 2.2 Schematic layout of the Dunn Solar telescope. The sunlight enters the telescope through the turret system (Fig 2.3), which directs it down to the main mirror at the very bottom of the the telescope. The main mirror focuses the light, which is reflected sideways by a folding mirror at ground level to feed the instruments on the observational platform.

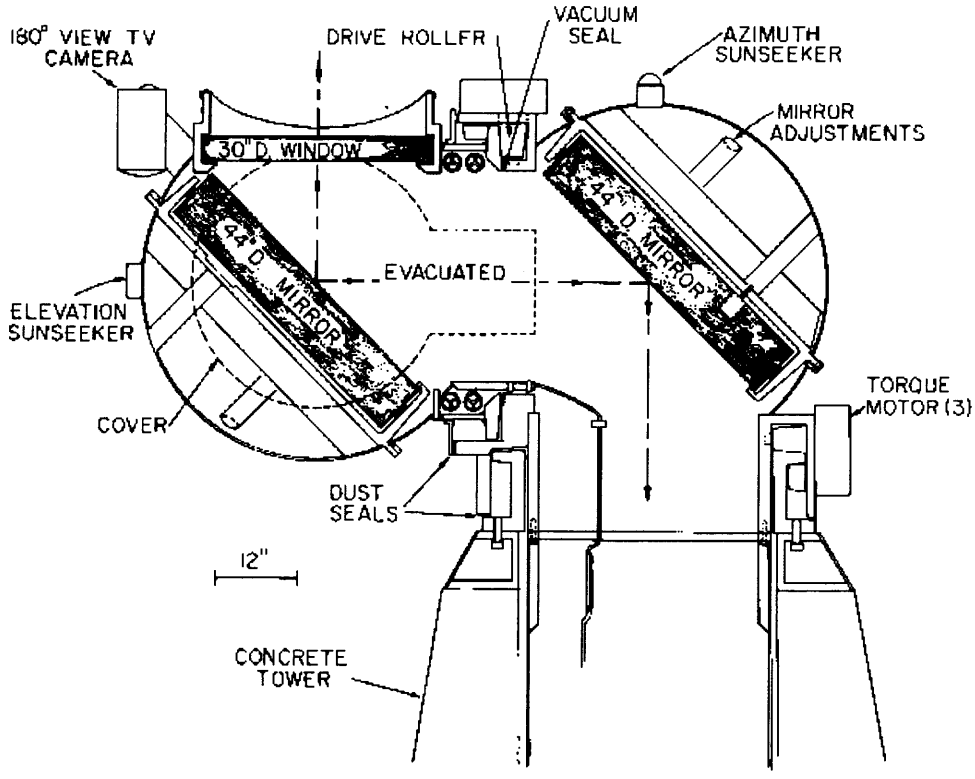

Figure 2.3 Layout of the turret system used at the DST.

2.2 Adaptive Optics

2.2.1 Introduction

High-resolution astronomical imaging is limited by the earth's atmosphere. Density gradients in the air influence the incoming wave-front and distort it from the plane wave. In the telescope prime-focus these distortions result in optical abberations that enlarge the Point Spread Function (PSF) and lower the Modulation Transfer Function (MTF). This reduces the amount of detail that can be seen in an image and leads to errors in measurements of physical quantities such as magnetic fields and velocities. One can control air turbulence locally by carefully designing telescopes that minimize local thermal effects. Such measures include placing the aperture high off the ground and evacuating the telescope. A considerable effort is made to pick a good seeing site to minimize the influence of high altitude turbulence. Nevertheless, long-exposure images from ground based telescopes are limited by seeing to a resolution of typically 1.0 arcsec, and in the most favorable conditions to 0.5 arcsec, independent of the size the telescope when the aperture is larger than 20 cm. Compared to night-time seeing, the day-time seeing is significantly worse, thus severely limiting the use of large solar telescopes. Even though the sun is very bright, the instruments filter out most of the incoming photons, and due to the large image scales used in high resolution imaging, the remaining photons are spread out over a large area. This leads to exposure-times in spectroscopic studies in the range of one second, which is about 100 times the correlation time of the seeing caused by the earth's atmosphere. We refer to exposures longer than 0.1 seconds (100 ms) as long-exposures. For spectroscopic studies it is therefore impossible to freeze moments of good seeing, and the resolution is limited to the average seeing that the atmosphere permits. This severe limitation stimulated a substantial effort to find ways to compensate for the degrading effects of the earth's atmosphere. The approach that finally succeeded was Adaptive Optics. Other, quite successful post processing methods such as speckle interferometry, phase diversity and blind deconvolution will not be discussed here.

2.2.2 The Principle of Adaptive Optics

An AO system measures and corrects the wave-front distortion of the incoming light in real time, i.e. with a rate greater one kHz. It does so by measuring the wavefront-distortions and correcting them with a deformable mirror.
The general principle of an AO system can be divided into the three following main steps:

- Wavefront measurement

  There are several ways of measuring the wavefront error, but only the method of Shack-Hartman [5] will be discussed, since it is used in the Sacramento Peak AO system.

A Shack-Hartman wavefront sensor works in the following way: The telescope entrance pupil is re-imaged onto a lens-let array (Fig. 2.4). This lens-let array divides the large aperture of the telescope into several small sub-apertures and therefore divides the atmospheric disturbances into local areas as well. When the image of the sun is formed behind the lens-let array, one obtains one image for each sub-aperture (Fig. 2.5). This corresponds to an array of telescopes with a smaller aperture. The abberations are averaged over each of the sub-apertures in this process, but the global abberations of the whole wavefront remain. These global abberations result in a shift of each sub-aperture image. These shifts represent the local wavefront tilt of the global wavefront in two orthogonal directions averaged over each sub-aperture. If one takes a reference aperture and cross-correlates all the other sub-apertures with it, the result will be shift vectors of the sub-apertures relative to each other. These shifts are related to the slope (derivative) of the incoming global wavefront at the location of the sub-apertures. Since the geometry of the lens-let array is known, the incoming wavefront can be reconstructed from the measured shifts of the sub-apertures. This measured wavefront is usually decomposed into Zernike polynomials [38], which is a set of orthogonal functions on the unit circle. The number of sub-apertures is finite allowing only a finite number of Zernike polynomials to be measured.

This limitation leads to the following tradeoff: Increasing the number of sub-apertures allows for a finer sampling of the wavefront, but it also corresponds to a reduction of the sub-aperture size. This reduction in sub-aperture size reduces the contrast due to diffraction and therefore increases the measurement error in the cross-correlation procedure [5]. This is especially severe for a low-contrast object such as the solar granulation. It is necessary to find the optimum number of sub-apertures before designing the system taking into account the site characteristics. If the observed object is the sun, there is a natural limit for the minimal sub-aperture size, because the solar granulation has a scale of about one to two arcsec. A sub-aperture diameter of the order of ten centimeters is needed to reach a high enough contrast for tracking on solar granulation (about two to three percent). The Sacramento Peak system uses sub-apertures of twelve centimeters diameter.

- Calculation of the mirror drive signal

  Once the wavefront has been measured, the drive-signal for the deformable mirror is calculated. The information, which electrical signal will create a certain Zernike mode on the deformable mirror must be determined beforehand and is stored in the 'reconstruction matrix'. By adding the drive-signals for the different Zernikes with the amplitudes measured from the incoming wavefront the opposite wavefront distortion at the deformable mirror is created.

The linear treatment of this problem is possible since a deformable mirror reacts linearly to the applied electrical signal. The created deformation of the mirror compensates the abberations of the incoming wavefront. The calculations have to be performed very rapidly, since the correlation-time of the earth's atmosphere is about 10 ms (Fig 2.6). One also has to be careful about which modes can be corrected and which modes can be measured. A mode that can be measured but not corrected is a waste of degrees of freedom of the wavefront-sensor. A mode that can be corrected but not measured is even worse, since it can introduce abberations due to crosstalk of other modes that cannot even be detected.

- Deformable mirrors

  There are three different kinds of deformable mirrors. The first type consists of several adjacent hexagonal flat mirrors, which can be individually tilted and moved back and forth. The most severe drawback of these mirrors is the difficulties in flattening the mirror, since there is an ambiguity for the piston of each single mirror by an integral number of a wave. The second type of mirror is a reflective surface on a layer of piezo-electric material. By applying voltage to various points on the back of the mirror with electrodes it is possible to deform the mirror. The third type of deformable mirror consists of a thin glass mirror which has a set of piezo-electric actuators on the non-reflective backside. These actuators have pistons that can be moved by applying current to a voltage to them. The pistons poke the mirror surface from the back and deform it. The Sacramento Peak AO system uses this type of mirror. The mirror of the third type mirror responds linearly to electrical driving signals which is very important if a linear calculation for determining the drive-signal form the wavefront-distortion is to be applied. With this drive-signal the mirror is deformed in a way opposite to the incoming wavefront in order to make it a plane wave again and correct for the distortions. Since it is important to know what correction the deformable mirror does to the wavefront, it is essential that the wavefront sensor is placed *behind* the deformable mirror. Otherwise one could never check if the adaptive mirror is working correctly and one might introduce abberations without even knowing it.

2.2.3 Limitations of an Adaptive Optics System

All AO systems are imperfect since there are several physical limitations that allow the correction of the distorted wavefront only to a certain degree. The *sampling errors* affect every single image even at the center of the corrected image because the wavefront-abberations can never be corrected perfectly by an AO system. For points in the field of view away from the center of correction the abberations are different from the center which leads to the *anisoplanasy error*. The last type of error is called

differential seeing and is a result of changing seeing conditions between images taken sequentially
To quantify the performance of an AO system the Strehl ratio is used. The Strehl ratio is defined as the ratio of the peak intensity of the image of a point source and the maximum possible peak intensity for a perfect system. The Strehl ratio is an estimate of the resolution a telescope can reach compared to the theoretical perfect performance.

- Sampling errors
  - Sampling error due to the number of sub-apertures
    This error is a result of the tradeoff for the sub-aperture size. Too large sub-apertures result in a too coarse sampling of the wavefront, but a too fine sampling using small sub-apertures increases the error of the cross-correlation due to diffraction effects.
  - Sampling error due to the number of actuators of the deformable mirror
    Even if the wavefront was to be measured perfectly no adaptive mirror could reproduce the wavefront perfectly. The reason is the finite number of actuators on a deformable mirror.
  - Sampling error due to the operating speed of the AO system
    The finite frequency at which an AO system cam operate is the cause for the bandwidth error. The correlation time of the earth's atmosphere is about 1 ms or 1000 Hz (Fig. 2.6). If the AO system cannot resolve and correct abberations up o this frequency there is a residual error due to time-sampling.

Due to these errors the generated wavefront does not match the incoming wavefront exactly and therefore residual abberations remain. These abberations lower the Strehl ratio achieved by the telescope. In moments of best seeing a typical AO system reaches a Strehl ratio of 70 percent but usually this value is much lower, around 10-30 percent in good seeing conditions [47]. We call this effect the 'blurring' of the image since it lowers the spatial resolution. The resulting point spread function has a diffraction limited core is surrounded by the seeing halo. The size of the diffraction limited core is determined by the aperture of the telescope and the size of the seeing halo, a Gaussian function, is determined by the seeing. The ratio between the peak intensity of these two components is a measure for the efficiency of the AO system [5].

- Anisoplanasy error

  All AO systems built so far have another principal limitation. They only correct for the point in the field of view which is used for the correlation (lock-point of

the AO system). Since the earth's atmosphere changes in different directions the abberations change with the position in the field of view. These changes increase with increasing distance from the lock-point. The residual abberations increase since the measured wavefront at the lock-point is different from the wavefront at other points and the Strehl ratio decreases with increasing distance from the lock point. The area in which the difference between the measured wavefront and the actual wavefront is not larger than a seventh of the wavelength is called isoplanatic patch. The size of the isoplanatic patch depends strongly on the seeing conditions and varies between five and twenty arcsec. Anisoplanasy causes a degradation of the image as well as in differential image motion. The further away from the lock-point, the larger these differential movements will be. Since typical exposure-times of spectroscopic investigations are about one second, most of this motion is transfered into a blurring of the image as well. Nevertheless, some motion still remains. We call this remaining motion 'differential motion'.

- Differential seeing

  For two-dimensional spectroscopy, usually two or more images with different wavelength are taken sequentially to produce dopplergrams or magnetograms. Seeing conditions can vary significantly in a short time and the different images are affected by the varying seeing variations. The resolution of the images varies due to blurring. Points on the solar surface away from the lock point of the AO system are shifted to different locations on the images due to differential motion.

The different errors affect the physical measurements in different ways. The blurring leads to a general reduction in sensitivity for small features on the solar surface. The blurring mixes physical values from close-by locations and therefore increases the measurement error, especially for small features.
Anisoplanasy on the other hand is not a problem for single images, but usually physical measurements require a sequence of images which suffer from differential seeing. Differential motion again mixes the physical information from different locations on the solar surface and therefore increasing the measurement error. Again, smaller structures are more affected by the differential motion. The other effect of the differential seeing, the differential blurring, is mixing the information differently in each image used to obtain the physical information. The effect is the same, a larger measurement error for small structures.

The blurring, and also in part the differential blurring can be reduced by using an AO system that corrects more Zernike mode and therefore reduces the residual wavefront abberations. There is, however, the limitation of the minimum size of one sub-aperture as described before. This limits the number of Zernikes that can be corrected. Therefore no perfect AO system can be built.

The problem of image motion can be mostly overcome by a multi-conjugate AO system which uses more than one deformable mirror to correct the atmospheric disturbances in different heights. The isoplanatic patch of a multi-conjugate AO system will be much larger (about one to two arcmin) but unfortunately no multi-conjugate AO system is operating so far.
Therefore we choose another way to overcome the problem of differential seeing and recorded all images strictly simultaneously. This ensured the differential seeing effects are the same for all images at all wavelength. Since we only need one exposure with good seeing in varying seeing conditions to produce a physical measurement, the chances of obtaining good measurements increase dramatically. We achieve the simultaneity by using a special mode of the Universal Birefringent Filter (UBF), which is described in Chapter 2.3.2.

2.2.4 The Adaptive Optics System of the Sacramento Peak Observatory

The AO system of the Sacramento Peak Observatory was installed in 1998 as the first AO for solar research (Fig 2.8, Fig. 2.7). Since then, other test systems have been online at the Swedish Tower in La Palma and the German VTT. Only the AO system of the Sacramento Peak Observatory has been operating on a regular basis. The Sacramento Peak System AO system uses a Shack-Hartman wavefront sensor with 24 sub-apertures. The deformable mirror has 97 actuators, and the signal processing as done by a SHARC DSP cluster. The system can operate at a frequency as high as 1.6 kHz depending on the camera used. It has produced outstanding results since it came online. The Sacramento Peak AO system can achieve Strehl ratios of 70 percent in excellent seeing conditions. In typical seeing conditions it can reach Strehl ratios of ten percent to 30 percent, which is still a huge improvement over the Strehl ratios of two to seven percent usually reached for a solar telescope of this size without the use of an AO system [47]. These relatively low Strehl ratios still severely effect physical measurements as explained in Chapter 2.4.3. It is difficult to correct for this effect in post-processing, especially since we do not have the wave-front sensor data to reconstruct the residual wave-front abberations. Therefore, we do not perform a reconstruction for the quantitative measurements.

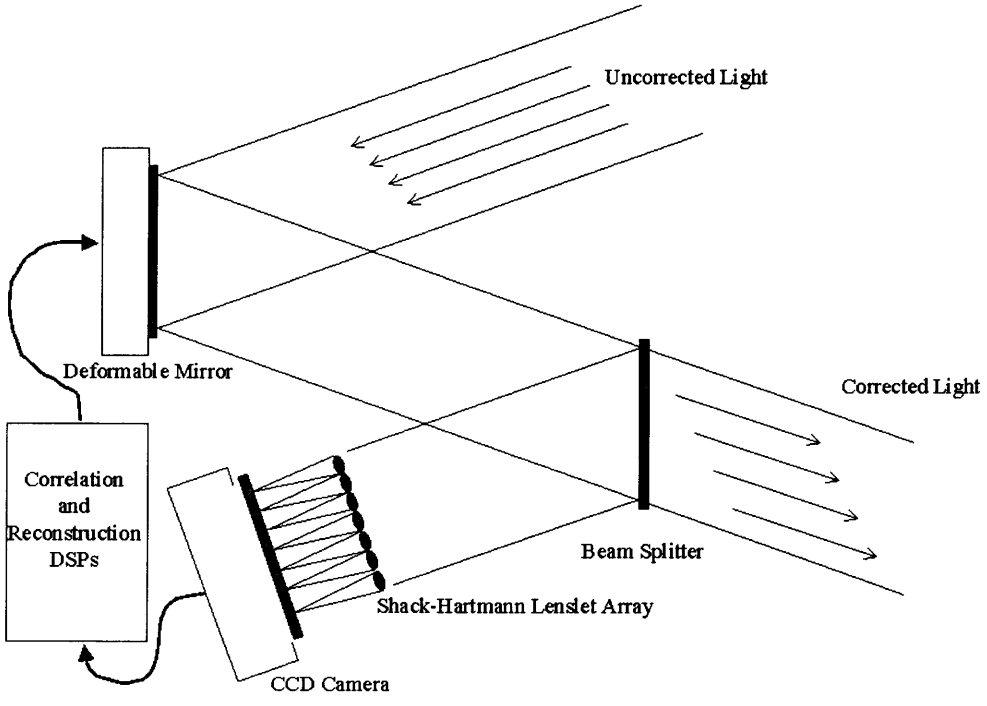

Figure 2.4 Working-principle of an Adaptive Optics system. The light is reflected off the deformable mirror. Part of the light if diverted to the wavefront sensor but most of the light passes on to the the scientific instruments.

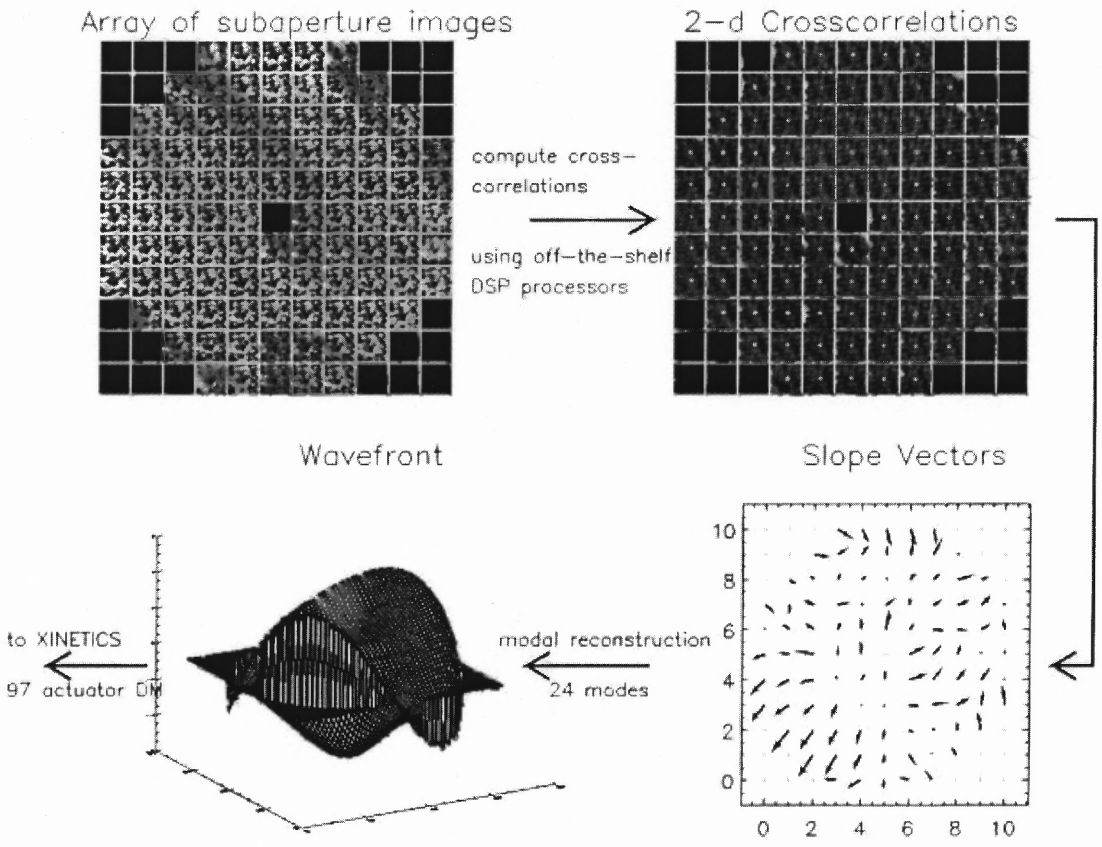

Figure 2.5 These images show how the wavefront-error is determined. First, the large telescope aperture is split into smaller sub-apertures. These sub-apertures produce an array of sub-aperture images. One sub-aperture is chosen as the reference. All other sub-apertures are cross-correlated to the reference sub-aperture to determine the shift which is proportional to the slope vectors of the wavefront. Finally, the Zernike decomposition of the wavefront is calculated from the shift vectors.

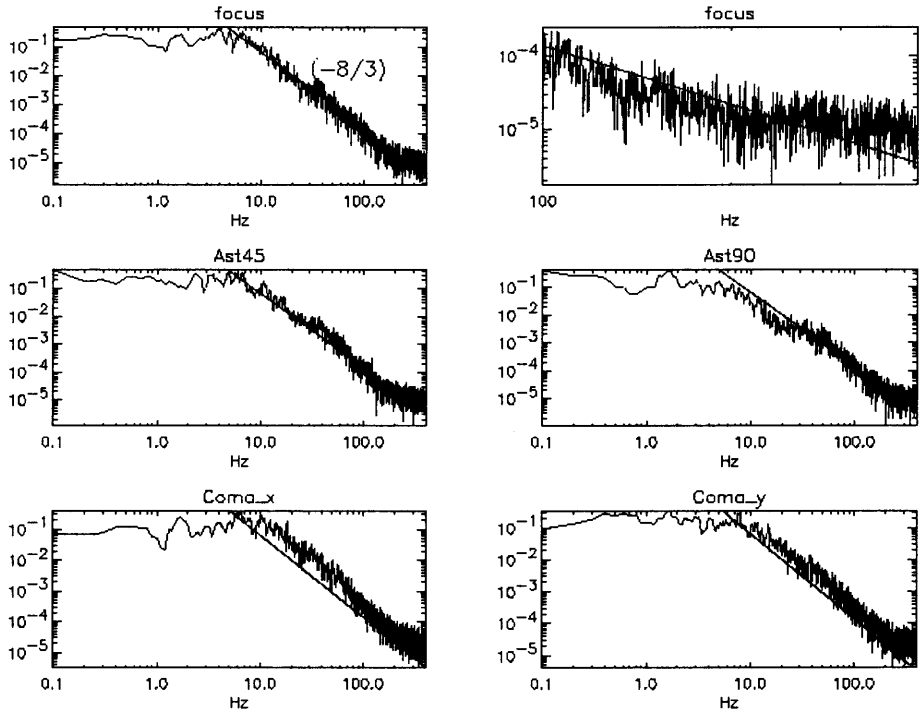

Figure 2.6 Time-power-spectra of some of the Zernike modes for an uncorrected wavefront. They can be used to determine the design goals for the AO system.

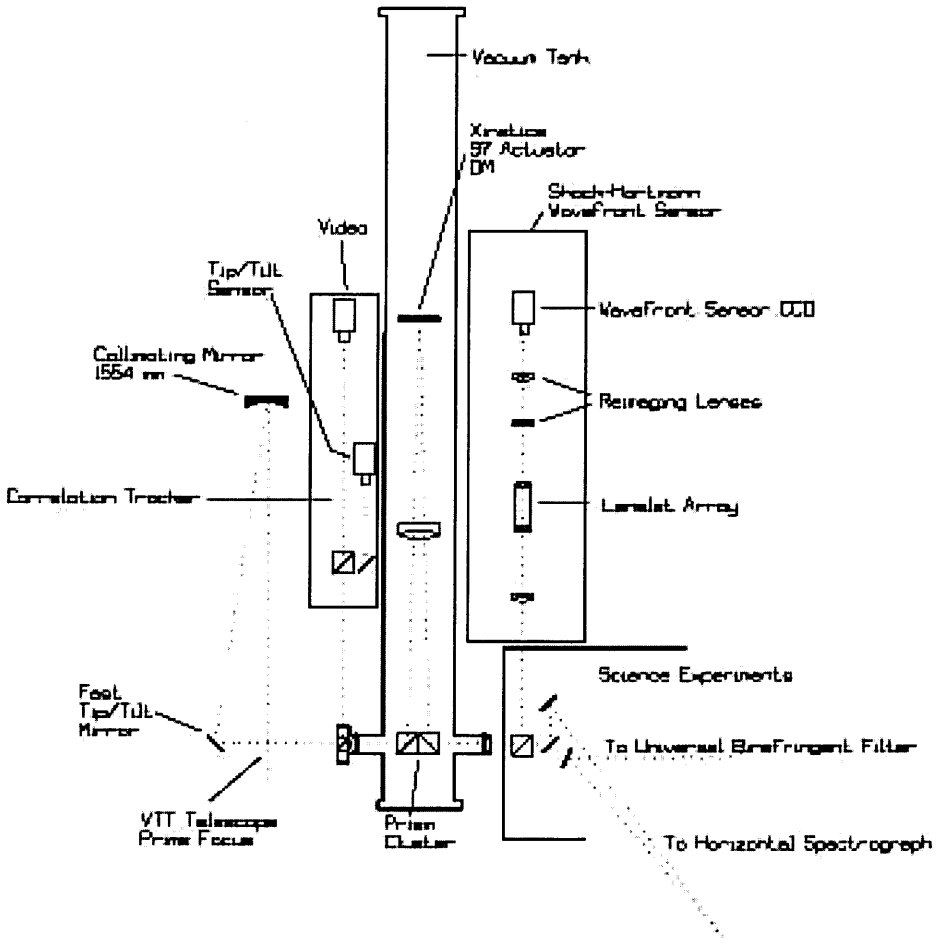

Figure 2.7 Diagram of the detailed layout of the AO system installed at the Dunn Solar Telescope.

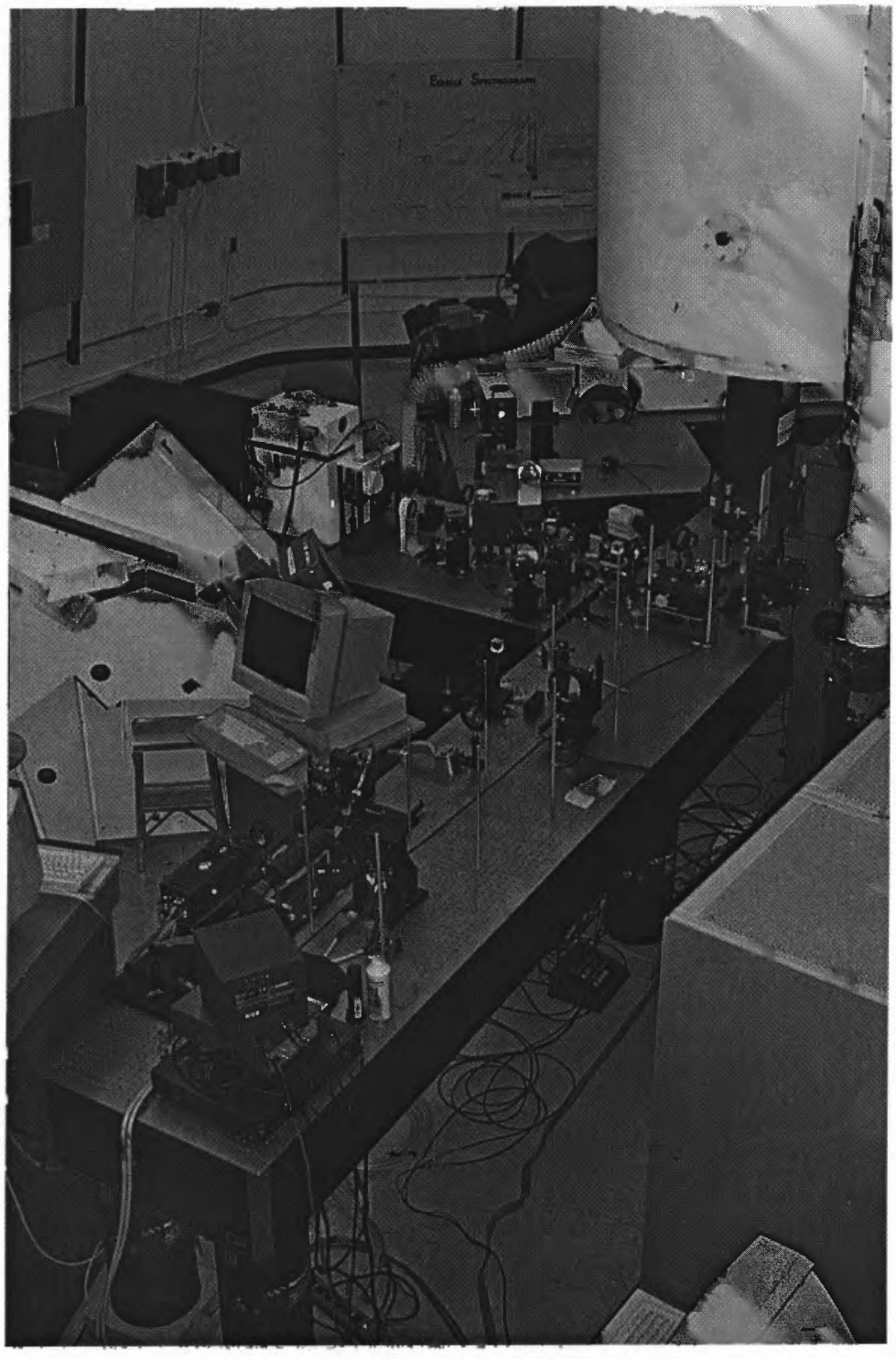

Figure 2.8 The AO system installed at the DunnSolar Telescope.

2.3 Instruments of Solar Study

The physical conditions on the sun are mainly studied by analyzing the solar spectrum. This can be done in various ways. The oldest method is the analysis with a spectrograph using a prism or a grating. This method provides a very high spectral resolution of up to 5 mÅ, but suffers from the fact that only a small slice of the solar surface can be examined at the same time. This drawback can be eliminated by a technique proposed by Jansen [22] in which the spectrograph-slit is moved over the prime-focus image of the sun. Although this method yields a two-dimensional image it has the disadvantage of being seeing-sensitive. Each point of the image has the same exposure-time as a conventional spectrograph and is therefore affected by seeing. It takes up to several minutes to obtain one complete image and this leads to differential seeing across the image. Moreover substantial changes on the solar surface can occur within seconds and therefore this method cannot give sufficient time-coverage for time evolution studies.

These problems have led to the development of narrow-band filters which are used to obtain a two-dimensional image of the solar surface at the same time. These filters provide a spectral resolution of up to 20 mÅ and are of limited use for studies needing the highest spectral resolution such as measurements of line-asymmetries. In the following, we will describe the instruments we used to obtain the data for this study, namely the horizontal spectrograph and the UBF.

2.3.1 Spectrograph

The layout of the horizontal spectrograph at the DST is shown in Figure 2.9. For wavelength in the visible it utilizes a grating with 316 lines/mm and a ruled area of 206 mm x 128 mm. It is usually used in the orders from 9th to 14th and has a efficiency of 63 percent at 5086A - 11th order [25]. It is blazed at 63 degrees 23 minutes. The resolution of the grating is $\frac{\lambda}{\Delta\lambda} = 472596$ at 5000 Å which is about 66 percent of the theoretical resolving power. This reduced resolution power of the grating is a result of the imperfections of the manufacturing process such as uneven ruling. This yields a resolving power of about 7.0 mÅ at 5000 Å in the 11th order. We used a fixed Chromium slit with a width of 25 microns microns. The f-number at the entrance slit is 36 which results in a resolution element with a size of about 20 micron for a wavelength of 500 nm according to the formula $1.12 \cdot \lambda \cdot$ f-number. We therefore do not take advantage of the full resolution of the telescope. The spectrograph is capable of scanning the solar surface in multiples of 1/13 arcsec which matches the slit-width.

Usually images of the slit-jaw are taken to locate the slit position on the solar surface. This has the disadvantage that the actual intensity on the slit at the moment of the exposure cannot be determined since the area of interest is passed through the slit onto the grating. Pictures with a different slit position are of no help since seeing

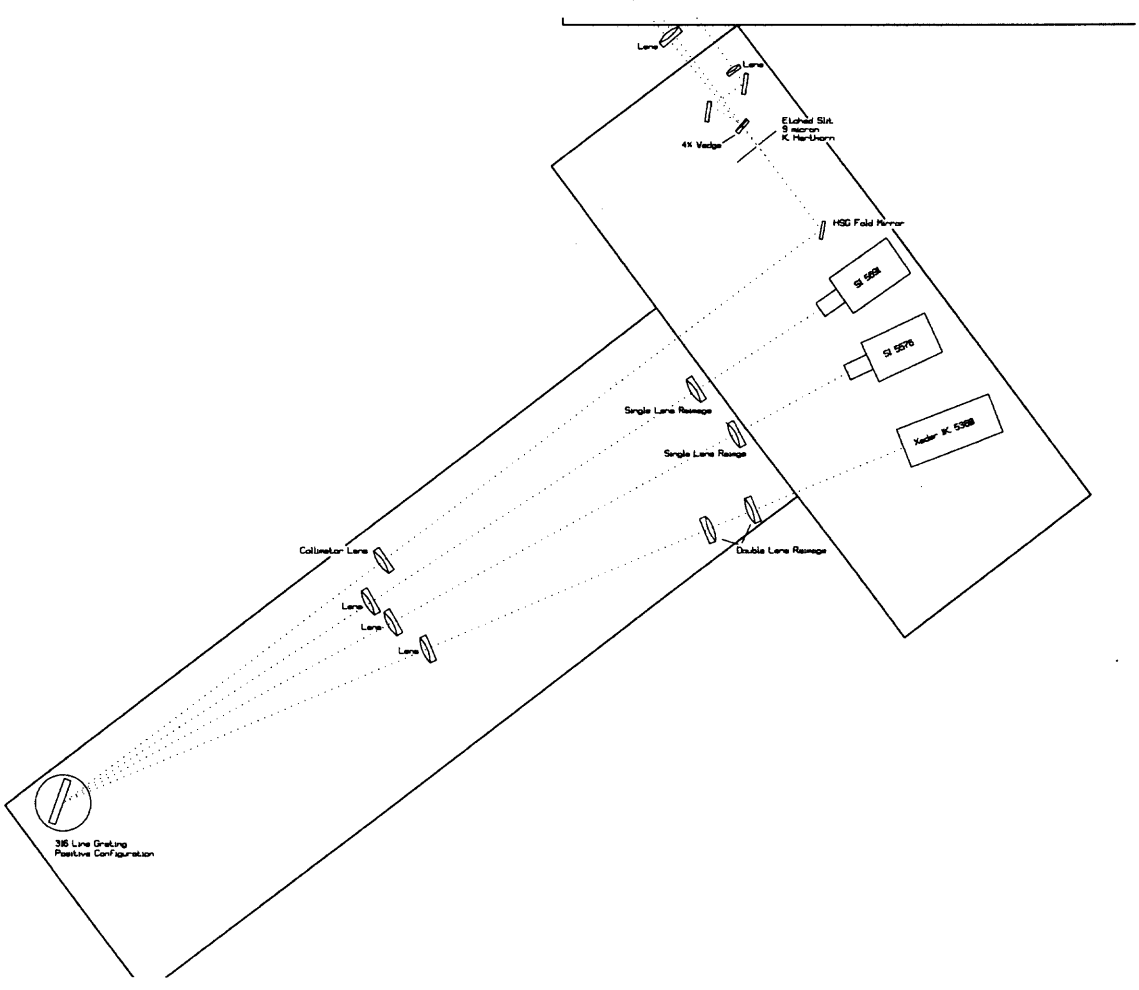

Figure 2.9 The horizontal spectrograph of the Dunn Solar Telescope. The grating is not used in auto-collimation. Instead, the different wavelength are recorded in slightly different angles from the incident light.

conditions vary greatly. To avoid these problems we obtain a slit-less image along with the slit-jaw image. The slit-jaw image is only used for locating the slit-position. A spectrograph can only investigate a small slice of the solar surface at an instant but it can gather information about several spectral lines at the same time. At the Dunn Solar Telescope typically three to four different solar lines can be investigated simultaneously. This is done by imaging the different spectral regions using collimator lenses which focus the spectral lines onto different cameras. One has to be careful to orient the spectrograph slit in North-South direction, since the atmospheric differential refraction is in this case shifting the image of the solar surface along the slit.

2.3.2 Universal Birefringent Filter

In the 1930's Bernhard Lyot [32] and Y. Oehman [39] independently discovered a method of using the birefringence of certain crystals (mainly quartz and calcite) to obtain a narrow-band filter. These filters work according to the following principle: A simple element of the filter consists of two polarizers and a crystal cut parallel to its optical axes between them. The polarizers are oriented at 45° to the optical axes. When the polarized light enters the crystal it is split into two polarization states in the direction of the slow and the fast axes of the crystal. Behind the crystal the two directions are recombined by the second polarizer. They interfere and the result is an intensity variation that depends on the wavelength according to $I = I_0 \cdot cos^2(\frac{\pi\mu l}{\lambda})$ where μ is the difference of the refractive index between the ordinary and the extraordinary rays, l is the length of the crystal and λ is the wavelength. For the construction of the filter several elements of the thicknesses 1:2:4:8 and so on are combined (Fig. 2.10). These additional elements eliminate more and more of the transmission-peaks around the center-wavelength. The final resulting transmission-function for a filter with n elements is

$$I = I_0 \cdot \frac{sin^2(2^n \frac{\pi\mu l}{\lambda})}{2^n \cdot sin^2(\frac{\pi\mu l}{\lambda})}$$

The basic filter composed only of the simple elements described above can be improved in several ways, since it has a very limited field acceptance due to that fact that inclined rays result in a wavelength shift, and that it is only usable for one wavelength. It is possible to construct a wide-field element where the crystal of a simple element is split in half. The second crystal is rotated by 90° and a half-wave plate is inserted between the two pieces with an orientation of 45° to both crystals. The wide-field element allows for a much wider field of view than a simple element or a Etalon. A quartz wide-field element accepts rays inclined about 18 times as much as a simple element. A calcite element wide-field element accepts rays inclined about 6 times as much as a simple element. Since inclination is only a problem for narrow bandwidth and since for these bandwidth calcite elements are used due to their higher birefringence the improvement of wide field acceptance is a factor of 6. Compared to an air-spaced etalon the field acceptance is about 12 times greater; 6 times because of the wide-field and 2 times because the refractive index of calcite which is around 1.5 compared to 1.0 for an air-spaced etalon, which yields a factor $(1.5)^2 = 2.25$.

The wide-field Lyot-filter can be improved further by making it wavelength tunable. This can be done in various ways. The temperature can be controlled to exploit the variation in birefringence with temperature or the elements can be made to vary their thickness. These two methods are technically difficult to realize. The method that is usually implemented is the following: After each element, simple or wide-field, a

quarter-wave-plate is added. Rotating an adjacent polarizer results in a wavelength-shift. If all the elements of a filter are made adjustable, the bandpass of the filter can be shifted to any desired wavelength. There is, however, the significant problem that the wave plates have to be achromatic. Otherwise the principle of wavelength shift and wide-field elements would only work for one wavelength perfectly. The achromacy of a wave-plate is achieved by combining wave-plates of quartz and MgF in an appropriate way. The principle described above was implemented with the Universal Birefringent Filter (UBF) [4]. A picture of this instrument can be seen in Figure 2.11.
The UBF consists of nine elements of which four are wide-field elements. Four of the elements are made of calcite, five are made of quartz. The filter has a FWHM of 252 mÅ at a wavelength of 700 nm decreasing to a FWHM of 95 mÅ at a wavelength of 450 nm which is also the smallest usable wavelength due to the poor transmission of polarizers in the blue. The total transmission is about 7.1 percent in the red and dropping to about 3.5 percent in the blue. The UBF uses interference pre-filters with a half-width of about 50 Å to block of the side maxima to the transmission of the crystals. These side maxima occur at wavelength further away from the wavelength of the central transmission peak than the FWHM of the thinnest crystal. The bandpass around 5500 Å is shown in Figure 2.12. The convolution of the solar spectrum with the UBF, i.e. the graph the UBF would produce if used as a spectrometer is shown in Figure 2.13.

A major advantage of the UBF compared to Fabry-Perot Systems is that one can observe two wavelength at the same time, called dual mode. This has been exploited before by Lyot [32] to image the green and red coronal line together with H-α at the same time. When Lyot filters with narrower band-passes became available, this method was applied to obtain dopplergrams and magnetograms in the dual mode [3].
The fact that the left and the right wing are recorded simultaneously is a big advantage since the main source of measurement errors in dopplergrams is the differential seeing explained in Chapter 2.2.4. The simultaneity of the left-wing and the right-wing image eliminates this error source. Furthermore, the probability of obtaining a good dopplergram increases dramatically, since only one good picture has to be taken to obtain a measurement instead of two in a row. The increase in measurement accuracy is about two to four depending on the seeing-conditions. This was determined by a comparison of previous observations in the single mode with the observations performed for this investigation. The inherent loss of measurement sensitivity on the other hand is only about 20 percent. The exact values are given in table 2.1. The measurement-range which is defined as the range in which the linear relationship between I_n and velocity is better than one percent on average is given in table 2.2. The gain in measurement accuracy due to the simultaneity of the dual mode exceeds the inherent loss of the dual mode by far.

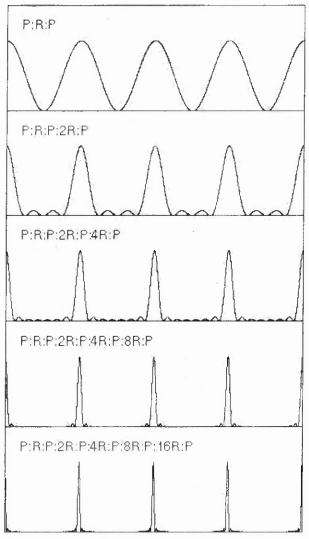

Figure 2.10 Transmission curves of a Lyot filter with one (top) to five (bottom) simple elements.

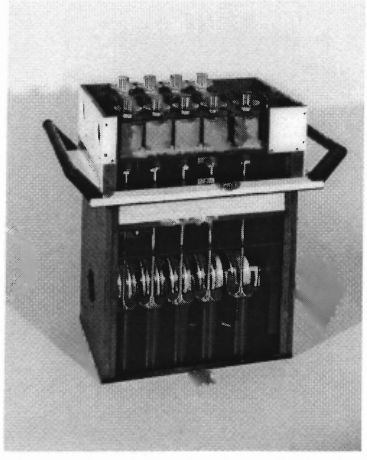

Figure 2.11 The Zeiss Universal Birefringent Filter (UBF) used at the DST without its cover. The length of the instrument is about 40 cm.

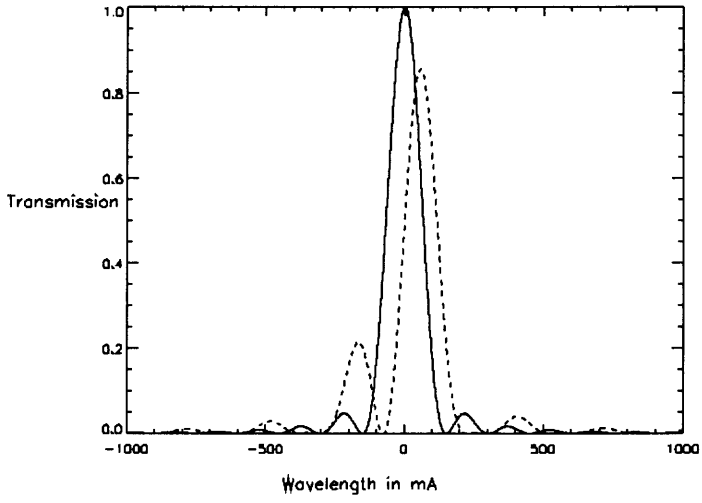

Figure 2.12 Bandpass of the Zeiss Universal Birefringent Filter (UBF). The solid line shows the single mode transmission profile. The dashed line shows the transmission profile with the thickest element tilted by 45°. This corresponds to the bandpass in the dual mode which is used in the setup for all observation runs of this thesis.

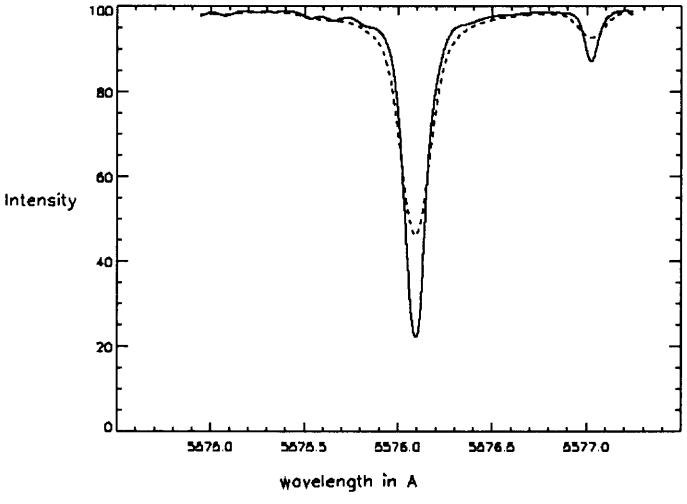

Figure 2.13 The 5576 Å spectral line intensity of the Liege atlas (solid line) and the convolution of this line intensity with the UBF bandpass profile in the single mode (dashed line).

The UBF can be used in the dual mode by removing the last polarizer behind the element with the smallest FWHM and replacing it with a polarizing beam-splitter oriented at 45°. The two images behind the beam-splitter have a center-wavelength separated by the FWHM of the largest element. The separation is suitable for velocity measurements since the two band-passes fall in the left and the right wing of a typical photospheric spectral line. The displacement of the bandpass is shown in Figure 2.12. The convolution of the left bandpass with the spectrum is compared to the convolution with the UBF bandpass of the single mode in Figure 2.14.
A comparison between the single and the dual mode in graphical form, both with a bandpass distance of 160 mÅ can be seen in Figure 2.15. This comparison is performed for the three different wavelength that we used i n our investigations to obtain dopplergram. One can see that the reduction in measurement sensitivity is the largest for the weakest spectral line, the C I 5380 line. This is to be expected, but even for this line, the loss in sensitivity is only 27 percent (Tab. 2.1).
Two effects can be studied in Figure 2.16 which compares three wavelength spacings of the single mode with the dual mode. The top three graphs show the effect of the distance between the two band-passes. Increasing the distance results in lower the sensitivity while the dynamic range is increasing. The optimum value of separation is reached when the measurement range is just sufficient to cover the velocities that one wants to measure. Since a measurement range of ± two km/s is desirable a bandwidth-distance of 130 mÅ would be optimal. The natural spacing of the dual mode of 160 mÅ is very close to this value, i.e., the UBF in the dual mode has the right spacing for the observations we want to perform.

The dual mode of the UBF can also used to record the residual intensity pictures. To do so, one bandpass is now positioned at the line center while the other bandpass is positioned a FWHM of the UBF (about 160 mÅ around 550 nm) towards the red. Since most lines have a width smaller then 100 mÅ , the second bandpass usually falls into the continuum allowing simultaneous observation of the core and the continuum of a spectral line. The results of the simulation of the dual and single mode of the UBF applied to obtain residual intensity images are very similar to the results of the calculations for the dopplergrams presented here. The loss in accuracy is again about 20 percent. The graphs for the residual intensities are not displayed, since they are very similar to the graphs of the dopplergrams.
The simulation of the dual mode plays an important role in the case of the residual intensity measurements. Since less than one third of the light passing the UBF originates from the line core and the rest originates from the continuum, it is necessary to determine the real residual intensity from the measured values by an inversion procedure. To calibrate this procedure we wrote a simulation that varies the line depth of the used solar lines over a wide range. The spectral profiles of these lines were taken from the Liege atlas [14]. The line profiles were convolved with the UBF bandpass and the 'measured' intensity was calculated. The result is a table

of real core intensity compared to the measured intensity. We will use this table in Chapter 3.1.3.3 to calibrate the residual intensity measurements.
This simulation is not needed for the dopplergrams because the calibration can be measured directly in this case. The shift in the spectral line which is proportional to the velocity is simulated by shifting both band-passes of the UBF by a known wavelength. We perform a series of equally spaced wavelength shifts and obtain a table with the wavelength shift that is proportional to the velocity on one side and the normed intensity difference on the other side. This table is used in the actual measurement convert the measured normed intensities into velocities.

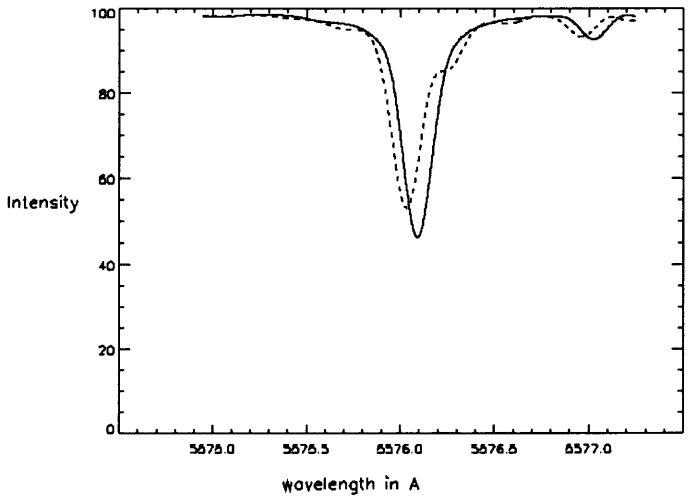

Figure 2.14 Convolution of the 5576 Å line intensity of the liege atlas with the UBF profile of the single mode (solid line) and with the UBF profile of the double mode (dashed line). This plot shows the effect of the reduced transmission of the center wavelength and the increased transmission of the sidebands of dual mode of the UBF compared to the single mode.

	5576	5691	5380
Single mode: 1000 $m/s = I_n \cdot$	0.097	0.037	0.015
Double mode: 1000 $m/s = I_n \cdot$	0.080	0.033	0.011
Ratio	0.82	0.89	0.73

Table 2.1 Measurement sensitivity of the UBF for the single mode and the double mode. The bottom row shows the ratio between the two modes.

	5576	5691	5380
Single mode range in m/s	2475	2319	2565
Double mode range in m/s	1937	1898	2119
Ratio	0.78	0.82	0.83

Table 2.2 Dynamic range of the UBF (i.e. where the linearity is better than one percent) for the various lines (left to right) and the single and double mode as well a their ratio.

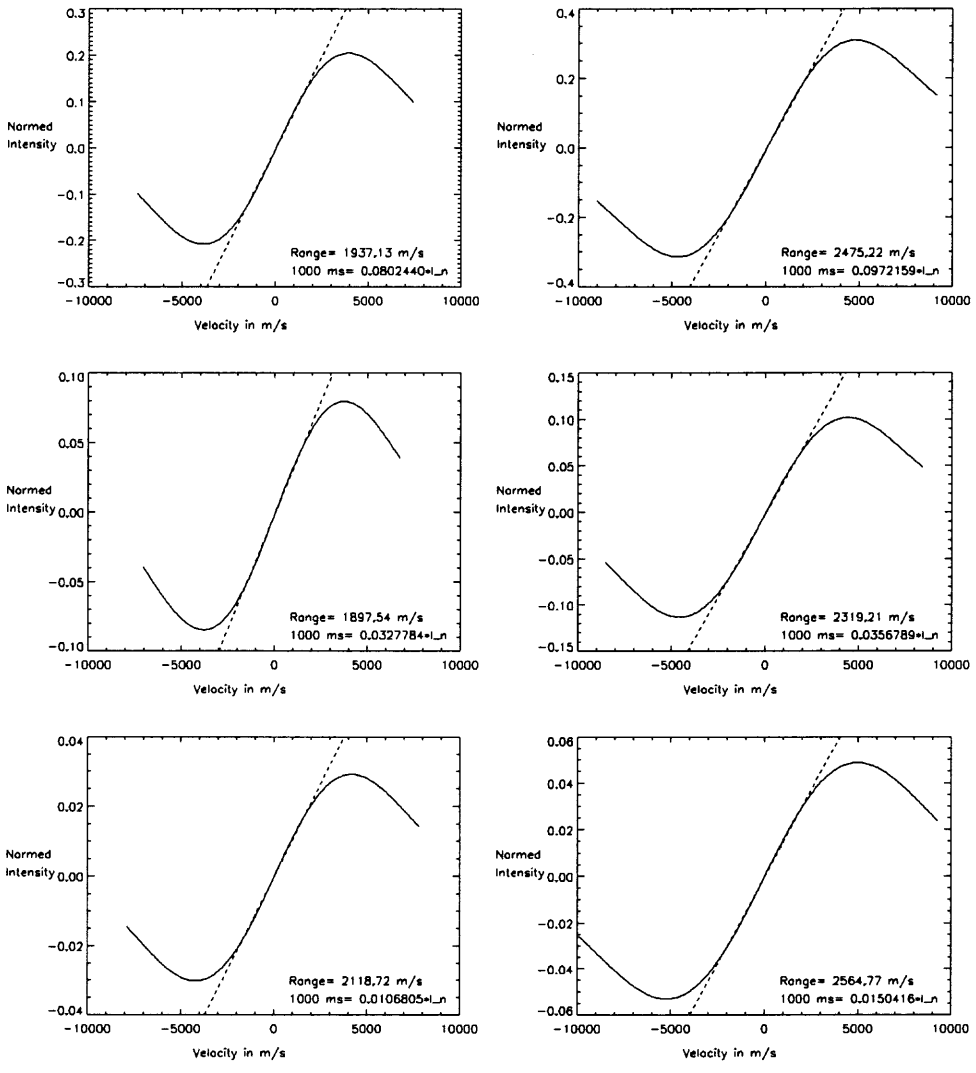

Figure 2.15 Comparison between the UBF single mode (left) and the UBF double mode (right) for the spectral lines are Fe I 5576 Å (top), Fe I 5691 Å (middle) and C I 5390 Å (bottom). The single mode is set to the spacing of 160 mÅ, the same spacing that occurs naturally in the dual mode. These plots demonstrate that the loss in measurement sensitivity for the dual mode is only minor.

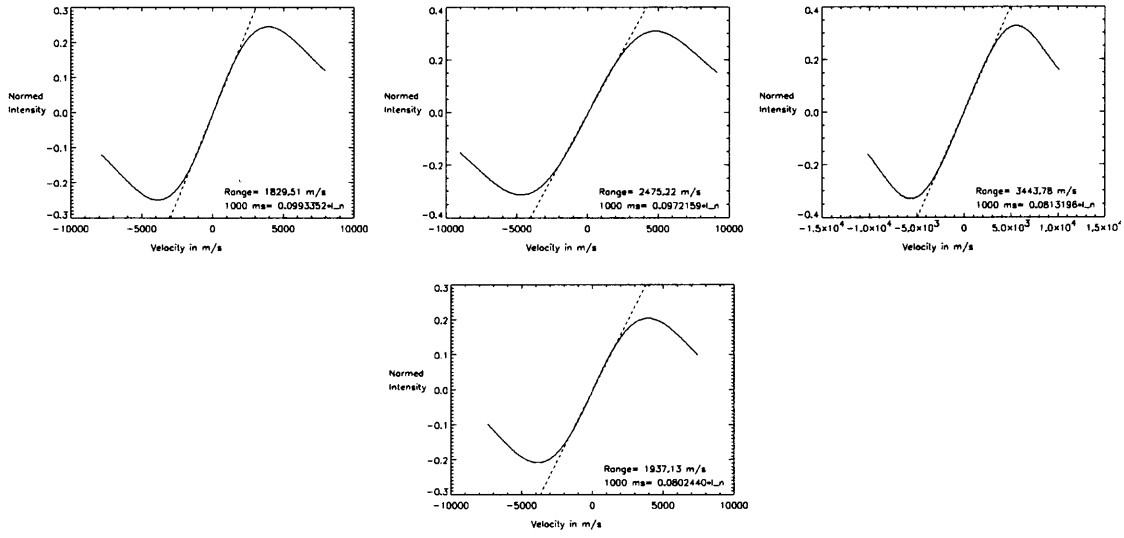

Figure 2.16 Comparison between different spacings of the single mode (top) and the dual mode with a fixed spacing of 160 mÅ (bottom). The spacing between the band-passes of the UBF is 100 mÅ (left), 160 mÅ (middle) and 200 mÅ (right). One can see how the dynamic range increases form left to right as the sensitivity decreases.

2.4 Spectral Lines and Physical Measurements on the Sun

2.4.1 Spectral Lines and their Formation

The light emitted by the sun does not have a spectral profile following the law of black body radiation. Apart from the global differences which are a result of the temperature changes with radius and the changing opacity with wavelength, there exist many intensity variations on a much smaller spectral scale.

These intensity variations, called spectral lines, are a result of the following process: the light emitted from the core of the sun does not contain spectral lines. It is produced by nuclear fusion and transformed by inelastic scattering. Gradually, as the solar plasma cools down toward the 'surface' of the sun, atoms and molecules form. The light passing this layer is absorbed selectively since the atoms and molecules have discrete energy levels and photons with exactly these energies have a much higher possibility of being absorbed by the atoms or molecules. In other words, the opacity (optical density) of the solar atmosphere is higher in a spectral line. Therefore, one cannot see as deep into the sun meaning one can only see higher layers. Since these layers are cooler, they are darker, which is the reason why photospheric spectral lines are dark.

The absorbed photons are either remitted with a different wavelength or the same wavelength, since the de-excitation of an atom or a molecule can take place in several steps with each step having a lower energy than the initial excitation. Therefore, parts of the continuum are 'missing' due to the absorption of the atoms and molecules. The result of this process, the solar spectrum, is shown in Figure 2.17.

Only when specific conditions in the solar atmosphere are present an atom or a molecule exists in a sufficient number to form a spectral line. For most atoms or molecules these conditions such as temperature and pressure only exist in a certain and relatively narrow layer of the solar atmosphere. Therefore, the light absorbed by a specific atom or molecule originates from a certain layer in the solar atmosphere with a certain height. This height is referred to as the formation height of a spectral line. If we measure light from the core of a spectral line, we gain information about the composition of the solar atmosphere at the formation height of the specific spectral line. This fact will be exploited throughout this investigation.

In Figure 2.17 one can see that spectral lines are no lines in the mathematical sense, but have a certain line width, because the molecules have a high temperature of about 5800 K and therefore the exact absorption wavelength of each atom or molecule at rest is shifted by the Doppler effect. Additionally, collisions shorten the time of emission for the atoms on molecules which results in a broadening of the emission profile due to the uncertainty principle. The resolution line profiles, called Voigt-profile, is therefore a combination of the Doppler profiles due to the temperature and the damping profile due to collisions.

Even though the shape of the line profile varies to some extent for different spectral lines, it is convenient to introduce two numbers to describe the shape and strength

of a spectral line. The width of a line is defined the Full Width at Half Maximum (FWHM) of its line profile, which is around 20-50 mÅ for a typical spectral line but can have values up to 10 Å for very strong lines like the Calcium K-line at 393.3 nm. The strength of a spectral line, called the equivalent width, is defined as the area the function $A = I_c - I/I_c$ where I_c is the intensity of the (average) continuum of the spectral region and I is the measure intensity of the spectral line profile. The equivalent for spectral lines of medium strength in the solar atmosphere is around 100 mÅ.

The strength of the absorption in a spectral line depends on the possibility of absorption for one atom or molecule in general for any given wavelength. The total absorption in a spectral line depends on the number of atoms present. The number of atoms depends highly on the temperature and on the pressure in the solar atmosphere. This can be exploited to calculate the number of atoms from the measured absorption in a spectral line and ultimately draw conclusions about the atmospheric conditions of the solar structure observed.

Spectral lines change their appearance under the influence of a coherent velocity field or a magnetic field. A coherent velocity field results in a shift of wavelength which is proportional to the velocity according to the Doppler-Effect.

$$\Delta\lambda = \lambda \cdot \frac{v}{c}$$

where λ is the wavelength of the un-shifted spectral line, v the velocity of the molecule in the line-of-sight, c the speed of light and $\Delta\lambda$ the resulting wavelength shift.

A magnetic field splits the single core of a spectral line into several components according to the Zeeman effect. The number of the components as well as the magnitude of the separations depends on the atom or molecule that produces the spectral line. For a given line however, the splitting of the lines is

$$\Delta\lambda = 4.7 \cdot 10^{-5} \cdot g \cdot \lambda^2 \cdot B$$

where λ is the wavelength of the un-shifted spectral line, B is the magnetic field strength in Gauss, g is the Landee-factor and $\Delta\lambda$ is the resulting wavelength shift. The Landee-factor g is a measure for the intrinsic magnetic sensitivity of an atom or a molecule and can be calculated by the quantum numbers of the electron transition. Since both effects are proportional to the velocity and the magnetic field strength respectively, and the factors of proportion can be calculated a measurement of the wavelength shift of the spectral line allows the determination of these quantities. The details of the measurement process will be given in Chapter 2.4.3.

Figure 2.17 Spectrum of the sun in the visible light including the spectral lines.

2.4.2 Spectral Lines used in this Investigation

An important question at the beginning of this investigation was which spectral lines we should use for the different observing runs. Since we decided to use the UBF for this thesis, a spectral line had to fulfill several requirements:

- Line separation

  The UBF has a FWHM that changes from 120 mÅ in the blue to 250 mÅ in the red. We want to measure individual solar lines. This implies that the solar lines must be separated by more than the FWHM of the UBF or otherwise a mixing of lines would occur. This excludes spectral regions in the blue of the solar spectrum lower than 500 nm since spectral lines are too numerous in the blue.

- Line strength

  The UBF has a FWHM of about 160 mÅ FWHM at a wavelength of 550 nm and an equivalent width of 320 mÅ. We want to measure a solar line that has a contribution of at least ten percent to the total intensity passing through the UBF. This implies that spectral line has to have equivalent width larger than 36 mÅ. Moreover, the sensitivity of velocity and residual intensity measurements scales approximately with the ratio of the equivalent width of the line over the equivalent width of the filter. It is therefore desirable to use spectral lines as strong as possible.

- Magnetic properties

  A non-magnetic line (g=0) is not effected by the magnetic field and does not split into several components because of the Zeeman effect. This splitting influences velocity and residual intensity measurements. We do not perform magnetic studies in this investigation and therefore want to choose non-magnetic lines. Unfortunately, it is not always possible to choose non-magnetic lines because the number of spectral lines with the required separation and strength is limited, especially for low-forming spectral lines.

- Formation height

  Most photospheric spectral lines have a certain height where most of the light emitted at the center wavelength of the line originates as described in Chapter 2.4.1. It can only be determined by radiative transfer calculations [68]. It is of advantage to cover a large area of heights in the photosphere by choosing lines with different formation heights. This is important because we have little information beforehand about the structures that we want to investigate such as the bright points or the G-Band.

The first two conditions are mandatory to allow physical properties to be measured by the UBF while the last two properties are only desirable. According to the criteria above, we choose the spectral lines described below.

- Fe I 5576 Å

  This is the strongest line used in this investigation since it has an equivalent width of 113 mÅ and a center wavelength of 5576.099 Å. It is a non- magnetic Fe I Iron line that forms in a height of about 320 km [68] above the photosphere (Fig. 2.18). It is was chosen because it forms high, is strong and non-magnetic.

- Fe I 5691 Å

  This line has a center wavelength of 5691.505 Å and an equivalent width of 38 mÅ. It is also a non-magnetic Fe I line. This Fe I Iron line is very similar to the Fe I 5576 Å line except for its formation height which is around 160 km above the photosphere (Fig. 2.18). Therefore, it is perfect for testing a variation in height within solar structures.

- Ti II 5381 Å

  This line has a center wavelength of 5381.028 Å and an equivalent width of 56 mÅ. It is a magnetic Ti II line that has a Landee factor of g=1.087. The formation height of this line is about 160 km above the photosphere (Fig. 2.18), which is about the same as for the Fe I 5691 Å line. Therefore, the Ti II 5381 Å line cannot provide any new hight information, but it allows us to check the calculations of Steiner who predicts a different behavior for these two lines (Ch. 1.5.2).

- C I 5380 Å

  This line has a center wavelength of 5380.322 Å and an equivalent width of 26 mÅ . Therefore, it is the weakest spectral line in this investigation. The C I 5380 Å line is marginal in terms of how weak a line can be to be measured with the UBF. Furthermore, this C I carbon line is magnetic with a Landee factor of g=1. We selected this line since it contains a formation height of about 40 km above the photosphere (Fig. 2.18), and is therefore one of the lowest forming lines which are observable with the UBF at all.

We do not use all lines in all investigations. The UBF has a cycle time of about 10 s per image-pair in the dual mode and since substantial changes on the solar surface can occur within 10 to 30 seconds, we limited the number of wavelength to three per run. For the residual intensity pictures we used the Fe I 5576 Å line, the Fe I 5691 Å line and the Ti II 5381 Å line. We used the Ti II line to test the predictions of Steiner about the mechanism of bright point contrast enhancement. For the dopplergrams we used the Fe I 5576 Å line, the Fe I 5691 Å line and the C I 5380 Å line. We

used the C I 5380 Å line instead of the Ti II 5381 Å line because for dopplergrams the Ti II 5381 Å line does not contain any additional information when compared to the Fe I 5691 Å line, whereas the C I 5380 Å line provides a much better height coverage. We used all spectral lines in the spectrograph observations since the Ti II 5381 Å line and the C I 5380 Å line are close enough to fit onto the same camera, enabling us to acquire the information all four spectral lines simultaneously.

While line properties like center-wavelength, line depth and equivalent width can be measured, other important properties like the line formation height and temperature sensitivity are derived from models. These properties are essential if a solar line is to be used for an investigation of a solar structure. Only if all properties of a solar line are known it is possible to translated measured values into physical properties of the investigated solar structures.
All calculated data in this theses was produced by the program RH-code [68], [70]. This program was written by Han Uitenbroek, who provided the results of the calculations for the use in this thesis. He also transformed all the atmospherical datasets from various calculations into the suitable format for RH-code. Without his kind sharing of his work, there would be no calculations section. His program will be explained later in detail in the 'calculations'-section along with some atmospheric models.

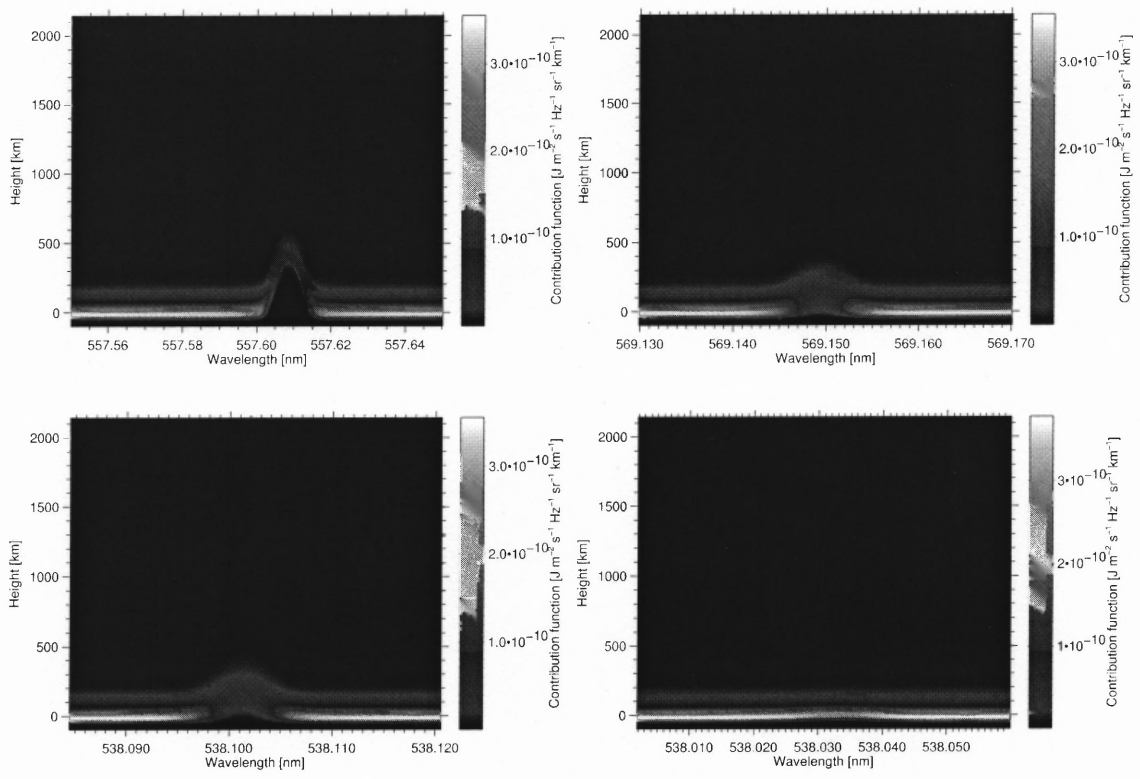

Figure 2.18 Contribution functions of the Fe I 5576 Å line (top left), the Fe I 5691 Å line (top right), the Ti II 5381 Å line (bottom left) and the C I 5380 Å line (bottom right). The wavelength is the horizontal axis, the height is the vertical axes. The contribution function is color-coded on the right side. A contribution at a certain height is the amount of the intensity of the light emitted by the line from solar plasma in this height level. The maximum contribution from the Fe I 5576 Å line core originates from 320 km above the photospheric level $\tau = 1$, the main contribution of Fe I 5691 Å and the Ti II 5381 Å originates from layers around 160 km height, and the C I 5380 has a maximum contribution from a height of about 40 km.

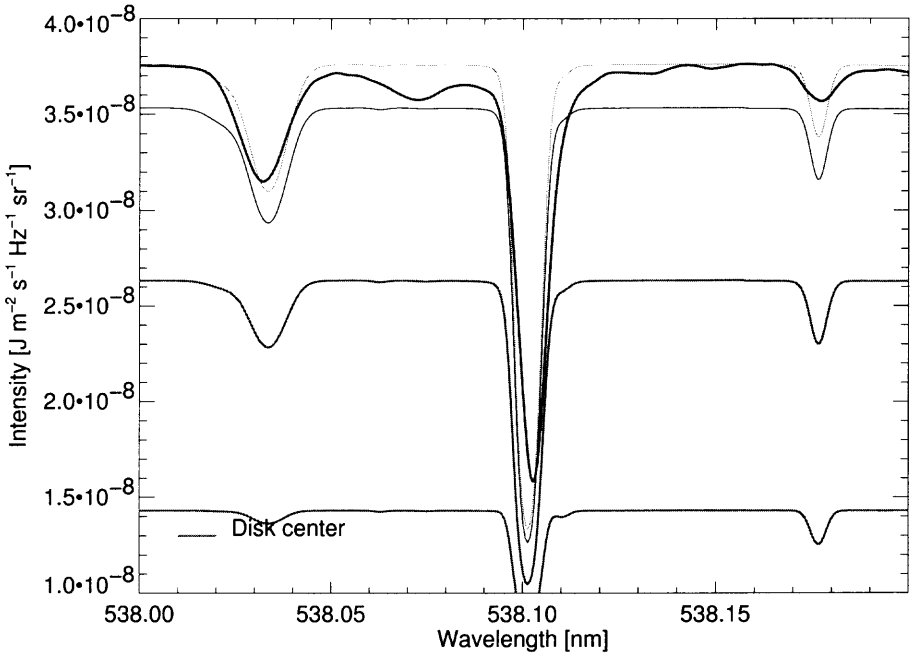

Figure 2.19 Comparison between the calculated profiles of the Fe I 5576 Å line (dotted (highest) line for disc center) and the measured profile (Liege Atlas) (highest solid line). This plot shows the good agreement between the calculations and the measurement which confirms the accuracy of the contribution function calculations.

2.4.3 Residual Intensity and Velocity Measurements

2.4.3.1 Residual Intensity Measurements Residual intensity measurements compare the appearance of a solar structure in different heights by comparing an image taken at the core of a spectral line with the image taken in the continuum. Light originating from the core of a spectral line originates from the formation height of the line which is higher than the photospheric level 0 km and thus contains information from this atmospheric level. Light from the continuum originates from the surface of the sun with a height of 0 km. The comparison between the appearance of solar structures in the different heights is done by dividing the core image by the continuum image.

$$I_{res} = \frac{I_{core}}{I_{continuum}}$$

The division of the core intensity by the continuum intensity ensures that the intrinsic brightness of the structure does not influence the measurement. We will use this method throughout this investigation.

2.4.3.2 Velocity Measurements Atoms or molecules moving coherently along the line-of-sight in the height a spectral line originates from cause the CWL of a spectral line to be shifted by the Doppler effect according to

$$\Delta\lambda = \lambda \cdot \frac{v}{c}$$

where λ is the wavelength of the un-shifted spectral line, v the velocity of the molecule in the line-of-sight, c the speed of light and $\Delta\lambda$ the resulting wavelength shift. Since the wavelength of the spectral line is known and the shift of the spectral line can be measured, the velocity of the plasma can be determined from the wavelength-shift. The method of determining the shift of the wavelength depends on the instrument used and will be described in the different observation Chapters.

2.4.3.3 General Remarks about Measurement Errors and Measurement Accuracy The measurement error of physical parameters on the sun is the result of the measurement error in intensity since intensity is the only quantity we can actually measure on the sun. The relation between the error in intensity and the velocity or the residual intensity is linear in our study, but this is only valid for the specific way we perform our measurements.
The measurement error of intensity is composed of the dark-noise of the CCD chip, the readout noise of the CCD chip and the photon noise. Further sources of error are an imperfect flat-field which maps the sensitivity differences between the individual pixels of a CCD chip.

The absolute measurement error alone does not determine the usefulness of a measurement since it disregards the spatial resolution. The point spread function, a

result of the diffraction at the telescope aperture and the seeing, causes a mixing of spatially different points on the solar surface. Therefore, a physical value measured for a certain point on the solar surface is averaged with the value of this physical property of surrounding pixels. It is obvious that a larger structure in which all the pixels have the same value for the specific physical quantity is less effected than a smaller structure. Therefore, this mixing error increases with decreasing structure size.
To quantify this effect we introduce a new quantity called 'limit of detection'.

$$ld = err \cdot r \cdot r$$

where err is the absolute measurement error and r is the resolution of the image defined as the FWHM of the PSF. The limit of detection states a sensitivity for a measurement taking the size of the structure into account. The limit of detection not only depends on the instrument used but also on the seeing conditions. We will state the accuracy for each instrument and each observation run separately.
The meaning of the limit of detection is the following: if a structure is small, i.e. in the order of the resolution limit, the limit of detection can be used to decide if a certain structure on the sun can be observed with an instrument or not. For example Steiner [64] predicts down-flows around bright points of 3 km/s and a size of 100km. Therefore the limit of detection is $ld = 57.9 \cdot \frac{m}{s} \cdot arcsec^2$. In Chapter 3.2.2 we find that the limit of detection for the UBF is for the Fe I $ld = 0.6 \cdot \frac{m}{s} \cdot arcsec^2$ 5576 Å line and $ld = 3.8 \cdot \frac{m}{s} \cdot arcsec^2$ for the Fe I 5691 Å line. Therefore the predicted down-drafts should be observable.
For structures much larger than the resolution limit different rules apply. Their detectability depends on the absolute measurement error as well as the number of pixels measured of a certain structure and the statistical gain this number yields.

CHAPTER 3

Observations

This chapter is organized into three different parts which describe the three different observing runs performed between February 2001 and February 2002.

During the first run in February 2001, we recorded residual intensity images using the UBF. We used the residual intensity images to compare the intensity of solar structures in different heights of the solar atmosphere (Ch. 2.4.3). The objective was to test the predictions of Steiner [63] and Sanchez-Almeida [50] about the formation height of the G-band. Furthermore, we tested the prediction of Steiner that bright points have an enhanced contrast in the Fe I lines but not in the Ti II lines. We also investigate if bright points change their size or position with increasing height in the solar atmosphere. An increase in size with increasing height maybe suggested by the calculations of Steiner [64]. During this observing run, we had excellent seeing conditions an obtained diffraction-limited pictures. Unfortunately, the seeing conditions were not stable enough obtain a time-series.

The second run in April 2001 provided high-resolution dopplergrams of umbral dots and penumbral grains in different wavelength, as well as dopplergrams of a small number of bright points. Again, we used the UBF in the dual mode, but this time with the two band-passes positioned symmetrically in the blue and red wing of the spectral lines. Dopplergrams show the plasma flow in the investigated physical structures and can be used to answer essential questions about the heating mechanisms of the investigated structures. Velocity measurements also allow for a comparison between the observations and the theoretical predictions for sunspots (Weiss [29], Parker [42]) and bright points (Steiner [64], [65]). We derived an approximation of the residual intensity by combining the left and the right wing of the dopplergrams. This method results in a lower sensitivity of the residual intensity measurements as compared to the previous observing run because the combination of left and right wing of the dopplergram results in an effective broader bandpass of the UBF. Nevertheless, we could perform some interesting correlation studies of the G-band residual intensity derived from the G-band filtergrams and the atomic spectral lines.

For the third run in February 2002 we used the horizontal spectrograph to obtain spectra of umbral dots and penumbral grains simultaneously in three different wavelength regions which covered all spectral lines used in the UBF investigations. This allowed us to verify the results of the UBF investigations by using the spectrograph since we can study the same solar lines with a much higher spectral resolution. On the other hand, we did not reach the spatial resolution of the UBF observations because of the size of the slit and the seeing conditions. Moreover, a

spectrograph only provides one-dimensional spatial information. This means that the investigation is complementary to the two proceeding observation runs in the sense that we can reach much higher spectral, but only a significantly lower spatial resolution. Unfortunately, the seeing conditions made it impossible to obtain spectra of bright points.

3.1 Residual Intensity Images

3.1.1 Motivation

We record residual intensity images with the UBF in the dual mode. We use the lines Fe I 5576 Å with a formation height of 320 km above the photosphere, Fe I 5691 Å with formation height of 160 km and the Ti II 5381 Å line which forms at the same height (Ch. 2.4.2). Additionally, we record broad-band filtergrams in the G-band. This enables us to study the contrast of bright points in all used lines which allows us to test the predictions of the Steiner that bright points will have a higher intensity for the Fe I but not for the Ti II lines. We investigate individual bright points to detect size and shape changes with height as well as an inclination of bright points. We also check the correlation of the G-band with the other solar lines to draw conclusions about the formation height of the G-band.

3.1.2 General Remarks about the Observations

We recorded the data on February 17, 2001 at the Dunn Solar Telescope (DST) of the National Solar Observatory at Sacramento Peak. We used the low-order AO system installed at the Dunn Solar Telescope (Ch. 2.2.4) to correct the first 20 Zernike modes. The smallest structures we could resolve had a size of about 0.16 arcsec. This was determined be measuring the smallest FWHM of bright structures in the G-band image and is therefore an upper limit.

We recorded narrow-band filtergrams using the Universal Birefringent Filter (UBF) in the dual mode (2.3.2). Behind the UBF we placed a Quarter-Wave Plate and a Polarizing Beam-splitter as well as two 16-bit 1kx1k SI CCD-cameras to record the filtergrams. We used a Xedar 2kx2k 12-bit CCD camera (reading out only 1kx1k) behind a 10 Å interference filter centered at 4305 Å to record the G-band images. All pictures were taken simultaneously with an exposure-time of 1500 ms. The pixel-scale was 0.039 "/ pixel for all cameras resulting in a field of view of 40"x40". The layout of this setup is shown in Figure 3.1 and Figure 3.2.

Each exposure yielded the following three images: the core and the continuum filtergram behind the UBF in the desired wavelength and the image behind the G-band filter. We do not have a separate white-light channel and use the continuum wavelength image instead. The exposures were taken in the sequence two times Fe I 5576 Å, two times Fe I 5691 Å and two times Ti II 5381 Å. This sequence was

taken twice and saved into one file. The cycle-time to record one set of images was ten seconds. Unfortunately, the seeing was not stable enough to obtain a consistent time-series.

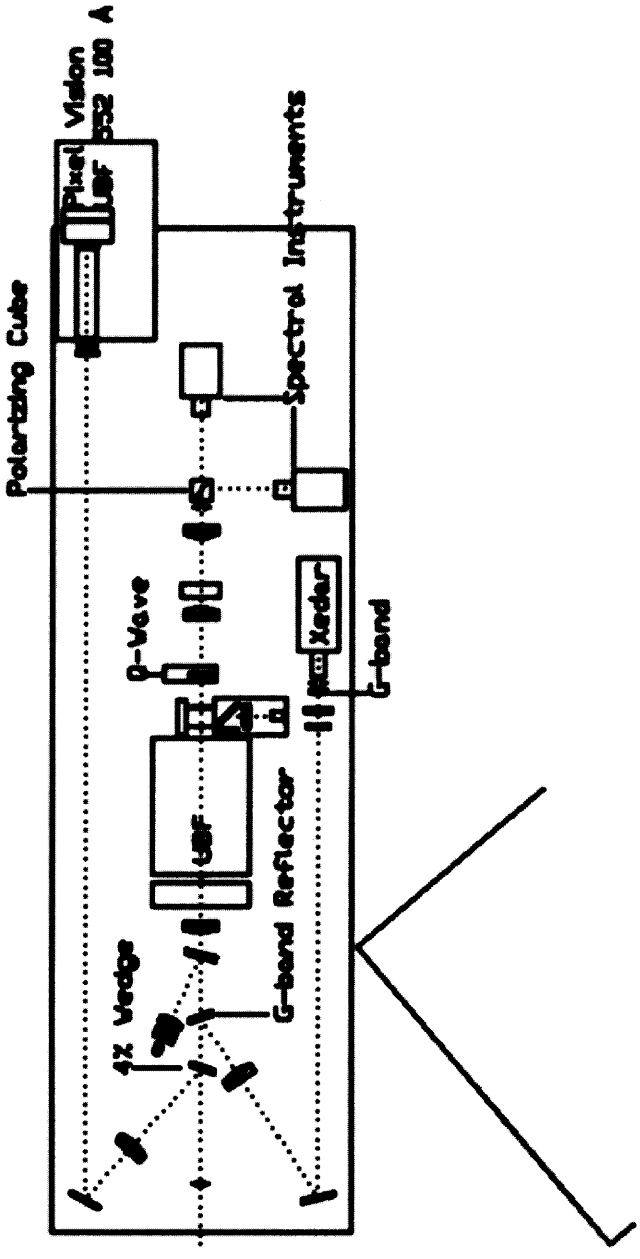

Figure 3.1 Setup used to record the residual intensity images using the UBF in the dual mode. The light enters from the left. The spectral region from 400-450 nm is reflected by the G-band reflector onto the Xadar camera used to record the G-band image. The four percent wedge, which reflects four percent of the light onto the white-light camera was not used due to camera problems. The remaining light is passed on to the the UBF which produces two narrow-band filtergrams recorded by the two SI-cameras.

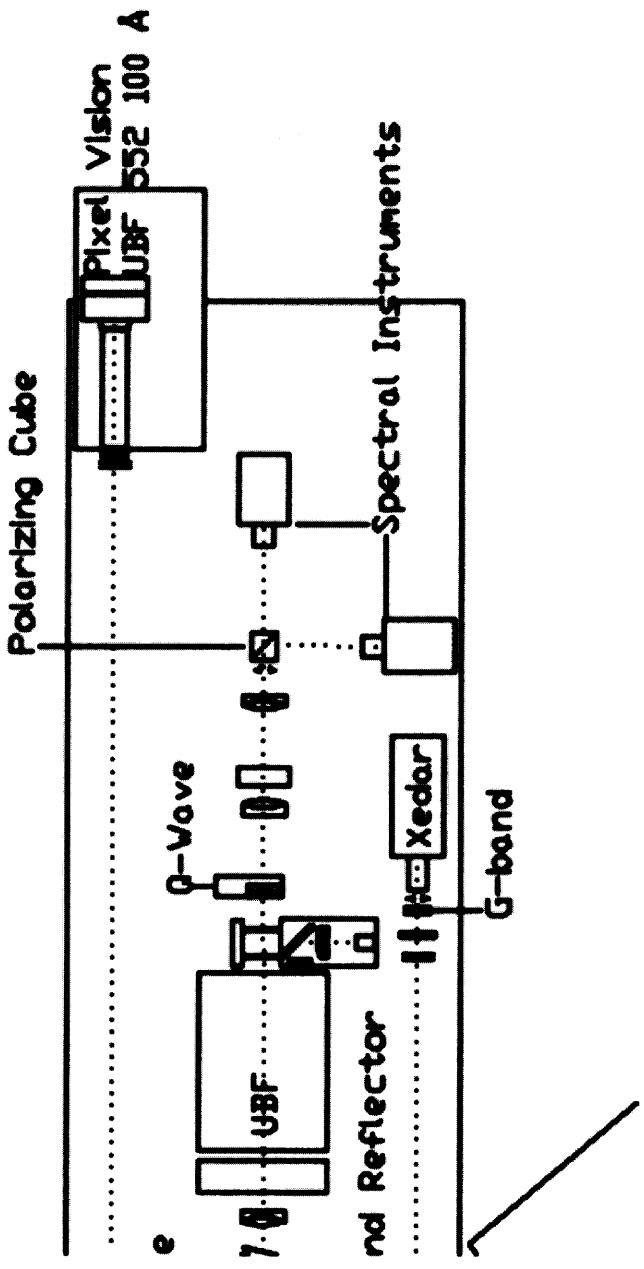

Figure 3.2 Closeup of the UBF section from the setup shown above (Fig. 3.1). Immediately behind the UBF we can see the calibration diode used to calibrate the crystal positions of the UBF at the beginning of each observing run. The light passes the Quaterwave-plate which translates a phase-shift of the light into polarization direction and passes the polarizing beam-splitter which separates the left wing and the right wing image. The two images are recorded by the two synchronized SI-cameras.

3.1.3 Data Reduction

3.1.3.1 General Remarks All images were flat-fielded and a dark-frame subtraction was performed. For each wavelength the best 60 images, from a total of 720 images were selected automatically by a program calculating the RMS image contrast of the G-band images. From these 60 images we selected the best image for each wavelength visually. The pictures were aligned using target images. The overall alignment for the red and blue wing was better than 0.5 pixels meaning that the shift between the left and the right wing image was smaller than 0.5 pixels. The alignment accuracy for the G-band images was about 1.0 pixel, depending on the position in the field of view. We determined the size of the alignment-errors by processing target images in the same way as the solar images and determining the deviation of the resulting image from a zero-image. The G-band images were normalized to a mean intensity of 1.0.

We selected various solar structures of interest using an automatic procedure. This procedure generates masks that select various solar structures. These masks are 1.0 for all pixels identified as a certain structure and 0.0 otherwise.
An important tool in this analysis is the 'Fourier-decomposition' of the spatial information of an image. The image is blurred by averaging every 3x3 pixel area. This blurred image is subtracted from the original image and the resulting image is saved as component zero. The blurred image is the start image for the next iteration and is blurred again by a 5x5 pixel algorithm, subtracted from the 3x3 blurred image to yield the first component. This process is repeated iteratively with a blurring of $(2^n + 1)$x$(2^n + 1)$ pixels until the blurring area is larger than the image itself. The Fourier components contain detail of a certain size and a combination (adding) of several components enables us to pick structures of a certain size range. If all components are added, we retain the original image. This method can be understood in the context of a Fourier analysis which shows that each component of the Fourier-decomposition can be obtained by applying a filter in the Fourier domain. This filter is shaped like a Gaussian ring which enhances only details of a certain frequency, i.e. size and removes or suppresses detail of other size. The Fourier-decomposition could be replaced by this filtering process in principle. However, the Fourier decomposition has the advantage that it only operates in the image domain which avoids the Gibbs phenomenon. Moreover, it is faster than Fourier filtering. An example of this Fourier-decomposition is shown in Figure 3.3.

3.1.3.2 Selection Criteria and Procedures

- G-Band bright regions

  We found regions on the solar surface that show a high intensity in the G-band residual intensity image. We selected every pixel with an intensity greater than 1.06 as 'G-band bright'. This threshold was chosen because of the visual

appearance of the G-band bright regions. These regions are not an effect of the enlarged point spread function due to seeing conditions as shown in Chapter 3.1.4.4. These bright regions contain all bright points, but they cover more surface area than the bright points themselves. We study the G-band bright regions as an independent structure on the solar surface.

- Bright points

  We selected individual bright points in the following way: we removed intensity variations with spatial scales larger than 0.5 arcsec by applying the Fourier-decomposition to the G-band image. Then we selected every pixel with a local intensity larger than 0.21 as 'bright point' and every pixel with a (local) intensity larger than 0.065 as 'bright point with surroundings'. The procedure above selected some of the bright, small granules as well. We eliminated these granules by performing an 'AND' operation with the 'G-band bright region' mask since the observations show that bright points lie exclusively in G-band bright regions.

- Photosphere, granulation and intergranular lanes

  We selected every pixel with an intensity greater than 0.65 in the white-light image as photosphere. We removed all intensity variations larger than nine arcsec by using the suitable components of the Fourier decomposition. We selected every pixel with an intensity greater than 0.0 as granule and every pixel in the photosphere not selected as granule as intergranular lane.

- Pores

  We selected pixels in the white-light picture with an intensity lower than 0.65 as pore.

The selection process is summarized in Figure 3.4. An example mask generated by this process can be seen in Figure 3.5. Histogram 3.6 shows the area distribution of the different solar structures where we can see that about 14 percent of the pixels are selected as G-band bright regions, six percent are selected as bright points with surroundings and 2.5 percent a bright points. In bad seeing condition only four percent of the pixels are selected as G-band bright regions and no pixels are selected as bright points.

The selection process we used is new in some respects. The selection of the granules and intergranular lanes yields a larger percentage of lanes compared to the granulation as other processes. We choose this selection nevertheless, since there is no other natural boundary than a local brightness greater or smaller than zero. The selection process for the bright points is mostly new as well. Mueller [35] identifies bright points visually. Berger [7] uses different methods for the identification of

bright points, among them the 'blob' method which closely resembles a special case of the Fourier decomposition we use. Since he does not have G-band images and white-light images at the same time, he has to remove bright granules manually. We use the method of selecting G-band bright regions instead. This allows us to use a fully automized selection process which does not depend on subjective criteria like the human eye.

The results of the selection process depend on the seeing conditions. The seeing conditions vary to some extent even though we used the AO system. In poor seeing conditions, the Strehl ratio is reduced and therefore the general contrast of the images is reduced. Thus, less bright points are selected since their contrast falls below the threshold. It is difficult to determine the quantitative influence of the seeing conditions on the measurements. We do not have any measurements of the residual wavefront error from wavefront sensor data and therefore we cannot correct for seeing effects. We address some effects of the seeing variations, e.g. in Chapter 3.1.4.1 where we include a dataset recorded in bad seeing conditions. Generally we try to minimize the effect of seeing by choosing the best images for each wavelength.

Selection algorithm of bright points
We wrote a program to identify individual brights points using the G-band image. One bright point is defined as a connected area of pixels from the bright point mask. We pick a pixel selected as bright point and identify all other selected pixels not separated from the original pixel by non-selected pixels. All pixels connected to the original pixel form one individual bright point. Each bright point is analyzed for its shape, surface area, intensity and residual intensity and then removed from the mask. The procedure is repeated with the remaining bright points in the mask.

Histograms and scatter plots
For all histograms in the residual intensity section, we used a binning of 30 bins. The error-bars superimposed on the scatter-plots uses a binning of 20 bins. The length of these bars is determined by the rms variation of the data-points and represents the $one - \sigma$ uncertainty.

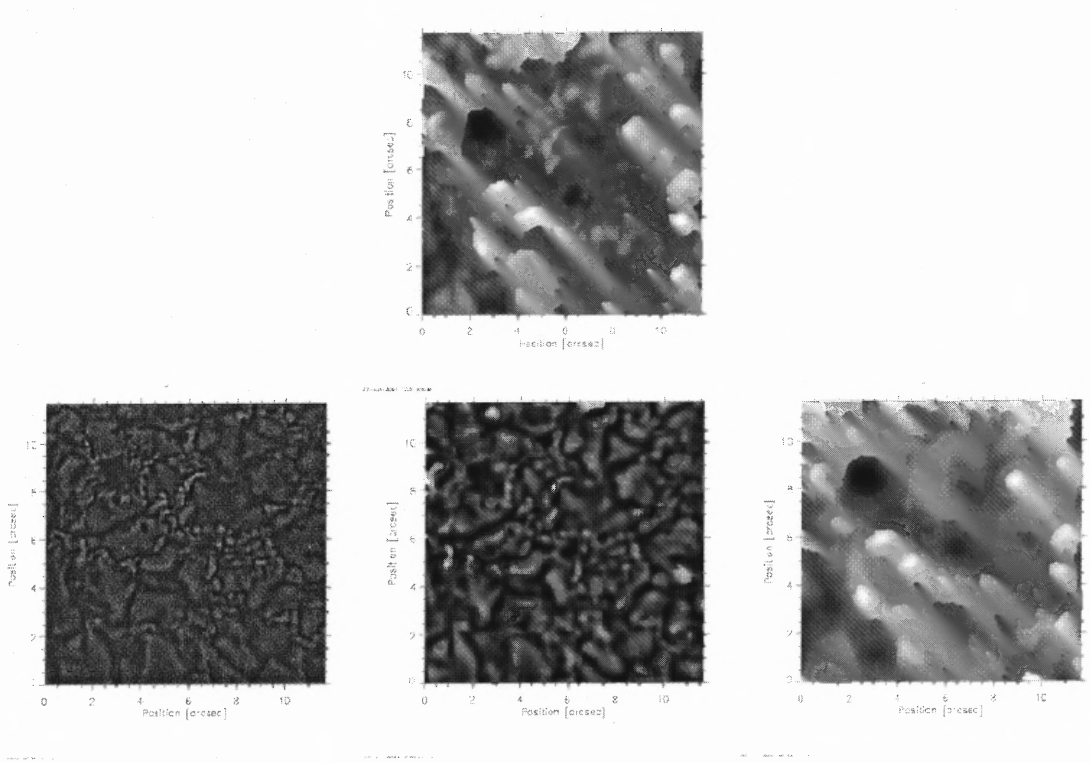

Figure 3.3 The Fourier decomposition used for the selection of the solar structures. The top image is the original picture, the lower left is the 0-component containing most of the noise and some structure. The lower center image is used for the selection, containing the 1-,2- and 3-component and therefore enhancing the bright points. The lower right image contains all the higher components and therefore only the large-scale detail.

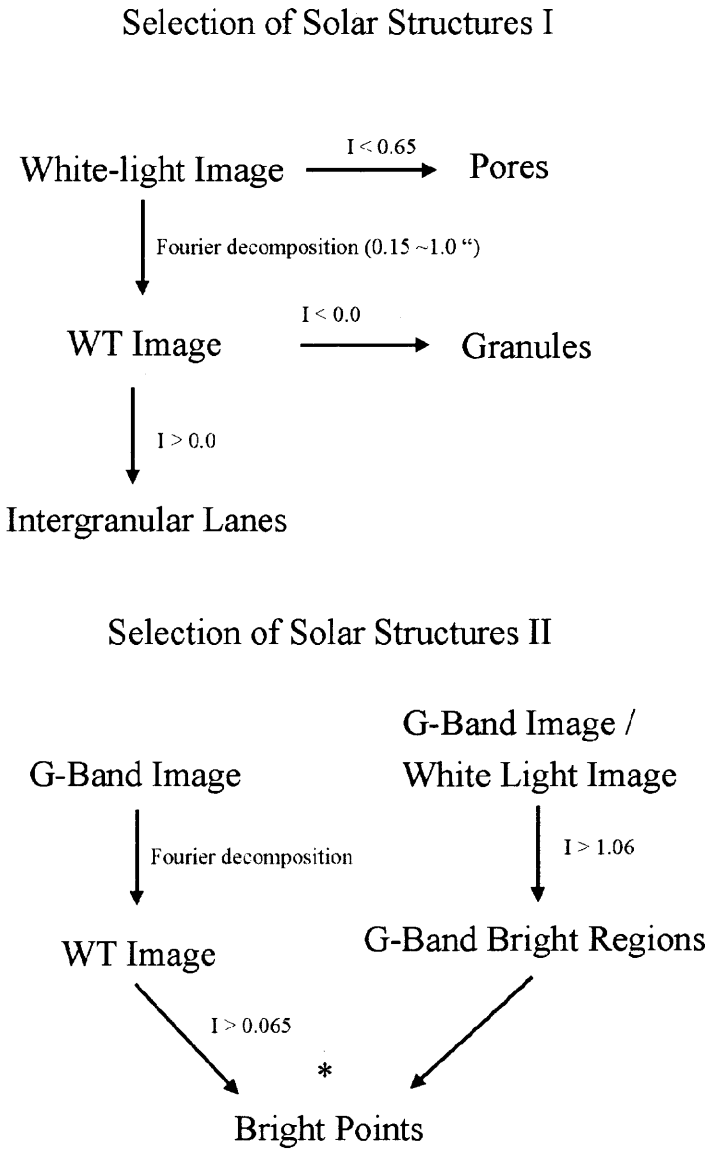

Figure 3.4 The selection process of the solar structures as a flowchart.

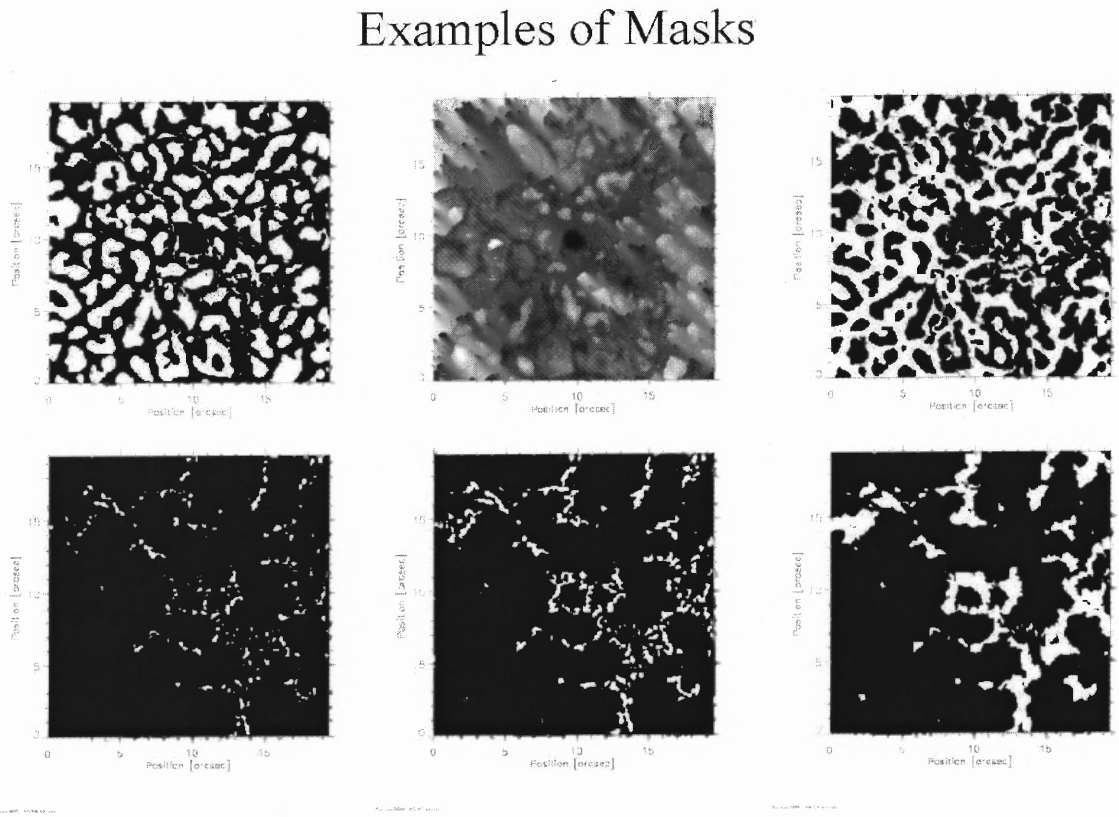

Figure 3.5 Example of masks obtained by the selection process. The center upper image is the original image. The top left images shows the granule-mask, the upper right the mask for the intergranular lanes. The bottom row shows from left to right the bright point mask, the mask for bright points with surroundings and the mask for the G-band bright regions.

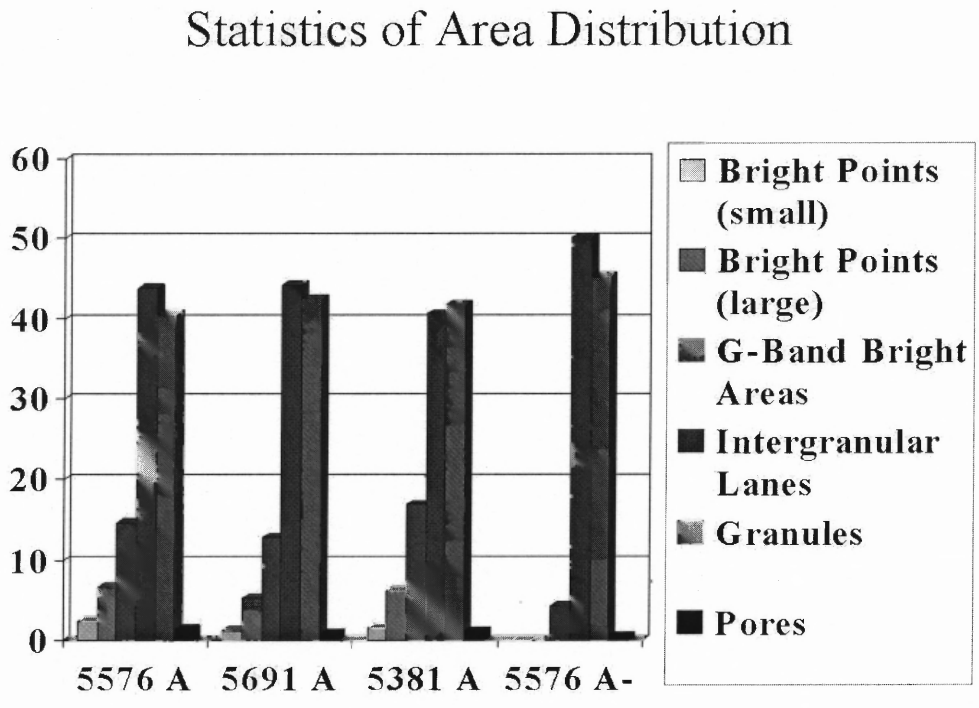

Figure 3.6 The area distribution in percent for the different lines we use in this analysis. The bars above 5576 Å - represent a data sample recorded during bad seeing conditions where no individual bright points can be identified anymore. It is included for comparison.

3.1.3.3 Calibration of Residual Intensities The residual intensity pictures are formed by $I_{res} = \frac{I_{core}}{I_{continuum}}$. Because the UBF has a bandpass with half-width of 160 mÅ for the used wavelength range, most of the transmitted light, about 70 percent to 85 percent depending on the spectral line, originates from the continuum surrounding the solar line. The real intensities of the line core are calculated from the measured mix of core, wing and continuum using the simulation routine described in Chapter 2.3.2.

To determine the measurement error we remove all structures larger than one pixel from the residual intensity image. This only leaves the noise since we determined the shift-error to be smaller than 0.5 pixels. We measure the rms variation of the noise which is equivalent to the measurement error. We determine the error to be 0.0049 independent of the line used. In the best images which we used for the analysis, we measured the resolution to be better than 0.16 arcsec. Therefore, the limit of detection is ld=$1.25 \cdot 10^{-4} \cdot arcsec^2$.

3.1.4 Results

In the first part, we study the selected solar structures in a statistical sense by averaging over all selected pixels of a structure and calculating the average value. We investigate whether the bright points are significantly different from other solar structures or if they have similarities to other, well know solar structures. Furthermore we check the predictions of Steiner [63] that bright points have an enhanced contrast in the Fe I lines but not in the Ti II lines.

In the second part, we study individual bright points. This enables us to investigate the structure 'bright point' itself. We determine the effect that shape and size of a bright points have on the physical properties. This information is essential for understanding the contrast enhancement mechanism of bright points and allows us to distinguish between the different proposed contrast enhancement mechanisms.

In the third part, we study the physical properties of the solar atmosphere a pixel by pixel basis. Contrary to the first section we do not average over all pixel nor do we average over each bright point as in the second part but study the distribution of the physical values of the individual pixels. This yields information about local atmospheric properties.

In the fourth and last part we examine pictures of individual solar structures as representative examples. The goal is to determine changes of solar structures with height. Especially we check for an increasing diameter of bright points with height as suggested by the calculations of Steiner [64] and and the inclination of bright points. Furthermore, we can check again the prediction of Steiner [63] about the contrast of bright points in the atomic lines.

3.1.4.1 General Statistics The most general way of analysis is to average the measured values over all the pixels of a specific solar structure. This disregards the shape and size of the structures but gives very good statistics for the mean physical parameters since the number of pixels analyzed are large and the measurement error decreases with the square-root of the number if we assume a Gaussian distribution. In our datasets, we average over about 100000 pixels selected as belonging to the G-band bright regions, 45000 pixels selected as belonging to the bright points with surroundings and 18000 pixels selected as belonging to the bright points with out surroundings. If we assume a Gaussian distribution, the the one σ measurement uncertainty is about $1.55 \cdot 10^{-5}$, $2.31 \cdot 10^{-5}$ and $3.65 \cdot 10^{-5}$ respectively.
The measurement values are shown in table 3.1 as well as in Figure 3.7 and Figure 3.8. Table 3.1 states the measured values of residual intensity for the selected solar structures compared to the wavelength of the residual intensity. Histogram 3.7 shows the residual intensity for the stated solar lines and different solar structures. The right set of bars represents a dataset with bad seeing conditions for comparison. In this dataset almost no bright points can be identified, and the number of pixels selected as belonging to the G-band bright regions is reduced to about 35000. Nevertheless, there is no significant change in the measured values for this dataset. The reason is probably that only the innermost parts of the G-band bright regions are selected during bad seeing conditions and that these innermost parts mainly coincide with the bright point selection during good seeing conditions. Since the bright points and the G-band bright regions (almost) have the same residual intensity, there is no change of residual intensity for G-band bright regions during bad seeing conditions. Histogram 3.8 shows the residual intensity in the G-band for the selected solar structures and for different datasets. Nevertheless, we arrive at the same results. This is an additional indication that our statistical results are mostly seeing independent.

Bright points have different residual intensities compared to all other solar structures for all investigated spectral lines, i.e. the atomic lines and the G-band CH-lines. Therefore, the atmospheric conditions in bright points must be significantly different from all other solar structures. Since we only measure two wavelength points we cannot determine whether the temperature, the temperature gradient, the pressure or the pressure gradient are responsible for the different residual intensity.
For the atomic spectral lines we do not find a difference in residual intensity between bright points (small area), the bright points with surroundings and the G-band bright regions. Only the G-band residual intensity (Fig 3.8) is different for the bright points (small area), the bright points with surroundings and the G-band bright regions although the intrinsic sensitivity of the residual intensity measurement is lower for the G-band than for the atomic spectral lines due to the much broader bandpass of the interference filter. This rules out that the unchanged residual intensity for the atomic lines is a result of the PSF.

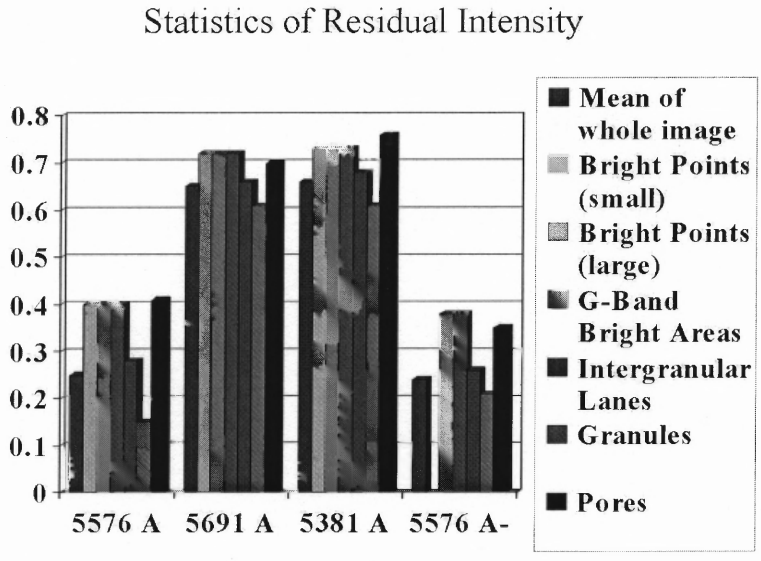

Figure 3.7 Residual intensity of all investigated solar lines against the various solar structures. '5776 A -' represents a dataset recorded during poor seeing conditions.

We draw two conclusions from this result. First, the atmospheric conditions and bright points and their surroundings so are similar that the atomic spectral lines we investigated cannot detect a difference. Second, the G-band is more sensitive to changes in the solar atmosphere since it does see a difference for the different regions around bright points even though the sensitivity for the measurement is smaller. This behavior may be explained by the fact that the G-band mainly consists of spectral lines of the CH-molecule. Molecular lines are sensitive not only to all factors that influence atomic solar lines but are prone to dissociation as well. This is an additional way, how temperature changes the number of CH molecules present and therefore changes the intensities of the CH lines and the G-band.
Figure 3.7 and Figure 3.8 show an enhanced intensity for all atomic spectral lines, i.e. the two Fe I lines and the Ti II line. Therefore, we find the contrast enhancement for the Fe I lines predicted by Steiner. However, we cannot confirm the prediction of Steiner [63] that the Ti II lines have no contrast enhancement.

Residual Intensity for	5576	5691	5380	5575 -	G-band
Mean	0.25	0.65	0.66	0.24	1.0
Bright Points	0.4	0.72	0.73	-	1.12
BP with surroundings	0.4	0.72	0.73	0.38	1.10
G-band Bright regions	0.4	0.72	0.73	0.38	1.10
Intergranular Lanes	0.28	0.66	0.68	0.26	0.99
Granules	0.15	0.61	0.61	0.21	0.97
Pores	0.41	0.70	0.76	0.35	1.04

Table 3.1 Residual intensity of all investigated solar lines against the various solar structures. '5776 A -' represents a dataset recorded during bad seeing conditions. '-' means that no measurement is available.

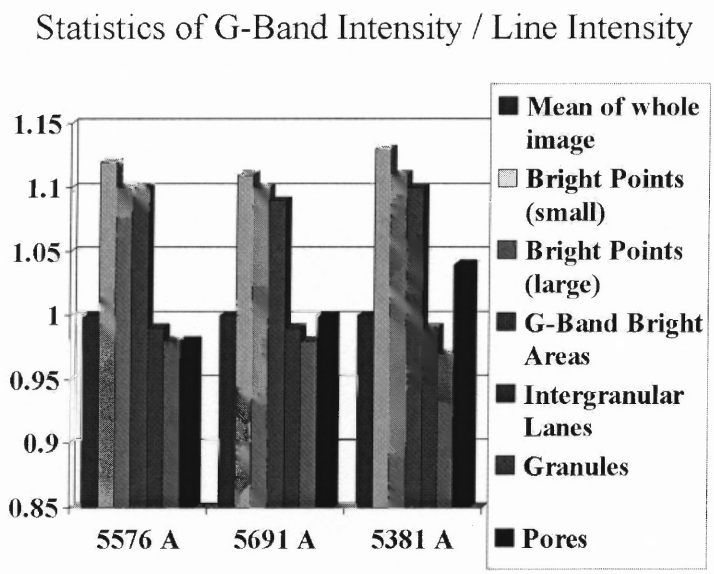

Figure 3.8 Residual intensity of the G-band for the various solar structures. The wavelength indicates which dataset was used for the G-band analysis.

3.1.4.2 Analysis of Individual Bright Points

3.1.4.2.1 General Properties and Morphology The area on the sun investigated in this observing run has a surface area of 1084 $arcsec^2$ or $5.6 \cdot 10^8$ km^2 and covers an active region with a few small pores. For the line Fe I 5576 Å we find 455 bright points, for the lines Fe I 5691 Å and Ti II 5381 Å we find 377 and 367 bright points respectively. This amounts to 0.42, 0.35 and 0.34 bright points/$arcsec^2$.
Since the G-band and white-light images used for identification of bright points are (mostly) independent of wavelength and the pictures were recorded minutes apart, we expect to find approximately the same number of bright points in all images. We attribute the differences to the varying seeing conditions. For the analysis of the morphology we used the Fe I 5576 Å line since it has the largest number of bright points and therefore the best seeing conditions.
The histograms 3.9, 3.10 show the area and circumference distribution of the bright points without surroundings divided in 30 bins. In the histograms we find data-points below the resolution limit. These points are a results of single pixels selected as a bright point. This can happen because sometimes small bright points with low contrast do not get entirely selected because only the brightest parts are brighter than the selection threshold. This does not mean that we find structures below the resolution limit but rather that we do not select the entire bright point. Unfortunately, this limitation is inevitable, since we cannot correct for the effects of diffraction.
Neither the area nor the diameter histograms show a peak since the peak in the border-length histogram vanishes when we use a different binning. We conclude that bright points are either smaller than the resolution limit of the DST and the larger bright points are formed by clusters of bright points or that there is no natural size for bright points in general.
Although there is no real peak in the size histogram, there is a substantial number of bright points with a quite large surface area and a large maximum diameter. In histogram 3.10, the drop-off in numbers of bright points to larger spatial sizes is much faster for the minimum radius than for the maximum radius indicating that bright points are elongated. This is confirmed the scatter-plot for area vs ellipticity ($\frac{d_{max}}{d_{min}}$) (Fig. 3.11). This scatter-plot shows a strong increase of ellipticity with increasing surface area which means that larger bright points are more elongated.
The scatter-plot area vs circumference 3.11 is best fit by a straight line, especially for larger areas. If bright points were round the best fit would be a square-root. This means bright points are more and more 'unround' the bigger they are. Whether the bright points seen in the pictures with the highest possible resolution possible today are composed of very small, individual features, or are just monolithic structures squeezed and deformed by convective motions (flux sheet) cannot be answered from this data.

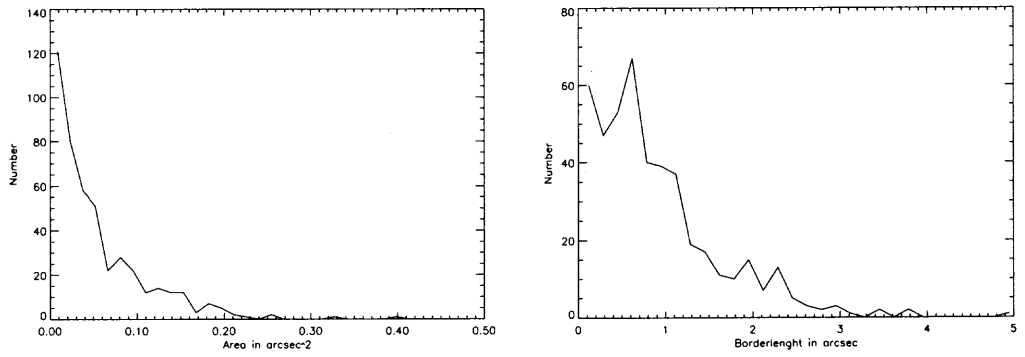

Figure 3.9 Area distribution of each bright point in $arcsec^2$ (left) and the length of their circumference in arcsec (right). There is no significant peak which indicates that bright points do not have a typical size or that larger bright points are composed of smaller ones. The peak in the right histogram is an artifact due to the binning.

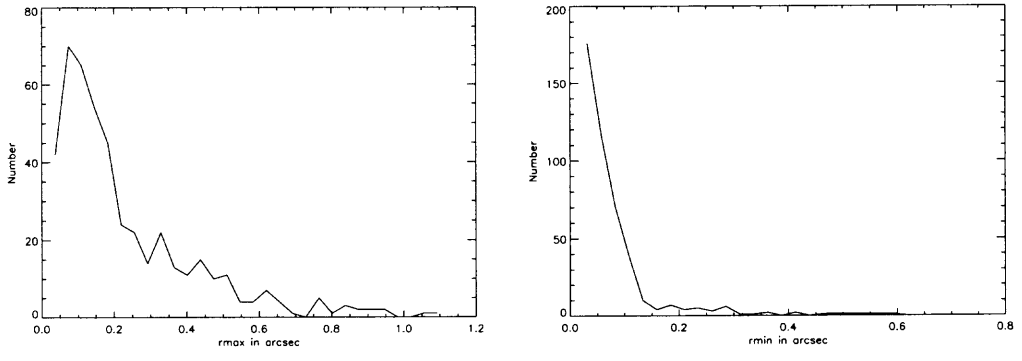

Figure 3.10 Maximum (left) and the minimum (right) radius distribution for each bright point defined as the maximum and minimum distance of the border of the bright point from its center of gravity.

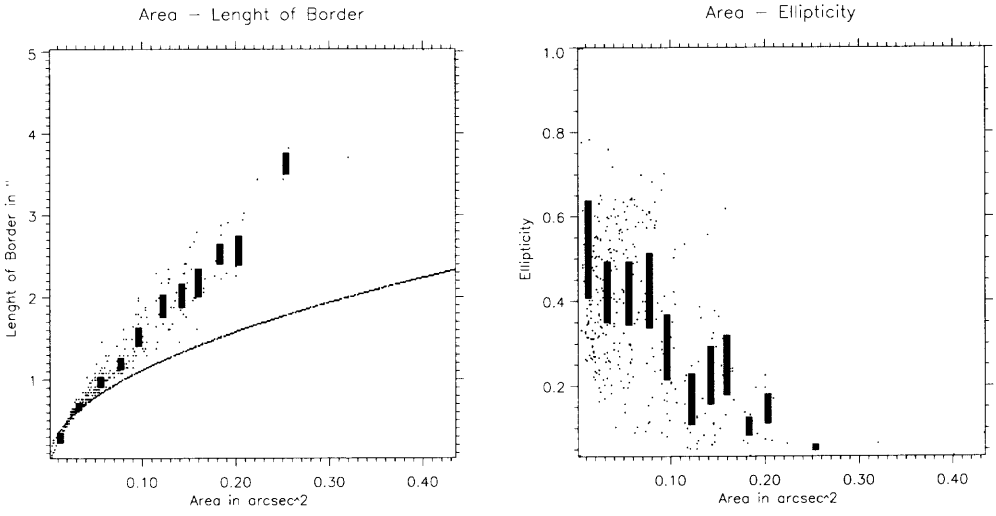

Figure 3.11 Area vs circumference (left) and ellipticity $\frac{d_{max}}{d_{min}}$ (right). The solid line in the left scatter-plot is the expected function for round bright points. One can see the almost linear relationship between the area and the circumference, which indicates a shape change with size. This can be seen as well in the area against ellipticity plot which show the increasing deformation of bright points with larger size. The smaller 'bright points' have a size of only one pixel and are obviously round. Bright points larger than the resolution-limit have an area of more than 0.02 $arcsec^2$ and are therefore found right of the second tick-mark.

3.1.4.2.2 Intensity and Residual Intensity Analysis of Individual Bright Points

Intensity distribution

The first set of histograms (Fig. 3.12) shows the distribution of the white-light intensity and the G-band intensity. In this set of histograms we also investigate the distribution of the residual intensities of the atomic lines and the G-band CH lines. Except for the G-band residual intensity, we find an approximately Gaussian distribution for the intensities indicating that bright points do have a well defined average value that we stated in Chapter 3.1.4.1. This suggests the existence of an 'average' bright point and therefore contradicts the assumption of a continuous size distribution of bright points. For the G-band residual intensity the Gaussian distribution is cut off for values lower than 1.06. This is inevitable since we have to use a threshold in G-band residual intensity to identify bright points at all.

Area vs intensity and residual intensity

The next set of graphs shows scatter-plots for the area of the bright points vs the white-light intensity, the residual intensity of the G-band and the residual intensity of the atomic lines and of the G-band (Fig. 3.13).

There is a positive correlation between the area and the white-light intensity as well as between the area and the G-band intensity. This means that larger bright points have a higher white-light intensity and G-band intensity on average. This correlation is independent of spectral lines and indicates the existence of a general contrast enhancement mechanism which is stronger for larger size.

This behavior is surprising since bright points are magnetic structures [6] as pores are as well. The white-light intensity of pores on the other hand decreases with increasing size. This can be explained with the suppression of convection by the magnetic field in a pore. It may be argued that bright points are too small to suppress the convection which explains why they are not dark, but it does not explain why bright point intensity increases with increasing size of the bright point.

The residual intensity in the G-band shows a positive correlation with the surface area of the bright points. This means that larger bright points have a higher contrast in the G-band. One can argue that this higher contrast is due to seeing since smaller structures lose more contrast due to diffraction and abberations. However, there is no correlation between the area and the residual intensity for the atomic spectral lines. If the contrast enhancement was due to seeing, it would affect all spectral lines equally.

The correlation between the area of a bright point and the G-band intensity along with the missing correlation of the other spectral lines with the surface area is confirming the result of the statistical analysis section that only the G-band residual intensity changes with the size of the bright point.

The special behavior of the G-band suggests the existence of a contrast enhancement mechanism that only works for the CH lines. This mechanism increases with the size

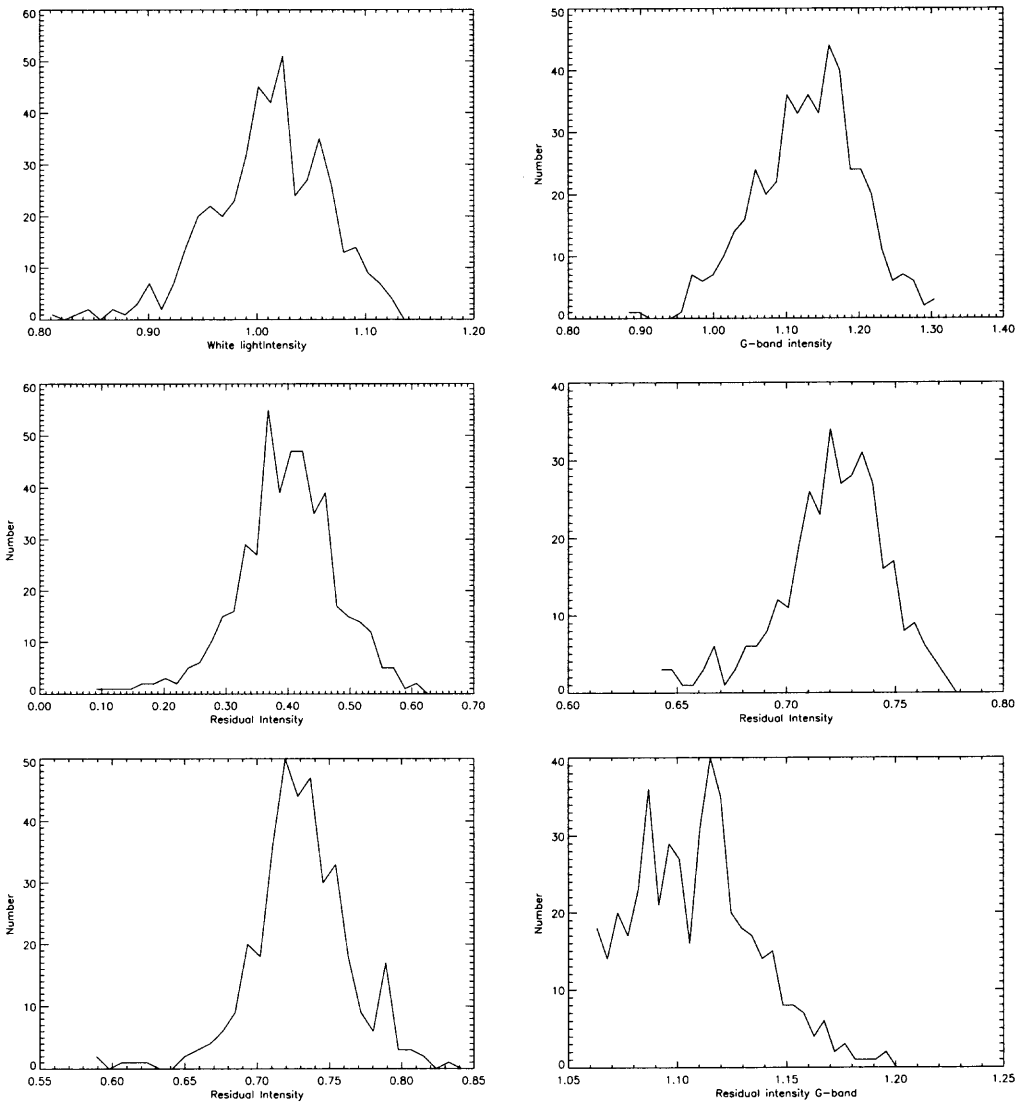

Figure 3.12 The white-light intensity (top left), the G-Band intensity (top right) the residual intensity of the Fe I 5576 Å line (middle left), the residual intensity of the Fe I 5691 Å line (middle right), the residual intensity of the Ti II 5381 Å line (bottom left) and the residual intensity of the G-band (bottom right). All histograms show a Gaussian distribution except for the histogram of the residual intensity of the G-band which is cut off by the threshold used in the selection process. The white-light image, the G-band image and the residual intensity image for the G-band have been normalized to 1.0 for the whole image. The average values for the residual intensities of the atomic spectral lines can be found in table 3.1. They are 0.25, 0.65 and 0.66 for the 5576 Å , the 5691 Å and the 5381 Å line respectively.

of the bright point. Therefore, we can exclude a boundary effect as proposed by Rutten [49]. The efficiency of a boundary effect would be decreasing with increasing size, since the ratio of circumference to area decreases with increasing size while we find just the opposite behavior.
The origin of this special mechanism for the G-band remains unclear. One important difference between the G-band and the other lines, as pointed out before, is the fact that the G-band is formed by the CH-molecule which can dissociate. It seems likely that the additional brightness enhancement is a result of dissociation of the CH molecule.

Intensity vs residual intensity
The scatter-plots 3.14 show the white-light intensity vs. the residual intensity of atomic spectral lines and the G-band. We find a weak negative correlation between the white-light intensity and the residual intensity of atomic spectral lines but a weak positive correlation between the white-light intensity and the residual intensity of G-band.
We interpret these results as follows: the positive correlation between the white-light intensity and the G-band residual intensity means that the G-band contrast for a bright point is increasing for increasing white-light intensity in a way that is more than linear. That means a bright point twice as bright in the continuum will have a G-band residual intensity *more* than twice as bright. This again confirms the existence of an additional contrast enhancement mechanism for the G-Band.
The negative correlation between the white-light intensity and the residual intensity of the atomic lines means the means the brighter bright points actually have a lower contrast in the residual intensity images of an atomic spectral line. This behavior is different from the G-band CH lines, which again confirms the existence of a different contrast enhancement mechanism for the G-band that is not shared by the atomic lines.

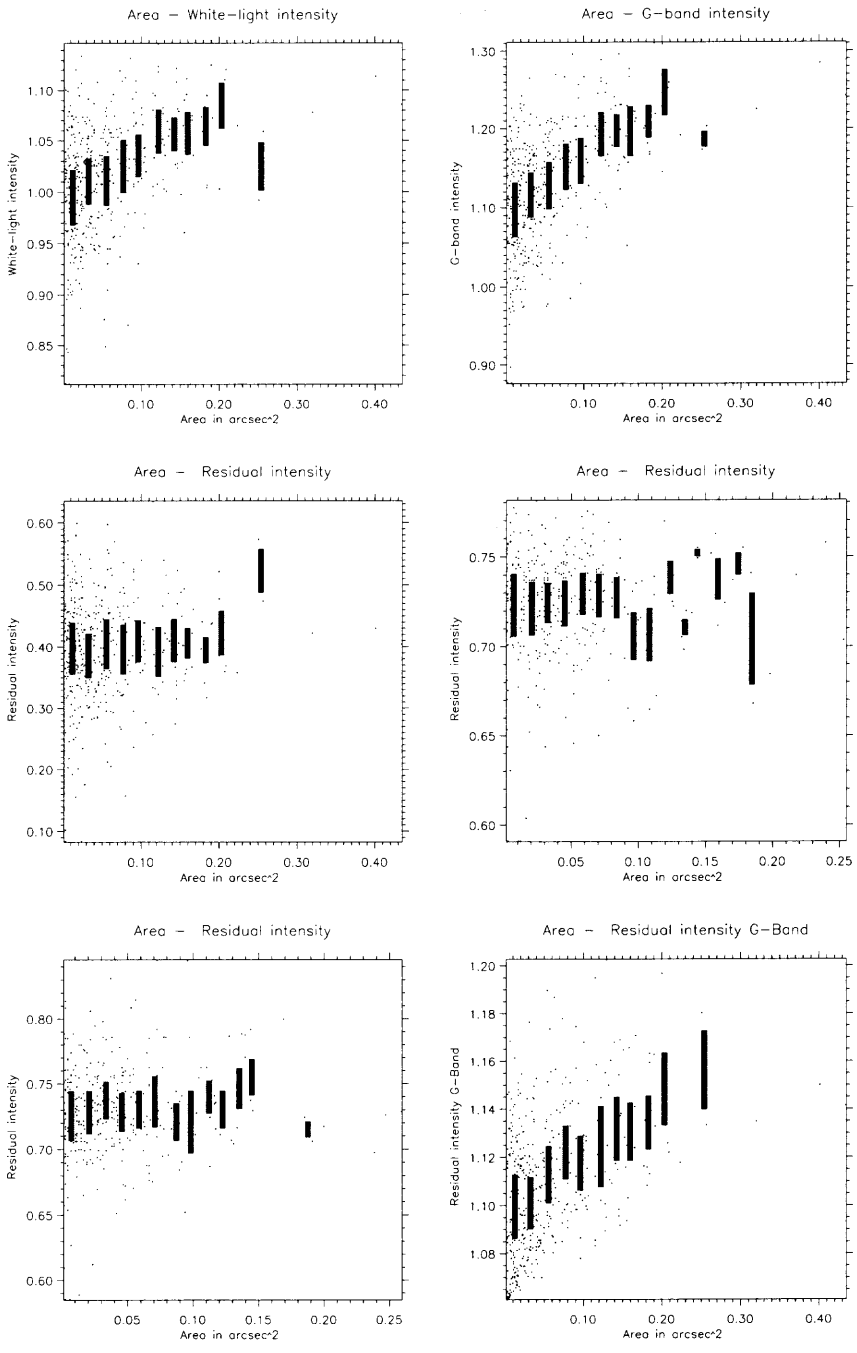

Figure 3.13 The area of the bright points vs the white-light intensity (top left), the G-Band intensity (top right) the residual intensity of the Fe I5576 Å line (middle left), the residual intensity of the Fe I 5691 Å line (middle right), the residual intensity of the Ti II 5381 Å line (bottom left) and the residual intensity of the G-band (bottom right). We find a positive correlation between the area of the bright points and the white-light intensity, the G-Band intensity and the the residual intensity of the G-band while we do not find any correlation for the atomic spectral lines.

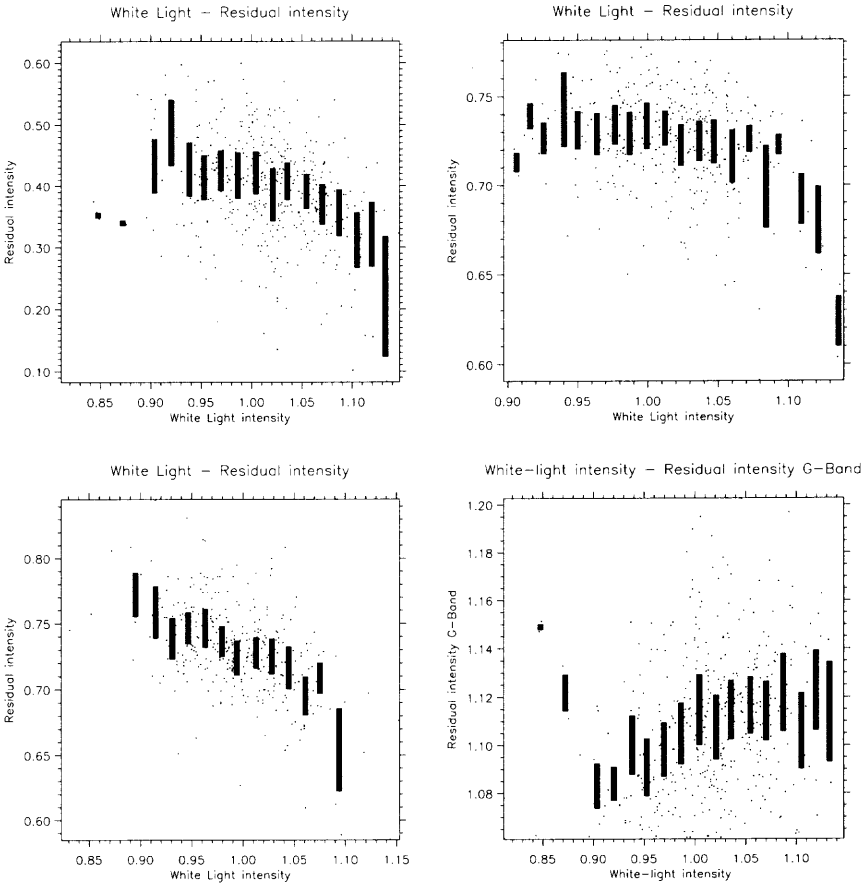

Figure 3.14 White-light intensity vs residual intensity of the 5576 Å line (top left), residual intensity of the 5691 Å line (top right), residual intensity of the 5381 Å line (bottom left) and the residual intensity of the G-Band (bottom right). The residual intensity of the atomic lines show a weak negative correlation with the white-light intensity while the G-band residual intensity shows a weak positive correlation with the white-light intensity.

3.1.4.3 Intensity Analysis of Bright Point Pixels In this section we analyze the residual intensities pixel by pixel. The difference to the previous section is that we disregard information about the shape of the structures we investigate. On the other hand we gain statistical significance due to the higher number of pixels than bright points. Since we disregard information about the shape of the objects this is an investigation of atmospheric properties at the location of the selected pixels.

The first set of plots (Fig. 3.15) shows the white-light intensity vs the residual intensity of the G-band, the white-light intensity against the residual intensity of the 5576 Å line and the residual intensity of the 5576 Å line against the residual intensity of the G-band for pixels selected as 'bright point'. The second set of plots show the same physical properties as the first set except the investigated spectral line is the Fe I 5691 Å line (Fig. 3.16). The third set of plot repeats the analysis for the Ti II 5381 Å line (Fig. 3.17).
All lines show similar behavior. They show the same correlations as in the analysis of individual bright points leading to the same conclusions as in the previous section. Since we disregarded spatial informations about the bright points we conclude that the results of the last part of the previous Chapter are due to the atmospheric conditions and not due to the properties of the individual bright point. This includes especially the increase of the residual intensity of the G-band vs. the residual intensity of the atomic spectral lines.

The last set of scatter-plots shows the residual intensity of the G-band against the residual intensities of the atomic spectral lines for various solar structures. In general, we find a positive correlation between these residual intensities. The correlation is the strongest for the 5576 Å line, and weakest for the 5691 Å line, which is quite similar to the 5381 Å line. Also, we note the peculiar appearance of the the scatter-plots for pixels identifies as pores. They appear to consist of several different samples, which is actually the right explanation. We investigate several pores which have a quite different appearance in the residual intensity since some are bright and some are dark in different spectral lines. A detailed analysis of this behavior is given in Chapter 3.1.4.4. This correlation shows the connection between the atomic lines and the G-band where the strength of the correlation indicates how similar the lines behave. Since the behavior of a line depends on the atmospheric conditions and the atmospheric properties depend on height, we conclude that the correlation between the residual intensity of the atomic line and the G-band indicates the amount of contribution to the G-band intensity originating from the same height as the specific atomic line. The correlation is the strongest for the 5576 Å which forms in a height of 320 km above the photosphere, but we also find a correlation for the Fe I 5691 Å and the Ti II 5381 Å lines which form in a height of 160 km. We conclude that a part of the light from the G-band CH lines originates from layers higher the photospheric level, which is in disagreement to Sanchez-Almeida [50]. There is

not only a contribution from a height of 160 km, but also a significant contribution from layers around 320 km height, which is in disagreement to Steiner [63] since he proposes a single formation height around 160 km.

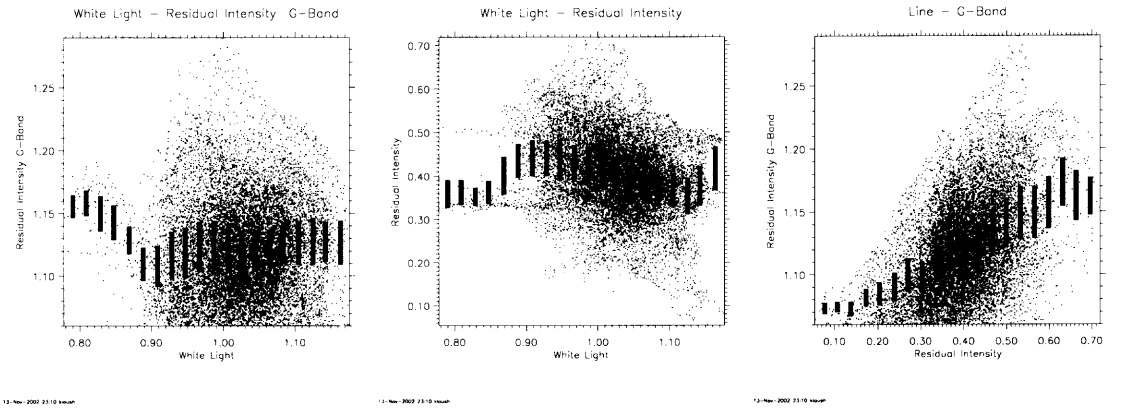

Figure 3.15 White-light intensity vs the residual intensity of the G-band (left), white-light intensity vs the residual intensity of the Fe I 5576 Å line (middle) and the residual intensity of the Fe I 5576 Å line vs the residual intensity of the G-band for bright points only (right). There is no correlation between the white-light and the residual intensity of the Fe I 5576 Å line and no correlation between the white-light intensity and the residual intensity of the G-band. There is, however, a positive correlation between the residual intensity of the Fe I 5576 Å line and the residual intensity of the G-band.

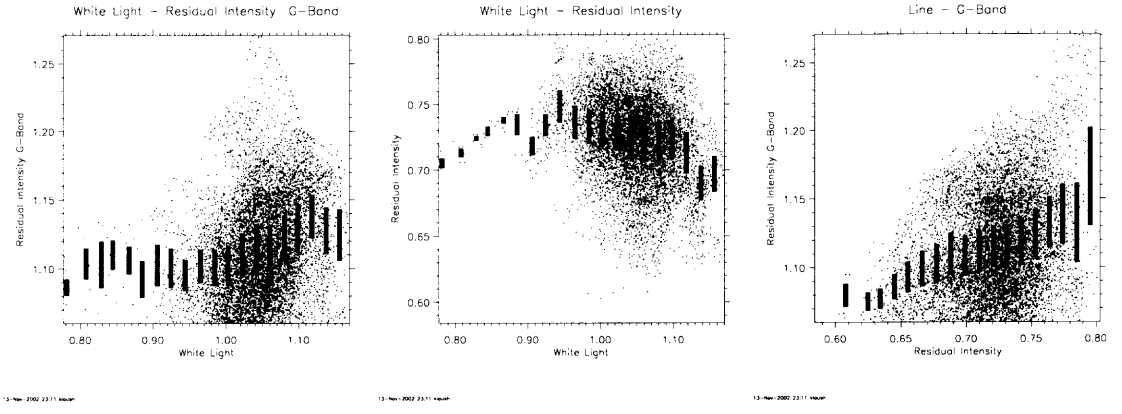

Figure 3.16 White-light intensity the residual intensity of the G-band (left), white-light intensity vs the residual intensity of the 5691 Å line (middle) and the residual intensity of the 5691 Å line vs the residual intensity of the G-band (right). Each data-point represents a pixel selected as bright point and not an individual bright point as in the previous section. There is no correlation between the white-light and the residual intensity of the 5691 Å line and no correlation between the white-light intensity and the residual intensity of the 5691 Å line. We find a positive correlation between the residual intensity of the 5691 Å line and the residual intensity of the G-band.

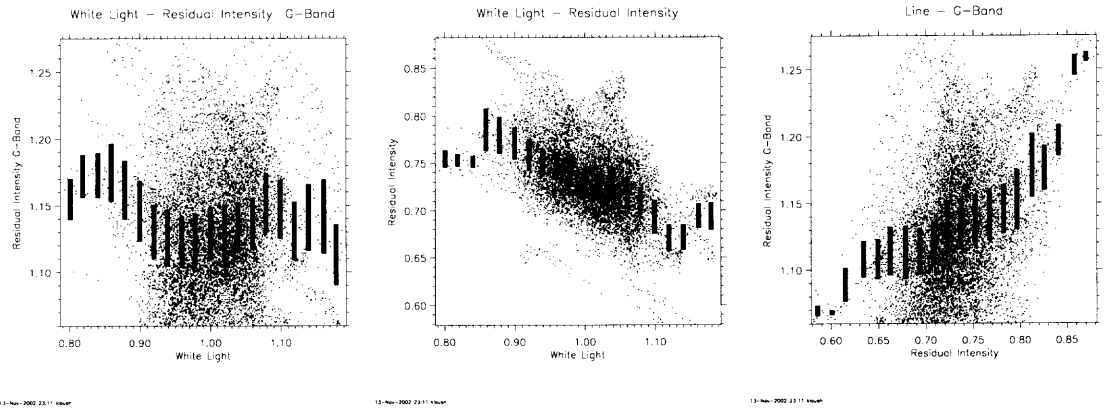

Figure 3.17 White-light intensity vs the residual intensity of the G-band (left), white-light intensity vs the residual intensity of the 5381 Å line (middle) and the residual intensity of the 5381 Å line vs the residual intensity of the G-band for bright points only (right). There is a slight negative correlation between the white-light and the residual intensity of the 5381 Å line and a slight positive correlation between the residual intensities themselves.

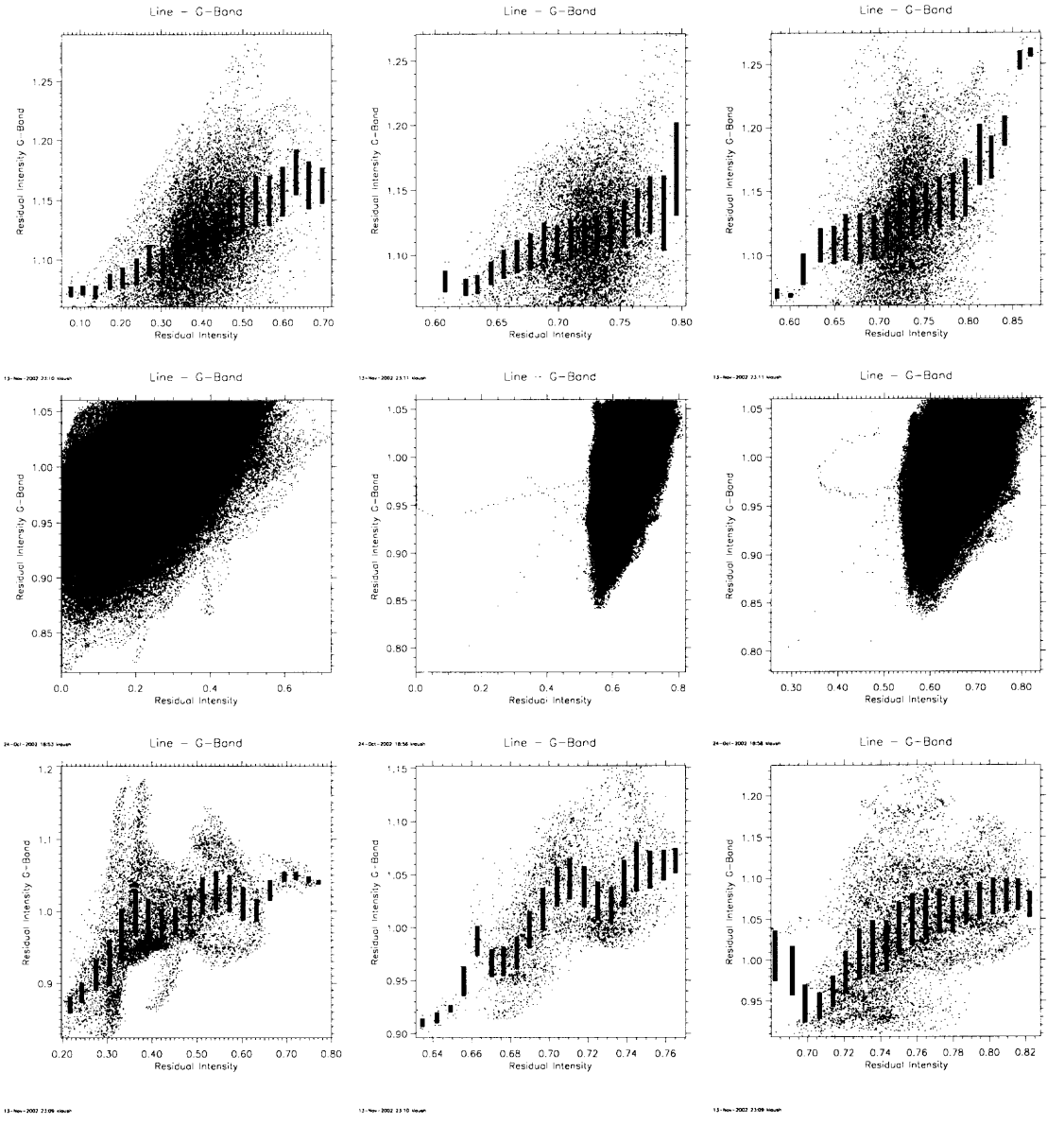

Figure 3.18 Residual intensity of the G-band vs the residual intensity of the Fe I 5576 Å line (left column), the Fe I 5691 Å line (middle column) and the Ti II 5381 Å line (right column). From top to bottom the selected structures are the bright points, the quiet sun (granulation and intergranular lanes) and the pores. The non-uniform appearance of the pores is a result of the fact that different pores can behave quite different.

3.1.4.4 Analysis of Images In all preceeding sections we performed quantitative statistical studies. These studies measure values but always lose spatial information due to the necessary simplification of the dataset. In this section we study images themselves. We do not perform any quantitative measurements but draw conclusions from the qualitative appearance of the structures. We check for shape changes of bright points by looking at the residual intensity images and compare the appearance of the different solar structures in general.

Total field of view
The first set of pictures shows the total field of view (Fig. 3.19). There are several interesting properties visible immediately. Bright points are much more conspicuous in the G-band image than in the white-light image. In the residual intensity image one cannot only see bright points but whole bright regions. These bright regions include all bright points but cover more surface area than the bright points alone. We call the regions 'G-band bright regions' and study them as a separate object (Ch. 3.1.4.1). The G-band bright regions are not an effect of the enlarged point spread function due to bad seeing since an analysis of subfields of this image shows bright points with a very high contrast at the border of the G-band bright regions (Fig 3.20, Fig 3.21, Fig 3.22, Fig 3.24). If the G-band bright regions were an effect of seeing, the smearing of high contrast bright points would be symmetrical, since we use a long exposure-time where the PSF is symmetrical due to the averaging effect of the earth's atmosphere.
Intergranular lanes show as brightenings in the residual intensity image of the line Fe I 5576 Å and the other atomic spectral lines as well but not as conspicuous in the residual intensity image of the G-band. This may be an indication of the different, more sensitive behavior to atmospheric properties of the G-band. It also means that the inversion of solar granulation associated with higher forming spectral lines is only shared in part by the G-band. This observation has the following implications: the fact that the inversion is partly visible in the G-band is an indication that at least a part of the G-band intensity must originate in higher layers of the solar atmosphere. The part of the light that seems to originate at photospheric level since it does not show the inversion may due to the fact that about 62 percent of the light passing through a G-band filter comes from the continuum. We did not perform an inversion for the G-band as for the other lines since there are other solar lines with unknown behavior in the G-band spectral region, and since we did not have a suitable continuum near the G-band.

Individual bright points
Bright points are always more conspicuous in the residual intensity image of the G-band than in the other residual intensity images. Examples of this behavior can be seen in Figure 3.21, Figure 3.24, Figure 3.25 and Figure 3.27. Bright points always have a high contrast in the residual intensity image for the G-band, but only

some of the bright points have an enhanced contrast for the the residual intensity images of the atomic lines investigated (Fig. 3.22, Fig. 3.23). We conclude that the atmospheres of bright points can be different even if they have the same contrast in the G-band. This poses a severe problem for all semi-empiric models since these model only use one type of bright point atmosphere. The different behavior of bright points in terms of residual intensity of the atomic spectral lines may also indicate the existence of different types of bright points. We did not find an indication of different bright point types in the previous chapters, however. There is no correlation between this behavior and the magnetic field since Berger [6] finds *all* bright points to be associated with magnetic fields.
The line Ti II 5381 Å does not behave any different that the other two lines investigated (Fig. 3.26, Fig. 3.27). We find an enhanced contrast for the Ti II 5381 Å line as well (Fig. 3.26) which is not in agreement with the prediction of Steiner [63] that bright points do not show an enhanced intensity in the Ti II lines.
We do not find a change in shape or size nor a displacement of bright points with height of more than 120 km over a height of 320 km which translates into an inclination of bright points of not more than 20°. This indicates that bright points are a relatively stable structure in the photosphere. This may be in disagreement to the expanding bright point model in the calculations of Steiner [63].

Pores
The next set of images shows some pores in the field of view. Figure 3.28 gives a general appearance of a pore in a residual intensity image. It is interesting that the pore is bright in the residual intensity image of the 5576 Å line, but dark in the residual intensity image of the G-band. There is a bright ring around the pore in the residual intensity image of the G-band, which indicates a different atmosphere in the immediate surroundings of a solar pore.
The investigation of several pores reveals an interesting pattern. The larger the pore the more lines of the residual intensity images turn dark. This can be seen in Figure 3.29, where only the G-band residual intensity image of the pore is dark. In Figure 3.30, the residual intensity image of the 5691 Å line begins to darken and finally in Figure 3.29, all residual intensity images are more or less dark, the brightest being the residual intensity image of the 5381 Å line. If we interpret a larger pore as having a lower temperature, we can conclude the following behavior of the lines: The G-band is the most temperature sensitive line since it is dark for all pores. It is followed by the 5691 Å line and then by the 5576 Å line. The least sensitive line is the 5381 Å line. It is also important to note that the bright ring around the pore is present in all solar lines. The ring may be an effect of radiation entering the the wall of the pore from the hotter plasma outside.
These measurements can be used to determine the sensitivity of different spectral lines to atmospheric conditions like pressure, pressure gradient, temperature and temperature gradient. Since we only measure two wavelength point we cannot

perform an inversion. Forward modeling is the only way to use this data to check the consistency of the atmospheric models. Once the properties of the spectral lines are known, they could be used to determine the atmospheric properties of bright points.

Granulation

The last set of images shows solar granulation. We find the solar granulation is inverted for residual intensity images except the G-band, which is only inverted in part. The not-inverted part can be explained by the fact that about 62 percent of the light originates from the continuum level. Taking that into account, we find a quite strong inversion as well, which means that a substantial part of the light of the G-band must originate from higher levels than the photosphere. This is not in agreement with the prediction of the formation height of the G-band by Sanchez-Almeida [50] of 40 km *below* the photosphere.

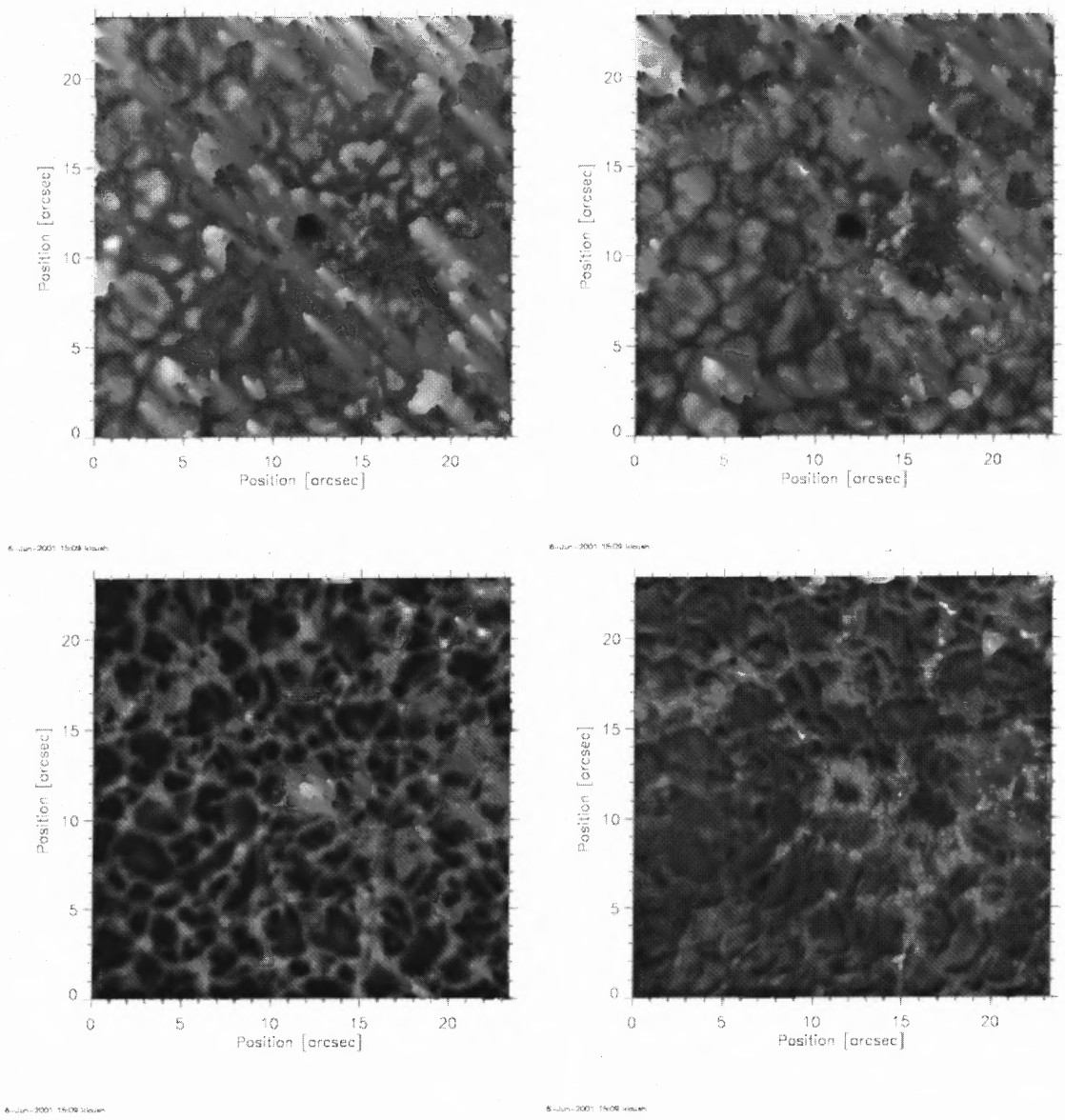

Figure 3.19 These images show the total field of view. Top left is the white-light image, top right is the G-band image. Bottom left is the residual intensity for the 5576 Å line, bottom right the residual intensity for the G-band. This order will be maintained throughout the residual intensity section.

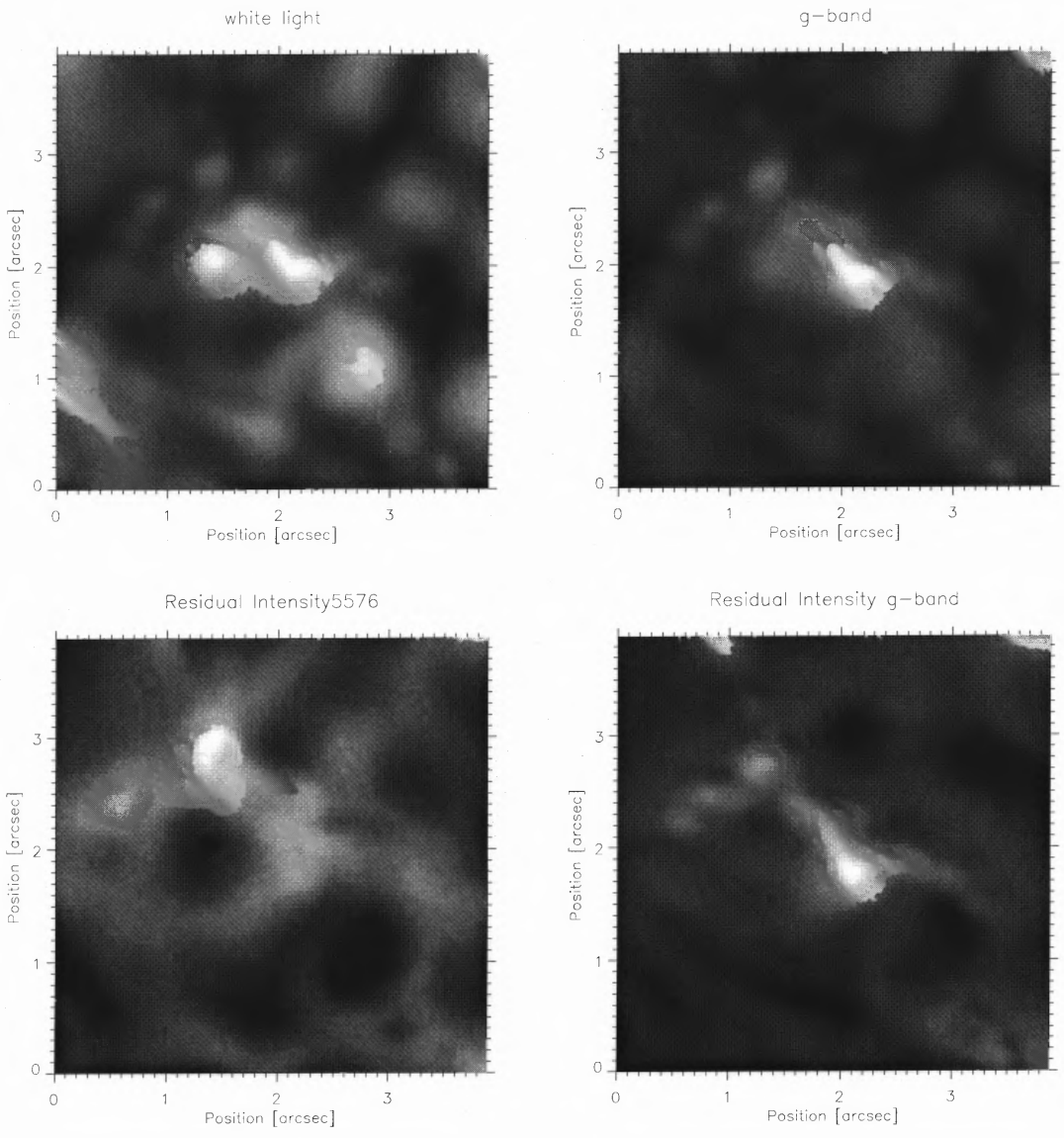

Figure 3.20 These four images show from top left and counterclockwise the whitelight image, the G-band image, the G-band residual intensity image and the residual intensity image in the Fe I 5576 Å line. The bright points are still visible in the residual intensity image of the 5576 Å line, but due to the enhanced brightness of the intergranular lanes, they are not a conspicuous as in the G-band residual intensity image. The resolution is about 0.15 arcsec, the exposure time is 1500 ms and the image scale is 0.039 arcsec/pixel.

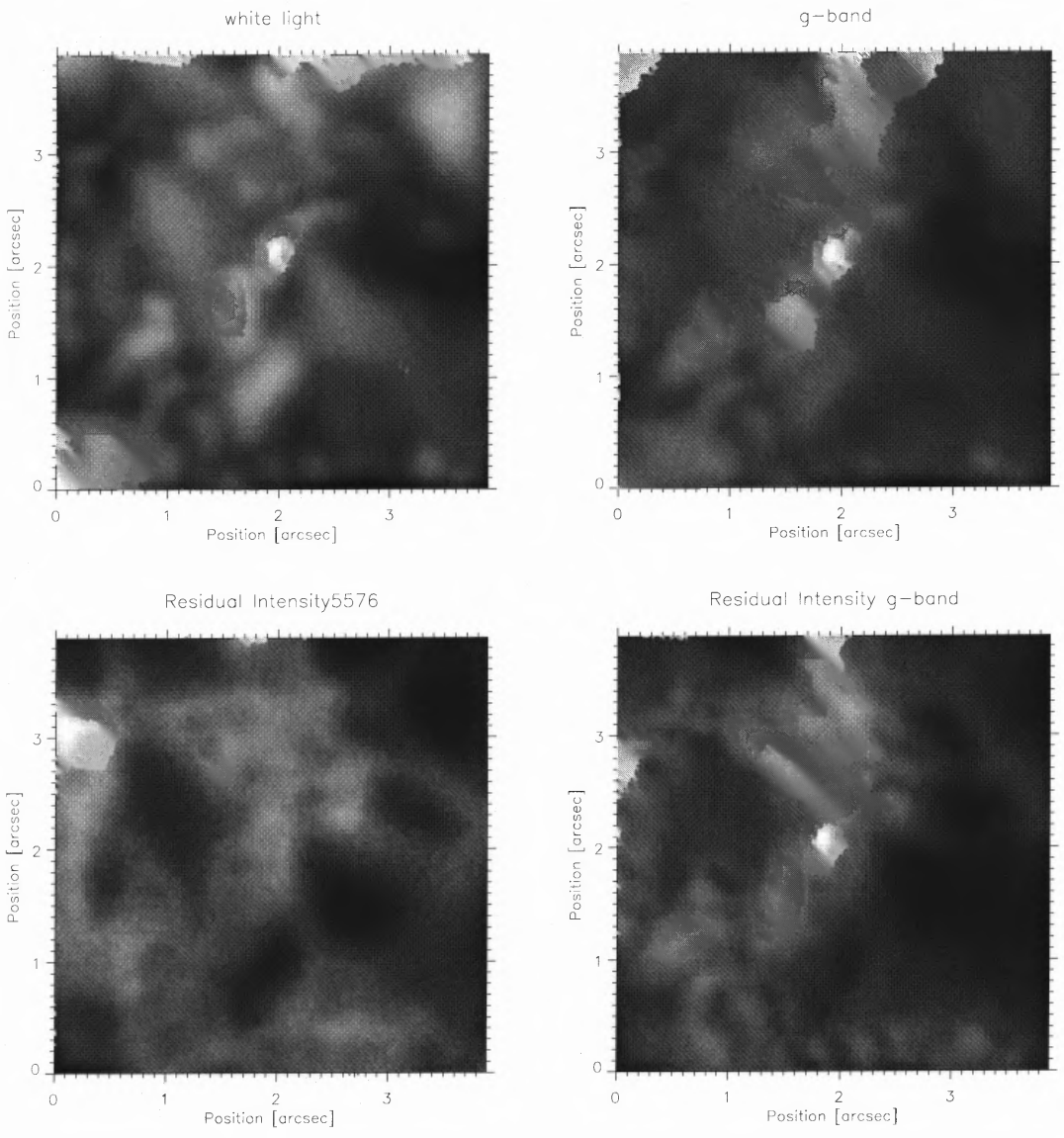

Figure 3.21 These four images show from top left and counterclockwise the whitelight image, the G-band image, the G-band residual intensity image and the residual intensity image in the Fe I 5576 Å line. These images show an example of a few bright points clustered together. It is easier to distinguish the individual bright points in the G-band residual intensity image than in all other images. On the other hand, even the most conspicuous bright point located at (2,2) is not conspicuous anymore in the 5576 Å residual intensity.

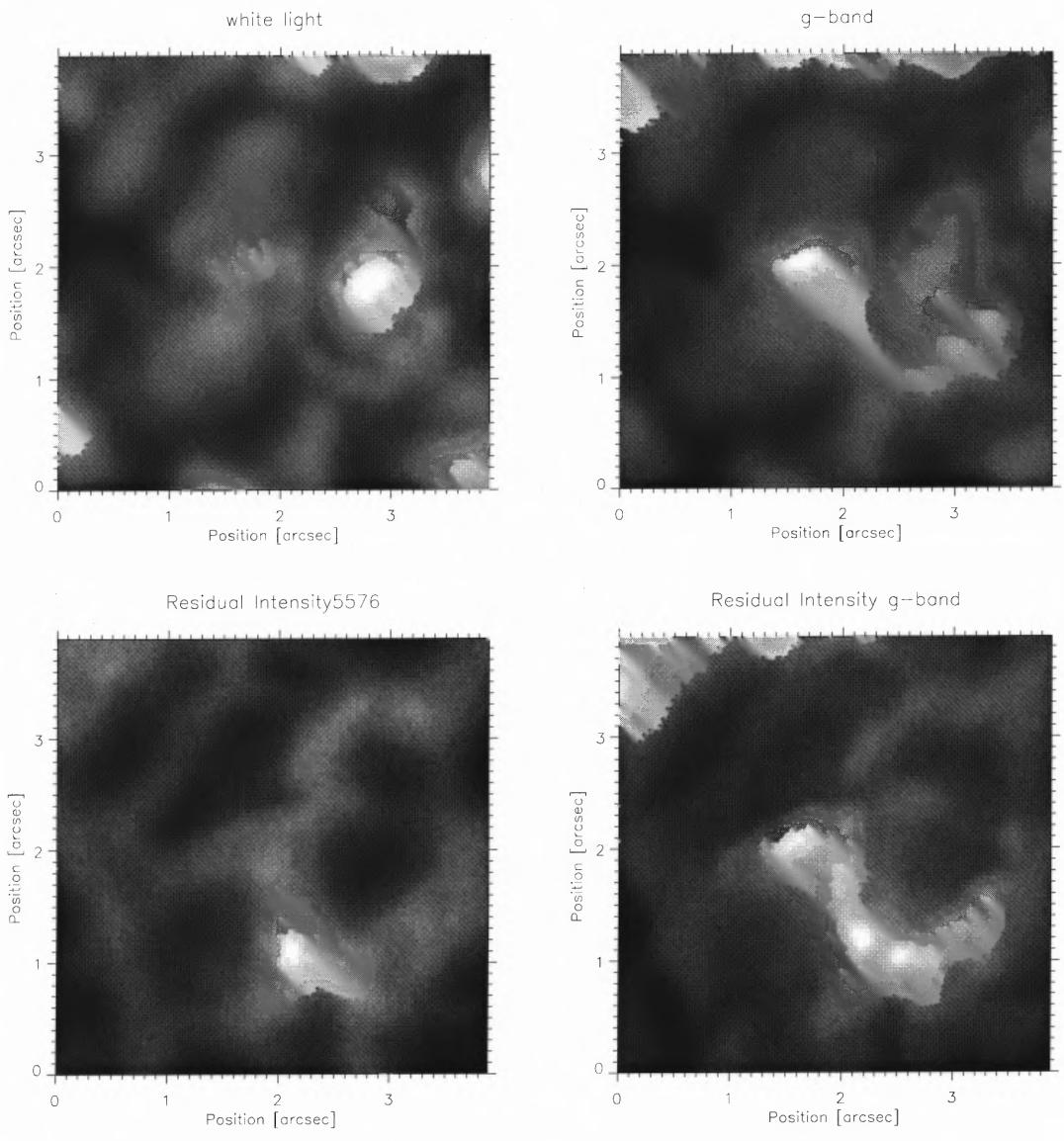

Figure 3.22 These four images show from top left and counterclockwise the whitelight image, the G-band image, the G-band residual intensity image and the residual intensity image in the 5576 Å line. Some bright points are bright in both residual intensity images at the location (2,1), but others only have enhanced contrast in the G-band residual intensity image (2,2)

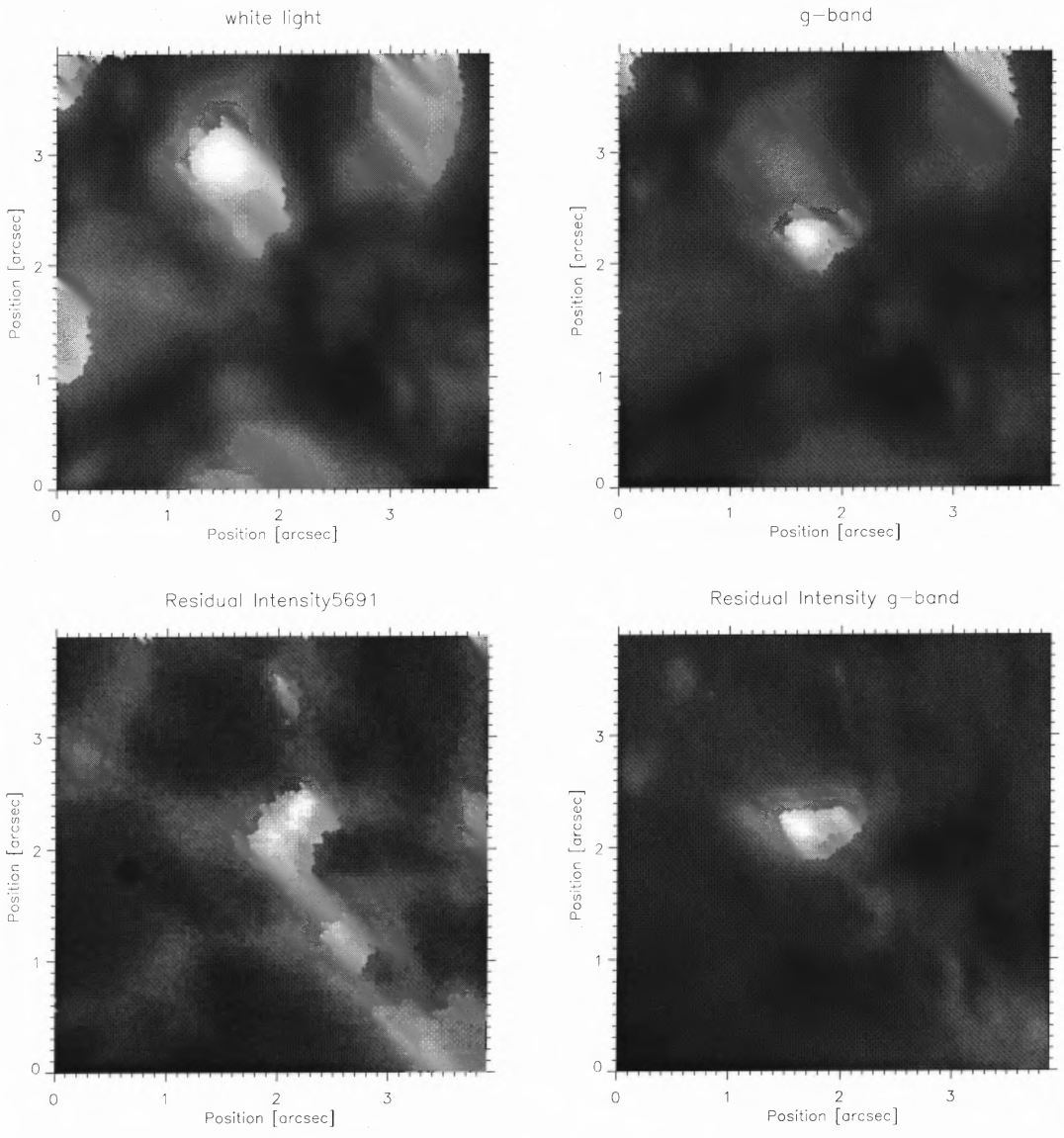

Figure 3.23 These four images show from top left and counterclockwise the whitelight image, the G-band image, the G-band residual intensity image and the residual intensity image in the Fe I 5691 Å line. The bright points have enhanced contrast in both residual intensity images. There is, however, a quite different appearance at the location (2.5,2.5) in residual intensity image in the Fe I 5691 Å line.

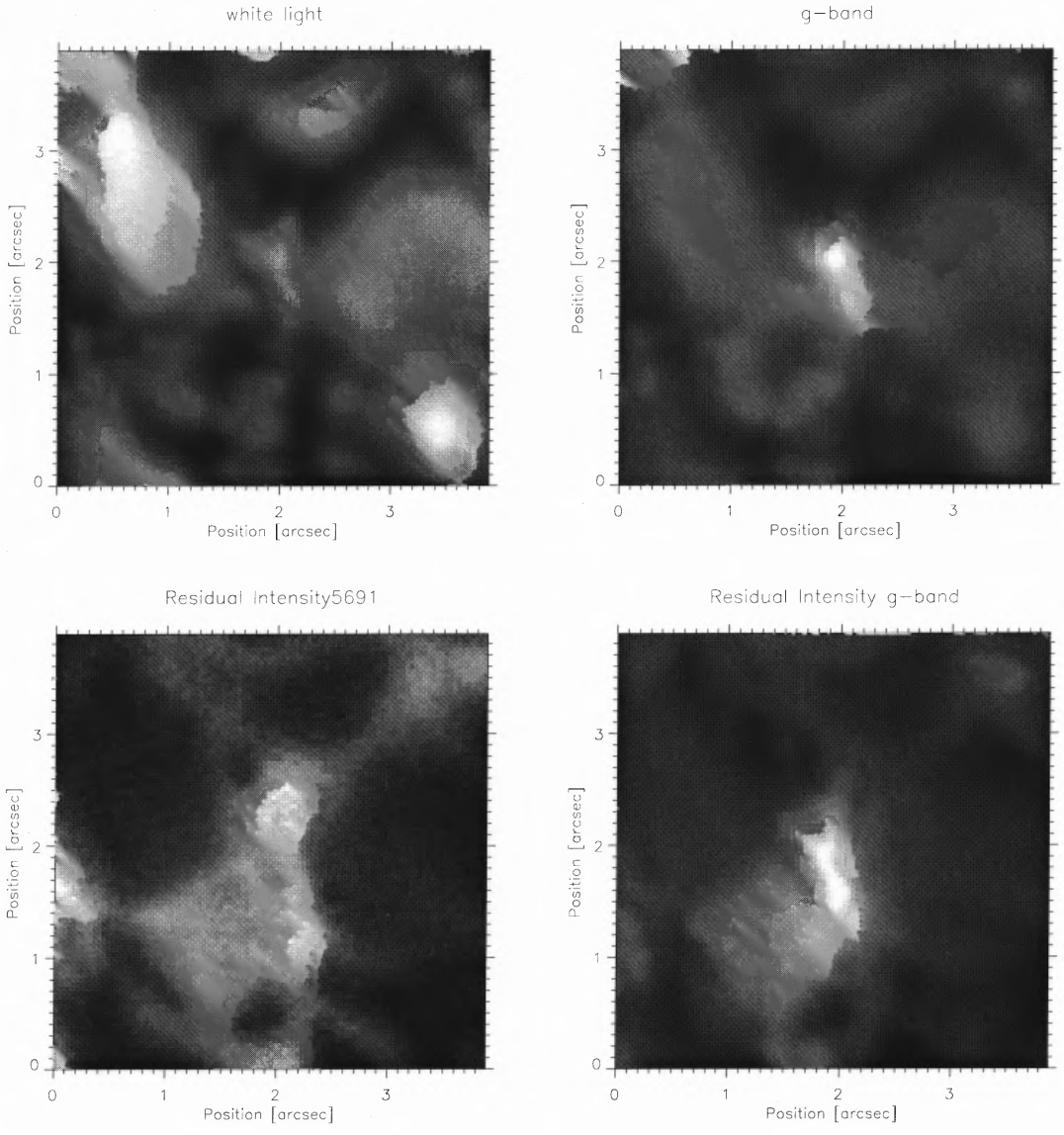

Figure 3.24 These four images show from top left and counterclockwise the whitelight image, the G-band image, the G-band residual intensity image and the residual intensity image in the 5691 Å line. This is another example of bright point contrast enhancement.

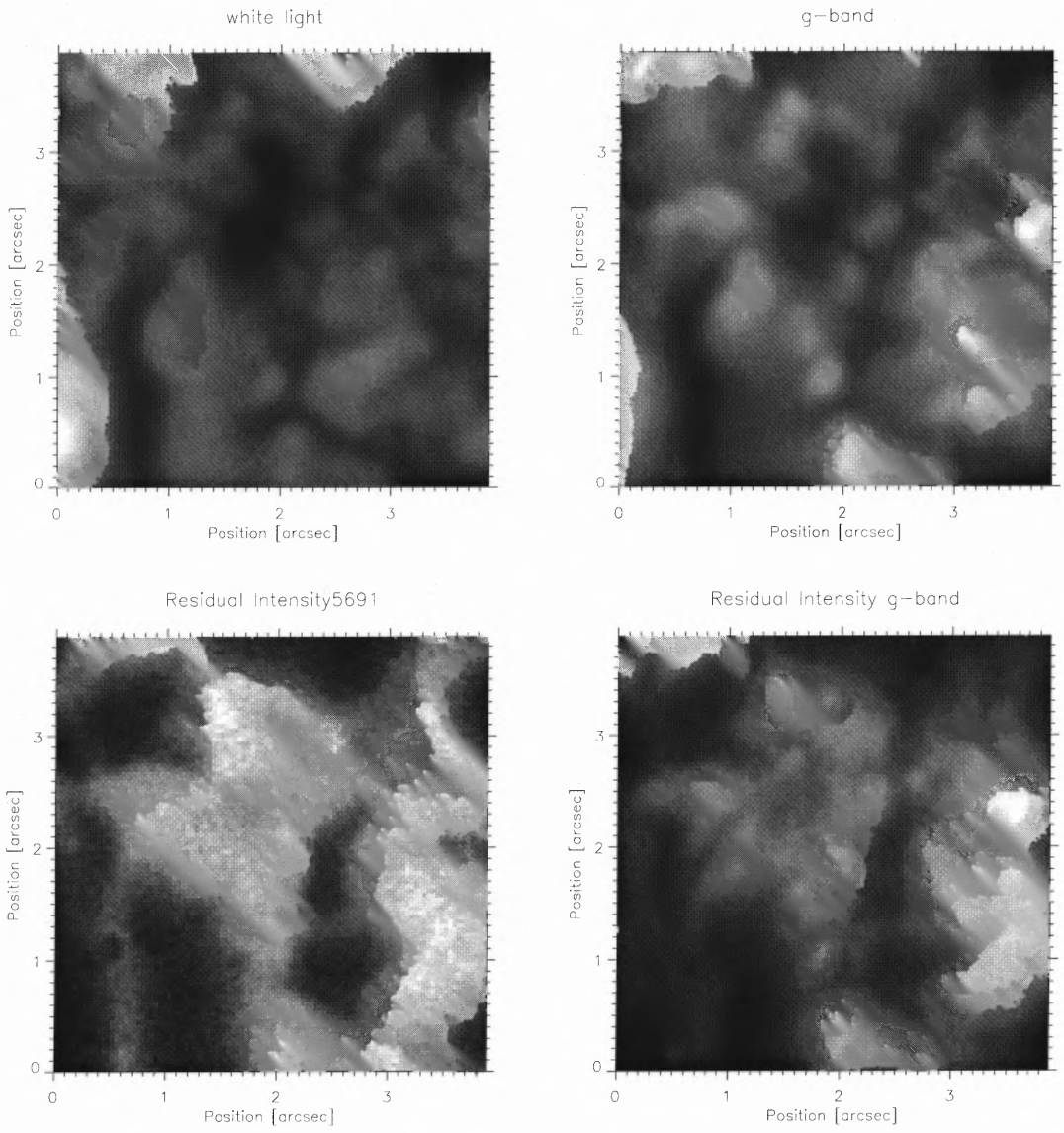

Figure 3.25 These four images show from top left and counterclockwise the whitelight image, the G-band image, the G-band residual intensity image and the residual intensity image in the 5691 Å line. In this images we can see a few bright points very close together. They can be distinguished clearly in the G-band residual intensity image, but form just a bright region in the residual intensity image in the 5691 Å line. It is also noteworthy that this bright area in the residual intensity image in the 5691 Å line is enclosed by a brighter rim.

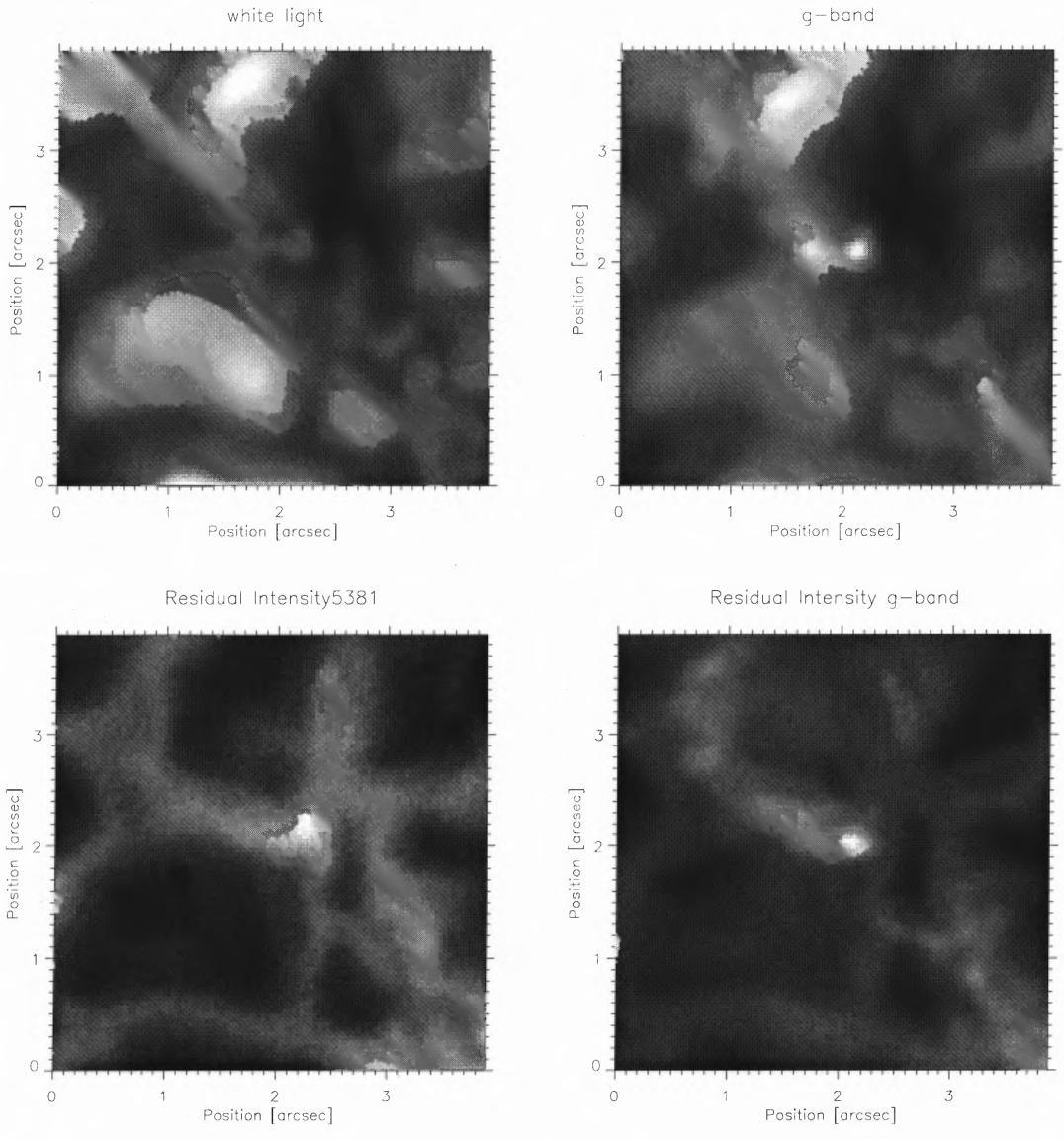

Figure 3.26 These four images show from top left and counterclockwise the whitelight image, the G-band image, the G-band residual intensity image and the residual intensity image in the 5381 Å line. These images shows that (some) bright points have an enhanced contrast in the Ti II 5381 Å line as well, which is not in agreement the prediction of Steiner [63].

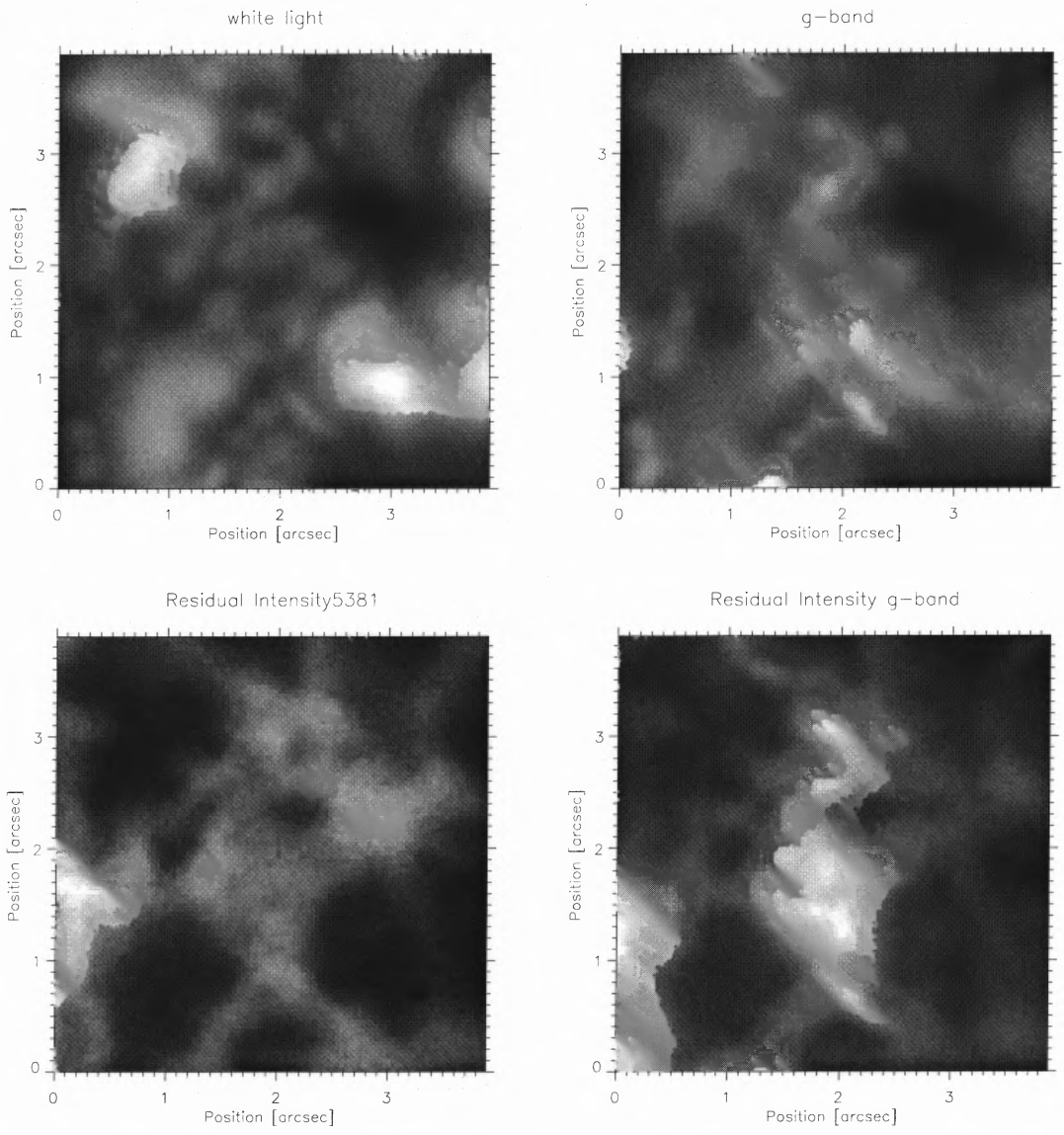

Figure 3.27 These four images show from top left and counterclockwise the whitelight image, the G-band image, the G-band residual intensity image and the residual intensity image in the 5381 Å line. We can see that bright points are better resolved in the G-band residual intensity image than in the residual intensity image of the 5381 Å line. This is common to all lines.

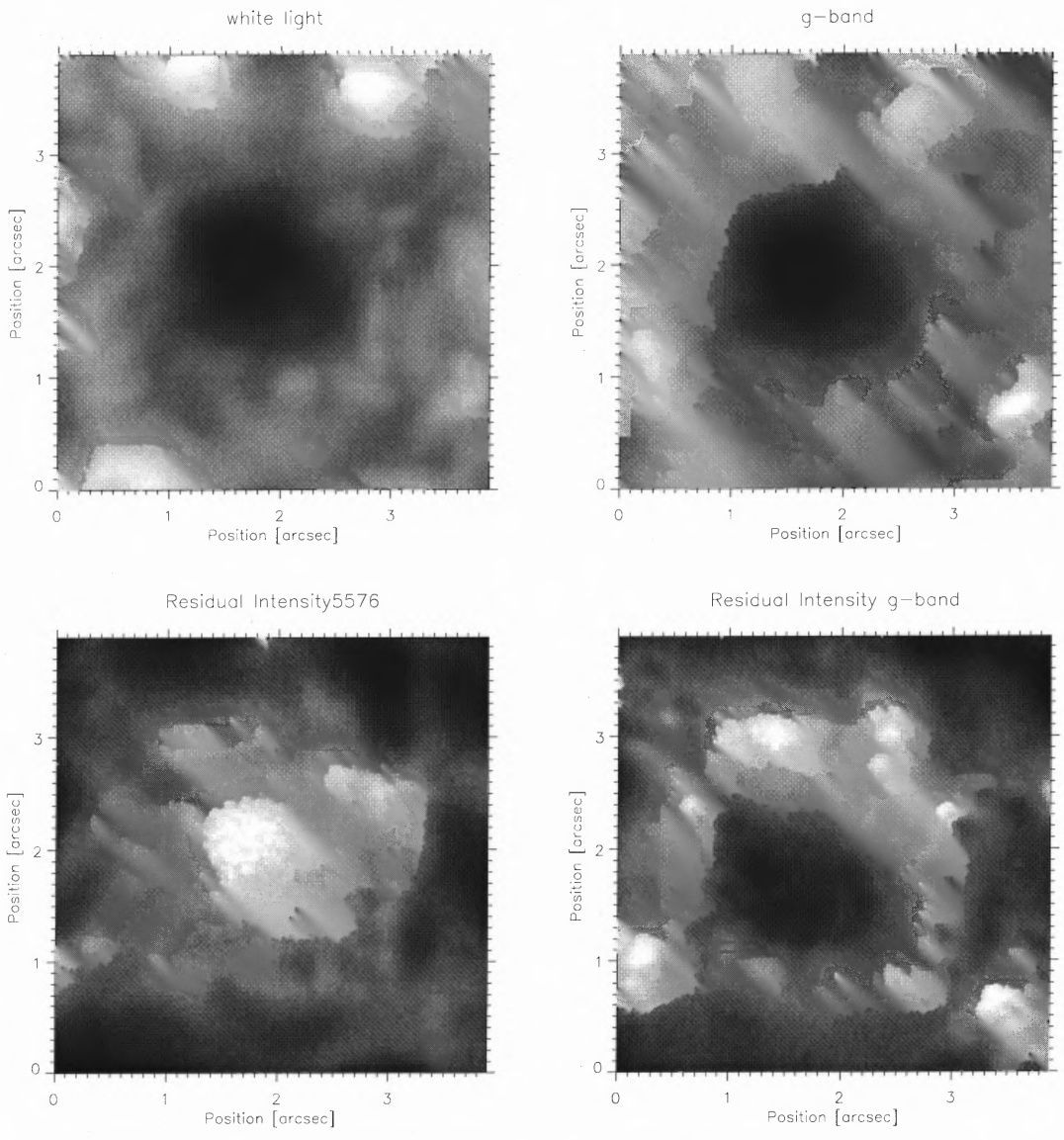

Figure 3.28 These four images show from top left and counterclockwise the whitelight image, the G-band image, the G-band residual intensity image and the residual intensity image in the 5576 Å line. We can see that the pore is dark in the G-band residual intensity image, but bright in the residual intensity image in the 5576 Å line. This may be an indication for the higher temperature sensitivity of the G-band.

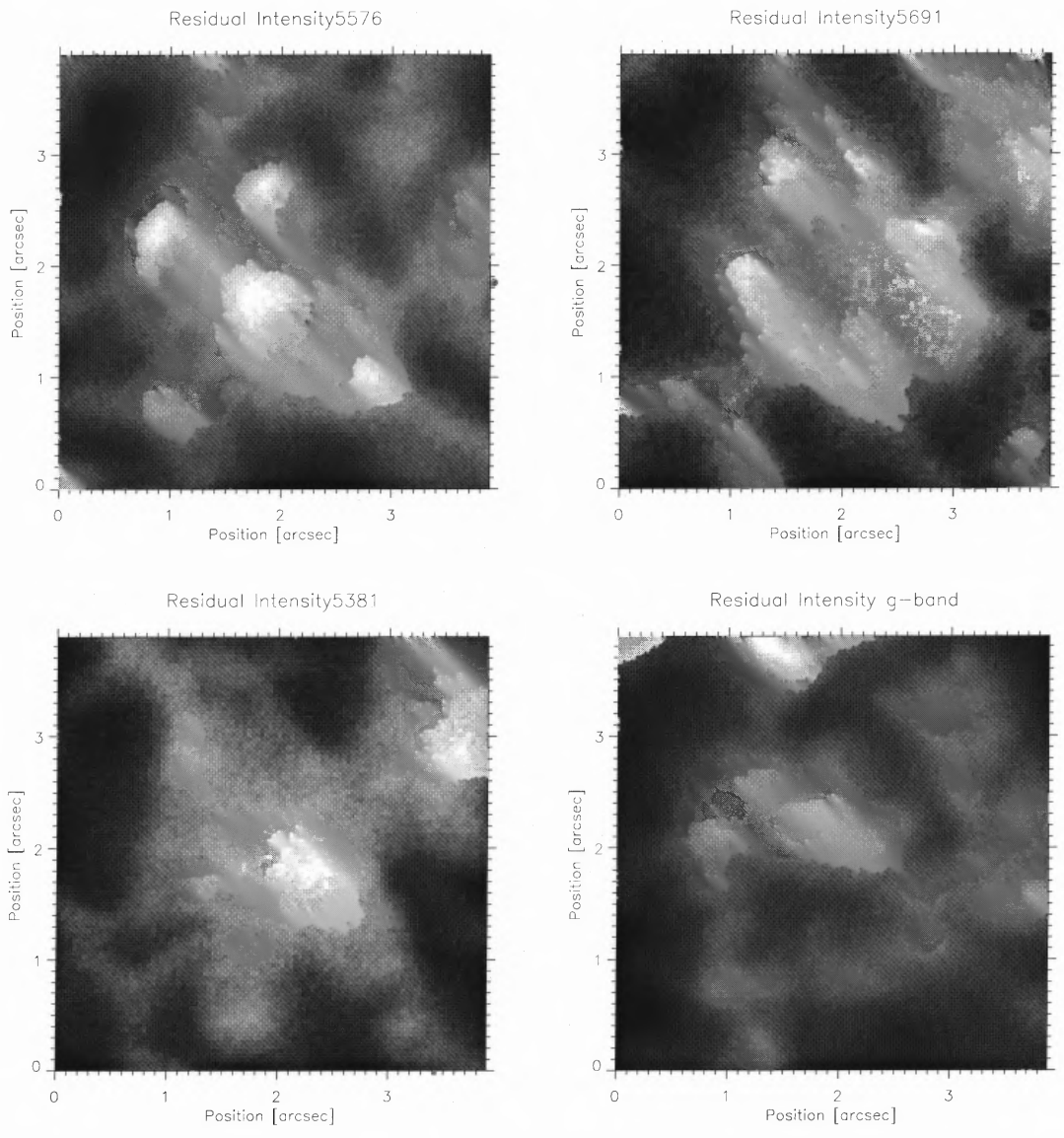

Figure 3.29 A solar pore in all four residual intensities. Top left is the 5576 Å residual intensity, top right is the 5691 Å residual intensity, bottom left is the 5381 Å residual intensity and bottom right is the G-band residual intensity. We can see that the pore is bright in all residual intensity images except for the G-band, where some parts of the pore are dark.

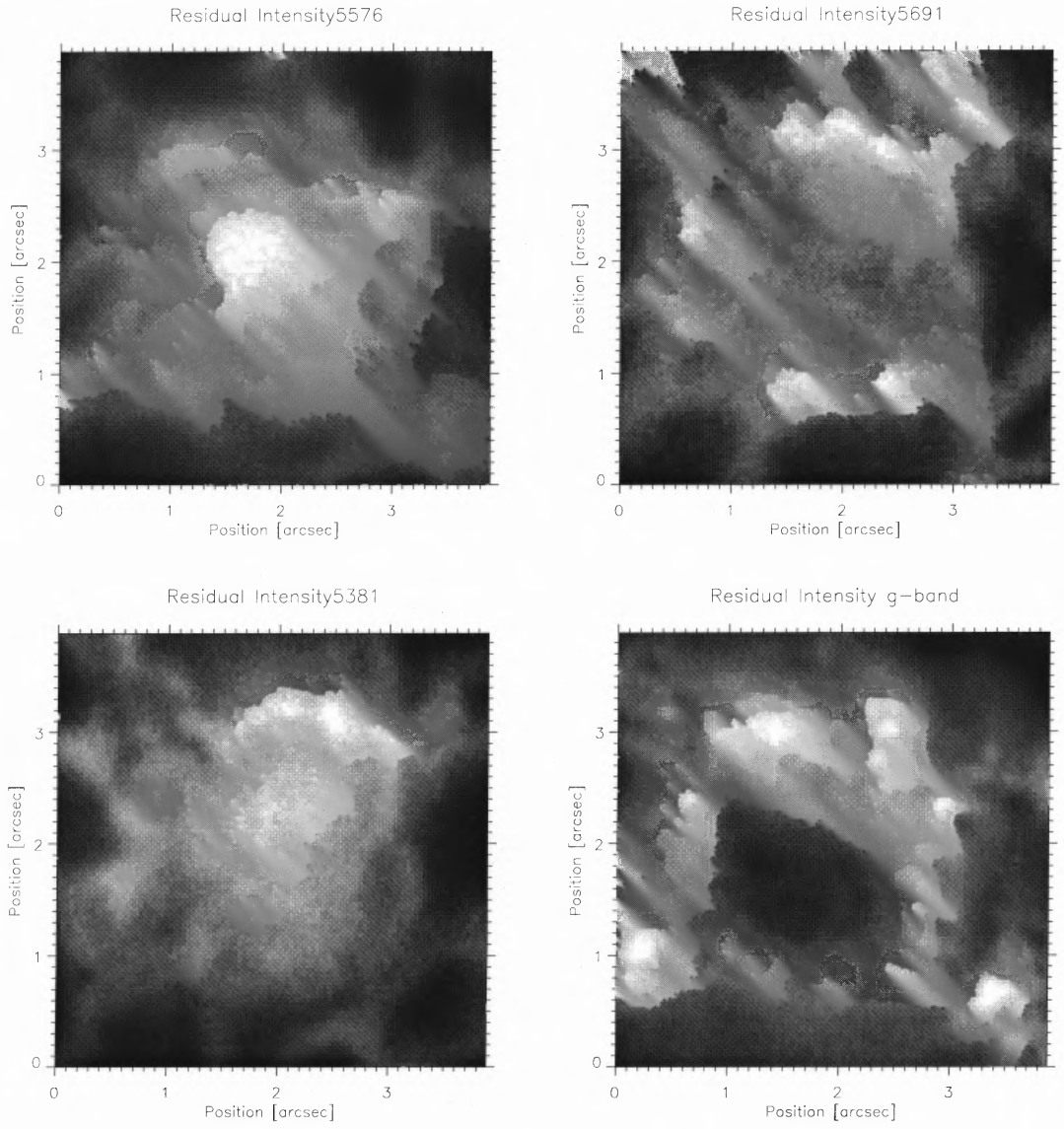

Figure 3.30 The pore of Figure 3.28, but this time in all four residual intensities. Top left is the 5576 Å residual intensity, top right is the 5691 Å residual intensity, bottom left is the 5381 Å residual intensity and bottom right is the G-band residual intensity. The pore is completely dark in the G-band residual intensity image except for a bright ring. Also, the residual intensity image of the 5691 Å line begins to darken. This may be an indication for the temperature sensitivity explained in the text.

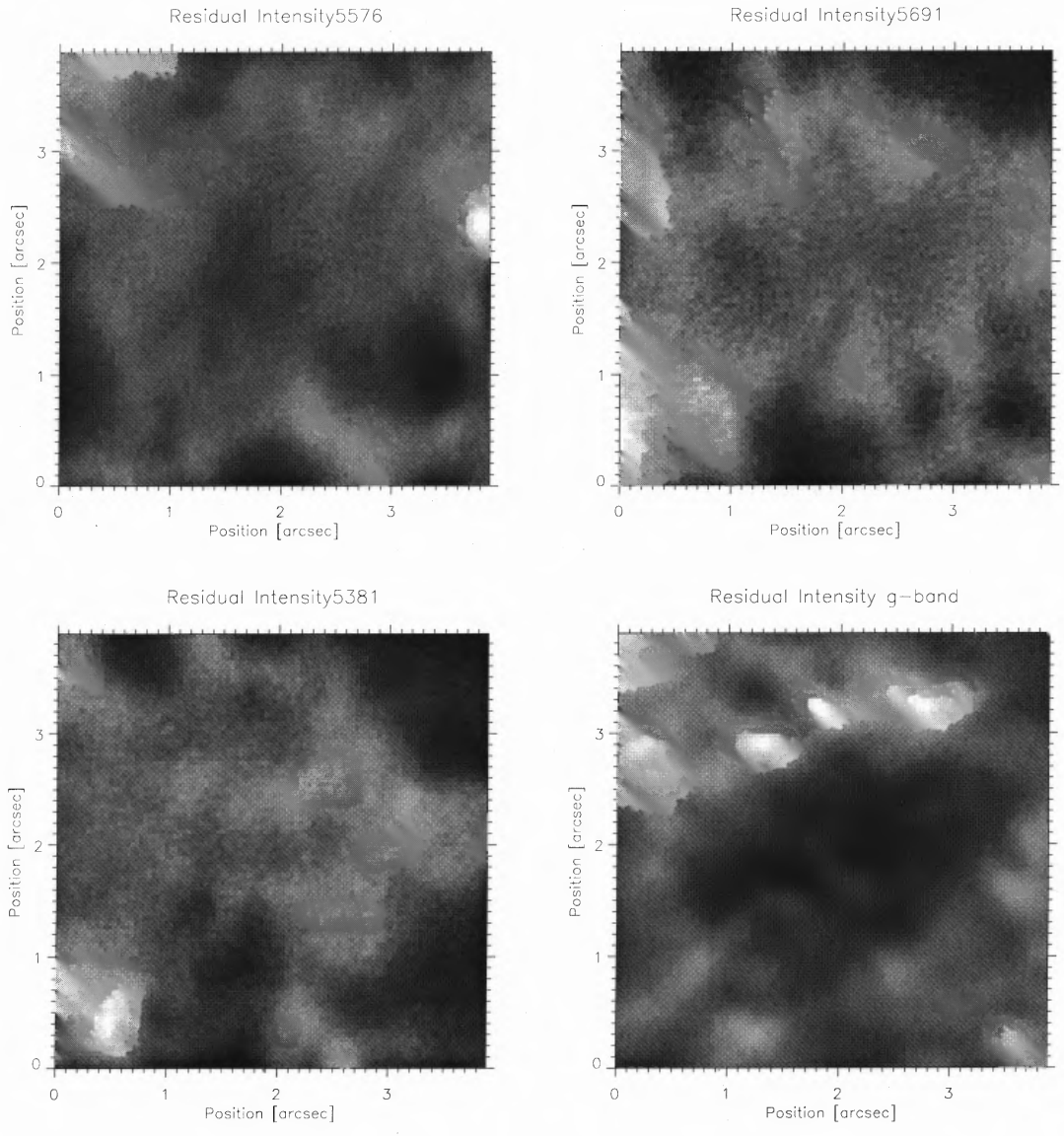

Figure 3.31 A third pore in all four residual intensities. Top left is the 5576 Å residual intensity, top right is the 5691 Å residual intensity, bottom left is the 5381 Å residual intensity and bottom right is the G-band residual intensity. This time, all residual intensity images of the pore are dark, the brightest being the residual intensity image of the 5381 line.

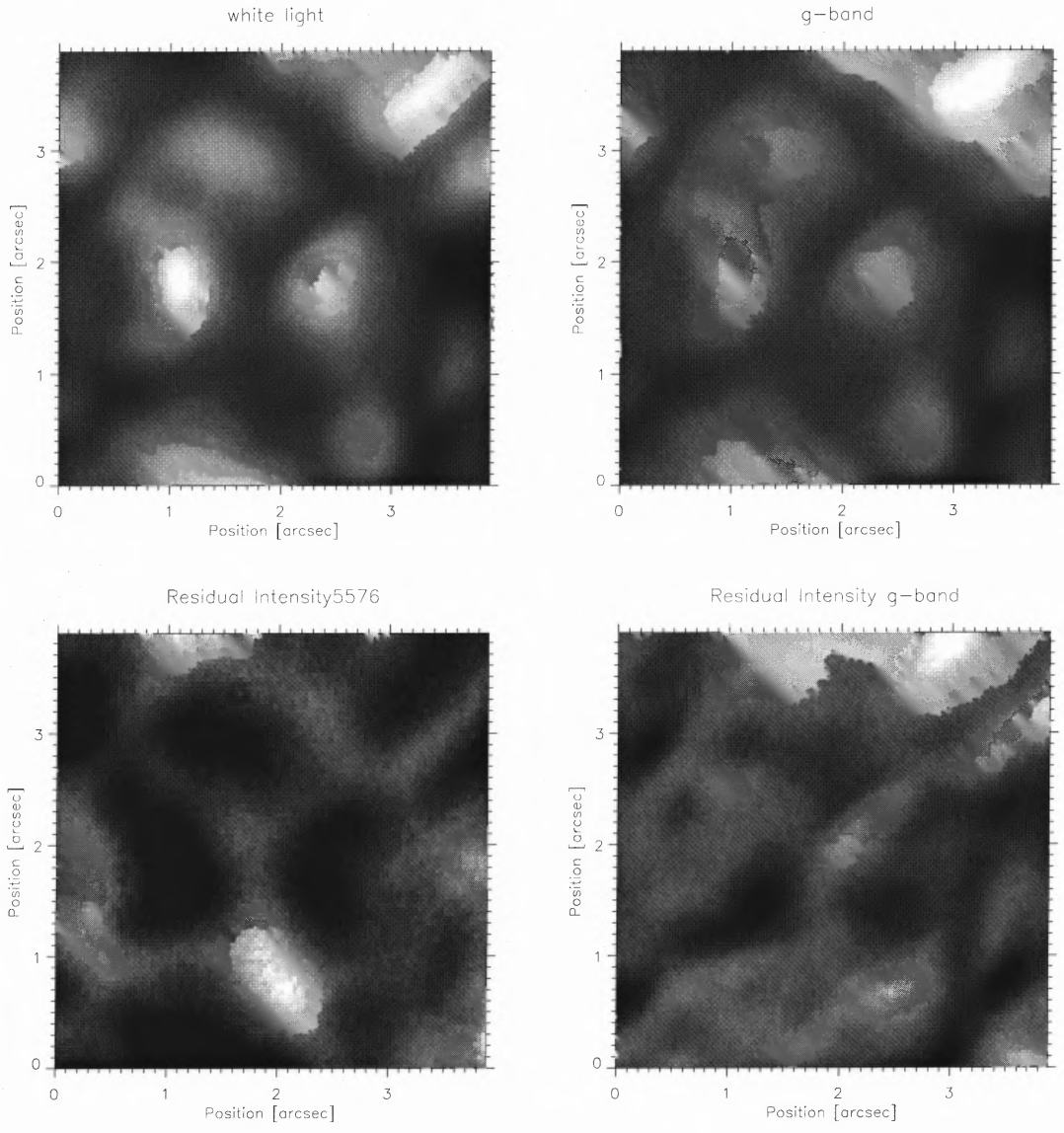

Figure 3.32 These four images show from top left and counterclockwise the whitelight image, the G-band image, the G-band residual intensity image and the residual intensity image in the 5576 Å line.

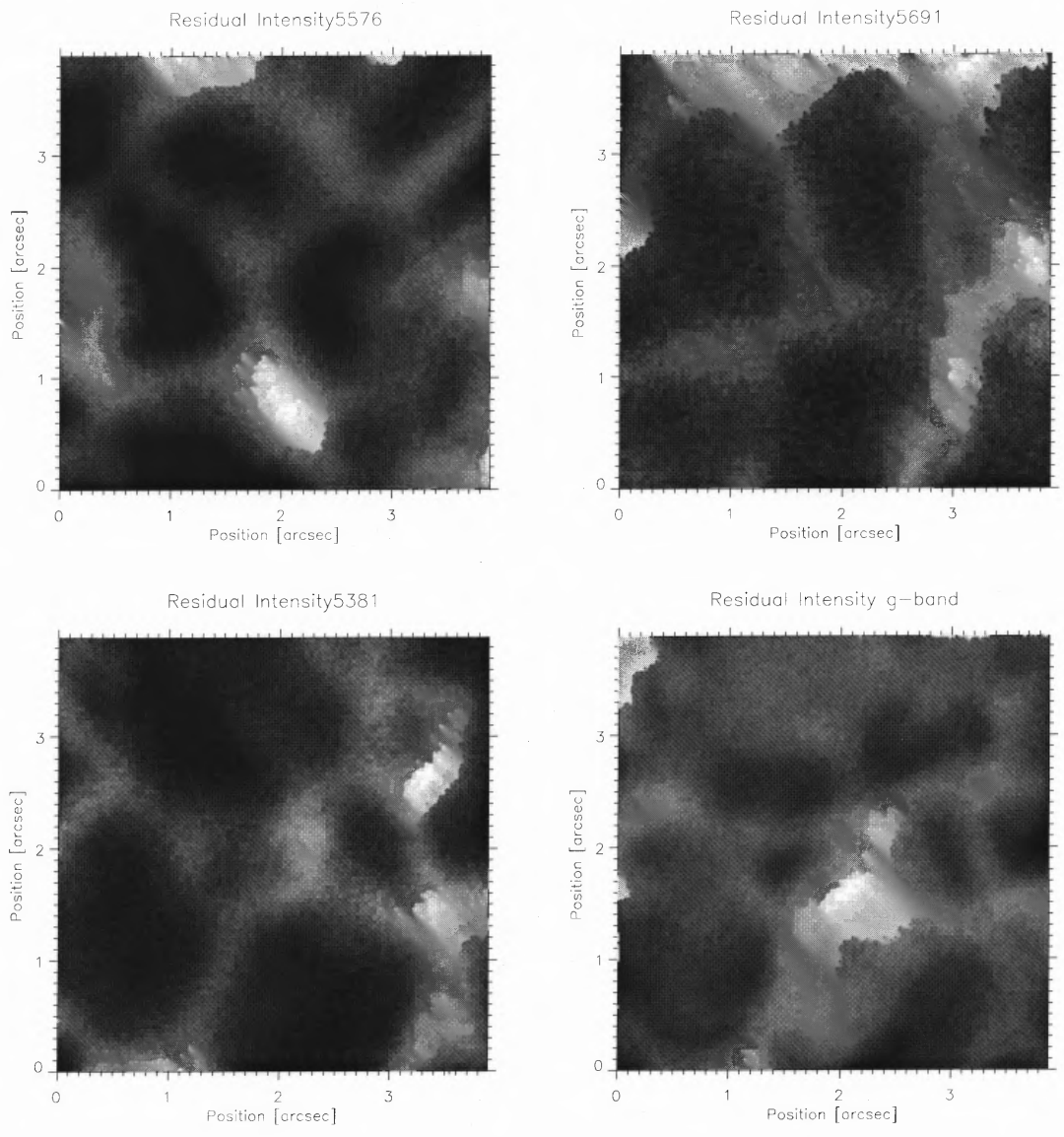

Figure 3.33 The granulation and the intergranular lanes for all residual intensities. Top left is the residual intensity of the Fe I 5576 Å line, top right is the residual intensity of the Fe I 5691 Å line, bottom left is the residual intensity of the Ti II 5381 Å line and bottom right is the residual intensity of the G-band. The three atomic spectral lines show the inversion of solar granulation common for spectral lines forming higher in the solar atmosphere. The G-band shows this inversion as well, but to a lesser extent. The fact that this inversion can be seen even though about 62 percent of the light passing the G-band filter originates from the continuum indicates that the G-band is forming high. This is not in agreement with the predictions of Sanchez-Almeida [50].

3.1.5 Summary

- Bright Points

  In Chapter 3.1.4.2 we found that the size distribution of bright points does not have a peak which indicates that either bright points do not have a distinct size or that the size is below the resolution limit of the telescope. Since we also find typical values for the intensity and residual intensity distribution, we suspect that a 'typical, average' bright points exists. Therefore, we also expect to find a typical size for bright points. Combined with the size distribution, we conclude that the size of a bright point is probably smaller than the resolution limit of 120 km. In the same chapter we found that bright points change their shape with size and become more elongated as their size increases. Bright points are exclusively found in the intergranular lines and only in G-band bright regions.

  In Chapter 3.1.4.1 we found that the mean residual intensity of bright points is significantly different from all other investigated solar structures for all spectral lines. This indicates that the atmospheric conditions in bright points are different from all other investigated other solar structures except for pores. Pores have almost the same residual intensity as bright points for the atomics spectral lines, but have a much different residual intensity for the G-band. The reason is that pores can be bright or dark in residual intensity of the G-band.

  The atomic lines Fe I 5576 Å, Fe I 5691 Å and Ti II 5381 Å do not have a different residual intensity for the bright points and the G-band bright regions, while there is a significant difference for the G-band residual intensity between these structures. This indicates that the atmosphere in G-band bright regions is slightly different from the atmosphere in bright points and that the G-band is more sensitive to atmospheric condition than the atomic spectral lines.

  In Chapter 3.1.4.1 found that bright points have an enhanced contrast in all atomic lines including the Ti II 5381 Å line, contradicting the prediction of Steiner [63] who predicts no contrast enhancement for Ti II lines. The contrast enhancement mechanism proposed by Steiner attributes the contrast enhancement of the bright points to the temperature dependent dissociation of the CH molecules. He predicts a similar behavior for atoms since the atoms can change their number as well by changing their ionization level due to temperature changes. This behavior should not occur for ionized atoms like Ti II due to the higher ionization potential. Since we find a disagreement to this statement and since atomic lines can be modeled well, we suspect that the atmospheric model used by Steiner which was proposed by Solanki [59] may be not accurate enough.

In Chapter 3.1.4.2 we found an increase of the white-light intensity with increasing surface area of the bright point. This is not in agreement with the heating mechanism proposed by Rutten [49]. Also, this indicates a change in the bright point atmosphere with changing size. This behavior is not modeled in the one-dimensional calculations. Moreover, the increase in white-light intensity for increasing surface area indicates that there is a general contrast enhancement mechanism that is independent of individual spectral lines but depends of the size of the bright point. We also find an increase in the G-band residual intensity with increasing surface area of the bright point, but no increase for the atomic lines. This indicates the existence of a contrast enhancement mechanism exclusively for the G-band.

In Chapter 3.1.4.4 we found that bright points do not change their size or shape between a height of 0 km and 320 km above the photosphere more than 120 km. There is no displacement indicating a larger inclination of bright points than 20°. We conclude that bright points are uniform and stable with height. This may not be in agreement with the model of Steiner [64], [65], which may predict that bright points increase their size with increasing height.

In Chapter 3.1.4.4 we also found that some bright points, although all bright in the G-band, do not have an enhanced brightness in the residual intensity of the atomic spectral lines. This behavior is not related to the magnetic field [6] and may indicate the existence of different types of bright points. However, additional observations are needed to confirm this result. This behavior in general indicates also problems for the one-dimensional model calculations since they do not use different bright point models.

- G-band

  In Chapter 3.1.4.1 we found that the G-band CH lines are more sensitive than atomic spectral lines. The G-band CH lines are the only spectral lines in our investigation that can distinguish between bright points and their immediate surroundings. They are also the spectral lines that are the most sensitive to temperature changes in solar pores (Ch. 3.1.4.4). The reason for this behavior remains unclear. One possible explanation may be that the G-band mostly consists of spectral lines of the CH molecule which is prone to dissociation. The collected data does not provide enough information to perform an inversion but it allows for forward check of theoretical models. We describe the comparison with theoretical calculations in Chapter 4.

  In the Chapter 3.1.4.3 we confirmed the existence of a separate contrast enhancement mechanism for the G-band since we find a positive correlation between the white-light intensity and the G-band residual intensity but a

slightly negative correlation between the white-light intensity and the residual intensity of the atomic lines.

We find a positive correlation between the residual intensity of the atomic spectral lines and the G-band residual intensity for the bright points, the quiet sun and the solar pores. This indicates that a substantial part of light of the G-band CH lines originates higher in the photosphere than the photospheric level. This is not in agreement with the predicted formation height of 40 km below the photosphere by Sanchez-Almeida [50]. We find a significant contribution from atmospheric layer in a height of 320 km above the photosphere. This is not in agreement with Steiner [63], who predicts a maximum contribution to the G-band intensity from a height of 160 km.

The result of a higher forming G-band is confirmed in the Chapter 3.1.4.4 where we find the inversion of the solar granulation not only for the atomic lines, but also, to some extent, for the G-band as well. The inversion of the solar granulation means that the G-band cannot form at photospheric height, which is not in agreement with the predictions of Sanchez-Almeida [50].

We cannot confirm most of the predictions that have been made about bright points or the G-band itself. We can only confirm the prediction of Steiner [63] that bright points have an enhanced contrast in the Fe I lines as well. We cannot confirm his prediction about the contrast in the Ti II lines or his prediction about the formation height since the G-band has contributions from other heights than 160 km above the photosphere. We also cannot confirm the predictions about the formation height of the G-band made by Sanchez-Almeida, since we find that most contribution to the G-band originates from atmospheric layers higher than photospheric level $\tau = 1$. Our results provide new information that has to be incorporated into G-band and bright point models to give a correct picture of these structures. We will conduct our own calculations in a later Chapter to forward check our results with the model of Stein [62] and the radiative transfer code from Uitenbroek [68].

3.2 Dopplergrams

3.2.1 Motivation

In the second observing, run we recorded dopplergrams with the UBF. We used the velocity measurements of bright points to investigate a possible heating mechanism and plasma flows. As described in detail in Chapter 1.4.2, the calculations of Steiner [64], [65] predict a strong down-flow of plasma during the formation of a bright point and a spatially smaller down-flow at the border of a bright point during its existence. The UBF in the dual mode provides enough sensitivity to detect these down-flows (Ch. 2.4.3).

Since the seeing conditions were highly variable, we chose a region on the sun that contained a medium-size, round sunspot close to disc center. The observation of a sunspot instead of quiet sun in medium seeing condition has the advantage that the sunspot can be used as a good lock point for the AO system. Furthermore, since the spatial size of penumbral grains and umbral dots is larger than the spatial size of bright points [58], there is a higher possibility of obtaining useful data in medium seeing conditions by observing a sunspot. Since the sunspot occupied most of the field of view, the number of bright points in the field of view is small which makes a statistical analysis impossible.

The sunspot we investigated provides the opportunity to study its fine structure. We investigate the line-of-sight velocity of umbral dots which allows us to check the different sunspot models of Weiss [29] and Parker [42]. We also investigate the different types of umbral dots [21].
Additionally, we investigate the properties of penumbral grains and a possible connection with umbral dots. Penumbral grains are known to penetrate the umbra [58] which poses the question if umbral dots and penumbral grains are of the same origin as predicted by Choudhuri [12].
We did not record residual intensity images, but we added the red (right) and blue (left) bandpass images of the UBF to obtain a 'single' bandpass of the UBF centered at the line core with a FWHM of about 230 mÅ . The broader bandpass essentially yields a measurement of the integrated line intensity of a spectral line. If we assume that the line-profile itself does not change its shape for different core-intensities, the core intensity is proportional to the integrated intensity of the line-profile. This linear relationship allows for a qualitative study of the residual intensity even although the sensitivity is lower due to the larger bandpass. However, we did not attempt to correct for the instrumental profile in this case since we do not have a close-by continuum as a filtergram and use the broadband continuum at 5500 Å instead. We perform this residual intensity investigation since we observe the line C I 5380 Å which forms about 40 km above the photosphere which contains information about the atmospheric conditions in a new height. Moreover, we now have the possibility to investigate new solar structures as well, since there is a sunspot with its umbra and penumbra in the field of view. The different atmospheric conditions in these two structures may be used to obtain complementary information to the first observing run.

3.2.2 General Information about the Observations

The observations were carried out on April 13, 2001 at the Dunn Solar Telescope (DST) of the National Solar Observatory at Sacramento Peak. We used the low-order AO system of the DST (Ch. 2.2.4) and corrected for the first twenty Zernike

modes. We could resolve structures as small as 0.20 arcsec which we determined by measuring of the FWHM of the smallest structure we found in the G-band images. We recorded narrow-band filtergrams using the UBF (Ch. 2.3.2). Behind the UBF we placed a Quarter-Wave Plate and a Polarizing beam-splitter as well as two 16-bit 1kx1k SI CCD-cameras to record the filtergrams. This enabled us to obtain two filtergrams simultaneously and therefore eliminate the degrading effect of differential seeing and atmospheric distortion (Ch. 2.2.3). This method uses the incoming photons efficiently since the SI cameras have back-illuminated CCD chips with a high quantum efficiency and we image both wings of the spectral line at the same time. Usually, the light of one of the wings is cut off.
We observed the Fe I 5576 Å line forming at a height of about h=320 km above the photosphere, the Fe I 5691 Å line forming at h=160 km and the C I 5380 line forming at h=40 km (Ch. 2.4.2). All lines except the C I line are non-magnetic. The C I line has a Landee-factor of 1.0. It is only used at one point in this investigation in order to compare residual intensities at different heights. Since the UBF has a half-width of about 230 mÅ when the left and the right wing are added the measurement is not affected by the Zeeman splitting.
At a wavelength of 550 nm the UBF itself has a half-width of about 160 mÅ and the wavelength-difference between the two filtergrams is therefore 160 mÅ as well. The UBF was centered at the line-core so that the center wavelengths of the two filtergrams are shifted about ±80 mÅ (Ch. 2.3.2).
Along with the filtergrams, we recorded G-band and white-light images. For the G-band images, we used a Xedar 2kx2k 12 bit CCD camera (reading out only 1kx1k) behind a 10 Å interference filter centered at 4305 Å. For the white-light images we used a Pixelvision 512x512 16-bit CCD camera behind a 100 Å interference filter centered at 5500 Å. All pictures were recorded simultaneously with an exposure-time of 1500 ms. The pixel-scale was 0.039 arcsec/pixel for all cameras resulting in a field of view of 40 arcsec x 40 arcsec and 20 arcsec x 20 arcsec for the white light image.

We observed the active region NOAA 9422, which consisted of two sunspots. For the final analysis we selected the sunspot with the larger umbra. The region was located at a latitude of S 12.6° and a longitude of E 1.66° yielding $cos\ \Theta = 0.98$ and a $sin\ \Theta = 0.22$, i.e., the vertical velocity contributes with 98 percent and the horizontal velocity contributes with 20 percent to the line-of-sight velocity.
1320 pictures were recorded in about 84 minutes, in the sequence of 2x5576 Å , 2x5691 Å and 2x5380 Å . The cycle-time was limited to about 4-5 s by the slow readout of the two SI-cameras. The whole setup can be seen in Figure 3.1.

3.2.3 Data Reduction

3.2.3.1 General Remarks The best 60 images of a total of 1320 images were selected automatically by a program calculating RMS variations in the intensity of

the G-band images and selecting the images with the highest contrast. From these pre-selected 60 images, the best image of each wavelength was selected visually.
The images were flat-fielded and then aligned and scaled to the same spatial scale as the blue wing using target images. This is necessary to produce the normalized intensity difference images for the velocity determination. The overall alignment for the red and blue wing was performed to better than 0.5 pixels for the left in right wing and for the other pictures it was performed to better than one pixel. The alignment was checked by processing target images in the same way as solar images and determining the deviation from a zero image in the resulting image.
The white-light and the G-band images were normalized to a mean intensity of 1.0 for the solar granulation. For the further processing of the sunspot observations of the sunspot only the field of view was restricted to the field of the white-light camera for all images.

3.2.3.2 Selection criteria and procedures The selection process and the Fourier decomposition algorithm have already been described in Chapter 3.1.3. However, we did not attempt to select bright points because the bright point selection algorithm requires better seeing conditions. Furthermore, the bright points that we did find, were not in the field of view of the white-light image. We optimized the selection process for the umbra, umbral dots, penumbra and penumbral grains to closely match the visual impression. We used the G-band image to perform the selection.

- Photosphere, Granulation and Intergranular Lanes

  We selected all pixels with an intensity greater than $0.9 \cdot I_{phot}$ in the white-light image as photosphere. We removed all intensity variations larger than nine arcsec by using the suitable components of the Fourier decomposition. We selected every pixel with an intensity greater than 0.0 as granule and every pixel in the photosphere not selected as granule as intergranular lane.

- Umbra

  We selected the umbra as the pixels in the G-band image with an intensity lower than $0.5 \cdot I_{phot}$. We made two further divisions of the umbra. We selected pixels closer than 1.2 arcsec to the edge of the umbra as outer umbra and the other pixels of the umbra as inner umbra. A second separation into bright and dark parts of the umbra was made where every pixel with an intensity greater than $0.3 \cdot I_{phot}$ was selected as bright and every pixel with an intensity lower than $0.3 \cdot I_{phot}$ was selected as dark.

- Umbral Dots

  We removed all brightness variations larger than one arcsec from the umbra by the Fourier decomposition. We selected every pixel brighter than 0.0 in

the 'filtered' image as umbral dot. This selection matched well with the visual impression of the position of bright structures. Sometimes a structure identified by the algorithm as a single umbral dot showed two or more intensity maxima, i.e. consisted of several, individual umbral dots. This does not represent a problem since we do not study the morphology of umbral dots but try to measure average physical parameters such as velocity. Outer and inner umbral dots were selected by identifying the umbral dots in the inner and outer parts of the umbra. Another, different separation was made for the umbral dots by dividing them into 'bright umbral dots' ($I > 0.45 \cdot I_{phot}$) and 'dark umbral dots' ($I < 0.45 \cdot I_{phot}$). The reason for the two types of selection are given in Chapter 3.2.4.

- Penumbra

  We selected the penumbra as the pixels with intensities between 0.5 and 0.9. To eliminate 'holes' caused by very bright penumbral grains, every pixel closer than 0.4 arcsec from a pixel initially tagged as penumbra was considered to belong to the penumbra as well. This leads to the inclusion of some granulation at the very edge of the penumbra. We removed these granules by excluding pixels which were closer than 1.2 arcsec to the outer edge of the penumbra. Applying this 'guard ring' around the penumbra excludes the regions of strong down-flow that we observe at the outer boundary of the penumbra. We treat the down-flows separately in Chapter 3.2.4.3.

- Penumbral Grains

  We selected the penumbral grains from the 'penumbra' pixels in the same way as the umbral dots from the 'umbra' pixels. We removed intensity variations larger than one arcsec and chose pixels with an intensity greater than 0.0.

3.2.3.3 Calibration of Dopplergrams

Sign Convention Throughout this investigation + means blue-shifted i.e. the plasma is flowing towards the observer and - means red-shifted i.e. the plasma is flowing away from the observer.
The normalized intensity difference (Ch. 2.4.3

$$I_n = \frac{I_{blue} - I_{red}}{I_{blue} + I_{red}}$$

was translated into the line-of sight velocity by multiplication with a calibration factor (Ch. 2.3.3). This factor was determined by analyzing lines-cans for each line with a step-width of 25 mÅ and 31 steps. The calculations of these line-scans were shown in Chapter 2.3.2. For the dopplergrams we can actually measure the calibration curves, analyze them and determine the calibration factor. The

calculated curves match the measured ones very well. This suggests the validity of the simulations in general, and specifically for the residual intensity pictures, which we cannot verify by measurement. The line-scans showed a linear relationship of better than one percent between I_n and v which allowed the use of a simple conversion factor.
The comparison between the measured calibration factors for the umbra and the quiet sun showed a small difference in sensitivity of 2.4 percent for the 5576 Å line and of 8.1 percent for the 5691 Å line. This difference is a result of stray-light and translates into a measurement error, which is discussed below. The 5380 Å line was found to be too weak to be useful for velocity measurements in the umbra with the broad band-pass UBF.

We set the zero-point of the dopplergrams to the average velocity of the umbra. The absolute zero-point is not important for our investigation since we only perform relative and local comparisons between velocities. We find umbral oscillations in our velocity maps. Since we compare the velocity of solar structures to the velocity of the immediate surroundings these oscillations only play a minor role. We discuss the oscillation in Chapter 3.2.4.1.

We find three error sources for velocity-measurements with the UBF. These are: alignment-errors caused by a shift of the left wing image relative to the right wing image, stray-light-errors, caused by a mixture of velocity signals from different points of the solar surface and noise-errors resulting from the CCD read-out noise and the photon noise.

- Alignment error

  We estimated the shift-error resulting from the imperfect alignment of the left and the right wing by removing all features larger than 0.05 arcsec from the velocity-maps using the Fourier decomposition. The filtered image contains only high frequency noise and a minor amount of detail. Since we know that the alignment is better than 0.5 pixels which corresponds to a spatial distance of 0.02 arcsec, we assume that the total noise due to the alignment error is contained in the filtered image. Also, all other sources of random noise like the photon and the dark current noise are contained in this image. The rms values for the intensities of the filtered images were 14 m/s for the Fe I 5576 Å line and 94 m/s for the Fe I 5691 Å line. Since not all solar detail was removed by the Fourier decomposition, these error-values are an overestimation.

- Stray-light error

  No stray-light correction was made. The lowest intensity in the sunspot umbra was $0.27 \cdot I_{phot}$, which was approximately the value to be expected for this wavelength [10]. We assume the stray-light to have the same intensity for

every point in the field of view. With this assumption, the influence of the stray-light for the velocity-measurement can be estimated by

$$\begin{aligned} I_n' &= \frac{(I_{blue}+S_{blue})-(I_{red}+S_{red})}{(I_{blue}+S_{blue})+(I_{red}+S_{red})} \\ &= I_n \cdot (1+\frac{S_{blue}+S_{red}}{I_{blue}+I_{red}})^{-1} + \frac{S_{blue}-S_{red}}{(I_{blue}+S_{blue})+(I_{red}+S_{red})} \end{aligned}$$

I_n is the real normalized intensity, I_n' is the normalized intensity changed by the stray-light. I_{blue} and I_{red} are the actual pixel intensities for the red and the blue wing filtergrams and S_{blue} and S_{red} are the corresponding stray-light intensities.

This formula shows two different error-terms. The first error term results in a reduction of sensitivity. The weaker the normed pixel intensity $\frac{I_{blue}-I_{red}}{I_{blue}+I_{red}}$, the greater the reduction in sensitivity, since the real velocity signal becomes smaller compared to the stray-light signal $\frac{S_{blue}-S_{red}}{I_{blue}+I_{red}}$. In a first-order approximation the reduction in sensitivity is equivalent to measured stray-light. Therefore, we can use measurements of the different sensitivity for the umbra and the quiet sun to determine the stray-light. We find the stray-light to be 2.4 percent for the 5576 Å line and 8.1 percent for the 5691 Å line. This is only true if the spectral line has the same equivalent width for the umbra and the quiet-sun. We confirmed this behavior for the Fe I 5575 Å and the Fe I 5691 Å line by comparing the umbral spectral profile [75] to the quiet sun spectral profile [14].

The second error term represents a shift of the zero-point velocity across the field of view towards the 'velocity' of the stray-light depending on the measured intensity of the solar surface at each point. This shift of the zero-point velocity increases with decreasing normalized pixel intensity. The 'velocity' of the stray-light was assumed to be the average velocity of the image, since the stray-light is wide spread. We measure an average velocity of the stray-light of -105 m/s for the 5576 Å line and -190 m/s for the 5691 Å line. We apply the formula for the second error term and use the amount of stray-light determined from the first error-term. We find the stray-light induced shift of the 0-velocity as -2.5 m/s (quiet sun) -7.6 m/s (darkest part of the umbra) for the 5576 Å line and -4.6 m/s and -13.7 m/s for the 5691 Å line. Therefore, the maximum shift difference was 5.1 m/s and 9.1 m/s respectively, which yields the error for any two structures measured in the field of view, since we only measure velocity differences. If we restrict the measurements to structures within the Umbra (or

penumbra) the shift-error is only half as large because the intensity difference in the umbra is only half as large.

Even though the error is systematic and we only measure relative and local velocities, we have to include the error since it only depends on intensity, and intensity variations occur on a small scale. Therefore, they are not removed by a relative or local measurement of the velocity.

- Noise-errors

  The noise errors are already included in the 'shift-error' section. Independently, we determined the noise from the dark-image and the flat-field by flat-fielding two flat fields and determining the rms intensity variation in the resulting image. These errors are independent of the spatial scale and were found to be negligible in comparison to the other error sources. Therefore, the main source of error is the imperfect alignment of the left and the right wing.

The different errors are treated statistically independent of each other and are therefore added quadratically. The total error of the velocity measurements is found to be 14.9 m/s for the 5576 Å line and 94.4 m/s for the 5691 Å line. The main error-source is the alignment error.
As stated above, the sensitivity of the UBF was found to be slightly different for the umbra and the quiet sun due to changes in the line and stray-light. We use the calibration for the quiet sun for all solar structures. Since we compare velocities of spatially close structures only, this does not affect the results.
The resolution during the dopplergram run was not as good as during the residual intensity run. We reached a resolution of 0.20 arcsec, which yields a limit of detection $ld = 0.6 \cdot \frac{m}{s} \cdot arcsec^2$ for the 5576 Å line and $3.8 \cdot \frac{m}{s} \cdot arcsec^2$ for the 5691 Å line.

Calibration of Residual Intensity Pictures

The 'residual intensity' pictures were formed by $I_{res} = \frac{I_{core}}{I_{continuum}}$ (Ch. 2.4.3). We added the left and the right wing of the dopplergrams to obtain the integral line (core) intensities. This results in a very large FWHM of the UBF of about 230 mÅ. Therefore, we measure the total light reduction of a spectral line. By the line of reasoning applied in Chapter 3.2.1, we assume that this integrated intensity is proportional to the core intensity. The core intensity for G-band was the G-band image itself with a half-width of 10000mÅ . We used the white-light images centered at 5500 Å as the continuum image for all wavelength. All residual intensity pictures were normalized to a mean value of 1.0. No UBF bandpass deconvolution was performed.

3.2.4 Results

To get an overview, the total field of view is shown in Figure 3.34. In top left image the contours of the selected umbra, umbral dots, penumbra and penumbral grains are superimposed to give an impression of the selection process.

3.2.4.1 Umbra

3.2.4.1.1 General Appearance As mentioned above, the average velocity of the umbra was set to 0 m/s. The total rms variation is 133 m/s for the 5576 Å line and up to 161 m/s for the 5691 Å line. This indicates some motion in the umbra in general (Fig. 3.35). A comparison with the observations of Aballe Viero [1] suggests that this motion is due to umbral oscillations since we find the same velocity range. However, we cannot verify this by a time-frequency analysis, since we were not able to record a long-enough time series because of the seeing conditions. In disagreement to Aballe Viero [1] we find an increase of the velocity amplitude (Fig. 3.35) with intensity. This increase is not a result of the better resolution of our observations since this effect vanishes when velocity variations larger than four arcsec are removed. We find a significant difference between brighter (corresponding well with outer) and darker (corresponding well with inner) umbra. The brighter umbra has a mean velocity of -42 ± 154 m/s for the 5576 Å line and -25 ± 165 m/s for the 5691 Å line. The dark umbra has a mean velocity of 58 ± 69 m/s for the 5576 Å line and $27 \pm 151 m/s$ for the 5691 Å line. The dark umbra has a greater (+) velocity than the bright umbra, while the stray-light-error will *decrease* the velocity of darker structures. Therefore, it is not a systematic effect. The reason for this behavior maybe the strong down-flows at the umbra-quiet sun border that we will discuss in this paragraph.

3.2.4.1.2 Umbral Dots When we analyze the umbral dots selected by the process described in Chapter 3.2.3.2, we find them to be a very non-uniform sample. Figure 3.36 suggest that umbral dots consist of several different types. We attempted to separate umbral dots into two separate types.
Two ways of separation were considered. The first way was to separate the umbral dots by their position in the spot (inner/outer or central/periphal umbral dots), the other way was to separate them by their intensity (bright/dark umbral dots). These methods coincided quite well with a 83 percent overlap for central/dark umbral dots and a 64 percent overlap for periphal/bright umbral dots. However, plotting histograms for the two different methods clearly shows that better separation was achieved by the intensity method (Fig. 3.37). Thus we separate umbral dots into bright and dark ones. This is different from studies that propose a separation into into central and periphal umbral dots [21]. Without a correct identification and

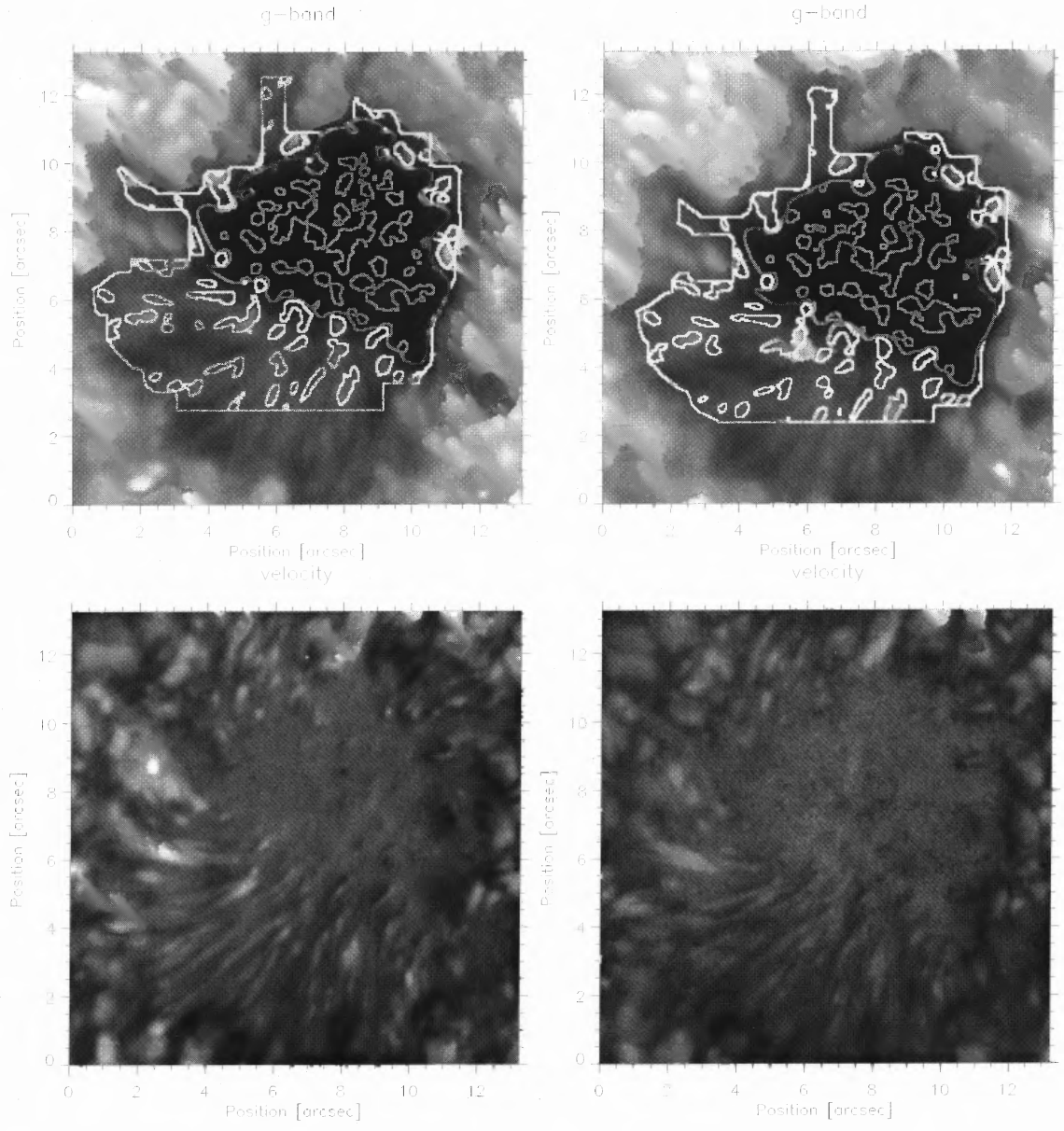

Figure 3.34 The G-band image (top) and velocity map (bottom) for the Fe I 5576 Å (left) and 5691 Å line (right) covering the field of view. The bright contours superimposed in the left image are the borders of the penumbra and the penumbral grains, the gray contours are the borders of the umbra and the umbral dots.

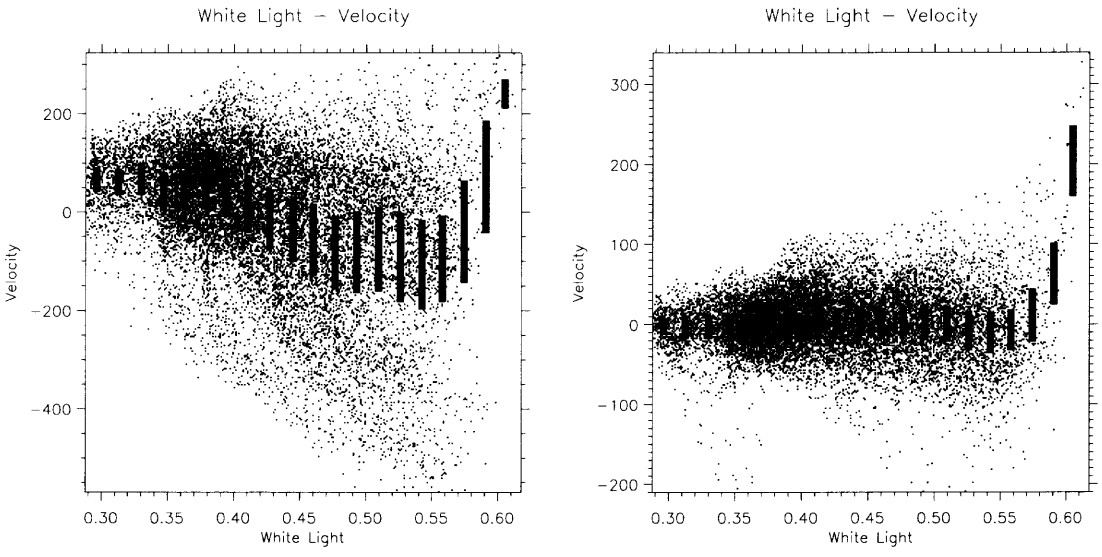

Figure 3.35 White-light intensity vs the velocity of the Fe I 5576 Å line for all pixels selected as umbra. We find a negative correlation as well as an increase of the rms variation with intensity. The left scatter-plot is identical to the right scatter-plot except for all velocity variations with a spatial scale larger than four arcsec have been removed. We can see that the correlation and the increase in rms variation a largely due to the larger-scale structures. The down-flows may be, however, a result of the strong down-flows that occur at the umbra-quiet sun border.

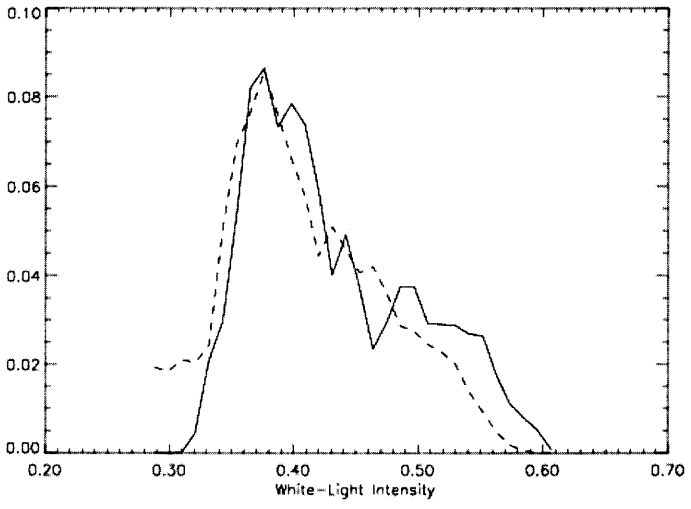

Figure 3.36 Distribution of the white-light intensity for umbral dots (solid line) and the umbra (dashed line). This histogram shows all pixels selected as 'umbral dot'. The double peak suggests the existence of two different types of umbral dots.

separation of umbral dots it is impossible to develop a theoretical understanding since a single model cannot explain two different structures at the same time.

'Dark' Umbral Dots

The 'dark' umbral dots occur mainly in the center of the umbra. They have a mean upward velocity of 64 ± 74 m/s compared to the umbra for the 5576 Å line and 12 ± 120 m/s for the 5691 Å line. The velocity of the dark umbra is 58 ± 69 m/s for the 5576 Å line and 27 ± 151 m/s for the 5691 Å line, i.e the dark umbral dots have only an insignificantly small velocity on average compared to their immediate surroundings.
In Figure 3.40 we observe a weak negative correlation between the intensity and the velocity for the Fe I 5691 Å line which means that the brighter structures show down-flows. We do not find this correlation for the Fe I 5576 Å line. This motion is most likely a result of umbral oscillations. We find a correlation between the residual intensity and the velocity, which is negative for the 5576 Å line, and positive correlation for the 5691 Å line. The G-band residual intensity shows almost no correlation with velocity. The negative correlation between the intensity and the velocity for the inner part of the umbra is confirmed by the Figures 3.38, 3.39.
We find a small number of distinctly different umbral dots. These umbral dots are associated with stronger down-flows. The strongest down-flow has a velocity of -250 m/s for the 5576 Å and over -300 m/s for the 5691 Å line (left column of Figures 3.38,3.39). These down-flows are larger than the measurement uncertainty

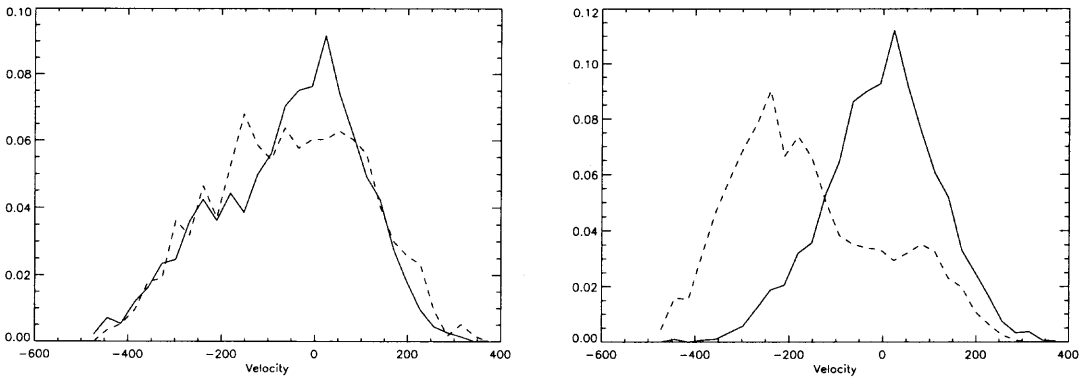

Figure 3.37 Distribution of velocity in the 5691 Å line for dark/inner (solid line) and bright/outer (dashed line) umbral dots. The left histogram is for the separation outer/inner umbral dots, the right histogram is for the separation bright/dark. The second histogram, which uses intensity as the selection, show a much better separation of the samples.

since the umbral dot in the left images of Figure 3.38 has a surface area of about (0.3 arcsec)*(0.3 arcsec)*π=0.28 $arcsec^2$. Therefore, the velocity per area is 70 $\frac{m}{s} \cdot arcsec^2$ which is far larger than the limit of detection of $0.6\frac{m}{s} \cdot arcsec^2$.
The results suggest that dark umbral dots are composed of two different types. One type seems is a bright-dark variation with a spatial scale of about 1-2 arcsec in which the distinct umbral dots are embedded. This intensity pattern corresponds to a similar sized velocity pattern. This velocity pattern is probably a result of solar oscillations [1]. The other type of umbral dots are spatially localized and well-defined umbral bright pots which are associated with quite strong down-flows. The localized umbral dots have never been observed before, and there is no theoretical model that predicts these structures.

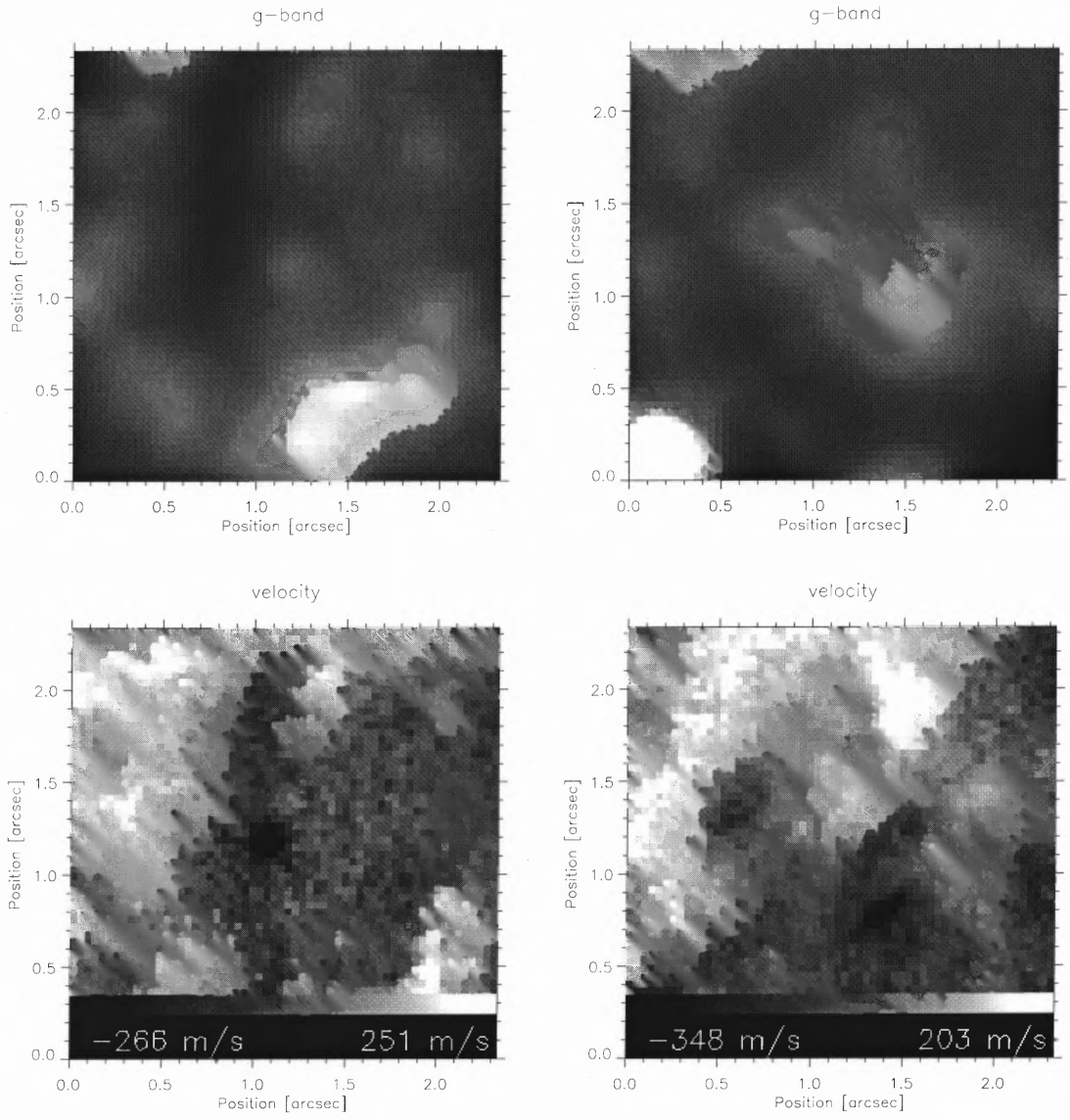

Figure 3.38 Dark umbral dots in the 5576 Å line. Top intensity (contrast enhanced), bottom velocity. In the left image, one can see an umbral dot located at (1.2,1.2) which is associated with strong down-flow of about 300 m/s. In the left image we can see the negative correlation between intensity and velocity.

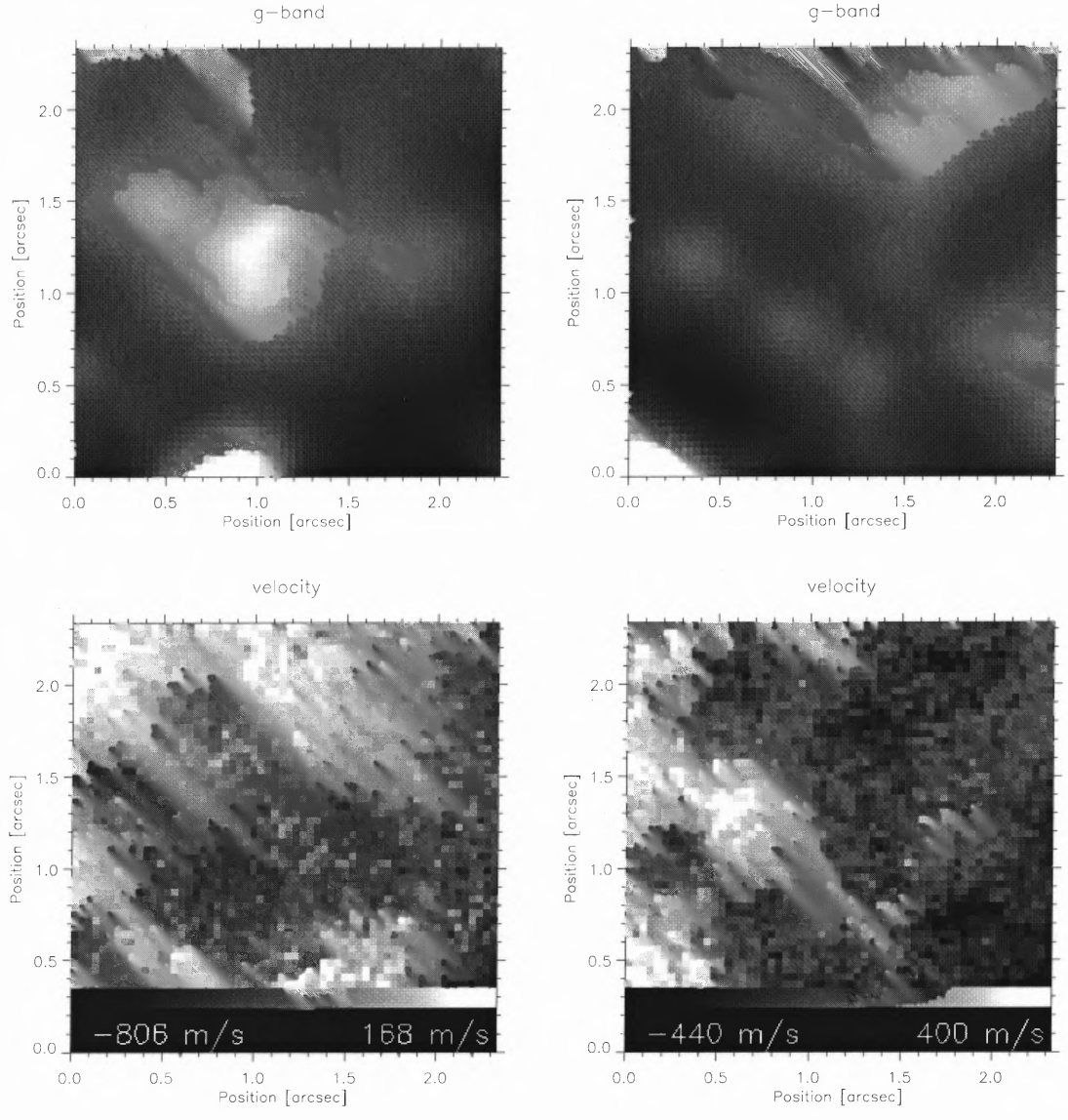

Figure 3.39 Dark umbral dots in the 5691 Å line. Top intensity (contrast enhanced), bottom velocity. On can see a weak negative correlation between the intensity and the velocity, i.e. bright structures seem to be associated with downflows. For the Fe I 5691 Å line, this holds true in general.

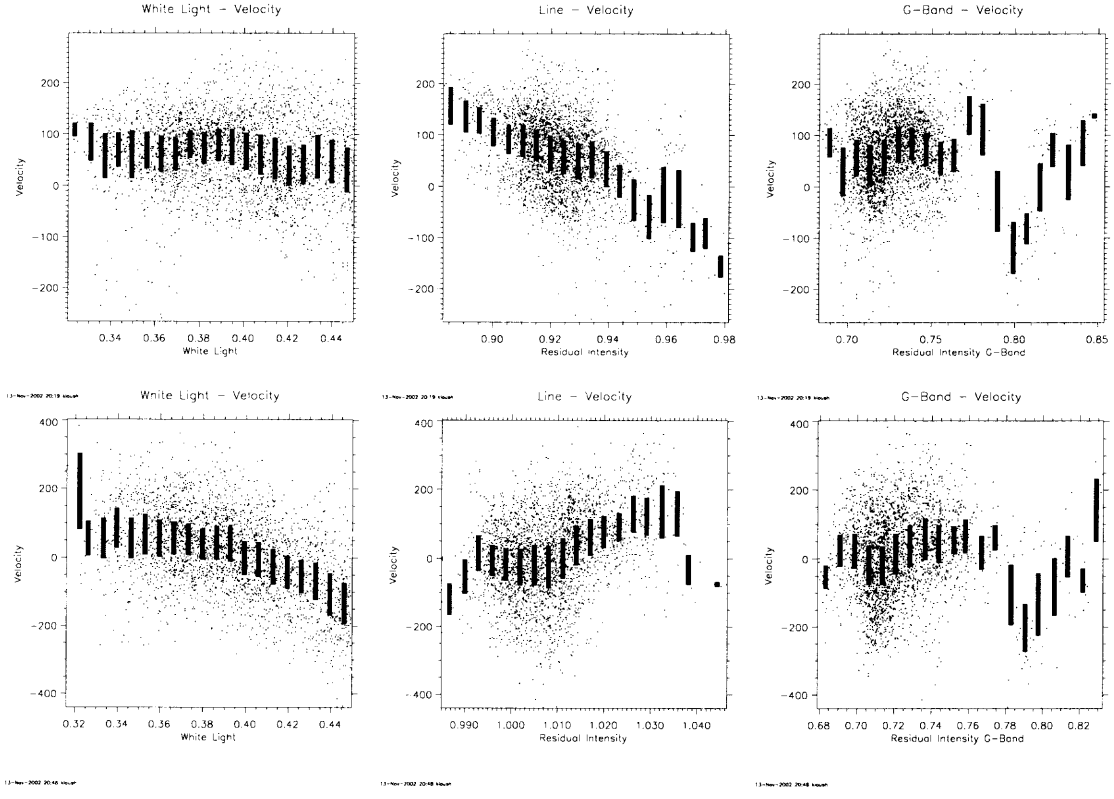

Figure 3.40 Velocity of the dark umbral dots for the lines 5576 Å (top) and the 5691 Å (bottom). One can see the negative correlation between velocity and intensity for the 5691 Å line. This may be a result of the umbral oscillations.

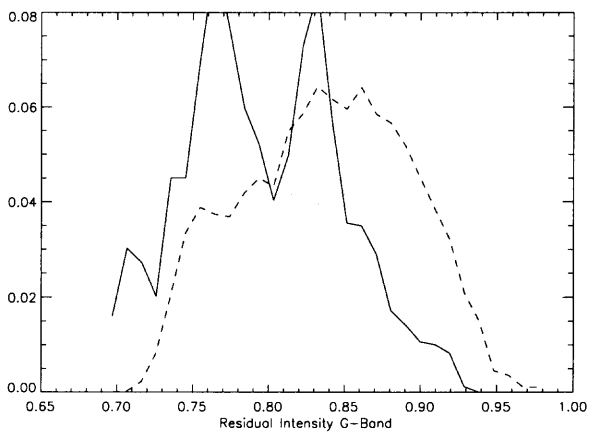

Figure 3.41 The G-band residual intensity of bright umbral dots (solid line) compared to the bright umbra (dashed line). The double peak suggests the existence of two different types of bright umbral dots.

Bright Umbral Dots

Bright umbral dots, mainly located at the border of the penumbra, are an even less uniform sample than the dark umbral dots (Fig. 3.41). They have an average velocity of -8 ± 142 m/s for the 5576 Å line and -144 ± 163 m/s for the 5691 Å line, i.e the bright umbral dots show down-flows relative to the bright umbra. However they show no velocity at all for the 5576 Å line and are up-flows with a mean velocity of 10 m/s for the 5691 Å line when they are compared to the average velocity of the penumbra.
The histogram 3.41 suggests that bright umbral dots consist of two different types. This view is supported by the scatter plot 3.42 which shows no correlation between the white-light intensity and the velocity for umbral dots with lower intensity but a positive correlation between the white-light intensity and the velocity for brighter umbral dots. Therefore, very bright umbral dots at the edge of the umbra are up-flows like penumbral grains. This view is further supported by Figure 3.43 where we can clearly identify penetrating penumbral grains by the shape in the intensity and the velocity map.
We conclude that 'bright umbral dots' consist of two different types: one type is the 'normal' umbral dots also found in the central part of the umbra whose signatures is a variation of brightness and a small, weakly anti-correlated velocity signal on a scale of one to two arcsec. They constitute the data-points in the left parts of the scatter plots 3.42. The other kind of 'umbral dots' are bright localized regions of up-flows from 100 m/s to 300 m/s with the appearance of penumbral grains. They constitute the data-points in the right parts of the scatter plots 3.42.

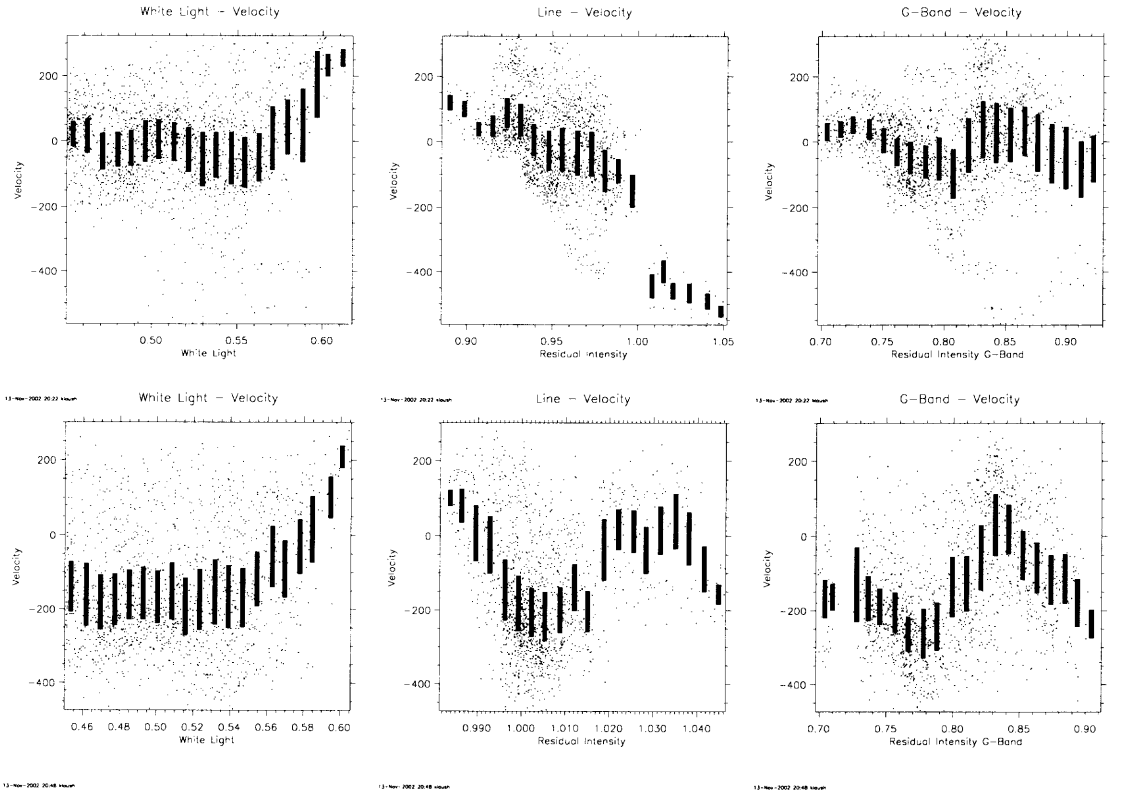

Figure 3.42 Velocity of bright umbral dots in the 5576 Å line (top) and the 5691 Å line (bottom). The left-most scatter-plots show almost no correlation between intensity and velocity. Only for the brightest umbral dots we find a positive correlation between intensity and velocity. This suggests the existence of two or more different types of bright umbra dots, one with little correlation between intensity and velocity and one type, brighter on average, with a positive correlation between intensity and velocity . There is a small negative correlation between the residual intensity and the velocity, especially for the 5576 Å line. There is no correlation between the residual intensity of the G-band and the velocity.

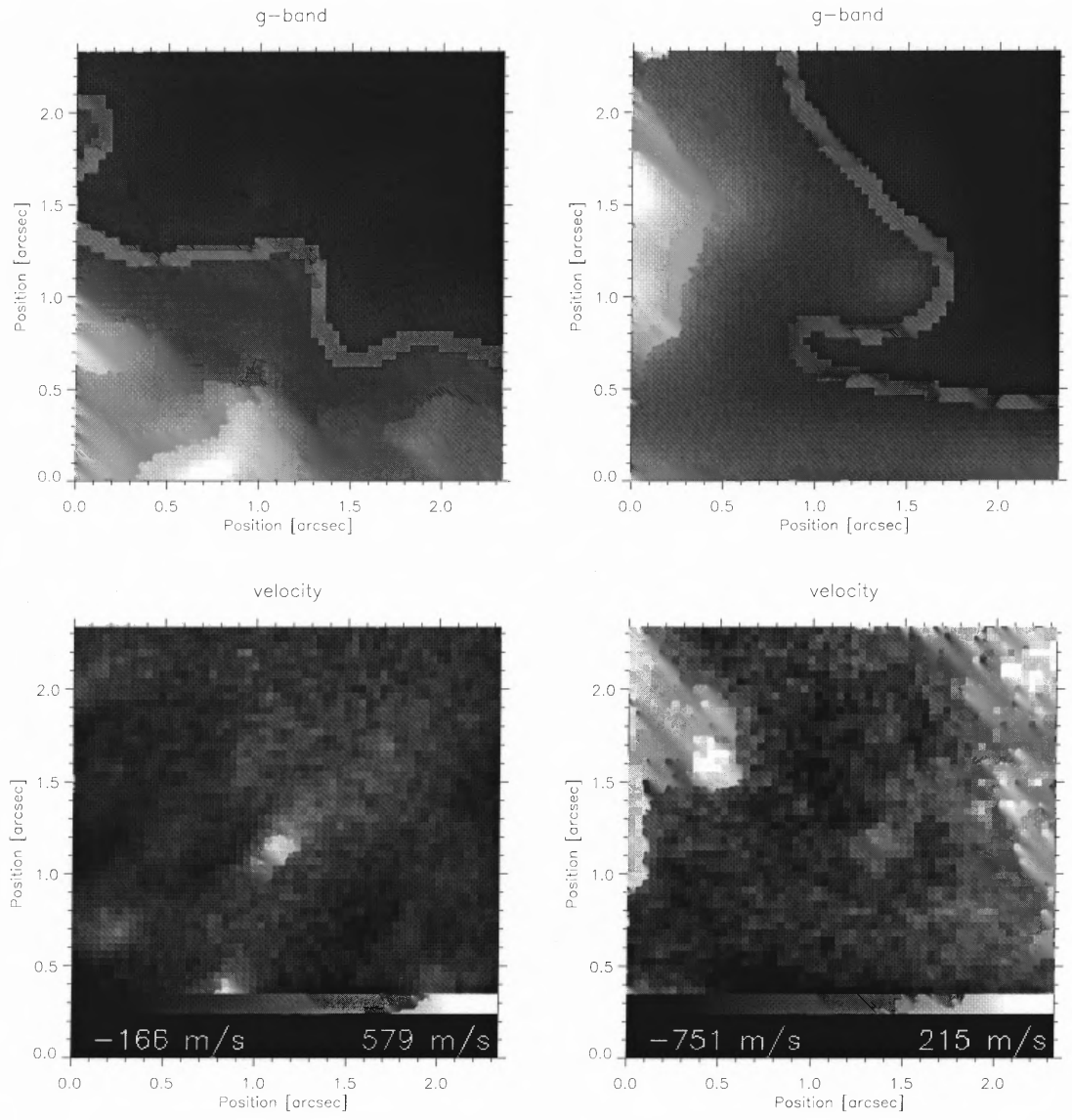

Figure 3.43 Bright umbral dots (penetrating penumbral grains). Top intensity (contrast enhanced), bottom velocity. Left 5576A, right 5691 Å . The umbra is on the upper right corner, the penumbra to the lower left. In the left image for the 5576 Å line, the penetrating penumbral grain can be seen at (1.0,1.5), at the right image for the 5691 Å line an example can be seen at (1.5,1.5). These grains are clearly inside the umbra, yet they are up-flows and even retain their 'comet tail' flow structure. All these signatures indicate that these structures are penumbral grains that have penetrated the umbra.

3.2.4.1.3 Down-Flows at the Umbra - Quiet Sun Border We find two remarkable features within the umbra. The first feature is strong down-flows at the umbra-photosphere boundary of up to $-854\ m/s$ for the 5576 Å line and $-1104\ m/s$ for the 5691 Å line. They occur outside of the umbra and only in places, where the penumbra is missing and the umbra is adjacent to the quiet sun. These down-flows maybe due to the radiative cooling of hot plasma of the photosphere at the boundary to the cooler penumbra. We are not aware of a theoretical prediction of this effect and we did not perform a calculation due to the lack of a theoretical model.
The other interesting feature are the bright areas (Fig. 3.44) which look like granules penetrating the umbra. At their locations we measure down-flows with a peak velocity of $-652\ m/s$ for the 5576 Å line and $-831\ m/s$ for the 5691 Å line. Both of the down-flows described above can be seen in Figure 3.44.

3.2.4.2 Penumbra

3.2.4.2.1 General Appearance The penumbra has an average relative velocity to the umbra of 0 m/s for the 5576 Å line and -155 m/s for the 5691 Å line, the rms-value in both cases are about 220 m/s. There is only a weak correlation between intensity and velocity (Fig. 3.45). Visual inspection reveals that some bright filaments show no up-flows at all, sometimes they show even a minor down-flow. On the other hand, some dark filaments are up-flows (Fig. 3.47). This is not in agreement with the common view that the bright structures in the penumbra are moving upwards [54]. The line of reasoning is that hot plasma streams upwards and cools radiatively, thus appearing bright.

3.2.4.2.2 Penumbral Grains All structures that are locally brighter than the penumbra were selected as penumbral grains (Ch. 2.3.2.3). These structures show a mean velocity of $19 \pm 242\ m/s$ for the 5576 Å line and $-131 \pm 222\ m/s$ for the 5691 Å line. In comparison to the background velocity of the penumbra, this is an up-flow of about $20\ m/s$ in average in both cases. This line-of-sight velocity (mostly up-flow) is weak if we assume that all bright structures are penumbral grains and an individual penumbral grain has an upward velocity of several hundred m/s.
Penumbral grains have the form of 'comets', a bright, distinct head with a fading tail. In all cases where we observe a distinct head of a penumbral grain, we also observe an up-flow at its location (Fig 3.47). These up-flows reach velocities up to $666\ m/s$ for the 5576 Å line and $396\ m/s$ for the 5691 Å line
The general correlation between intensity and velocity for pixels selected as penumbral grains is not strong however (Fig. 3.46) and comparable to the corresponding correlation for the whole penumbra. This supports the view, that the line-of-sight velocities in the penumbra are not localized in either the bright or the

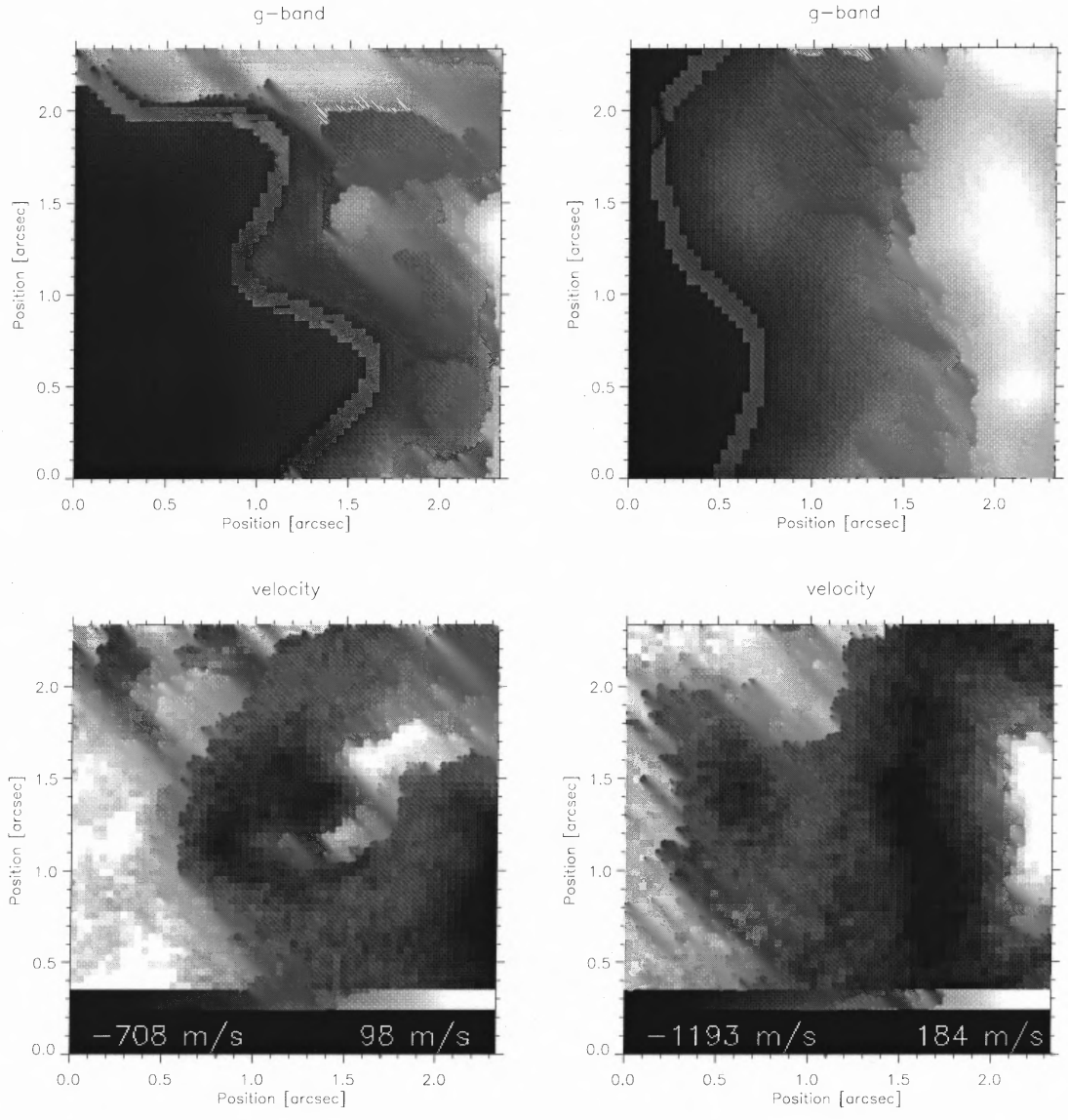

Figure 3.44 Down-flows at the umbra-quiet sun border. Top intensity (contrast enhanced), bottom velocity. Left 5576A, right 5691 Å . The umbra is to the left in both cases, the quiet sun to the right. The down-flows are located at (1.0,1.2) for the Fe I 5576 Å line and at (1.2,1.0) for the Fe I 5691 Å line.

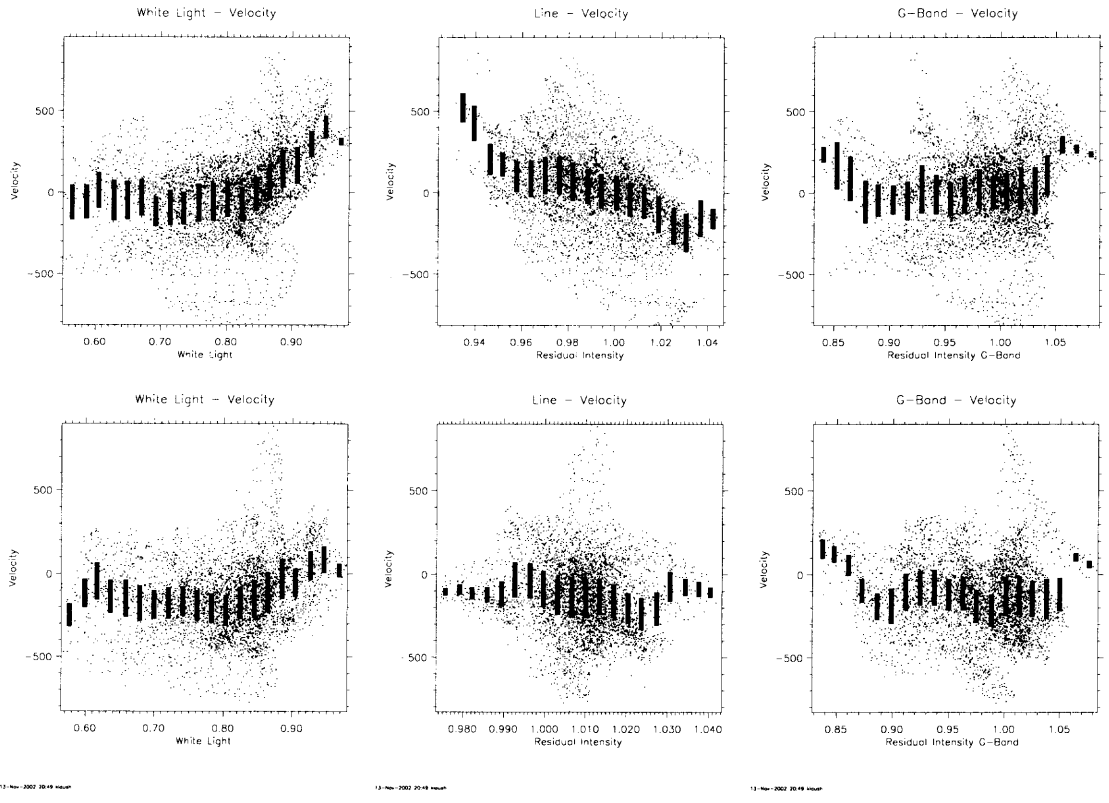

Figure 3.46 The velocity of penumbral grains in the 5576 Å line (top) and the 5691 Å line (bottom). The correlations are weak in general, especially for the scatter plot of intensity against velocity. This is not in agreement with the common view that brightenings are always up-flows.

dark filaments in general. We conclude that the heads of bright points are indeed up-flows, but that there is no general correlation between brightness and velocity.

3.2.4.2.3 Down-Flows at the Penumbra - Quiet Sun Border At the penumbra- granulation boundary, we measure strong down-flows with velocities up to -1100 m/s for the 5576 Å line and up to -1410 m/s for the 5691 Å line. These down-flows may be an indication of the Evershed effect since observations indicate [54], that the Evershed flow turns down into the photosphere at the border of penumbra-quiet sun. The down-flows cannot be identified with endpoints of either the bright or the dark filaments (Fig. 3.48) at that particular position at the boundary. Therefore we conclude that that there is no definite correlation between brightness and horizontal flow. This is in agreement with the results of the previous two paragraphs.

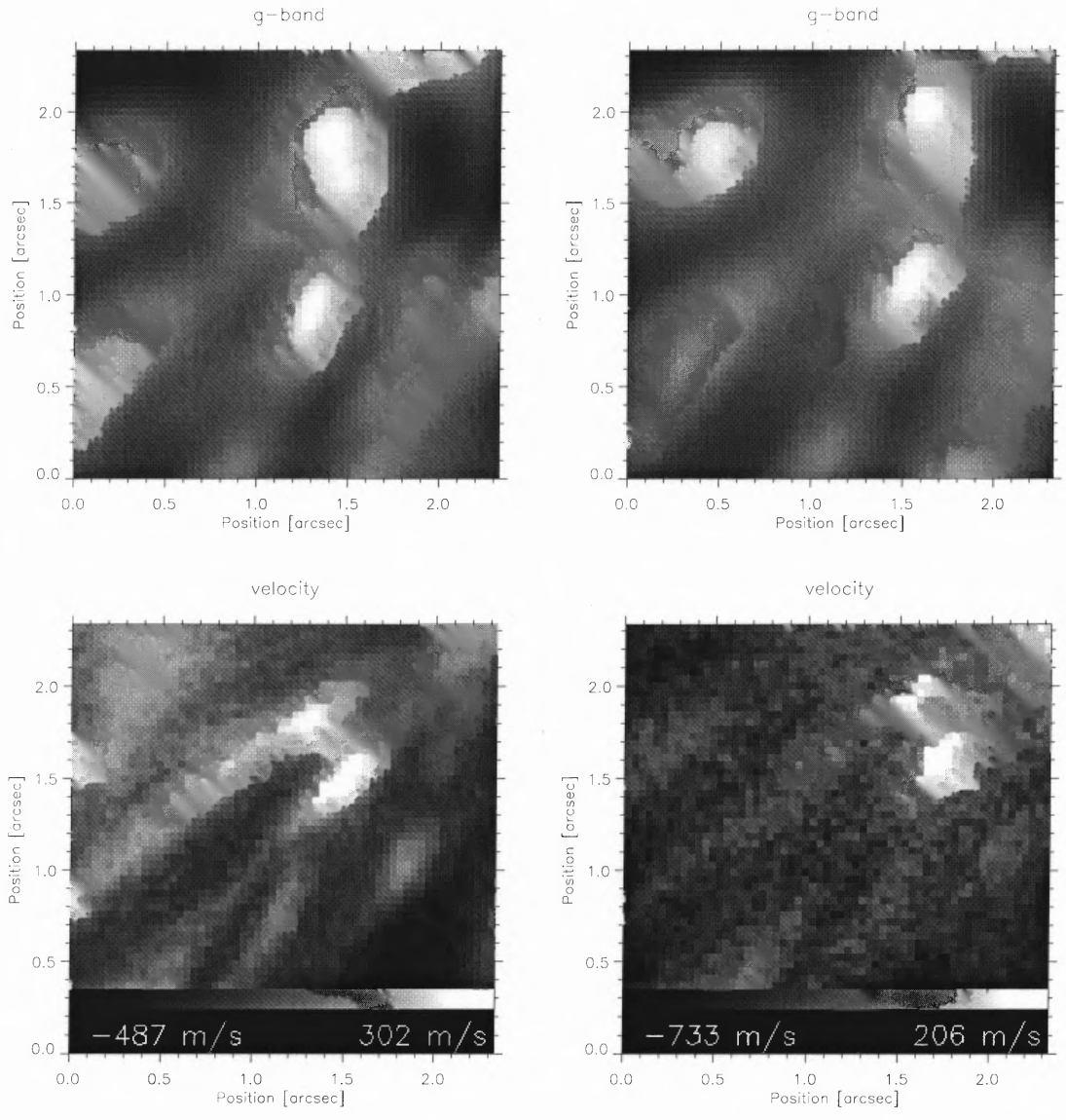

Figure 3.47 Penumbral grains. Top intensity (contrast enhanced), bottom velocity. Left 5576 Å, right 5691 Å . In this set of images one can see penumbral grains with their typical 'comet head with tail' appearance.

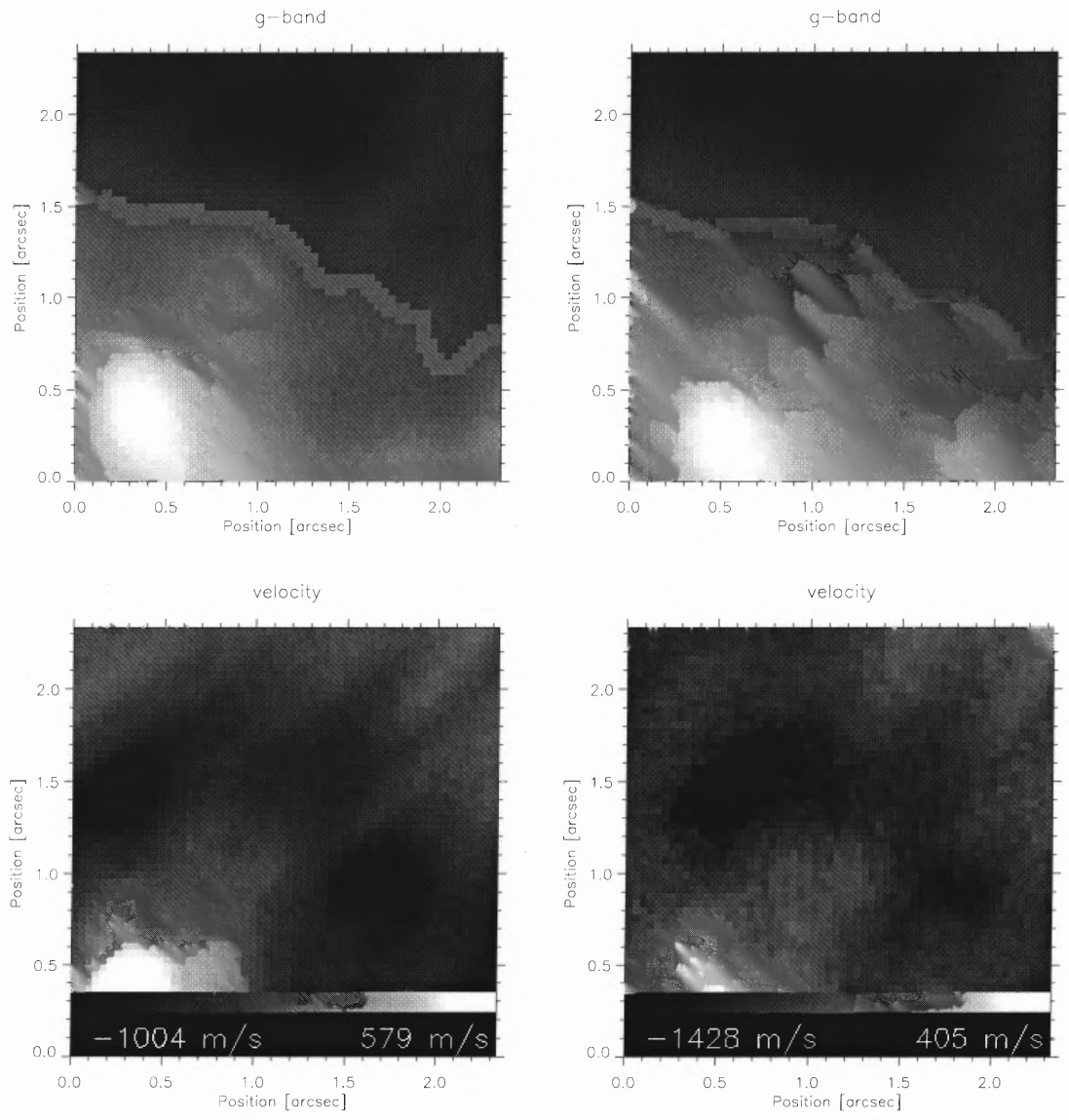

Figure 3.48 Down-flows at the penumbra-quiet sun border. Top intensity (contrast enhanced), bottom velocity, the Fe I 5576 Å line is left, the Fe I 5691 Å line is right. The penumbra is in the upper part of the image. The down-flows are located at (1.2,0.5) in the left image and at (0.3,1.0) in the right image. These down-flows have magnitudes of over 1 km/s.

3.2.4.3 Bright Points We find only a few bright points in the field of view. This is due to the relatively small fraction of quiet sun in the field of view and the seeing conditions. Moreover, the magnetic flux outside the sunspot was smaller than for the region that we selected for the residual intensity investigation. Nevertheless, we can perform velocity measurements which can be seen in Figure 3.49 and Figure 3.50. We do not measure any velocity at, or around the bright point that is any different than the velocity of the intergranular lanes itself. Since we reach a limit of detection of 2.7 $\frac{m}{s} \cdot arcsec^2$ or better and Steiner [64], [65] predicts down-flows of 3 km/s with a spatial scale of 100 km, we should easily detect such down-flows if they are existing. This is in clear disagreement to the calculations. If the flux-tube atmosphere has the predicted temperature and low pressure, the plasma at the edges of the flux-tube would inevitably cool radiatively and flow downwards. This line of reasoning can also be applied to a cluster of bright points. We conclude that fundamental changes have to be made to the theoretical model if it is to fit the observations.
However, we have to be cautious with any interpretation in respect to the theoretical model of Steiner [64] [65] for several reasons. We do not have a time series and so we cannot tell if a bright point is forming. Therefore, it is impossible to check for down-drafts during the formation of a bright points. We can only see existing bright points which allows us to check for the smaller, spatially localized down-drafts at the borders of bright points. Furthermore, the predictions of Steiner are for atmospheric layers 220 km below the photosphere and for the photospheric level itself. We observe layers of the solar atmosphere at least 40 km higher. Since Steiner predicts a reduction in velocity with increasing height, the velocity of the down-drafts may be too small to be observed at the formation heights of the spectral lines we use.

3.2.4.4 G-Band We plot the G-band residual intensity against the residual intensity of the three atomic spectral lines in various solar structures (Fig. 3.51). These plots show a strong correlation between the G-band and the Fe I 5576 Å line, especially for the umbra and the quiet sun. There is a weaker correlation for the Fe I 5691 Å line, and only a weak correlation for the C I 5380 Å line (Fig. 3.51). The weak correlation for the C I 5380 Å line in the umbra and the penumbra has to be taken with caution since the line is weak in the umbra and penumbra. Moreover, 62 percent of the light passing through the G-band filter originates in the continuum (Ch. 4.1), and since the C I 5380 Å line forms at a height of 40 km which is close to the continuum we expect to find some correlation. These results are consistent with the findings in the residual intensity section when we compare the results for the quiet sun and the result for the umbra with the pores.
The correlation for the line Fe I 5691 Å is weaker than for the 5576 Å line even though the Fe I 5691 Å line has almost the same properties as the line Fe I 5576 Å . It is non magnetic and has about the same temperature sensitivity as the Fe I 5576 Å . The only difference is the formation height of 160 km instead of 320 km for

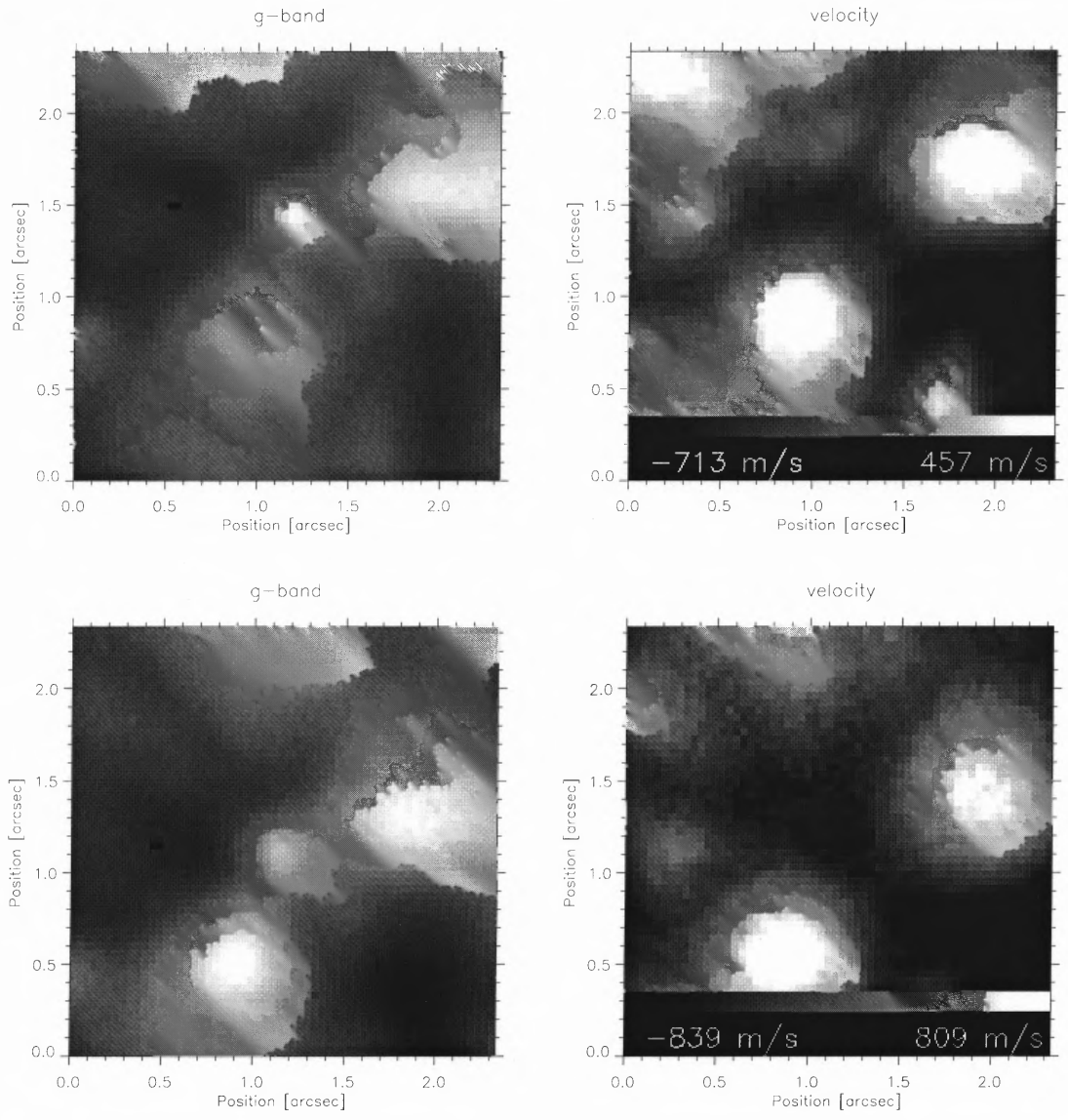

Figure 3.49 Velocity measurements of bright points in the lines Fe I 5576 Å (top) and Fe I 5691 Å (top). Left is the intensity image, right is the velocity image. We do not detect any local velocity variations at the locations of the bright points. The image noise increases from top to bottom since the the lines strength decreases top to bottom.

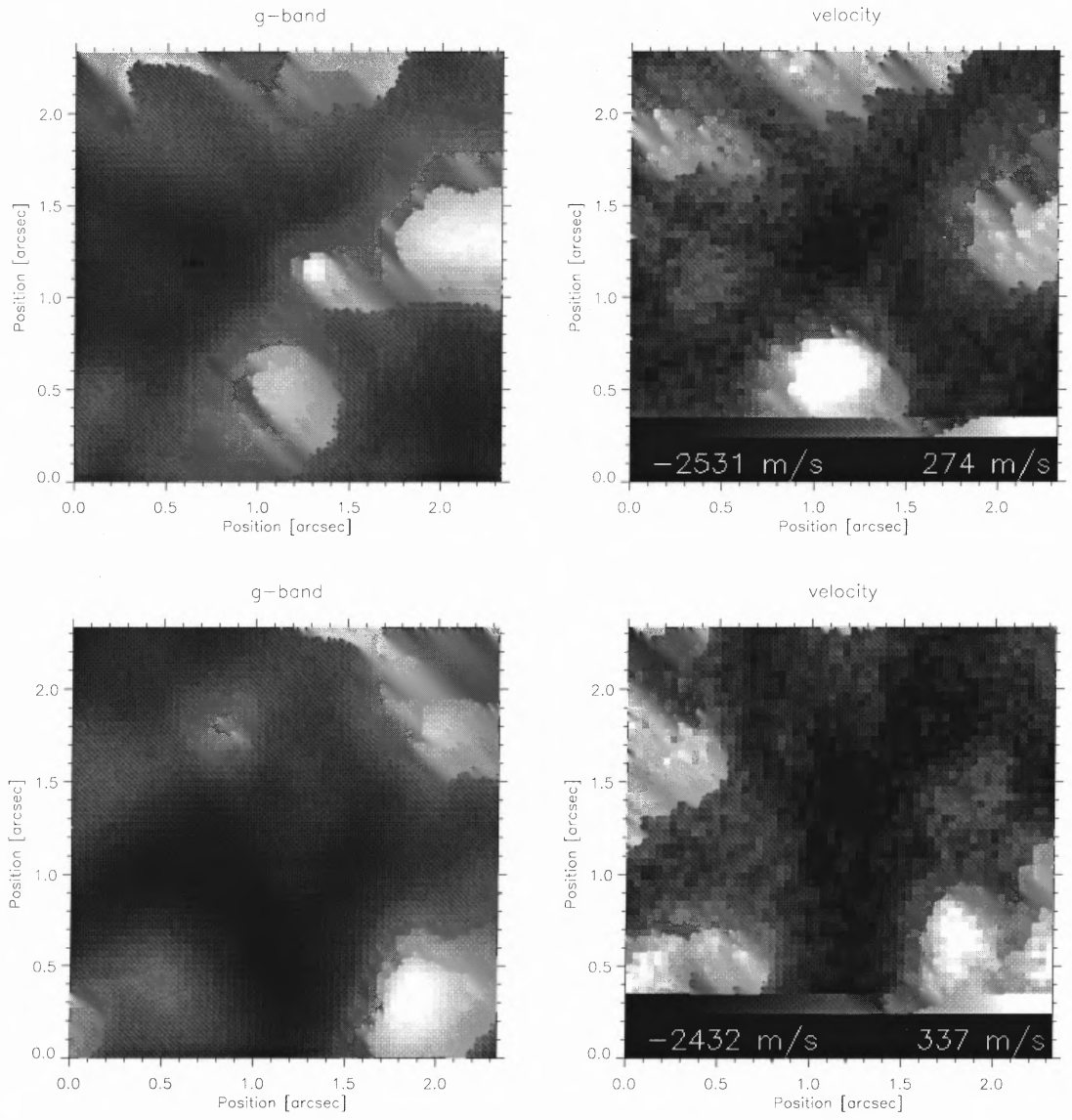

Figure 3.50 Comparison of velocity measurements of bright points in the line C I 5380 Å (bottom). Left is the intensity, right is the velocity. The top image is the bottom image of Figure 3.49. The right images demonstrate that the down-flow at the location of the bright point in the left image is just a coincidence.

the Fe I 5576 Å line. This indicates that atmospheric conditions in a height of 160 km above the photosphere influence the G-band CH-lines less than the atmospheric conditions in a height of 320 km above the photosphere.
The C I 5380 Å line has quite different properties than the Fe I 5576 Å line. It is magnetic and it is more temperature sensitive. Nevertheless we find almost no correlation between the residual intensity of the C I 5380 Å line. We conclude that the G-band CH lines are not sensitive to the physical conditions in the solar atmosphere in height of about 40 km above the photosphere. The combination of these results imply that the G-band has a larger contribution from atmospheric heights around 320 km, but little contribution from atmospheric heights of 40 km and 160 km above the photosphere. This in in disagreement to Steiner who predicts a formation height of the G-band with a maximum contribution at 160 km.

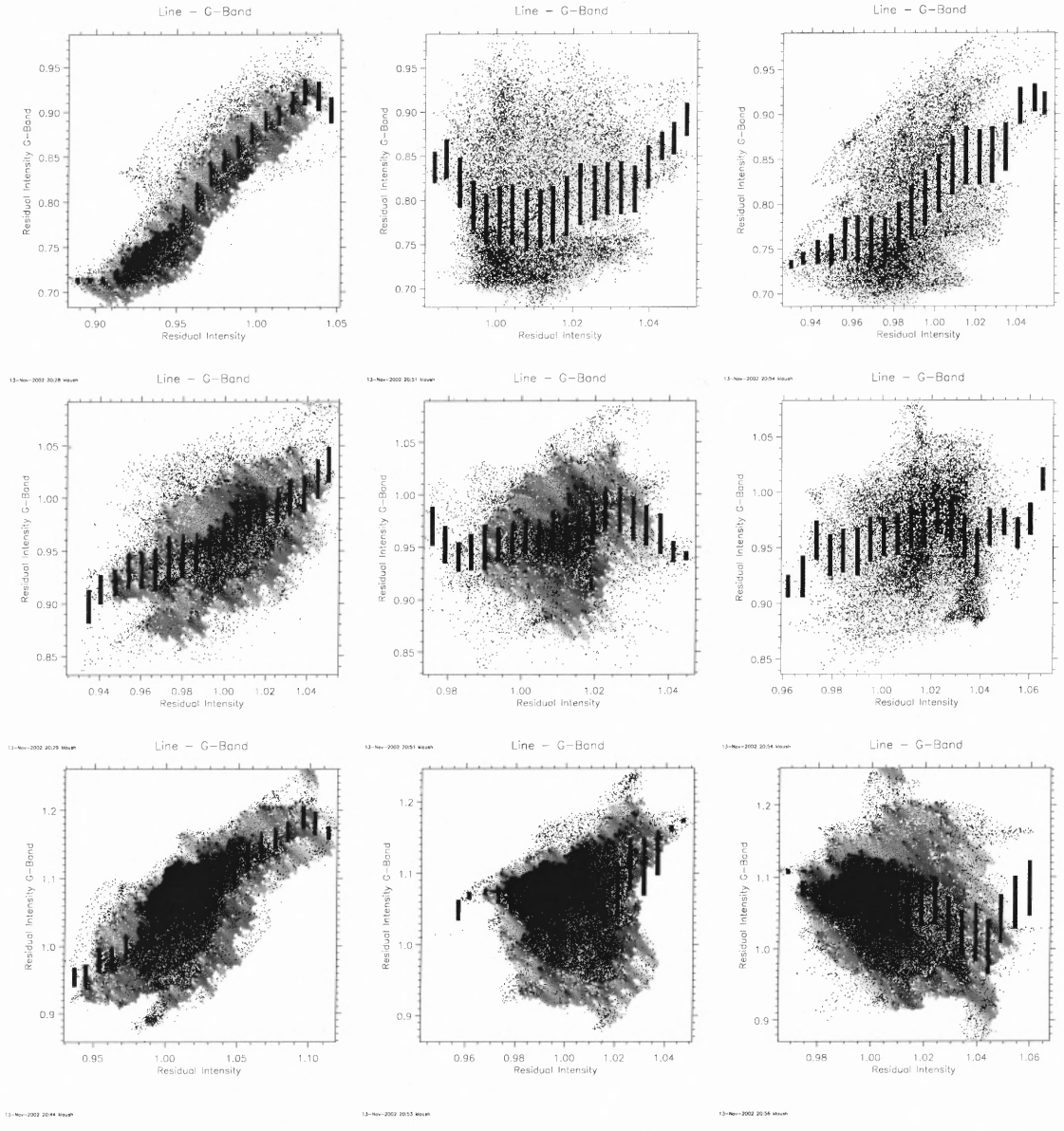

Figure 3.51 Residual intensity of the atomic spectral lines vs the G-band residual intensity. Top row is for the umbra, middle is for the penumbra and the bottom row is for the quiet sun. The line from left to right are 5576 Å , 5691 Å and 5380 Å . This plot shows a strong correlation between the G-band and the Fe I 5576 Å line. We find no other significant correlations. The correlation with the C I 5380 Å line is not very reliable in the umbra. This confirms the previous measurements of residual intensity that indicate that the G-band has significant contribution from atmospheric layers higher above the photospheric level $\tau = 1$.

3.2.5 Summary

- Umbra
  - General appearance of the umbra

    The umbra is a non-uniform structure. It shows intensity, residual intensity and velocity variations. We find a negative correlation between intensity, residual intensity and G-band residual intensity and velocity. This correlation is to be expected for umbral oscillations and has been observed before [1].
  - Umbral dots

    Our measurements show that umbral dots consist of three different types:
    * Penetrating penumbral grains

      Some umbral dots located at the outer border of the umbra have numerous properties in common with penumbral grains. Their appearance in brightness, velocity and residual intensity images closely resemble penumbral grains. We suspect, that these 'umbral' dots are penumbral grains that have penetrated the umbra. This result has implications on the plasma flow for 'real' umbral dots which are described below.
    * Larger-scale intensity-variations

      There is a general dark-bright variation in the umbra of a scale of one to three arcsec and a velocity pattern of the same dimension. This pattern is most likely the signature of umbral oscillations. We discuss this pattern here, since the brighter areas are selected as umbral dots. We find an increase in the rms variation of the velocity with increasing intensity that is mostly due to the larger structures. We also find a negative correlation between intensity and velocity for the Fe I 5691 Å line. Unfortunately, we are not able to give an interpretation since we lack the proper data, e.g. a long enough time series for frequency studies, to draw further conclusions.
    * Distinct umbral dots

      Some of the more distinct and localized umbral dots show strong down-flows of up to 300 m/s. This motion occurs, within the resolution- limit, at the same location as the umbral dot. The existence of bright structures in the umbra associated with down-flows is a fundamentally new result and disagrees with the predictions of Choudhuri [12] who predicts an up-flow at the locations of umbral dots if they are field-free regions.

- Relation to previous studies

  Previous studies of the umbra have found two different types of umbral dots (Sobotka [56], [57], Grossmann-Doerth [21], Schmidt [53], Tritschler [67]). Except for Sobotka [56], [57] all studies divided umbral dots into central and periphal ones. We find the separation of umbral dots by their intensity to be better than the separation by their position in the sunspot.

  The superiority of the intensity separation is also related to the existence of penumbral grains that are identified as umbral dots. Sobotka [56], [57] suspected from the appearance in the white-light images that some of the outer umbral dots were penetrating penumbral grains. Our study, using high-resolution pictures, dopplergrams and residual intensity pictures, confirms, that some bright umbral dots at the border of the umbra are penetrating penumbral grains.

  Our measurements do not agree with previous results about the velocity of umbral dots, since we measure down-flows at all inner umbral dots while all existing measurements yield up-flows (Kneer [28], Rimmele [46]) or velocities compatible with 0 m/s (Wiehr [73], Schmidt [53]). This may be due to the fact that the resolution in this study is two to three times higher than the resolution of previous studies, which leads to an increase in sensitivity of four to nine times since the size of umbral dots is probably below the resolution limit of current solar telescopes.

- Implications of our results

  * Penetrating penumbral grains

    Penetrating penumbral grains, as observed by Sobotka [58], were brighter than most umbral dots after entering the umbra. They stopped moving towards the center of the umbra and therefore occurred only at the outer boundary of umbra-penumbra. Sobotka [56] showed a clear correlation between the position of umbral dots, their brightness and their lifetime with the result that bright, periphal umbral dots had a short lifetime. These penetrating penumbral grains are still up-flows, as shown here for the first time. This leads the following interpretation: penumbral grains penetrate the umbra (Sobotka [58]) and still show a significant up-flow in the beginning. They are brighter than the average umbral dots (our result). However, brighter umbral dots at the border of the penumbra are short-lived (Sobotka [58]). Additionally, we find no significant up-flows in the inner part of the umbra.

    A possible interpretation is that the material up-flow of penetrating penumbral grains is stopped soon by the stronger magnetic field in the umbra which suppresses any horizontal motion. This explains the

short life time of penetrating penumbral grains. If this interpretation is correct, it falsifies theories of umbral dots that suggested some sort of convectional up-flow, because even a strong initial up-flow is stopped soon by the magnetic field of the umbra. This may not apply to the model of Weiss [29], since it predicts larger convection patterns.

* Relation umbral dots - penumbral grains
  Choudhuri [12] proposed that umbral dots and penumbral grains are of the same nature. He assumes both features to be up-flows of solar plasma in field-free regions. However, we find that umbral dots do not show up-flows at all, while penumbral grains, at least their inner parts, are up-flows of several hundred m/s. Moreover, there is evidence that an initial upward motion within the umbra is stopped. All these results prove that umbral dots and penumbral grains have different properties and can therefore not be two representations of the same physical process. This is not in agreement with Choudhuri [12].
* Small, localized umbral dots
  The 'real' umbral dots, which occur mainly in the center of the umbra, consist of distinct dots with associated down-flows and a larger underlying intensity-velocity pattern due to umbral oscillations. The down-flows at the localized umbral dots cannot not be associated with field free regions since field-free would produce small up-flows Choudhuri [12]. One explanation might be that the inverse Evershed-effect shocks in the umbra at the height of the photosphere and thus producing brightenings However, there is no convincing explanation for this type of umbral dots yet.

– Down-flows at the umbra-quiet sun border

  We find strong down-flows at the umbra-quiet sun border of up to $-854m/s$ for the 5576 Å Fe I line and $-1104\ m/s$ for the 5691 Å Fe I line. Their origin is unknown, but one possibility might be that hot plasma radiatively cools at the edge of the umbra since the density and temperature are much lower in the umbra. The cooler plasma has a higher density and moves downwards. If this interpretation is correct, it may be possible the determine some properties of the different atmospheres by the rate of the cooling.

- Penumbra

  - Penumbral Grains

    Our measurements show that penumbral grains are up-flows if it is possible to identify the penumbral grain by its shape in the intensity picture. This shape is a distinct brightening at the inner end of a bright filament.

    In general, we only find a weak correlation between intensity and velocity in the penumbra. This is in agreement with Hirzberger [24], but in disagreement to Schlichenmaier [54].

    We also checked for height-effects by comparing the white-light image, the G-band image and the line-core image. However, we could not detect any shifts in the position of bright filaments for either height.

  - Down-flows at the Penumbra-Quiet Sun Border

    These down-flows have been found also by Hirzberger [24]. Schlichenmaier [54] found a downward motion at the penumbra-quiet sun border although he did not state a velocity-value. These down-flows are probably due to the Evershed effect which may turn downwards into the photosphere at the edge of the penumbra. We find no clear correlation between velocity and the brightness of the endpoints of filaments. Therefore we cannot answer the question whether the bright or the dark filaments are responsible for the Evershed-effect.

- Bright Points

  We measure the velocity of a few individual bright points in the lines Fe I 5576 Å, Fe I 5691 Å and C I 5380 Å but we find no velocity difference between the bright points and the surrounding plasma. We do not detect a specific velocity signature of bright points with size larger than 0.2 arcsec and more then 100 m/s. This is contradictory to the model of Steiner [64] [65] who predicts significant down-flows during the formation of bright points and down-flows at the borders of bright points during their existence. We cannot check the behavior during the formation of bright points since we do not have a time series, but since we do not find plasma motion at all, this is strong evidence against the model of Steiner [64] [65]. However, some words of caution are in order: we only have a very small sample of bright points which means that we cannot perform any statistical studies. Since we do not have a time-series, we cannot observe the formation process of a bright points and therefore cannot check for the initial down-flow predicted by Steiner. Furthermore, we use two spectral lines for our investigations that form high in the photosphere where the predicted velocity is already greatly reduced. The only line close to the photosphere, the C I 5380 Å line, is also the line with the largest measurement

uncertainty since it is the weakest one (which is inevitably for any line forming close to the photospheric level 0 km).

- G-Band

  There is a strong correlation between the G-band and residual intensity of the Fe I 5576 Å line and only a weak correlation between the G-band and residual intensity of the Fe I 5691 Å line. Both lines are similar since they are non-magnetic and relatively temperature insensitive. The only difference is their formation height. We only found a weak correlation with the low forming C I 5380 Å line, especially if we take the large contribution from the continuum to the G-band into account. This is strong evidence that the G-band has a large contribution from a height of about 320 km above photospheric level $\tau = 1$ for the quiet sun, the umbra and the penumbra. There is a smaller contribution from a height 160 km above the photosphere and almost no contribution from a height of 40 km above the photosphere. This is not in agreement with the predictions of Steiner [63], who proposes a formation height of the G-band with a maximum contribution at a height of 160 km while we find a larger contribution from higher layers. Our results are also in disagreement to the prediction of the formation height by Sanchez-Almeida [50], since he predicts the formation height to be at an atmospheric level of 40 km *below* the photosphere.

3.3 Spectroscopic Observation of Umbral Dots and Penumbral Grains

3.3.1 Motivation

Spectra recorded with a spectrograph contain more detailed information about the profiles of spectral lines than observations conducted with the UBF since they measure about 20 wavelength points for a solar line instead of two. The disadvantage is the difficulty in the identification of solar structures from the one-dimensional spatial information. This limited spatial information lowers the number of measurement points for each solar structure and therefore the accuracy of the statistical analysis.

On the other hand, a spectrograph obtains all spectral information simultaneously which automatically eliminates the effects of differential seeing. This is not only true for one spectral line but also for widely separated wavelength regions. This simultaneity is not possible with the UBF even in the dual mode. The spectrograph also has the highest spectral resolution, about five to ten mÅ in this wavelength region vs 160 mÅ for the UBF. This is the reason why the spectrograph is the ideal instrument to perform quantitative spectral analysis like line profile and line asymmetry studies. We use the spectrograph as a tool that is complementary to the UBF.

We took high resolution spectra in the wavelength regions 5576 Å , 5691 Å and 5380 Å . This regions cover all spectral lines investigated with the UBF and provide the possibility to verify the results of the UBF investigations conducted in the previous Chapters. We look for the velocity pattern and the small localized downdraft within the umbra and we investigate the plasma motion of penumbral grains and bright and dark filaments in general.

3.3.2 General Information about the Observations

We observed at the Dunn Solar Telescope (DST) from February 8 2002 until February 15 2002. The day with the best seeing was February 14. We used the Horizontal Spectrograph (HSG) of the DST with the 316 lines/mm grating in place. The grating is used in the tenth order because of the blaze angle of 63° 26' (Ch. 2.3.1). The illuminated area on the grating has a diameter of about 83 mm. This yields a theoretical resolution of 263333 $\frac{\lambda}{\Delta\lambda}$, which is equivalent to a resolution of 23 mÅ at 550 nm. This represents an improvement of seven compared to the UBF at this wavelength region. We used a slit of 25 micron width which translates to spatial width of 0.187 arcsec. We performed scans with a step-width of 0.077 arcsec and 12 steps per scan. This covers a spatial regions of 0.92 arcsec which is sufficient to scan across bright points and umbral dots. However, the seeing conditions allowed only for a resolution of 0.5 arcsec or less. The slit was oriented in North-South direction to ensure that differential refraction moves the image along the slit.

We observed three different spectral regions simultaneously. The region around the wavelength 5576 Å was observed in the tenth order which yields a dispersion of 1.771 mm/Å. We used a SI 1kx1k CCD camera to record the spectra. The image scale was 6.93 mÅ/pixel in the spectral direction and 0.075 arcsec/pixel in the spatial direction. This matches the spatial and spectral resolution of the instrument by dividing one resolution element into an area of 3x3 pixels. The spectral region covered was 7.09 Å and the spatial region covered is 77 arcsec.
The region around the wavelength 5691 Å was observed in the tenth order as well which gives a dispersion of 2.009 mm/Å. We used the second available 1kx1k SI CCD camera to record the spectra. The image scale was 5.68 mÅ/pixel in the spectral direction and 0.083 arcsec/pixel in the spatial direction. The spectral region covered was 5.73 Å and the spatial region covered was 85 arcsec.
The region around the wavelength 5380 and 5381 Å was observed in the tenth order as well which yields a dispersion of 1.525 mm?Å. We used a Xedar 2kx2k CCD camera to record the spectra. This camera was binned in a 2x2 pixel mode. The image scale was 8.27 mÅ/pixel in the spectral direction and 0.075 arcsec/pixel in the spatial direction. The spectral region covered was 8.47 Å and the spatial region covered was 77 arcsec.

In addition to the spectral images, we used the reflection off the slit and re-imaged it into a Kodak 1kx1k CCD camera placed behind a 100 Å wide interference filter centered at 550 nm. The images from this camera enable us to determine the position of the spectrograph slit on the solar surface. Since we want to know the intensity within the slit, we divert light in wavelength region from 420nm to 440 nm, i.e. covering the G-band, using a G-band reflector before it reaches the spectrograph slit. We send the light of this wavelength region to another Kodak 1kx1k CCD camera which is placed behind an interference filter centered at 4305 Å (G-band) with a width of 10 Å. We measure the slit position in the slit-jaw image and transfer the slit position to the slit-less image as described in Chapter 3.3.3. This yields the intensities in the G-band on the slit. The whole setup is shown in Figure 3.52.

We observed the active region 9825 which contained a medium-size, round sunspot located at 14 N and 10 E. Thus, the region is 17.2 degrees off disc center and therefore 29 percent of the horizontal velocity and 95 percent of the vertical velocity contribute to the line of sight velocity.
We observed the sunspot for two hours and 40 minutes before the deteriorating seeing conditions made further observations impossible. During this time we recorded 171 scans with 13 steps each. It took about one minute to record one complete scan. Calibration data such as target, flat-field and dark images were recorded at the end of the observation sequence. The exposure time was 1500 ms for all images and we used the AO system of the DST as described in Chapter 2.2.4.

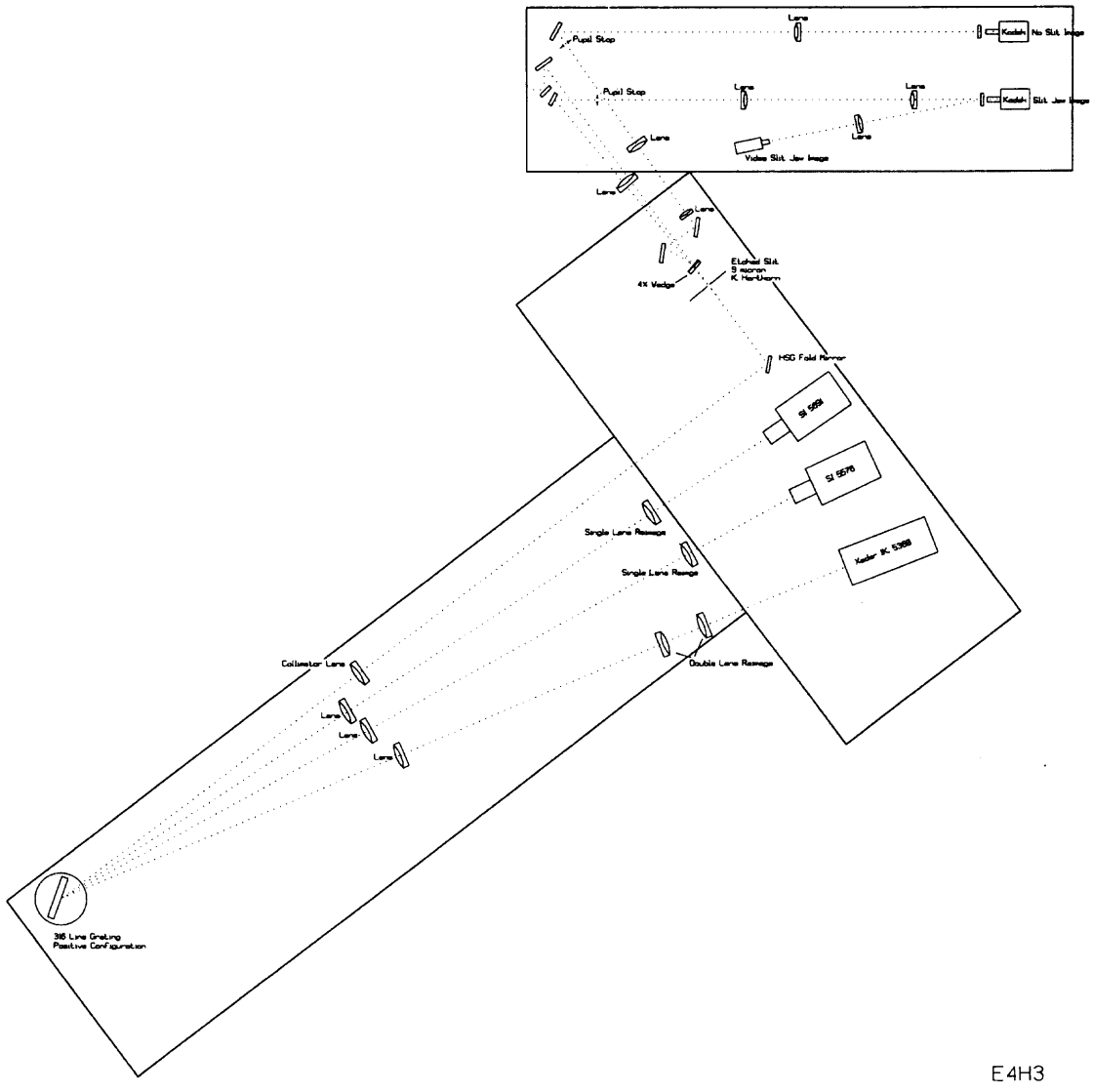

Figure 3.52 Drawing of the spectrograph setup. After passing a four percent reflector which sends part of the light to a CCD camera to record an image of the investigated solar region without a slit (slit-less image), the light is directed onto the spectrograph slit. The spectrograph slit reflects the light not passing through the slit back onto another camera that records the image with the slit (slit-jaw image). The light passing through the spectrograph slit is collimated onto the grating, where it is reflected at different angles for different wavelength. The spectral regions of interest are imaged onto the separate CCD cameras to record the solar spectral lines.

3.3.3 Data Reduction

3.3.3.1 Flat-Field and Reference Spectra The slit-less images and the slit-jaw images are flat-fielded and dark-corrected in the usual way. We determined the image-scale, rotation and coarse translation between the two images using target-images. We performed a fine alignment for each image-pair using a Fourier correlation to determine the individual shift. This was necessary since the two images were always slightly shifted due to table vibrations. The image-scale and the rotation angle are not affected by these vibrations. Once the images were aligned, we determined the slit-position in the slit-jaw image. For further analysis, we only use the slit-less image and add an artificial slit as needed.

The processing of spectra is more complicated than the processing of two-dimensional images. The generation of a flat-field is difficult, because we have to remove the spectral lines in the flat-field images before averaging the flat-field images. The flat-field images are generated by moving the solar surface during the exposure. This removes the spatial information of the image but not the spectral information, i.e. the spectral lines are still present in the flat-field image (Fig. 3.53). The spectral lines have to be removed from the final flat-field since the would eliminate the spectral lines in the images which contain all the physical information. We tried to use a lamp as an alternative light-source without spectral lines, but the image-illumination is very sensitive to the incident angle. This leads to a different illumination of the flat-field which makes the lamp flat-field unusable. This problem led to the development of a different approach to remove the spectral lines from the flat-field.

- Determination of the gradient

  We remove the gradient by fitting a parabola to each horizontal line of the spectra. For each line, we find the maximum of the fitted parabola and the original spectral profiles pixel by pixel. We replace the intensity of the original spectral profile with the maximum $I_{new} = max(I_{old}, I_{fit})$ for each pixel. This procedure raises the lowest intensity in the line-core of the spectral lines to the level of the first order fit. Yet, the overall fit represents an underestimation due to the influence of the spectral lines. Therefore, we repeat the fit once more with the first order fit. This process eliminates the underestimation as a result of the spectral lines.

  We obtain an image, where each line represents the best fit parabola to the continuum of the spectral profile. We smooth this image by using a 50x50 pixel averaging algorithm. This mostly preserves the parabola fit since the image is 1024 pixels wide, but eliminates the vertical irregularities the come from an uneven slit. We have to preserve these irregularities for the flat-field and so we have to remove them in the gradient image. The result is shown in Figure 3.54.

- Generating a reference line profile

The flat-field image is divided by the gradient image leaving only the spectral lines with an even level continuum. It is important to use an even level continuum because we average over all horizontal lines to obtain an average spectral profile. We choose a horizontal line in the continuum as the reference line and correlate each horizontal line with this reference line. This yields the shift of each line in respect to the reference line which is a result of the spectrograph. We perform these shifts and average over all lines. The result is the average spectral line profiles of the image.

- Generating reference spectra

  We correlate the reference line profile with each horizontal line of the flat-field image, because spectral lines are curved in a spectrograph. We shift the reference spectral profile accordingly and form the reference spectra in which each line is the shifted reference spectral profile. Since we average over many points on the solar surface, the reference spectra have the line positions of velocity zero. The reference spectra will be used to determine velocities and line-width. The reference spectra for the Fe I 5576 Å line is shown in figure 3.55.

  The original flat-field image is divided by the reference spectra which eliminates the the spectral lines and leaves the flat-field image with the gradient, slit imperfections and dust on the CCD chip. All flat-field images of sequence are averaged to obtain the final flat field (Fig. 3.56).

3.3.3.2 Calculation of Physical Information We identify spectral lines as connected regions of pixels with an intensity less than 90 percent of the continuum in the reference spectra image. We determine the preliminary line center as the pixel with the lowest intensity of the spectral line. We use the information about the center-wavelength of two spectral lines for each spectral region to determine the center wavelength of all other spectral lines and calculate the spectral scale in mÅ/pixel.
For a specific spectral line we determine the continuum intensity along the slit by determining the highest intensity of each horizontal line in the whole spectral region the spectral line is located.
We determine the core intensity of a line by picking the minimum intensity of each (spatial) line for a part of the spectra with a width of 100 pixels around the estimated center-pixel which corresponds to a spectral range of 700 mÅ. We use the minimum pixel instead of the pixel determined as the line core position since this eliminates the effect of the line shift resulting from velocity. The residual intensity is formed by dividing the line-core intensity by the continuum intensity.

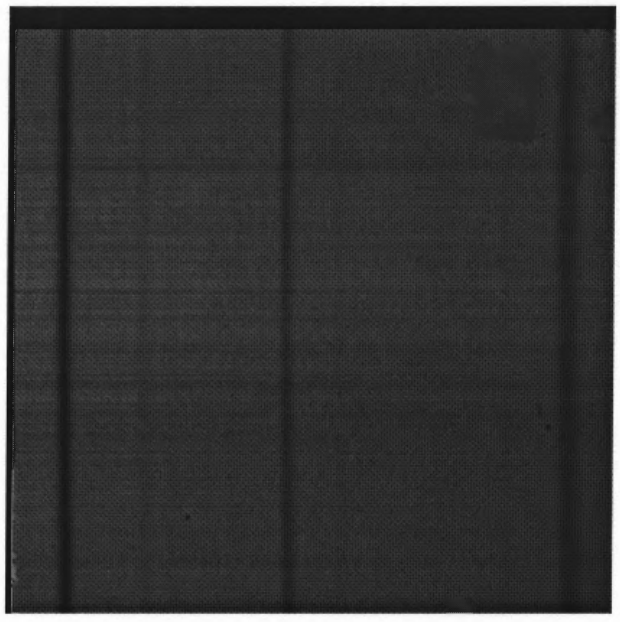

Figure 3.53 Unprocessed flat-field image of the Fe I 5576 Å line region. The Fe I 5576 Å line itself is the strong line on the right side of the image.

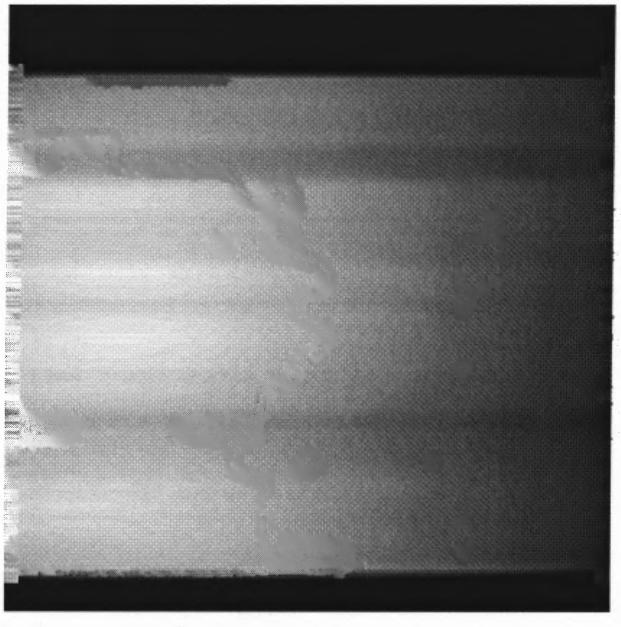

Figure 3.54 Gradient of the flat-field images of the Fe I 5576 Å line that is removed before determining and removing the average line profile. The gradient has to be removed in order to obtain an even-level continuum for the fitting procedures.

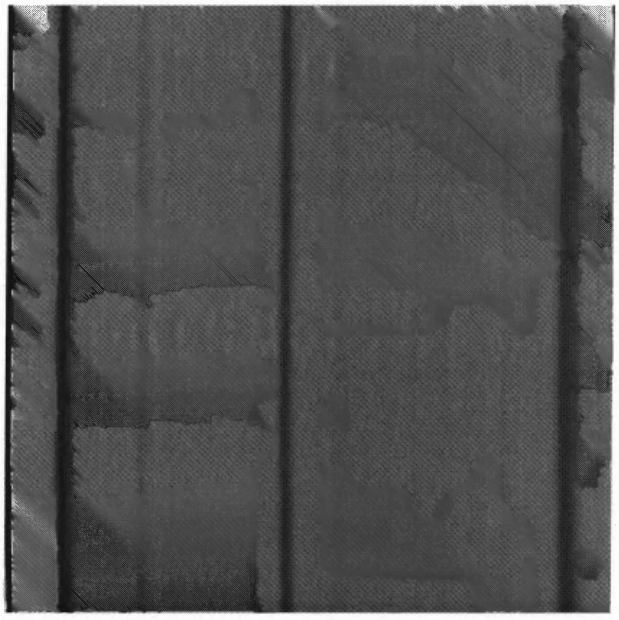

Figure 3.55 Reference spectra of the Fe I 5576 Å line. Each line contains the reference spectral profile that is shifted accordingly to the zero velocity position determined by the flat field.

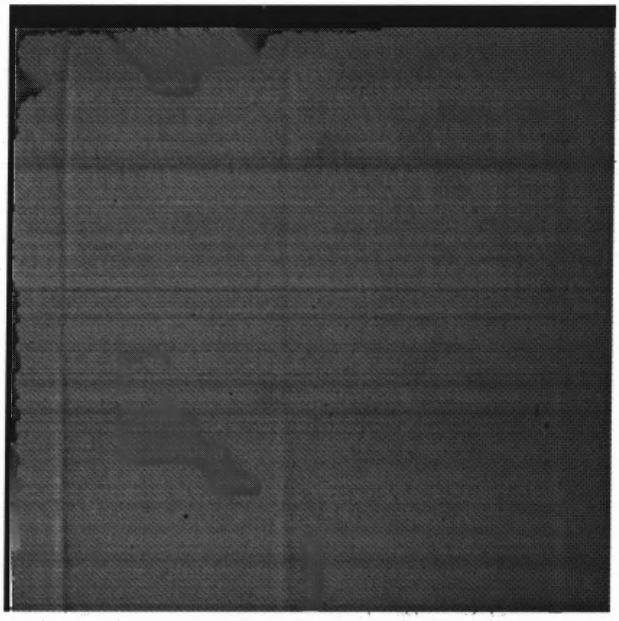

Figure 3.56 Final flat-field for the 5576 Å line. The spectral lines have been removed although some artifacts remain. Also, the small-scale gradient are present in the image.

We determine the velocity from a slice around the line-center with a width of 100 pixels of the measured line and the reference spectra which represents the zero-velocity position of the line. We correlate these two slices for each horizontal line and determine the shift in pixels which we convert into velocity. This measured velocity is an average velocity over the height range from the formation height of the line core to the continuum since the whole spectral line covers that height region.

3.3.3.3 Measurement Errors We determined the errors for the physical quantities by removing all fluctuations of the physical value larger than 0.07 arcsec with the Fourier decomposition leaving only the noise in the image. We determine the rms variation of the noise and take it as the measurement uncertainty of the specific physical value.
We found the velocity errors to be 20 m/s, 21 m/s, 187 m/s and 540 m/s for the lines Fe I 5576 Å , Fe I 5691 Å , Ti II 5380 Å and C I 5381 Å . For the measurement error of the residual intensity where we find the errors to be 0.0045, 0.0072 0.059 and 0.096 respectively.
The measurement error of the Ti II 5380 Å and C I 5381 Å line is much higher than the measurement error of the Fe I 5576 Å and Fe I 5691 Å line. This behavior can be explained by the fact that the noise in the Xedar camera was higher than in the SI-cameras. Furthermore, the Xedar camera has much a lower quantum efficiency. We set the exposure time to 1500 ms using the SI-cameras. For the 5576 Å line this yields a background noise (in the dark image) of 548 ± 4 counts while the (already dark corrected) image has an intensity of about 510 counts in the line core in the umbra. This yields a signal to noise ratio of 510:4 = 127.5:1. For the spectral region containing the Ti II 5380 Å and C I 5381 Å lines we measure a background noise (in the dark image) of 93 ± 20 counts while the (already dark corrected) image has an intensity of about 80 counts in the line core in the umbra for both lines. This yields a signal to noise ratio of 80:20 = 1:4. Due to the low signal to noise ratio, we decided not include the Ti II 5380 Å and C I 5381 Å line in this analysis.
The FWHM of the smallest structure that we can detect in the slit-less images is 0.6 arcsec. Therefore, we reach a limit of detection of $7.2 \frac{m}{s} \cdot arcsec^2$ and $7.6 \frac{m}{s} \cdot arcsec^2$ for the velocities of the Fe I 5576 Å and Fe I 5691 Å line and $1.6 \cdot 10^{-3} \cdot arcsec^2$ and $2.6 \cdot 10^{-3} \cdot arcsec^2$ for the residual intensity of the Fe I 5576 Å and Fe I 5691 Å line.
This should be compared to the a limit of detection $ld = 0.6 \frac{m}{s} \cdot arcsec^2$ for the 5576 Å line and $3.8 \frac{m}{s} \cdot arcsec^2$ for the 5691 Å line for the UBF dopplergram run and the limit of detection is ld=$1.25 \cdot 10^{-4}$ for both lines in the residual intensity run. The better limit of detection for the two UBF runs is mainly a result of the resolution which is a factor three higher for the dopplergram run, and a factor four higher for the residual intensity run. This lowers the limit of detection by a factor nine and sixteen respectively. Another contribution for the limit of detection on

favor of the UBF is the better signal to noise ratio since more light passes the UBF. Unfortunately, these numbers indicate that the spectrograph observations will not significantly enhance our precious observations.

3.3.3.4 Selection of Solar Structures We use the continuum intensity of the specific line we investigate for the selection process. This ensures that image shifts do not influence the measurements. The selection process follows the selection process of Chapter 3.2.3.2 as close as possible.

- Umbra

  We selected pixels in the continuum of the spectra that have less than 0.4 of the maximum continuum intensity as umbra.

- Penumbra

  We selected the penumbra as all pixels that have more than 0.4 of the maximum continuum intensity but less than 0.75 of the maximum continuum intensity. This process does not select bright penumbral grains. We therefore include all pixels not further away form an initially selected pixel than three arcsec *within* the original selected pixels. We remove pixels already found to belong to the umbra from this selection.

- Photosphere

  We select all pixels as photosphere that have more than 0.75 of the maximum continuum intensity and do not belong to the umbra or penumbra.

- Umbral Dots

  We perform a one-dimensional Fourier decomposition to remove all intensity variations larger than four arcsec. We select all pixels with a remaining (local) intensity larger as 0.0 as potential umbral dots. Only selected pixels that are actually inside the umbra are selected as umbral dots.

- Penumbral Grains

  The selection process for the penumbral grains is similar to the selection process of umbral dots. We perform a one-dimensional Fourier decomposition to remove all intensity variations larger than four arcsec. We select all pixels with a remaining (local) intensity larger as 0.0 as potential penumbral grains. Finally, every potential penumbral grain that is inside penumbra is selected.

3.3.4 Results

3.3.4.1 Total Field of View The first set of images (Fig 3.57) shows the slit-less images on the left side where the bottom image is contrast enhanced. On the right

side, the slit is superimposed onto the images. In the bottom, contrast enhanced image we can see that the slit is passing through several bright regions in the umbra (umbral dots) and penumbra (penumbral grains). These pictures are representative for the best scans we obtained.
The next set of plots (Fig. 3.58) shows the intensities for the whole length of the spectrograph slit. We can see the different behavior of the spectral lines in the umbra. The line Fe I 5576 Å is weaker in the umbra than in the quiet sun which can be seen by the higher residual intensity while the residual intensity of the Fe I 5691 Å line is unchanged. The velocity plots (Fig. 3.59) show the Evershed flow as the most prominent feature. The Evershed flow is a horizontal flow radially outward from the umbra and reaching velocities of up to six km/s. Since we observe the sunspot off disc-center and measure line-of-sight velocities, we observe a positive velocity on one side and negative velocity on the other side of the umbra. The positive velocity has its peak value at the location 22 arcsec and the negative velocity has its peak at the location 50 arcsec. We see the velocity signal of the solar granulation with the bright granules moving upwards and the intergranular lanes moving downwards. We find little motion in the umbra and the penumbra, which is in part due to the large velocity-scale necessary to include the Evershed flow. We will analyze the umbra and the penumbra by restricting the spatial range.

3.3.4.2 Umbra and Umbral Dots In this section we study in detail the spatial part of the spectra that contains the umbra. In the first set of plots (Fig. 3.60) we investigate the residual intensity of the different solar lines. In the lines Fe I 5576 Å and Fe I 5691 Å we can clearly see three umbral dots located at (4.5,6.0,7.0) arcsec and located at (6.0,7.5,9.0) arcsec respectively. The small difference in position is a result of spatial shift of the spectral regions relative to each other. We see the umbral dots in the residual intensity and find them to be negatively correlated with the intensity. However, we have to be careful with this interpretation. The light level in the line core and the umbra is very low and therefore the dynamic range is low. This may be the reason why it is hard to detect umbral dots in the core intensity at all (Fig. 3.60). If the measured core intensity is (almost) independent of the real core intensity due to instrumental reasons, the residual intensity will always be anti-correlated to the white-light intensity.

Plot 3.61 shows the same spatial part of the spectrum of the umbra as the previous plot 3.60. The solid line is the velocity and the dashed line is the continuum intensity with all structures larger than four arcsec removed and scaled to the maximum velocity value where we can see the three umbral dots. The velocity plots shows no correlation with the intensity plot. We do not measure any different velocity at the location of the umbral dots. This result compares to the findings of Chapter 3.2.4 in the following way. If we would scan across a small, localized umbral dot with a down-flow, we should be able to see it even though we have a lower spatial

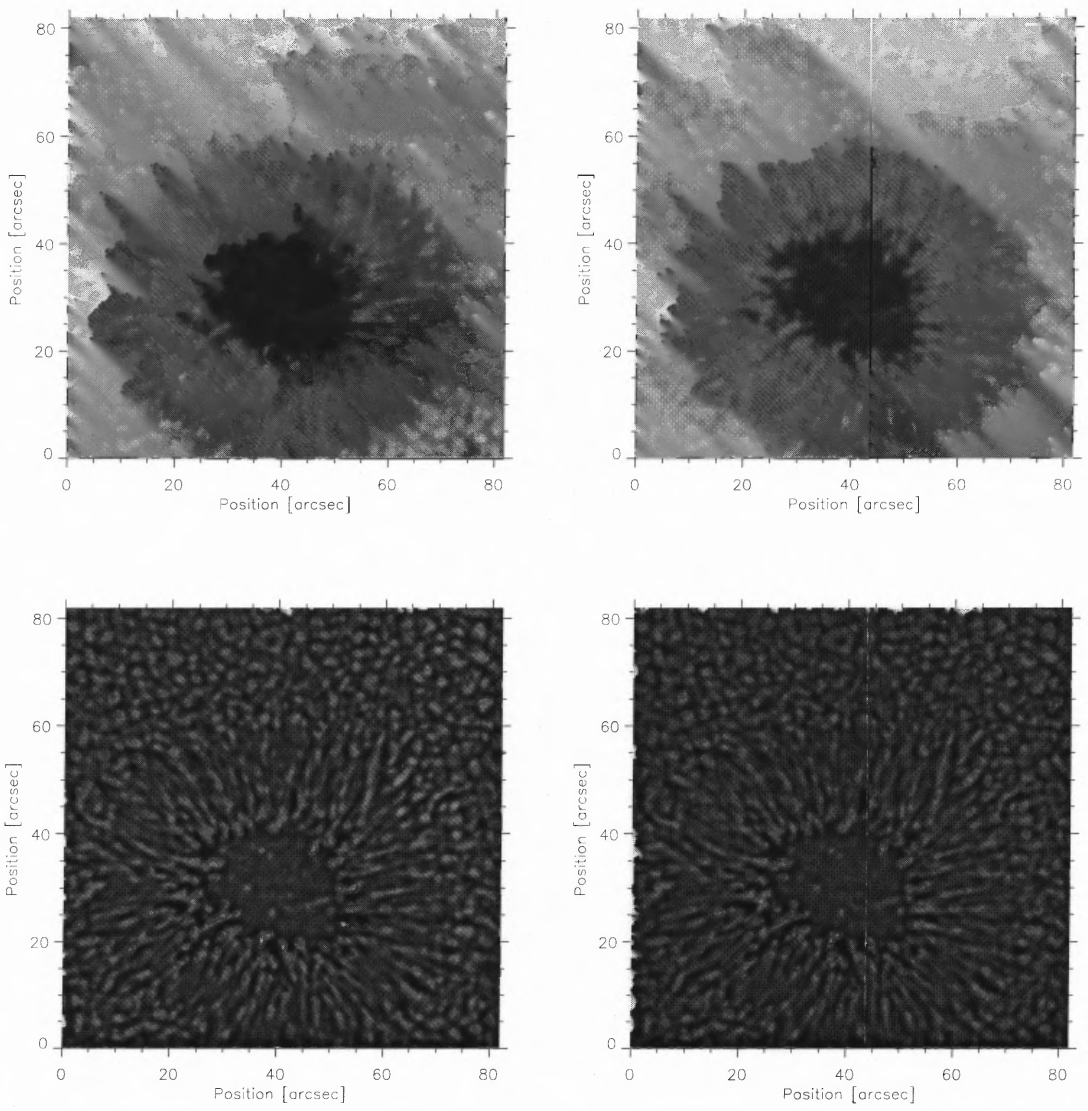

Figure 3.57 The field of view including the sunspot we investigate. The image top left is the slit-less image, the image top right is the image with the generated slit (slit-jaw image). The top row images are the contrast enhanced to allow the detection of umbral dots. The bottom left image is the slit-less image, the bottom right image is the slit-jaw image. In the bottom right image one can see the slit passing through some umbral dots.

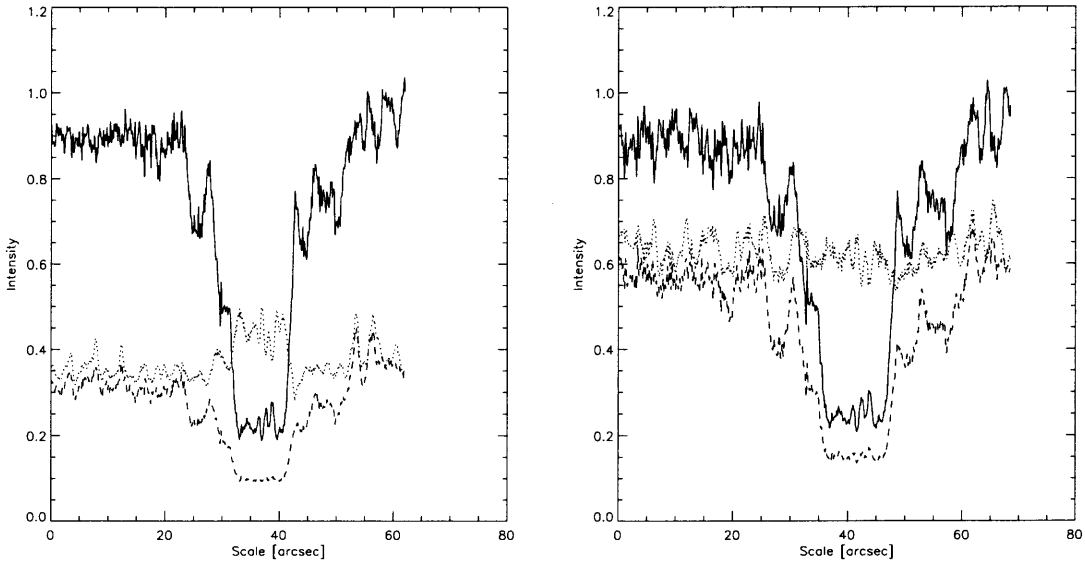

Figure 3.58 Intensity of the continuum (solid line), intensity of the line core (dashed line) and the residual intensity (dotted line) for the lines Fe I 5576 Å (left), Fe I 5691 Å (right).

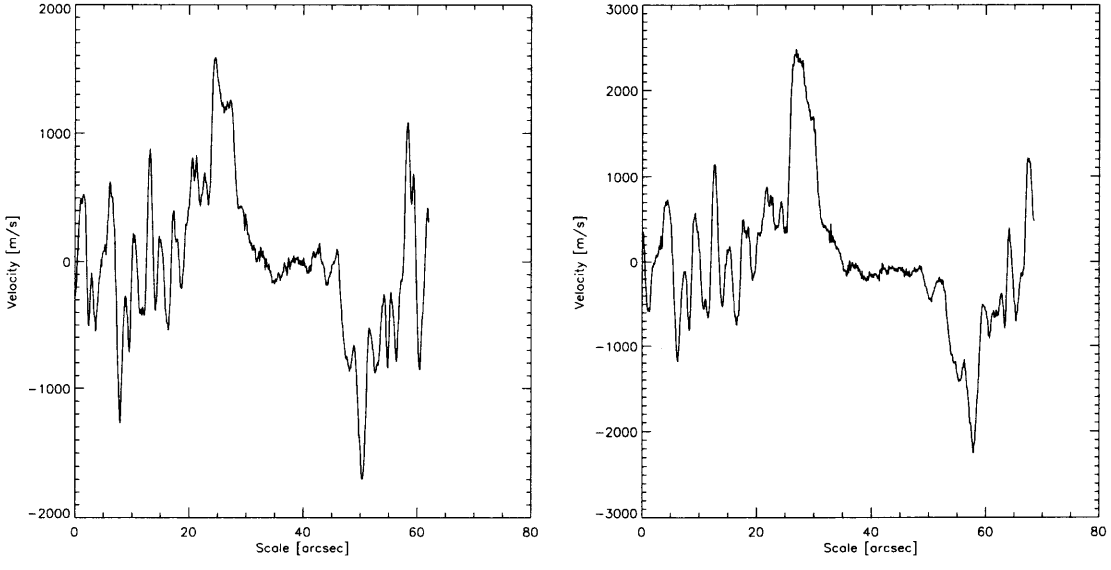

Figure 3.59 Velocity vs the spatial scale in arcsec for the lines Fe I 5576 Å (left), Fe I 5691 Å (right).

resolution. However, this type of umbral dot seems to be rare as we determined in Chapter 3.2.4 and we probably do not find an umbral dot of this kind in our scans. The much more common type of 'umbral dot', the umbral oscillations, does not show large down-flows and does not exhibit a correlation between intensity and velocity. This is consistent with our findings in Chapter 3.2.4.

We perform a statistical analysis of the spectra where we combine all twelve steps of a scan to gain statistical significance. Scatter plot 3.62 shows the relationship between the white- light intensity and the residual intensity for the investigated solar lines where we find a negative correlation. This negative correlation means that a bright structure in the umbra has a line core with a lower intensity, i.e the line is stronger. On the other hand we have to take the possibility of a low dynamic range of the observations into account, as we have discussed it above. Since we are not sure if the observations are significant, we refrain from an interpretation.
We find no correlation between the white-light intensity and the velocity (Fig. 3.63). This compares to the findings of Chapter 3.2.4 in the same we as stated above: we probably do not have one of the few small umbral dots in the field of view that is associated with strong down-flows. However, we do find velocities from -150 m/s to 150 m/s for the two Fe I lines which are a result of umbral oscillations which we already found in Chapter 3.2.4.1.
For a comparison, we include the scatter-plots for white-light intensity and the velocity (Fig. 3.64) where we only show the umbral dots. In these plots there are (obviously) fewer data-points, but the overall distribution is the same as for the scatter-plots of the whole umbra. This behavior is in agreement with the interpretation of the motion in the umbra as umbral oscillations.

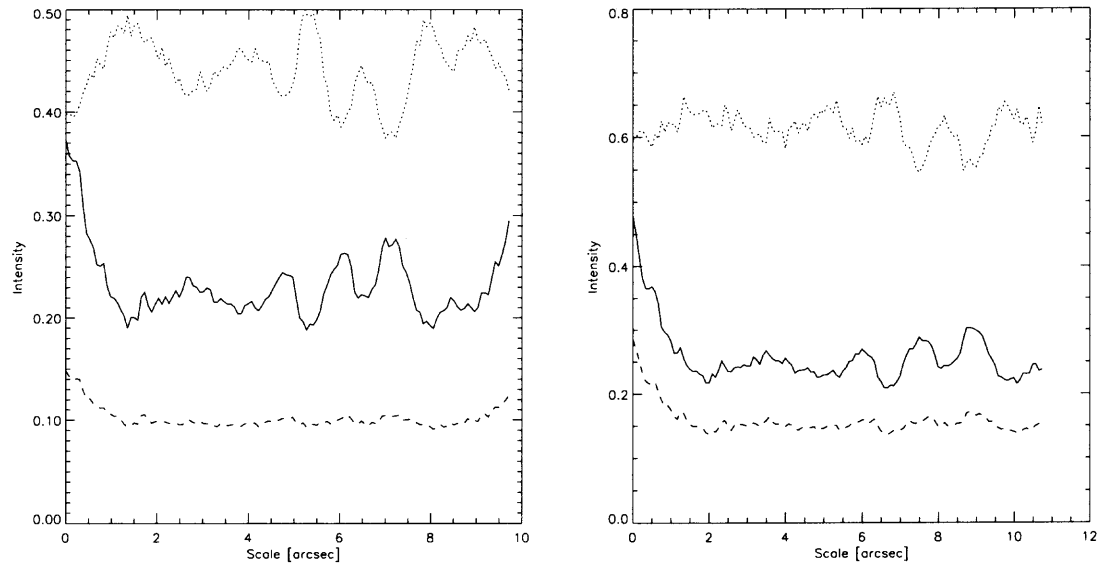

Figure 3.60 Closeup of the umbra for the intensity plot for the lines Fe I 5576 Å (left) and Fe I 5691 Å (right). Again, the intensity of the continuum is the solid line, the intensity of the line core is the dashed line and the residual intensity is the dotted line.

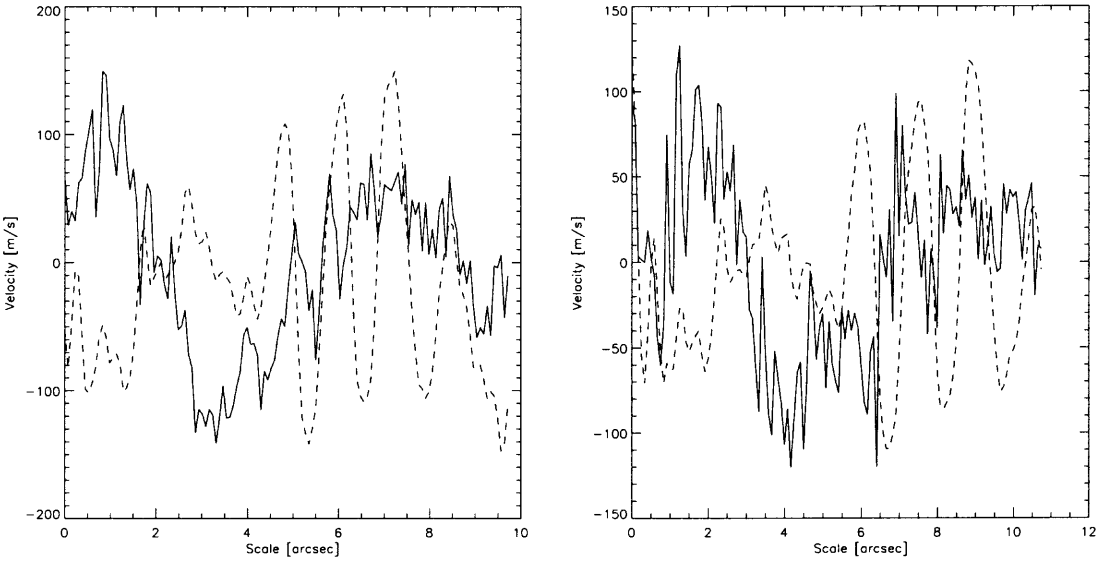

Figure 3.61 Closeup of the umbra for the velocity plot for the lines Fe I 5576 Å (left) and Fe I 5691 Å (right). The solid line is the velocity in m/s and the dashed line is the intensity after a wavelet transform that removes intensity variations larger than four arcsec.

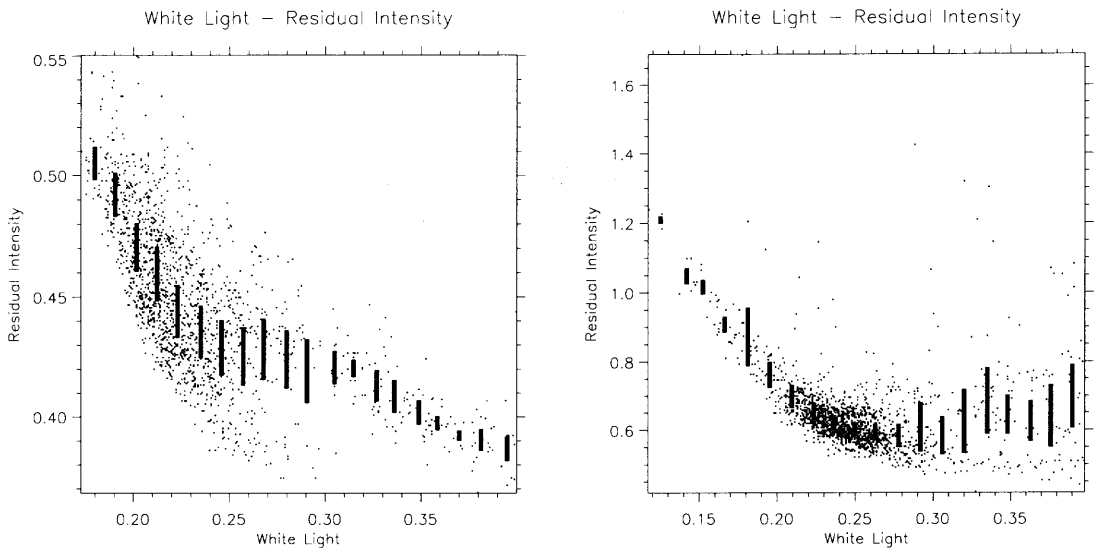

Figure 3.62 Residual intensity vs the white-length intensity for the lines Fe I 5576 Å (left) and Fe I 5691 Å (right).

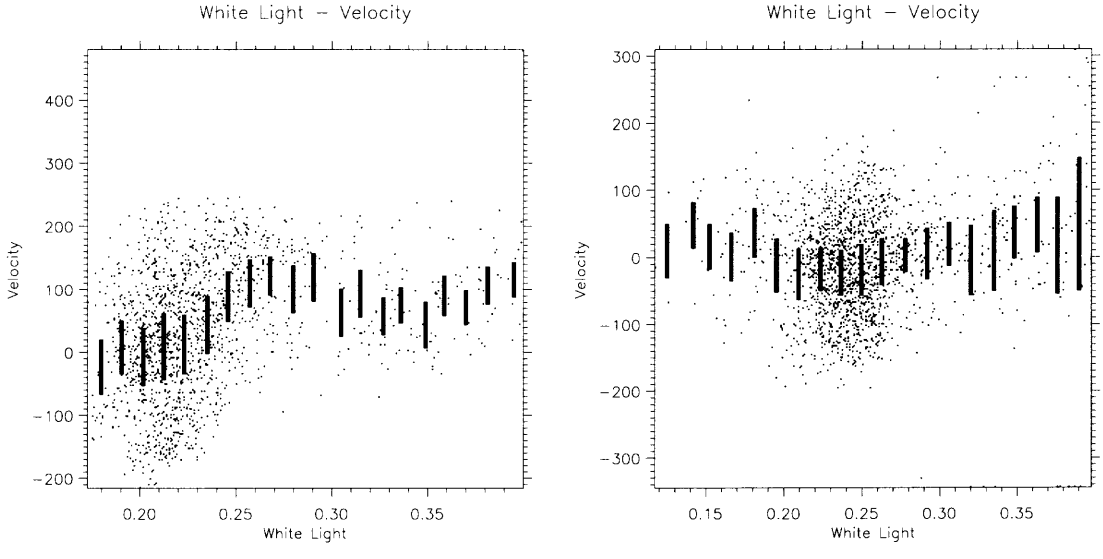

Figure 3.63 Velocity vs the white-light intensity for the lines Fe I 5576 Å (left) and Fe I 5691 Å (right) for the *whole umbra*.

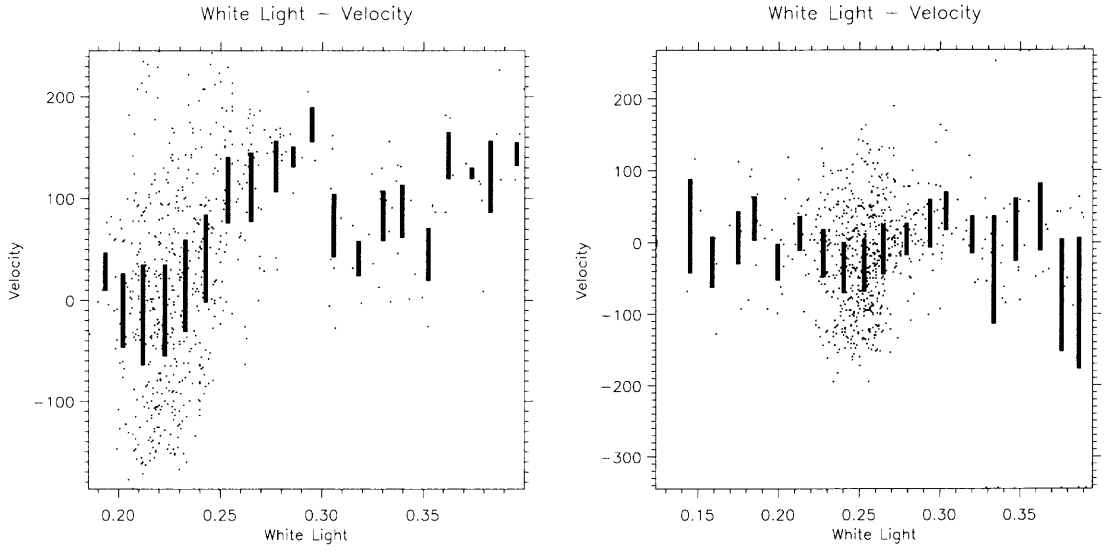

Figure 3.64 Velocity vs the white-light intensity for the lines Fe I 5576 Å (left) and Fe I 5691 Å (right) for the *umbral dots only.* We do not detect a significant change in distribution compared to the whole umbra which supports the view that the velocity is due to solar oscillations.

3.3.4.3 Penumbra and Penumbral Grains Plot 3.58 shows the intensities and residual intensities for the penumbra on one side of the sunspot only in the investigated spectral lines (top) as well as the corresponding velocities. We see a high velocity on both sides of the penumbra with opposite signs. This is the well known Evershed-effect, a radial outward flow in the penumbra that can reach several km/s. The inclination of the velocity field means that the velocity of the plasma is higher at the outer edge of the umbra than at the inner edge. This is also a known property of the Evershed-effect. A close-up of the penumbra can be seen in plot 3.65.
The scatter plot 3.66 shows the the white-light intensity vs the velocity for all pixels identified as penumbra. We see that the strength of the Evershed effect increases with decreasing formation height of the solar line used for the velocity measurement. We also can see the increase in the flow-velocity with intensity. This does not necessarily mean that bright filaments have a higher flow velocity, but is rather an effect of the increasing brightness of the penumbra towards the outer edge.
If we want to study local effects, we have to use local measurements. This is especially important here since the large velocities of the Evershed-effect, that contribute with 29 percent to the line of sight velocity, cover all possible smaller correlations between intensity and velocity. The result of the local analysis is shown in the scatter plot 3.66. In this plot, we removed all spatial variations larger than four arcsec from the intensity and velocity measurements. The general correlation between intensity and velocity is not very evident except for the positions 1.5 arcsec (left plot) and 3.75 arcsec (right plot) where we scan through a penumbral grain (Fig 3.57, lower section of the slit). This confirms our findings of Chapter 3.2.4 where we only find up-flows in the head of penumbral grains but little correlation otherwise.
A local analysis of the scatter-plot of local velocity vs local intensity on the same side of the penumbra (Fig. 3.68) reveals a positive correlation meaning bright structures have a line of sight velocity towards the observer. This is in agreement with Chapter 3.2.4. The first possibility is that bright structures move upwards. The second possibility is that bright structures have, even locally, a higher radial (horizontal) velocity. The third possibility is that the local analysis does not completely remove the global effect that the velocity of the Evershed-effect is increasing outwards. Our measurements do not provide the means to distinguish between the possibilities with a high certainty.

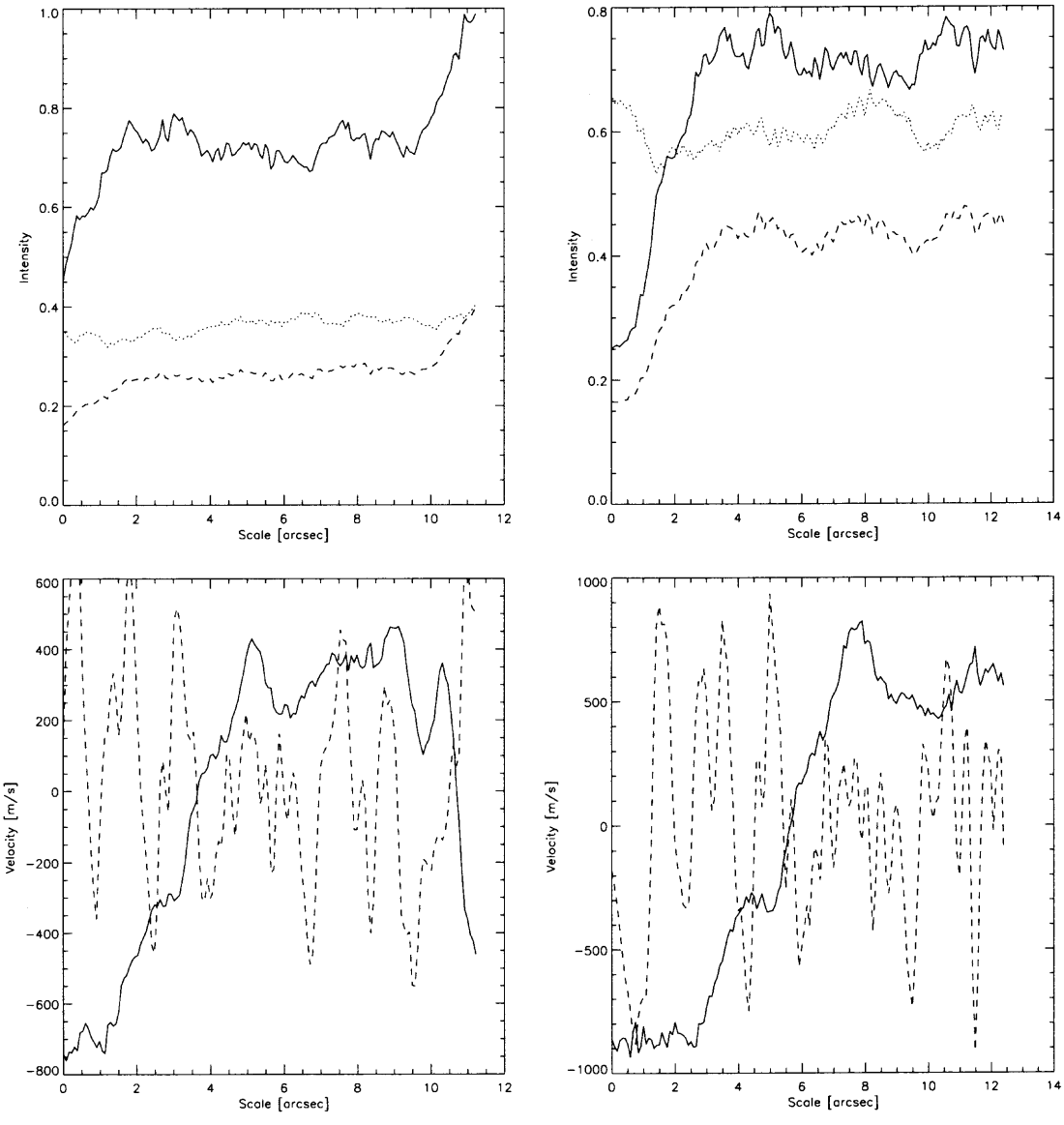

Figure 3.65 Closeup of one side of the penumbra for the lines Fe I 5576 Å (left) and Fe I 5691 Å (right) in terms of intensity (top) and velocity (bottom).

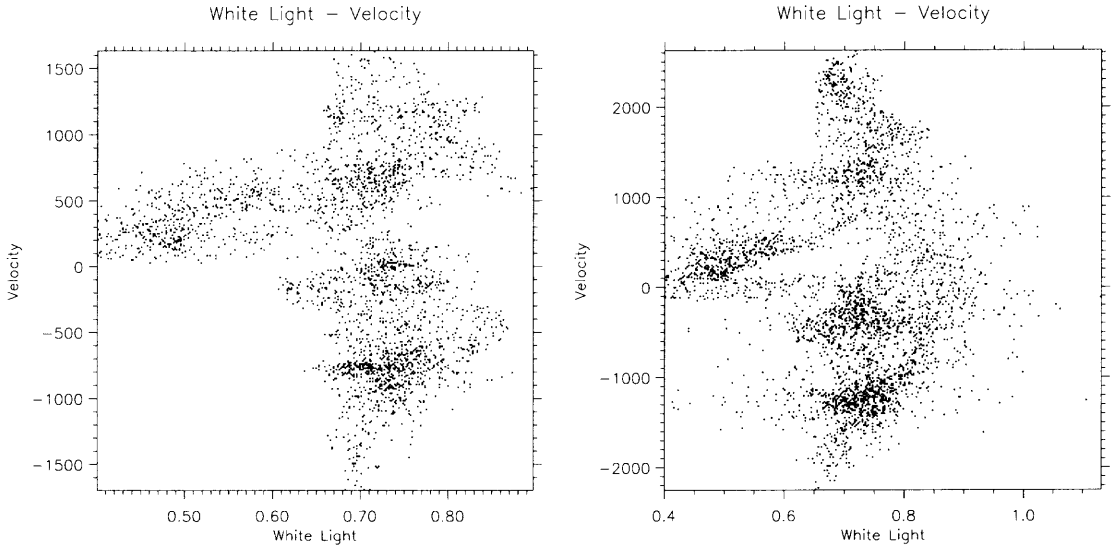

Figure 3.66 Velocity vs the white-light intensity for the lines Fe I 5576 Å (left) and Fe I 5691 Å (right) for all pixels selected as penumbra.

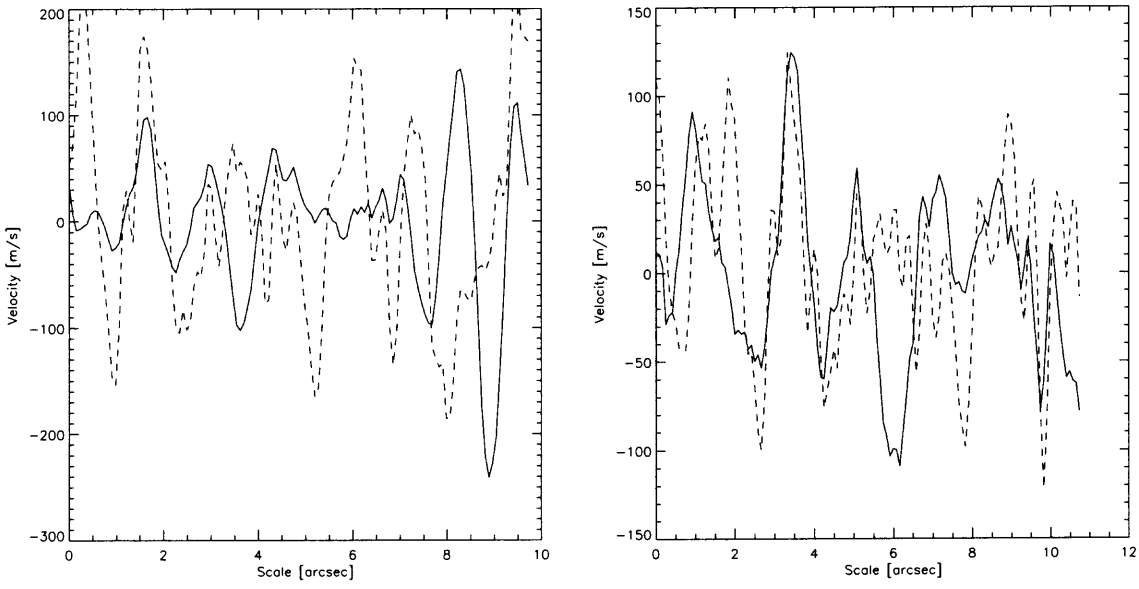

Figure 3.67 Closeup of the local velocity of the penumbra for the for the lines Fe I 5576 Å (left), Fe I 5691 Å (right) in terms of velocity. Local velocity means that the all velocity variations with a larger spatial scale than four arcsec have been removed. The dotted line is the superimposed local intensity with the same spatial scale removed. The penumbral grain is located at the position 1.5 (left) and 3.75 (right).

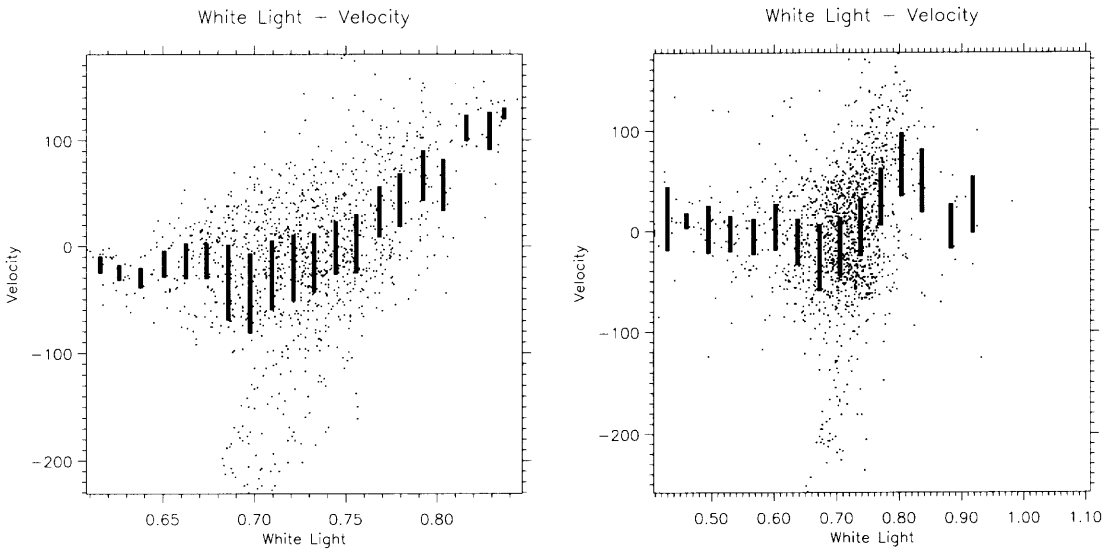

Figure 3.68 Velocity vs the white-light intensity for the lines Fe I 5576 Å (left) and Fe I 5691 Å (right) and the pixels selected as penumbra. This time all intensity and velocity variation with a larger scale than four arcsec have been removed. We can see a small positive correlation between the velocity and the intensity.

3.3.5 Summary

- Umbra

  We find no correlation between white-light intensity and velocity for the umbra. An examination of a single spectra also reveals no velocity differences at the location of the umbral dots. Therefore, we cannot confirm the existence of the small, localized umbral dots with down-drafts that we found in Chapter 2.4.3. However, we only scan 0.92 arcsec of a penumbral with a total length of 20 arcsec which means we only scan 4.6 percent of the length of the umbra. Since we only found two of these umbral dots in the whole umbra in our spectrograph observations, chances are, that we did not scan across such a bright point.

  On the other hand, we do find motion in the umbra which is not correlated to the intensity. We found a corresponding motion pattern in Chapter 2.4.3 that we identified as umbral oscillations.

- Penumbra

  Single spectra reveal a plasma motion in the penumbra directed away from the umbra. This is the well known Evershed effect [17]. The velocity of the plasma increases with increasing distance from the umbra. A local analysis reveals that the heads of penumbral grains are associated with an up-flow, but also that the general correlation between intensity and velocity is weak. This is in agreement with the results of Chapter 3.2.4.

In general, the spectrograph investigation provided little new information about the umbral dots or the penumbral grains. This has three reasons: worse seeing than during the UBF observations lowering the limit of detection by a factor nine to sixteen, observational mistakes by choosing a too short exposure-time and lower statistics since we only record one-dimensional spatial information. However, within the limits set by the data, we were able to confirm the results of Chapter 3.1 and 3.2.

For new observations with the spectrograph the following things have to be improved: longer exposure-times to obtain a higher signal to noise ratio. This requires even better seeing and is more demanding for the AO system. Longer scans should be performed, maybe with a larger step-width. This would enable us to cover more area of the sunspot and maybe detect all types of umbral dots. However, due to time limitations we only conducted one observing run using the spectrograph.

CHAPTER 4

Calculations - Forward Modeling

In this chapter, we present the results of radiative transfer calculations for a full three-dimensional MHD simulation with an added magnetic field. We determine the residual intensities and velocities at the heights in all spectral lines we used in our observations. We want to stress that the programs necessary to perform these calculations are the result of many years of work done by other people. We want to thank Bob Stein and David Bercik for allowing us to use the results of their three-dimensional MHD simulation. We are very much indebted to Han Uitenbroek, who provided us with the radiative transfer calculation program RH-code. He also was helpful with any problems we encountered during the calculations and he provided many useful ideas for the evaluation.

4.1 Introduction

4.1.1 The MHD Simulation

The MHD simulation of Stein and Bercik [62], [61] covers a cube of 125x125x63 data points. The horizontal dimension is 125x125 for every height with an even spacing of 96 km in each direction between the data points. This is equivalent to a scale of 0.13 arcsec/pixel for the average solar distance. This image-scale is about three times smaller than the image-scale of our observations. Future calculations should be able to resolve a scale of about 20-30 km. The spacing of 63 different height points varies in distance between 35 km and 90 km and covers a height range from 300 km below the photosphere up to 550 km above the photosphere. This means that all the spectral lines used in our observations are included in this height range. The modeling of the magnetic field was done by superimposing a uniform vertical field of 400 Gauss onto a field-free simulation of the solar plasma and studying the time evolution of the combined system. One time-slice in the later stage of this evolution is used for the calculation performed in this thesis.

The description and the analysis of the calculations presented here are quite brief and may be considered to be incomplete. We would like to cite Bob Stein himself, a man who has spent more than 30 years doing (M)HD simulations [62]:

"..... There is much work to be done analyzing these magneto-convection results and their implications for the solar dynamo and for observations. We need to look at many time steps and relate what is observable to what is happening in the simulation. For example, we need to try inverting Stokes profiles from the simulation as they would be observed after smearing by seeing and the telescope psf and compare the resulting inferred field with that producing the profiles. We need to investigate the process of G-band formation and how it depends on magnetic field configurations. We need to study in time the emergence and disappearance of magnetic flux from

the surface by calculating the evolution of selected magnetic field lines. We have just put our toe in the sea of possibilities. ...."

4.1.2 The Radiative Transfer Calculations

The result of the three- dimensional MHD simulation is a 125x125x63 cube of data points. For each data point we know the pressure, temperature, velocity chemical composition and the magnetic field. We compute the intensity that emerges from the solar surface for selected wavelength with the program RH-code written by Han Uitenbroek [68], [70]. This radiative transfer code is capable of performing one-, two- and three-dimensional calculations.
The one-dimensional LTE calculation with 3000 wavelength points for the evaluation of the contribution of the CH lines to the G-band takes about one second, the three-dimension LTE calculation with 31 wavelength points takes about four hours on a Sunblade 100 with a 500 MHZ processor and one Gigabyte of memory.

4.1.3 General Remarks about our Calculations

For a three-dimensional atmospheric model it is impossible to calculate a spectral region around each of the lines used in our investigation with a spectral resolution high enough to perform a convolution with the UBF profiles. We have to restrict the calculations to a few, selected wavelength points that allows us to recreate our observations as closely as possible. To achieve this goal, we calculate the intensity of the left and the right wing of every spectral line used in this investigation as well as in the line core and of the nearby continuum to determine the residual intensity. We thus performed calculations for the wavelength 557.610 nm, 557.626 nm, 557.602 nm, 557.618 nm, 569.150 nm, 569.166 nm, 569.142 nm, 569.158 nm, 538.032 nm, 538.048 nm, 538.024 nm, 538.040 nm, 538.103 nm, 538.119 nm, 538.095 nm, 538.111 nm. Furthermore, we included a reference continuum at 550.900 nm.

The calculation of the G-band residual intensity is more difficult. The G-band consists of several hundred lines we cannot calculate all due to limited computation power. Instead, we followed an idea of Uitenbroek and selected nine wavelength points, four in the core of CH lines and five in the continuum, and add them with a certain ratio to obtain the G-band intensity passing through the 10 Å filter.
In a first step, we determine the ration between the core of the CH lines and the continuum by performing a calculation of a one-dimensional quiet sun atmosphere for 3000 wavelength points in the G-band. One time we include the CH lines, the other time we do not include the CH lines. We multiply the calculated spectra with a 10 Å G-band filter profile and calculate the total intensity passing through the filter. We find, that including the G-band CH lines result in a reduction of 38 percent of the total intensity.

In the second step we chose five wavelength points that lie in the continuum of the G-band (430.340 nm, 430.345 nm, 430.330 nm, 430.335 nm, 430.340 nm) and four wavelength points in the cores of CH lines (430.345 nm, 430.335 nm, 430.340 nm, 430.345 nm). We averaged the continuum and the core points to get an estimation for the continuum and the core intensity in the G-band.
In the final step, we average the continuum and the core intensity images with a ratio 62:38 of to obtain the G-band intensity passing a 10 Å G-band filter. Finally, we divide the G-band intensity by the reference continuum intensity to obtain the residual intensity of the G-band.

We processed the calculations in exact the same way as we processed the observations. We used the same calibration routines, the same process for selecting the solar structures and the same programs to generate images and plots.
However, there are some inevitable differences between the observations and the calculations. As stated above, we could not calculate enough wavelength points to perform a convolution of the line profile with the UBF. This is not a problem for the residual intensity measurements of Chapter 3.1 since we corrected them for the UBF profile anyways. The velocity measurements, however, are more difficult. Since we measure the average shift of the whole line profile to determine the velocity, we average the velocity over different heights of the solar atmosphere. We do not perform a convolution with the UBF, therefore we disregard this effect in the simulations. However, we have the velocity information of several heights in the solar atmosphere and can therefore compare the observed velocity to the calculated velocity in different heights.
We also neglect the effect of the PSF, i.e. we do not convolve the spatial information with the degrading effect of the seeing and the telescope. This has several reasons: we performed several runs with different seeing conditions which means we would have to perform a separate comparison for each run, without knowing if a comparison is sensible at all. Furthermore, we do not know the PSF for any of the observing runs since we did not record the wavefront sensor data. This means we would have to estimate the PSF which will not improve the accuracy of this comparison. Therefore, we decided not to perform a convolution of the spatial information with the psf.

4.2 Results

4.2.1 General Properties of the Calculations

- Magnetic Field

  Figure 4.1 shows the vertical component of the magnetic field for different heights above photospheric level $\tau = 1$. The magnetic field is mostly concentrated in the intergranular lanes. We do not detect a significant change in appearance for the heights investigated, only a slight spreading out of the

magnetic field. We find areas of spatially larger magnetic concentrations at the positions (7/6) and (12/13) in the simulation. These areas can be associated with micro-pores, especially since the are dark in the intensity images. We do not find other magnetic concentrations that resemble flux-tubes.

- Temperature

  The temperature maps in the four hight layers of the solar atmosphere are shown in Figure 4.2. There is little difference in temperature between photospheric height and a height of 40 km. In a height of 160 km above the photosphere, we find the only the centers of the brightest granules remain hot. In highest layer of the solar atmosphere that we investigated which is 320 km above the photosphere, we can see that atmospheric inversion has occurred. In this layer, the borders of granules and the intergranular lanes are brighter than the centers of the granules.

  The temperature at the locations of the micro-pores are lower than the average photosphere. The reason for this behavior is that the strong magnetic field at these locations suppresses the convection of solar plasma. Convection is the main mechanism of energy transport in the photosphere.

- Velocity

  In Figure 4.3, we can study the velocity maps of the MHD simulation for different atmospheric heights. We can see that the magnitudes of the velocities are decreasing with height. In the highest layer of 320 km above the photosphere only the centers of the largest granules are still significant up-flows. We do not detect small, localized down-flows in the intergranular lanes in any atmospheric layers that resemble the down-flows at or around bright points as predicted by Steiner [64], [65]. The there is no significant plasma motion at the locations of the micro-pores since it is suppressed by the magnetic field.

4.2.2 Comparison with our Observations

Fig 4.4 shows the field of view of the calculation and should be compared to Figure 3.5. The images look realistic, but the selection of 'bright points' indicates a problem. Most features selected as 'bright points' are indeed bright granules. The reason is, that granules have an enhanced G-band brightness compared to our observations. On the other hand, we hardly see any features that resemble bright points at all! We do not find small brightenings in the intergranular lanes, but more G-band brightenings at the edges and sometimes at the center of granules. We did not find this behavior in any observations presented here. However, in previous observations (Fig. 1.2) we found brightenings of the edges of granules in the G-band as well. We can only speculate about the reasons of this behavior. Maybe the active regions we observed

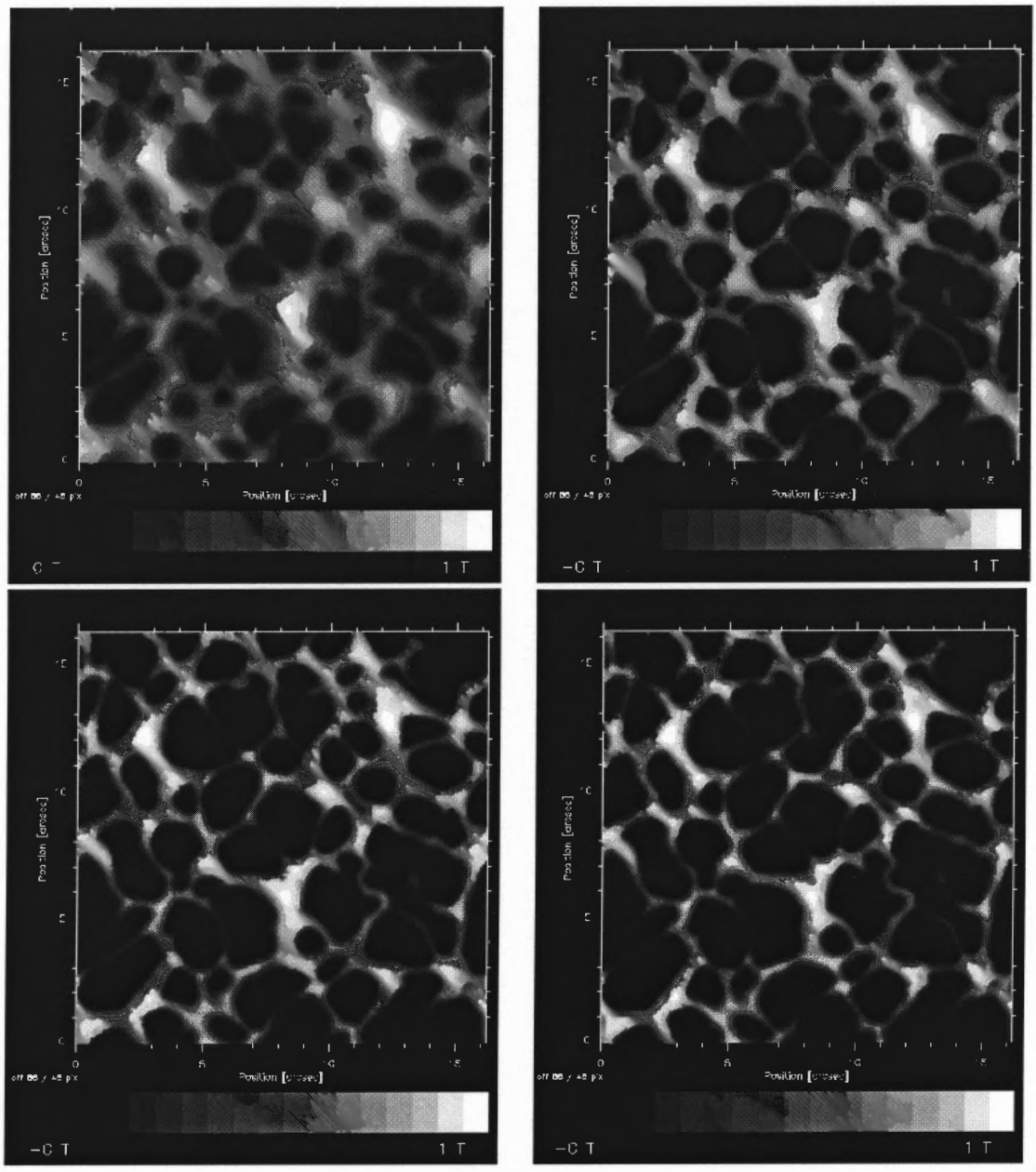

Figure 4.1 Vertical component of the magnetic field of different atmospheric layers from a snapshot of the model simulations of Stein and Bercik [62]. The top left image shows a height of 320 km above photospheric level $\tau = 1$, the top right image shows a height of 160 km. The bottom left image shows a height of 40 km above the photospheric level $\tau = 1$ and the bottom right image shows height 0 km. The magnetic field strength ranges from zero to one Tesla (zero to 10000 Gauss).

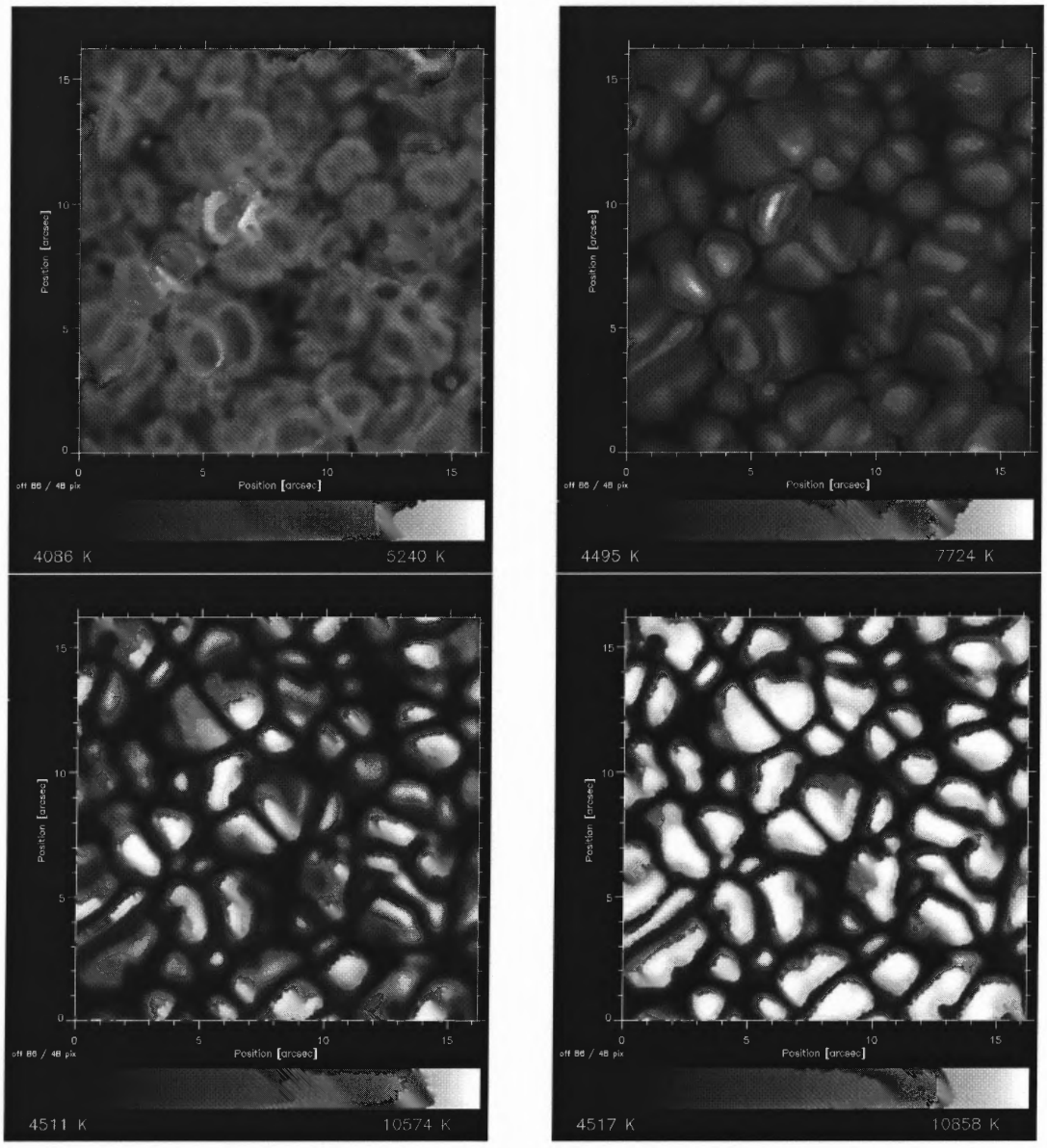

Figure 4.2 Temperature of different atmospheric layers from a snapshot of the model of Stein and Bercik [62]. The top left image shows a height of 320 km above photospheric level $\tau = 1$, the top right image shows a height of 160 km. The bottom left image shows a height of 40 km above the photospheric level $\tau = 1$ and the bottom right image shows height 0 km.

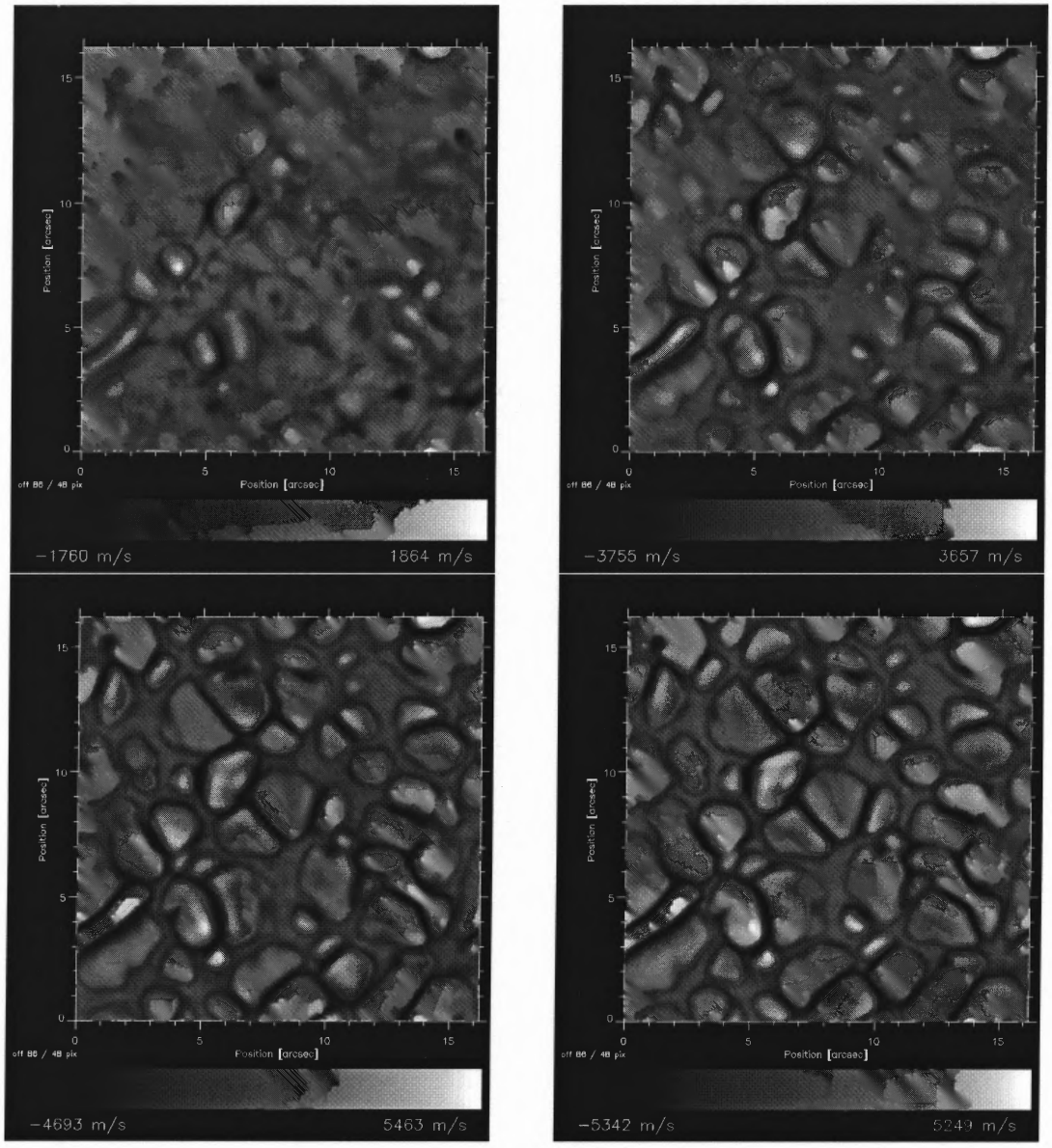

Figure 4.3 Velocity of different atmospheric layers from a snapshot of the model of Stein and Bercik [62]. The top left image shows a height of 320 km above photospheric level $\tau = 1$, the top right image shows a height of 160 km. The bottom left image shows a height of 40 km above the photospheric level $\tau = 1$ and the bottom right image shows height 0 km.

for this thesis are older than the region of Figure 1.2 and therefore all the emerging magnetic field has already been swept into the intergranular lanes. On the other hand, this me be just an effect of the PSF. Only the observations of several active regions can yield an answer to this question.
The misidentification also shows in a comparison of the selected 'bright points' with a selection of regions of high magnetic field strength. The overlap of these two selections is lower than ten percent. This means that enhanced G-band brightness and magnetic field do not spatially coincide which is in disagreement to the observations of Berger [6]. This result indicates a significant short-coming of the calculations. Nevertheless, we further evaluated the model in the same way as our observations to study the similarities or differences in detail.
The next set of images (Fig. 4.5) shows the residual intensities of all investigated spectral lines. These images should be compared to the images in Figure 3.19 of Chapter 3.1.5. The images look realistic in the way that the intergranular lanes are bright for the atomics lines but dark for the G-band. Apart from that, the calculations are very different form the observations in many respects. The G-band residual intensity image shows a lot more bright granules than the observations. This leads to the wrong selection of granules as bright points that we mentioned above. Furthermore, we only see very few brightenings in the intergranular lanes that could be interpreted as bright points. These possible bright points are only bright in the G-band and the Fe I 5576 Å line, but they do not have an enhanced contrast in the Fe I 5691 Å and the Ti II 5381 Å lines. This is in disagreement to our observations (Ch. 3.1) where we find an enhanced contrast for all lines.
This behavior can be studied quantitatively in table 4.1 where we can see that 'bright points' do not have an enhanced contrast for any lines other than the G-band and the Fe I 5576 Å line. We also can see that all spectral lines except the G-band detect a difference in residual intensity between the bright points and their surroundings. This behavior is contrary to our findings in Chapter where we find an enhanced contrast for all solar lines that we investigated, i.e. the Fe I 5576 Å , Fe I 5691 Å and Ti II 5381 Å lines.
The study of the micro-pores reveals similarities but also differences between the calculations and the observations as well. The pores are all dark in the G-band residual intensity image while some pores are bright in the residual intensity image of the other lines. This is in agreement with the results of Chapter 3.1.4. The pores in the lines Fe I 5691 Å and Ti II 5381 Å are surrounded by a bright ring which we also found in our observations. However, we do not find the rings around the pores for the Fe I 5576 Å line and the the pore at (12.5,12.5) even has a bright core with a dark ring around it in the residual intensity of the G-band while we find bright rings for all lines in our observations.
As explained before, we use the velocities derived directly from the model for our comparisons. However, the information contained in the velocity maps is of limited

use since we do not find bright points at all. Therefore, we cannot check for the down-flows predicted by Steiner [64]. We looked for small localized down-flows in the intergranular lanes not associated with any kind of brightening but did not find any. We did not find any down-flows around the micro-pores that we would expect from the observation of down-flows at the quiet sun-umbra border in Chapter 3.2.4.

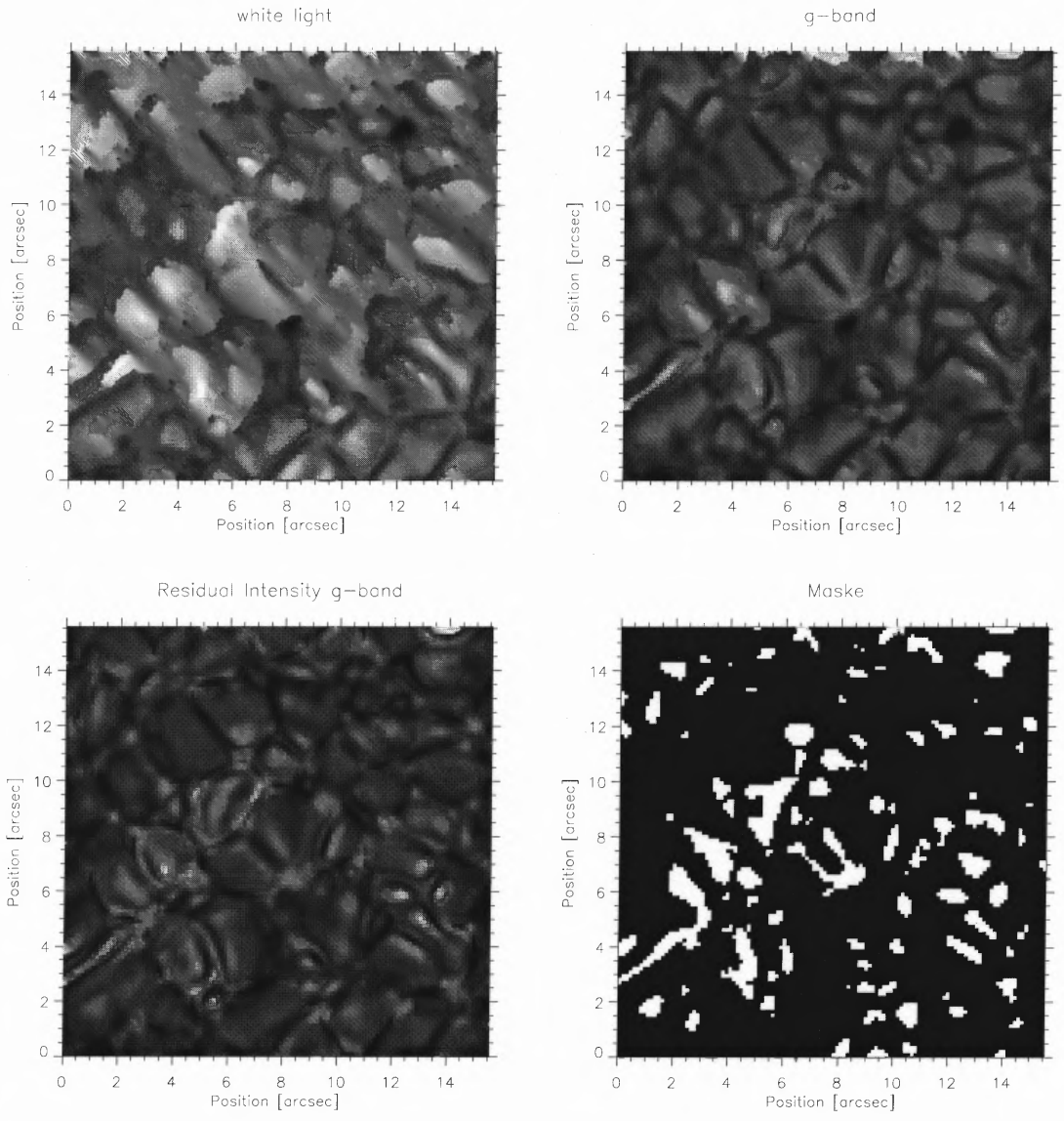

Figure 4.4 The selected mask for the bright points. Top left is the white-light image (continuum image near the Fe I 5576 Å line), top right is the G-band image, bottom left is the residual intensity image of the G-band and bottom right is the mask for the bright points.

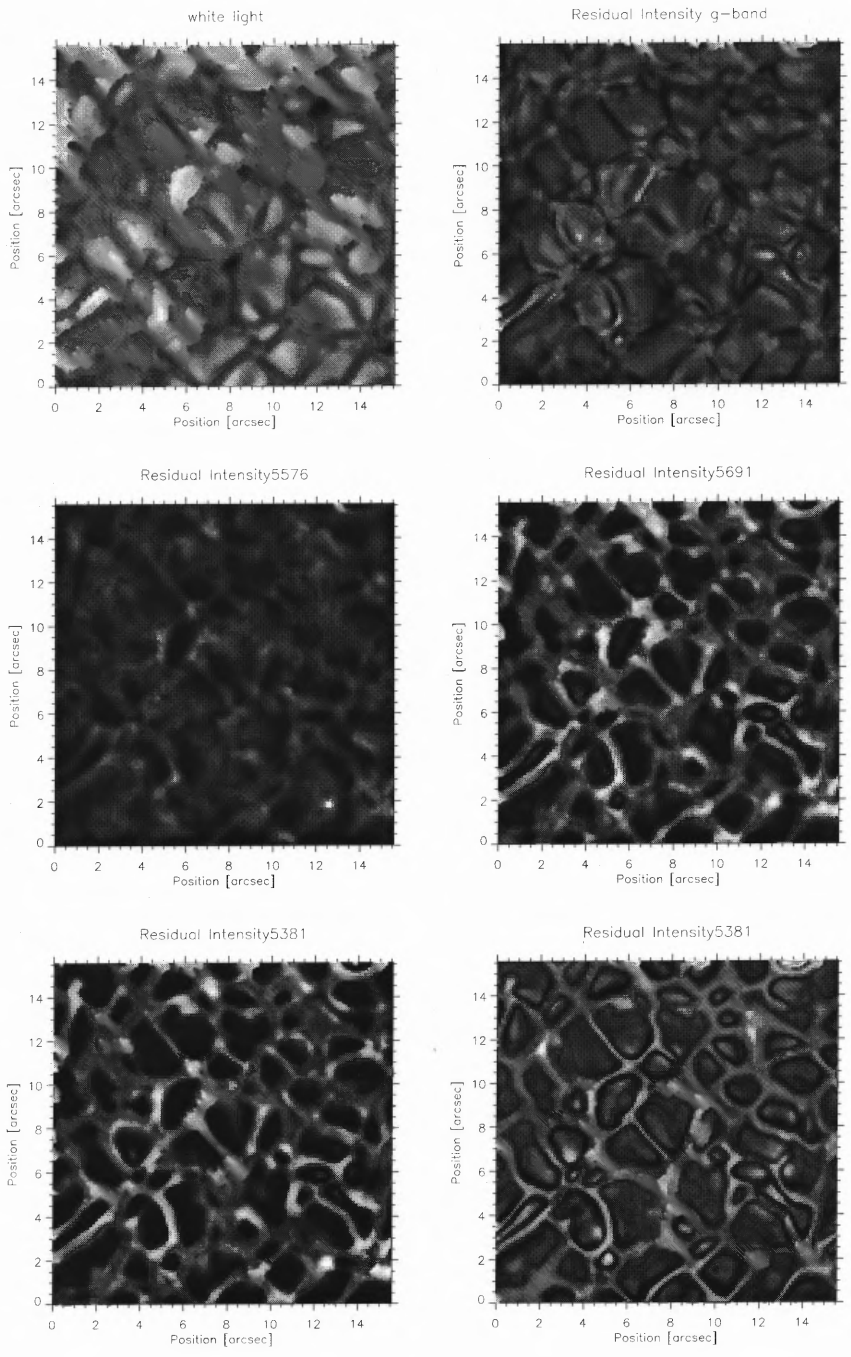

Figure 4.5 Whole field of view of the calculation. Top left is the continuum image near the Fe I 5576 Å line, top right is the residual intensity of the G-band. Middle left is the residual intensity of the Fe I 5576 Å line and middle right is the residual intensity of the Fe I 5691 Å line. Bottom left is the residual intensity of the Ti II 5381 Å line and bottom right is the residual intensity of the C I 5380 Å line.

Residual Intensity for	5576	5691	5381	5380	G-band
Mean	0.25	0.54	0.51	0.90	1.0
Bright Points	0.23	0.54	0.51	0.91	1.13
BP with surroundings	0.24	0.55	0.53	0.91	1.13
G-band Bright regions	0.25	0.61	0.59	0.92	1.12
Intergranular Lanes	0.27	0.56	0.56	0.90	0.96
Granules	0.22	0.40	0.38	0.38	1.0

Table 4.1 The residual intensity of all investigated solar lines for the various solar structures derived from calculations. One has to keep in mind that 'bright points' are mostly mis-identified bright granules. We kept the name and selection process to allow for a comparison with table 3.1.

4.2.3 Summary and Discussion

We find the visual appearance of the calculated images similar to the observations in some respects but a detailed analysis reveals several differences between the calculations and the observations.

First of all, we do not find structures resembling bright points at all. There are almost no correlation between the brightenings in the G-band and the magnetic field which is in disagreement to the observations of Berger [6]. Since we do not find bright points, we also do not find the down-flows around the as predicted by Steiner [64]. Actually, we do not find small, strong down-flows at all in the intergranular lanes, associated with brightenings of any kind or not.

The residual intensity images reveal many differences between the observations and the calculations. We find the intergranular lanes to be bright for the atomic lines but dark for the G-band which agrees with our observations in Chapter 3.1.4, but the bright bright structures in the G-band are only bright in the Fe I 5576 Å line as well but are dark in the lines Fe I 5691 Å and Ti II 5381 Å . The micro-pores only agree in part with our observations. Pores are darker in the G-band residual intensity images than in the residual intensity images of the atomic spectral lines which reflects the observations. However, the bright ring around the pores and only be seen in 5691 Å and Ti II 5381 Å lines. It is missing in the Fe I 5576 Å line and in the G-band we find a dark ring.

As a summary, we must conclude that, although state of the art and a definite improvement over previous calculations, the calculations performed here do not reflect the physical behavior of the solar surface very well. Further improvement and a detailed analysis of the shortcomings of the calculations will be needed.

CHAPTER 5

Summary and Conclusions

5.1 Goals of this Investigations

The goal of this thesis is to investigate bright points, umbral dots and the G-band as discussed in detail in Chapter 1.
Bright points a small brightenings in the intergranular lanes that are believed to be concentrations of magnetic flux [65]. These flux-tubes may be the essential building blocks that form the large magnetic structures, e.g. sunspots, on the solar surface. They may reveal information about the morphology of the solar magnetic field and the dynamo that produces it. Bright points are numerous and may carry substantial energy. Since they probably extend from the photosphere into the Chromosphere it is likely that they are connected to the coronal heating problem.
While bright points may be a very important structure on the solar surface, little is known about them. Bright points are small and it is difficult to investigate their physical properties with current solar telescopes. Therefore, our goal for this investigation is two-fold. We want to provide basic physical information needed to understand bright points and to develop flux-tube models. We also try to test the currently existing flux-tube models by our observations to point out their shortcomings and provide information for the refinement of these models. In this context we perform calculations ourselves to compare them to our observations.

The G-band is a region of the solar spectrum around 430 nm that contains the bandhead of the CH molecule. The G-band is important, since molecular lines are more sensitive to atmospheric conditions like pressure, pressure gradient, temperature and temperature gradient. This sensitivity shows e.g. in the high contrast that bright points have in the spectral region of the G-band. The high contrast allows an easy identification of the bright points and the large number of CH lines in the G-band allows the use of a simple broad band filter and short exposure-times. Bright points are known to be connected to the emergent magnetic flux [6], which may be used for in-proxy measurement of the magnetic field. Therefore, the G-band may be used as an important diagnostic tool, but this is only possible if it is fully understood. Although the G-band can be modeled quite well by current radiative transfer calculations, important information like the formation height of the G-band is not known. We investigate the connection between the G-band and the bright points in order to obtain information about both structures. We also perform a correlation analysis with other, well known spectral lines to determine the formation height of the G-band.

Umbral dots are small brightenings within the umbra, which itself is a substructure of a sunspot. Umbral dots are important in two ways: they may be responsible for the unsolved umbral heating problem, the fact that the umbra has a much higher

temperature than expected for a uniform magnetic field. Second, the umbral dots are the crucial dividing point for the two competing sunspot models by Weiss [29] and Parker [42]. Determining the nature of umbral dots would clearly allow to validate one of the models. Also, we check the prediction of Choudhuri that umbral dots and penumbral grains are two representations of the same physical structure [12].
We obtain velocity measurements to determine the physical nature of umbral dots. This allows us to test some of the predictions made by the two competing sunspot models. We check for different and new types of umbral dots as well as for the connection between umbral dots and penumbral grains.

5.2 Methods used to obtain the Observations

All the observations proposed in the previous section have one problem in common: the physical investigation of solar structures requires long exposure-times since the instruments used for these investigations cut off most of the incoming photons. Long exposure-times have the disadvantage that the earth's atmosphere degrades the image due to turbulence ('seeing') and thus lowers the resolution of the recorded images. On the other hand, the structures we want to investigate are very small. This disagreement has made impossible up to now to perform the observations proposed above.
The crucial, new instrument, used in a PhD thesis for the first time in Solar Physics, is the Adaptive Optics system of the National Solar Observatory, Sacramento Peak. This system was developed by Thomas Rimmele, Kit Richards and Richard Raddick. This system came online in November 1998. This system corrects for the turbulence of the earth's atmosphere in real-time with a frequency of up to 1000 Hz and provides the possibility to obtain diffraction-limited long-exposure images. This a very important step in the investigation of solar fine structure. In addition to the AO system, we use a narrow-band filter in a special mode that allows us to obtain velocity measurements in one exposure. This eliminates differential seeing and increases the measurement accuracy.
The application of these two methods, Adaptive Optics and simultaneous observation, results in physical measurements of structures on the solar surface with a spatial resolution and a sensitivity that has never been reached before. Therefore we are able to provide new information about the different topics discussed above.

5.3 Results and Interpretation

In this section, we present the results of our observation organized by the topics we have investigated.

- Bright Points

  - Morphology

    Bright points do not show a peak in the size distribution and their number increases to the diffraction limit. This means that either bright points do not have a typical size or that this typical size is below the diffraction limit of the DST which is 0.13 arcsec (100 km) in the G-band. Since we find 'typical values' for the intensity and residual intensity of bright points we expect to find a typical size as well. Therefore we have reason to believe that they are smaller than the resolution limit of the Dunn Solar Telescope (Ch. 3.1.4.2) of 120 km in the G-band. Their shape changes with size, they become more elongated with increasing size (Ch. 3.1.4.2). The reason for this elongation is probably that several bright points in an intergranular lane form an unresolved group of bright points that is elongated because it is confined in the intergranular lanes. This view is supported by the fact that bright points are exclusively found in intergranular lanes (Ch. 3.1.4.4).

    The inspection of residual intensity images reveals that bright points do not show any shape-changes or displacement within a height region from 0 km above the photosphere to 320 km above the photosphere that are larger than 120 km horizontally (Ch. 3.1.4.4) which is equivalent to an inclination of 20°. This is probably in disagreement to the two dimensional calculations of Steiner [64], [65], which predict a significant expansion of the magnetic field of a flux-tube with height.

  - G-band Bright Regions

    In addition to the bright points themselves we find larger regions of enhanced G-band brightness (Ch. 3.1.4.4). These regions maybe related to the long-known plages and may be a sign for emergent magnetic flux. We find all bright points to be located inside the G-band bright regions. Therefore, we use the G-band bright regions to exclude small bright granules otherwise selected as bright points.

    We investigate the atmospheric properties of these G-band bright regions in Chapter 3.1.4.4. We find that the atmosphere of G-band bright regions is similar to the atmosphere within bright points. Only the CH lines detect a slight difference between bright points and G-band bright regions (Ch. 3.1.4.1).

- Bright Point Residual Intensities

  Bright Points have a significantly different residual intensity than granules and intergranular lanes in all investigated spectral lines (Ch. 3.1.4.1). The residual intensity of pores is similar for the atomic spectral lines, but different for the G-band. We conclude that the atmosphere within bright points must be significantly different from other solar structures, the most similar being the pores. This may indicate that bright points do have a lower temperature than the average photosphere like pores and/or that bright points have a lower pressure than the average photosphere. The latter would be consistent with the observation that bright points are associated with the solar magnetic field. Since the gas pressure and the magnetic pressure inside the flux tube are equal to the gas pressure outside the flux-tube, a magnetic field results in a reduced gas pressure inside the flux-tube. A similar mechanism of pressure reduction can be observed in sunspots and pores. The slight difference between pores and flux-tubes can be explained by the fact that flux tubes are too small to suppress convection, and that due to the larger ratio of surface area to volume, radiative heating may play a more important role than for pores.

  We find an enhanced contrast of the bright points for all atomic spectral lines, the Fe I 5576 Å line, the Fe I 5691 Å line and the Ti II 5381 Å line (Ch. 3.1.4.1). Steiner [63] predicts a contrast enhancement for the two Fe I lines which we confirm, but no contrast enhancement for the Ti II line which is in disagreement to our observations.

- Contrast Enhancement Mechanisms for Bright Points

  We measure an increasing intensity with increasing size of the bright points as well as with increasing circumference (Ch. 3.1.4.2). We conclude that the brightening enhancement mechanism cannot be related to the walls of a bright point, since the efficiency of such a mechanism is decreasing with decreasing ratio of area to circumference. Even if we imagine a bright point as a bundle of flux-tubes, the contrast in the G-band should be independent of the (total) size. We therefore reject the contrast enhancement mechanism proposed by Rutten [49], who explains the brightening as a result of photo-dissociation of the CH Molecule due to radiation (hot wall effect). This result also implies that the atmospheric condition in a bright point change with increasing size. This behavior has not been modeled in the one-dimensional simulations performed so far [59], [63], [50].

  In Chapter 3.1.4.4 we found that although all bright bright points have a higher residual intensity in the G-band, only some of them have a higher contrast in the atomic spectral lines. This behavior is not related to the magnetic field (Berger [6]) and may indicate the existence of different

types of bright points. However, more observations are needed to confirm this result.

We measure an increase in the white-light intensity with increasing bright point area (Ch. 3.1.4.2) indicating the existence of a general brightening mechanism, independent of spectral lines, that is stronger for larger bright points. That is an unexpected result since pores are considered to be flux-tubes with a large diameter but have a decreasing intensity with increasing size.

We find a negative correlation between the white-light intensity and the residual intensities of the atomic lines for bright points (Ch. 3.1.4.2). This means that the brighter a bright point is in white light, the less contrast it has in the core of a spectral line. The behavior for the G-band is contrary, the G-band contrast is higher the brighter the bright point is. This different behavior shows the existence of a brightening mechanism exclusive for the G-band.

We can draw some conclusions about the nature of the brightening mechanism from the behavior of the residual intensity for bright points. The increasing brightness with increasing surface area is not compatible with a mechanism related to the wall of the flux tube. Therefore a volume mechanism is more likely. One possible way of contrast enhancement is that the lower gas pressure inside the flux tube results in a lower opacity of the solar plasma. Therefore, the light emitted at the location of the flux-tube originates at deeper atmospheric layers. These layers are hotter, and therefore brighter. Contrary to pores, convection is not suppressed in flux-tubes because of their smaller size, and the flux-tubes are not dark. The special behavior of the CH lines is probably due to the fact that CH as a molecule is prone to dissociation, which is basically the mechanism that enhances the contrast in the models of Steiner [63] and Sanchez-Almeida [50].

- Velocities of Bright Points

  We did not detect any velocities in heights of 160 km and 320 km above the photosphere at the locations or at the edge of bright points that exceed a size of 0.2 arcsec and a velocity of 100 m/s (Ch. 3.2.4) This is not in agreement with the two-dimensional calculations of Steiner, which predict an initial down-flow during bright point formation with a subsequent upward shock-front, and down-flows at the edge of bright points during their existence. However, we have to be careful with this interpretation since we measure the velocity in higher atmospheric layers then evaluated by the calculations.

- Simulations of Bright Points

  Our own calculations (Ch. 4) using the results of a three-dimensional MHD simulation of Stein and Bercik [62] as well as a radiative transfer code by Uitenbroek [69] did not agree with the observations. The models do not predict structures like bright points at all. We did not find isolated G-band brightenings (except for micro-pores), we did not detect any larger velocities in the intergranular lanes that might be associated with bright points. Moreover, the G-band brightenings and the location of the magnetic field did not coincide. Also, the relative residual intensities of bright structures are not predicted correctly.

As a summary we found that bright points are probably smaller than the resolution limit of current solar telescopes. We find two separate brightening mechanisms, one independent of the spectral lines and only dependent on size, and second brightening mechanism exclusively for the G-band. We do not detect an increase of bright point size with height in disagreement to Steiner [64], [65] nor do we find the down-flow predicted by this model. We also could not confirm the prediction of Steiner [63] about the different behavior of the Ti II lines compared to the Fe I lines in terms of bright point contrast. The failure of all proposed theoretical models indicates a fundamental flaw. Since atoms and molecules are modeled well, the differences result most likely from the atmospheric models of bright points.

- G-Band

  - Sensitivity of the G-band to atmospheric conditions

    The G-band CH lines are more sensitive to atmospheric conditions than the atomic spectral lines in general. For bright points, only the G-band residual intensity is different for bright points itself and bright points with surroundings (Ch. 3.1.4.3). Also, only the G-band residual intensity shows a positive correlation between the residual intensity and the white-light intensity for bright points (Ch. 3.1.4.3). We explain this behavior by the fact that the CH molecule can dissociate and therefore change the strength of the G-band in addition to all other line-strength changing mechanisms that are common to atomic lines as well.

  - Formation Height of the G-band

    We find the strongest correlation between the G-band residual intensity and the residual intensity of the Fe I 5576 Å line which forms in a height of 320 km above the photosphere. The correlation between the G-band residual intensity and the residual intensities of the Fe I 5691 Å and Ti II 5381 Å lines is weaker indicating that the contribution to the G-band from an atmospheric height around 160 km is smaller than the contribution to

from a height of 320 km. There is a correlation between the G-band residual intensity and the residual intensity of the C I 5380 Å line. We explain this correlation by the large contribution of 68 percent from light originating at the continuum to the G-band due to the very large FWHM of 10 Å of the G-band interference filter (Ch. 3.1.4.3).

Therefore, we find that the largest contribution to the CH-lines is originating from a height of 320 km above the photosphere with some contribution from layers around 160 km as well. There is only a small contribution from the photosphere and atmospheric layers with a height of 40 km. This view is supported by the fact that residual intensity images in the G-band show the inversion in granulation common to lines forming higher in the solar atmosphere.

- Calculations

  The one dimensional model calculations of Steiner [63] and Sanchez-Almeida [50] do not describe the G-band well in terms of the prediction of formation height. Steiner [63] states a formation height with it maximum contribution at a height of 160 km above photospheric level $\tau = 1$ and Sanchez-Almeida [50] proposes a formation height of about 40 km below photospheric level $\tau = 1$. We clearly find that a large part of the light originating in the G-band does not originate from photospheric heights or below which is in disagreement to Sanchez-Almeida. We also find strong evidence that the G-band does not originate mainly from heights of 160 km above photospheric level $\tau = 1$ as suggested by Steiner.

We found the G-band to be more sensitive than the atomic spectral lines. This can be explained by the fact the G-band lines are mostly caused by the CH molecule is prone to dissociation. We found that the light originating from the G-band forms in layers higher in the solar atmosphere, with contributions form layers in a height of 160 km and 320 km. This is not in agreement with the predictions of Steiner [63] and Sanchez-Almeida [50].

- Pores

We find the residual intensity in pores to be strongly dependent on the size of the pore (Ch. 3.1.4.4). This is an indication for the sensitivity of the different spectral lines toward temperature and pressure. Moreover, in the residual intensity images of all lines we can see a bright ring around the pores which indicates a different atmosphere at the border of pore and quiet sun. This maybe a region where energy transfer by radiation plays an important role.

Smaller pores seem to have almost the average intensity of the quiet sun (Ch. 3.1.4.4). Bright points are brighter than the average photosphere, bigger pores are darker. This indicates the existence of two opposing mechanisms, one

that darkens magnetic structures with increasing size and one that brightens magnetic structures with increasing size. The mechanism for the increasing darkening is most likely the increasing suppression of convectional heating due to the increasing magnetic field. The brightening mechanism is not known yet, but it is suspected the evacuation of magnetic structures maybe the reason.

- Umbra and Umbral Dots

  - Umbral Dots

    Our measurements show that umbral dots consist of three different types (Ch. 3.2.4.1):

    Penetrating Penumbral Grains Some umbral dots located at the outer border of the umbra have numerous properties in common with penumbral grains. Their appearance in brightness, velocity and residual intensity images closely resemble penumbral grains. We therefore conclude that these 'umbral' dots are penetrating penumbral grains.

    Larger-scale Intensity-Variations There is a general bright-dark variation in the umbra of a scale of one to three arcsec and a velocity pattern of the same dimension. The brighter areas are selected as umbral dots. There is a negative correlation between intensity and velocity for the Fe I 5691 Å line. We interpret this motion as umbral oscillations.

    Distinct Umbral Dots Some of the more distinct and localized umbral dots show strong down-flow. This motion occurs, within the resolution-limit, at the same location as the umbral dot and not on the sides.

    Relation to previous studies

    Previous studies of the umbra have found two different types of umbral dots (Sobotka [56], [57], Grossmann-Doerth [21], Schmidt [53], Tritschler [67]). Except for Sobotka [56], [57] all studies divided umbral dots into central and periphal ones. We find the separation of umbral dots using their intensity to be better than separation by the position of umbral dots in the sunspot.

    The superiority of the intensity separation is also related to the existence of penumbral grains that are identified as umbral dots. Sobotka [56], [57] suspected from the appearance in the white-light images that some of the outer umbral dots were penetrating penumbral grains. Our study confirms that some bright umbral dots at the border of the umbra are penetrating penumbral grains using high-resolution pictures, dopplergrams and residual intensity pictures.

    Our measurements disagree with most previous velocity studies of umbral dots since we measure down-flows at all inner umbral dots while all

existing measurements yield up-flows (Kneer [28], Rimmele [46]) or velocities compatible with 0 m/s (Wiehr [73], Schmidt [53]). This may be due to the fact that the resolution in this study is two to three times better than the resolution of previous studies, which leads to an increase in sensitivity of four to nine times since the size of umbral dots is probably below the resolution limit of current solar telescopes.

- Implications of our results
  * Penetrating penumbral grains
    Penetrating penumbral grains were observed by Sobotka [58] and, after entering the umbra, these penumbral grains were brighter than most umbral dots. They stopped moving towards the center of the umbra and therefore occurred only at the outer boundary of the umbra. Sobotka [56] showed a clear correlation between position in the umbra, brightness and lifetime with the result that bright, periphal umbral dots had a short lifetime. These penetrating penumbral grains are still up-flows, as shown here for the first time. This leads the following interpretation: penumbral grains penetrate the umbra (Sobotka [58]) and while they do so they still show a significant up-flow and are brighter than the average umbral dots (our result). However, brighter umbral dots at the border of the penumbra are short-lived (Sobotka [58]). Additionally, we find no significant up-flows in the inner part of the umbra.
    A possible interpretation is that the material up-flow of penetrating penumbral grains is stopped soon by the stronger magnetic field in the umbra compared to the penumbra since any horizontal motion is suppressed by the vertical magnetic field. This explains the short life time of these penetrating penumbral grains. If this interpretation is correct it falsifies theories of umbral dots that suggested some sort of convectional up-flow because even a strong initial up-flow is stopped soon by the magnetic field of the umbra. This may not apply to the model of Weiss [29], since it predicts larger convection patterns.
  * Relation umbral dots - penumbral grains
    Choudhuri [12] proposed that umbral dots and penumbral grains are of the same nature. He assumes both features to be up-flows of solar plasma in field-free regions. However, we find that umbral dots do not show up-flows at all, while penumbral grains, at least their inner parts, are up-flows of several hundred m/s. Moreover, there is evidence that an initial upward motion within the umbra is stopped. All these results suggest, that umbral dots and penumbral grains have different properties and can therefore not be two representations of the same physical process. This is not in agreement with Choudhuri [12].

  * Small, localized umbral dots
    The 'real' umbral dots, which occur mainly in the center of the umbra consist of distinct dots with associated down-flows and a larger underlying intensity-velocity pattern due to umbral oscillations. The down-flows at the localized umbral dots cannot not be associated with field free regions since field-free would produce small up-flows Choudhuri [12]. One explanation might be that the inverse Evershed-effect shocks in the umbra at the height of the photosphere and thus producing brightenings. However, there is no convincing explanation for this type of umbral dots yet.

  Our observations confirm the existence of two different types of umbral dots and indicate the existence of a third type. We establish the fact that umbral dots and penumbral grains are different physical structures, which does not agree with the predictions of Choudhuri [12]. Our observations could not confirm either one of the two competing sunspot models nor did we find strong evidence against any model. Only high-resolution observations of the magnetic field of sunspots will be able to decide between the two models.

- Down-flows at the Umbra-Quiet Sun Border

  We find down-flows in excess of 1000 m/s at the edge of the umbra-quiet sun border (Ch. 3.2.4). The down-flows may be a result of the cooling of hot plasma at the umbra-quiet sun border. The umbra is much cooler than the quiet sun and the hotter plasma outside the umbral looses its energy radiatively. This observation may be used to check the atmospheric structure of a sunspot umbra.

- Penumbra

  - Bright and dark filaments

    We find a weak positive correlation between the velocity normal to the solar surface and the white-light intensity (Ch. 3.2.4.2). Therefore, it is not clear, whether the dark or the bright filaments are streaming upwards on average. Only at the locations of distinct, bright penumbral grains, we observe up-flows. This is in agreement with the model of Schlichenmaier [51], [52] but this model does not explain bright filaments without up-flows or dark filaments in general.

  - Horizontal Velocity - Evershed-effect

    We find a significant line-of-sight velocity in the penumbra (Ch. 3.3.4.3) that increases radially outward - the well known Evershed-effect. The correlation between white-light intensity and velocity as well as an analysis of individual spectra show no correlation between local intensity an

velocity. Therefore, we cannot decide whether the bright or the dark filaments are streaming.

In Chapter 3.2.4.2 we find strong down-flows at the penumbra-quiet sun border. Previous observations of suggest that the Evershed-effect is turning downwards at the penumbra border [54]. We check for a correlation between the magnitude of the down-flow at a certain position at the penumbra border and the intensity of the filament ending at that location. We do not find any correlation, which is consistent with our previous finding that there is no correlation between plasma flow and intensity of the filament.

5.4 Outlook

Our observations disagree, at least in part, with most of the proposed theoretical models. Therefore, work has to be done to refine and improve these models in a way that accommodates the new results. Only when this improvements have been done, there will be new theoretical predictions that can be tested with observations.

From a purely observational point of view, the following improvements are possible: the seeing for the dopplergram and the spectrograph run was not excellent. We estimate, that we only reach a resolution of about 60 percent of the maximum in the dopplergram run and 25 percent in the spectrograph run. New observations during better seeing conditions could help to refine the results. Also, the use of a narrower slit in the spectrograph would provide a further gain in resolution and therefore in the limit of detection, but has the drawback of a much longer exposure-time. It seems doubtful whether any improvement can be achieved with this setup.
The largest improvement with the instruments used in this investigation could be made by changing the setup of the UBF observations to obtain magnetograms. It is possible to use the UBF in the dual mode for recording magnetograms, but it is impossible to obtain dopplergrams or residual intensity images at the same time with this setup. High-resolution magnetograms could confirm the connection between bright points and the magnetic field found by Berger [6]. Observing a sunspot with this setup should answer the controversial question of reduction of the magnetic field strength in umbral dots. This measurement would clearly allow to distinguish between the sunspot model of Weiss [29] who predicts no reduction in field strength or the sunspot model of Parker [42] who predicts umbral dots to be field-free.

The use of more elaborate instruments can provide more detailed information about the physical condition of the structures we have investigated. These instruments have e.g. the capability to measure the polarization of light in addition to the spatial and spectral information. These instruments are called polarimeters. Examples of polarimeters are the DLSP (Diffraction Limited Spector-Polarimeter) of the

Sacramento Peak Observatory, POLIS of the Kiepenheuer Institute or the TIP (Tenerife Infrared Polarimeter) of the IAC at the Canary Islands. The analysis of the polarization state of the incoming light can e.g. be used to obtain all three components of the magnetic field vector. Without this information, only the line-of-sight component can be determined. The extended information obtained with a polarimeter can be used to calculate various parameters like temperature, velocity and pressure in different heights of the solar atmosphere. This inversion process is not possible with the limited information recorded with the UBF.

The disadvantage of spectro-polarimeters is the fact that they require even longer exposure-times, since the light is divided into the different polarization states. Exposure times of ten seconds or more are common. The result of these long exposure-times is, that the degrading effects of the earth's atmosphere are even worse than for common filtergrams. Since it is not possible to obtain all the information simultaneously with a polarimeter, these instruments suffer from the degrading effects of residual seeing.

This leads to the most obvious improvement that can be made for all observations with all instruments mentioned in this investigation: build a better AO system. This is as hard as it sounds easy, but nevertheless there is high order AO system being built at the Sacramento Peak observatory and at the Big Bear Solar Observatory, that will be able to correct 50 Zernike modes. It will replace the old system in 2003. Especially in medium seeing conditions we expect a big improvement over the old system. The development of a multi-conjugate AO system that can correct atmospheric distortion in different heights is desirable since it will have a much larger iso-planatic patch. However, a project to technically difficult at the present time.

The last and most obvious way to enhance the measurements is to build solar telescopes with a larger aperture. As already mentioned in Chapter 1, there are already several project on the way to build solar telescopes with apertures of up to 4.0 m.

REFERENCES

1. Aballe Villero M.A., Marco E., Vazquez M., Garcia de la Rosa J.I. 1992, AAP 267, 275.

2. Bahng J. D. R., Danielson J.B., Rogerson J. B., Schwarzschild M., 1959, Astrophysical Journal 64, 323.

3. Beckers J.M., 1970 Appl. Opt. 9, 595.

4. Beckers J.M., Dickson L., Joyce R.S., 1975, AFCRL-TR-75-0090, No. 227.

5. Beckers J., 1993, Ann. Rev. Astron. Astrophys. 31, 13.

6. Berger T. E., Title A. M., 2001 , AJ 553, 449.

7. Berger T. E., Schrijver C. J., Shine R. A., Tarbel T.D., Title A. M., Scharmer G., 1995, AJ 454, 531.

8. Biermann L., 1941, Vierteljahresschr. Astr. Ges. 46, 194

9. Brandt P.N., 1970, Sol. Phys. 13, 287.

10. Bray R., Loughead R., 1965, *Sunspots*, John Wiley and Sons Inc.

11. Bruls J. H. M. J., von der Luehe O., 2001, A&A 366, 281.

12. Choudhuri A.R., 1986, AJ 302, 809-826.

13. Cope A.D., Luedicke E., Danielson R., Schwarzschild M, 1968 , Astrophysical Journal 73, 9.

14. Delbouille L., Roland G., Nieven L., 1989, *Photometrique Atlas of the Solar Spectrum (Univ. de Liege).*

15. Dorotovic I., Sobotka M., Brandt P., Simon G., 2002, A&A 387, 665.

16. Dunn R.B., Zirker J.B., 1973, Sol. Phys. 33, 281.

17. Evershed J., 1909, MNRAS 39, 454.

18. Fleck B., Domingo V., Poland A. (editors): *The SOHO Mission*, Kluwer, Dordrecht 1995.

19. Fraunhofer J., 1817, Denkschriften der Muench. Akad. der Wissenschaften 5, 193.

20. Grevesse N., Sauval A. J. 1973 A&A 27, 29.

21. Gossmann-Doerth U., Schmidt W. S, Schroeter E.H., 1986 A&A 156, 347.

22. Jansen J., 1892, L'Institut 37:I, 397.

23. Hale G. E., 1908, ApJ 28, 315.

24. Hirzberger J., Kneer F., 2001, A&A 378, 1078.

25. http://www.nso.edu/sunspot/dstwww/vttusers/instruments/horizontal-spectrograph/ hsg.html

26. Hunaerts J., 1947, Ann. d'Astr. 10, 237.

27. Kirchhoff, 1867, Astr. Nachrichten 69, 17.

28. Kneer F., 1973, Solar Phys. 28, 361.

29. Knobloch E., Weiss N.O., 1984, Mon. Not. R. astr. Soc. 207, 203.

30. Langhans K., Schmidt W., 2002, A&A 382, 312.

31. Lockyer N., Baxandall F., MNRAS 65, 25.

32. Lyot B., Annales d'Astrophysique 7, 31.

33. Mehltretter J.P., 1974, Sol. Phys. 38, 43.

34. Moore C. E., Minnaert M. G. J., Houtgast J., 1966, National Bureau of Standarts Monograph, Washington: US Gov. Printing Office.

35. Mueller R., 1984, Sol. Phys. 100, 237.

36. Mueller R., Roudier Th., 1984, Sol. Phys. 94, 33.

37. NASA, http://pwg.gsfc.nasa.gov/istp/outreach/workshop/bt/6.html

38. Noll R.J., 1976, J. Opt. Soc. Am. 66, 207.

39. Oehman Y., 1938, Nature 141,157.

40. Parker E.N., 1975, Sol. Phys. 40, 291.

41. Parker E. N., 1978, ApJ 221, 368.

42. Parker E.N., 1979, ApJ 230, 905.

43. Parker E.N., 1979, ApJ 230, 914.

44. Parker E.N., 1979, ApJ 234, 333.

45. Priest E., Forbes T., 2000, *Magnetic Reconnection*, Cambridge University Press.

46. Rimmele T., 1997, ApJ 490, 458.

47. Rimmele T., 2000, Proc. SPIE 4007, 218.

48. Rimmele T., 1998, Proc. SPIE Vol. 3353, p. 72.

49. Rutten R. J., Kiselman D., van der Voort L. R., Plez B., 2001, ASP Conf Ser. 236, 445.

50. Sanchez-Almeida J., Asensio-Ramos A., Trujillo-Bueno J., Cernicharo J., 2001, AJ 555, 978.

51. Schlichenmaier R., Jahn K., Schmidt H.U., 1998 A&A 337, 897.

52. Schlichenmaier R., Jahn K., Schmidt H.U., 1998 AJ 493, L12.

53. Schmidt W., Balthsar H., 1994, A&A 283, 241.

54. Schmidt W., Schlichenmaier R., 2000, A&A 364, 829.

55. Secchi P.A., *Die Sonne*, 1871.

56. Sobotka M., Brandt P.N., Simon G.W., 1997, A&A 328, 689.

57. Sobotka M., Brandt P.N., Simon G.W., 1999, A&A 348, 621.

58. Sobotka M., Brandt P.N., Simon G.W., 1997, A&A 328, 689.

59. Solanki K. S., Brigljevic V., 1992, A&A 262, L29.

60. Spruit H. C., 1979, Sol. Phys. 61, 363.

61. Stein R., Nordlund A., 1989, AJ 342, 95.

62. Stein R. F., Bercik D., 2003, ASP Conf. Ser. 286.

63. Steiner O., Hauschildt P. H., Bruls J., 2001, A&A 372, L13.

64. Steiner O., 1999, ASP Conf Ser. 184, 33.

65. Steiner O., Knoelker M., Schuessler M., 1994, NATO ASI Series C-433.

66. Stix M., *The Sun*, 2002 Springer.

67. Tritschler A., Schmidt W., 1997, A&A 321, 643.

68. Uitenbroek H., Calculations with RH-Code, http://www.nso.edu/PPAGES/uitenbr/rh.html

69. Uitenbroek H., Private Comunication 2001.

70. Uitenbroek H., 1998, AJ 498, 427.

71. Weiss N.O., 1990, IAUS 142 (A92-30901 12-92), 139.

72. Weiss N.O., 1993, Nature 362, 208.

73. Wiehr E., 1994, A&A 287, L1.

74. Withbroe G.L., 1967, ApJ 147, 1117.

75. Woehl H., Wittmann A., Schroeter E.H., 1970, Sol. Phys.13, 104.